Stellar Spiral Structures in Realistic Dark Matter Haloes

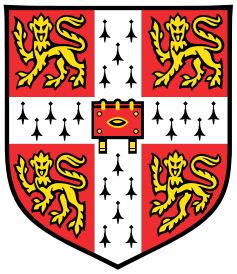

Shaoran Hu

Supervisor: Dr. Debora Sijacki

Institute of Astronomy
University of Cambridge

This dissertation is submitted for the degree of
Doctor of Philosophy

Churchill College October 2017

Abstract

In this Thesis, I explore the formation and evolution of stellar spiral structures embedded in realistic dark matter haloes with very high resolution simulations. I first study the impact of the shape of the dark matter haloes. I find that non-adiabatic changes to the dark matter halo shape, commonly found in cosmological simulations due to the assembly history of haloes, can trigger strong two-armed grand-design spiral structures extending from the inner disc to the outer region. The nature of the spiral structures is found to be consistent with kinematic density waves based on the study of their power spectra. Such grand-design spiral structures may help the formation of transient multi-armed spiral structures if the self-gravity in disc is strong enough. Evolution of spiral structures is similar when the disc and the halo are misaligned, although warps develop additionally. I further find a strong correlation between the torque strength from the halo and the strength of the corresponding spiral structures. In the second part of my Thesis I then study the influence of subhaloes by including them from realistic cosmological simulations. I identify five different massive subhaloes that hit the central region of the disc, two out of which hit the disc twice. Aside from disc heating, three distinct generations of spiral structures are found in the stellar disc, which can be related to different subhaloes. For each generation, counter-rotating single-armed spiral structures develop first. They wind up very quickly before two-armed spiral structures become prominent. These spiral structures are again identified as kinematic density waves. We find that rather than interacting with the disc through resonances, subhaloes preferentially trigger spiral structures impulsively, due to their relatively short impact time with the disc. The strength of spiral structures can be related to the integrated strength of the torque generated by subhaloes. The correlation between the torque strength exerted by a triaxial dark matter halo and by subhaloes and the spiral strength may provide constraints on the distribution of dark matter.

献给我的父母

Declaration

I hereby declare that This dissertation is the result of my own work and includes nothing which is the outcome of work done in collaboration except

- Chapter 3, which contains work in paper *'Stellar Spiral Structures in Triaxial Dark Matter Haloes'* published in Monthly Notices of the Royal Astronomical Society, Volume 461, p.2789-2808. This was conducted in collaboration with Dr Debora Sijacki.
- Chapter 4, which contains work in paper *'Impact of Cosmological Satellites on Stellar Discs: Dissecting One Satellite at a Time'* submitted to Monthly Notices of the Royal Astronomical Society. This was conducted in collaboration with Dr Debora Sijacki.

This dissertation is not substantially the same as any that I have submitted, or, is being concurrently submitted for a degree or diploma or other qualification at the University of Cambridge or any other University or similar institution except as declared in the Preface and specified in the text. I further state that no substantial part of my dissertation has already been submitted, or, is being concurrently submitted for any such degree, diploma or other qualification at the University of Cambridge or any other University or similar institution except as declared in the Preface and specified in the text. This dissertation contains fewer than 60,000 words including summary/abstract, tables, footnotes and appendices.

Shaoran Hu
October 2017

Acknowledgements

I wish to express my sincere gratitude to Dr Debora Sijacki, who kindly supervised my PhD project. Work carried out in this Thesis would be impossible without her supervision and support. I would also like to thank Prof. Cathie Clarke, Prof. Martin Haehnelt, Prof. Jim Pringle, Dr Denis Erkal, Prof. Christophe Pichon and many other people for their invaluable feedback on my project. I wish to thank my colleagues and office mates at the Institute of Astronomy, with whom I have had many interesting discussions and happy office times. I also want to thank Ms Margaret de Vaux, who offered me great help in the English language. Besides, I am very grateful to my friends for their help in so many ways in the past four years, especially to Di Jin, Lindsay Oldham and Harley Katz. Finally, I wish to thank my parents for their love and support.

Table of contents

List of figures

List of tables

Chapter 1

Introduction

1.1 General Introduction to Galaxies

Galaxies are systems that consist of stars, gas, dust and dark matter bounded by gravity. Galaxies were originally thought as "nebulae" within our own Galaxy, until Edwin Hubble studied the distance to classical Cepheid variables in the Andromeda Galaxy and proved that they are not part of the Milky Way. By the time Hubble (1926) classified galaxies based on their morphology, statistics of 400 galaxies were used. Since then the number of galaxies known to us has grown significantly with millions of galaxies found in large galactic surveys. For instance, the Baryon Oscillation Spectroscopic Survey (BOSS, Dawson et al., 2013) covered 1.5 million galaxies with redshift $z < 0.7$, while its successor, the extended Baryon Oscillation Spectroscopic Survey (eBOSS, Dawson et al., 2016) is expected to add 250,000 more galaxies to it. In total, the Sloan Digital Sky Survey (SDSS) observed spectra of more than 2.4 million galaxies in their 12th release (Alam et al., 2015). The Dark Energy Survey (DES, Dark Energy Survey Collaboration et al., 2016) had found about 100 million galaxies by December 2015 with redshift up to $z \sim 6$, and is expected to find 300 million galaxies by completion. The Large Synoptic Survey Telescope (LSST, Ivezic et al., 2008) is expected to observe 10 billion galaxies. To the high-redshift end, McLure et al. (2013) studied the luminosity function of galaxies at $z = 7$ and $z = 8$ with a sample of 576 high redshift galaxies ($z \sim 6.5$-10) using the Hubble Space Telescope (HST) Ultra-Deep Field 2012 (UDF12) campaign. McLeod et al. (2016) studied a catalogue of 33 galaxy candidates at $z \geq 8.4$ from the Hubble Frontier Fields (HFF) and the Cluster Lensing And Supernova survey with Hubble (CLASH) surveys. These studied have shed light on the early evolution of galaxies.

1.1.1 Classification of Galaxies

The morphology of galaxies varies considerably. One of the early and influential attempts to classify the galaxies based on their appearance is the so-called Hubble sequence (Hubble, 1926), as shown in Figure 1.1. In the Hubble sequence galaxies are classified as

- elliptical galaxies that look visually like ellipses, including subcategories from E0 to E6 based on their ellipticity,
- spiral galaxies without a bar, including Sa, Sb, and Sc types which have tightly wound, less tightly wound and loosely wound spiral structures, respectively,
- spiral galaxies with a bar, including SBa, SBb and SBc based on the winding of the spiral structures similar to above,
- lenticular galaxies S0, and
- irregular galaxies with or without bars, IBm and Im, respectively.

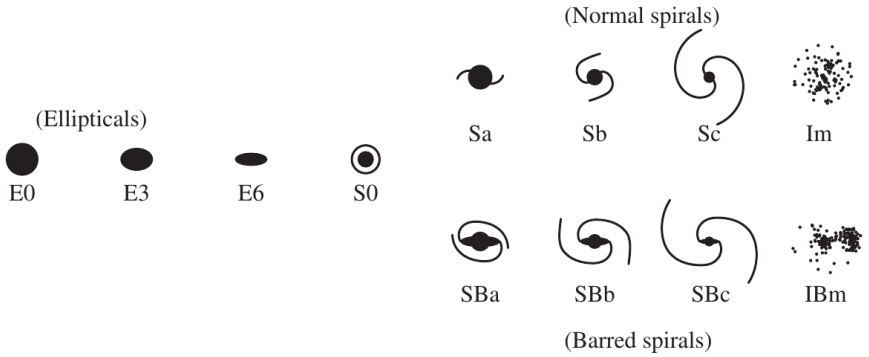

Fig. 1.1 An illustration of the Hubble sequence taken from Abraham (1998). Galaxies are classified according to their morphology, i.e. if they appear elliptical, have a disc component and if a bar structure is present.

A widely used extension of the Hubble sequence is introduced in de Vaucouleurs (1974). In this extension, ring structures are taken into consideration and finer sub-types of spiral and irregular galaxies are added. A beautiful example of such a classification, created by the recent imaging and spectroscopic survey of nearby galaxies KINGFISH (Kennicutt et al., 2011), is shown in Figure 1.2.

It is also common to refer to elliptical galaxies and lenticular galaxies as “early-type” galaxies, spiral galaxies as “late-type” galaxies and irregular galaxies and galaxies with an on-going merger as “peculiar” galaxies. However, this does not mean that galaxies simply evolve

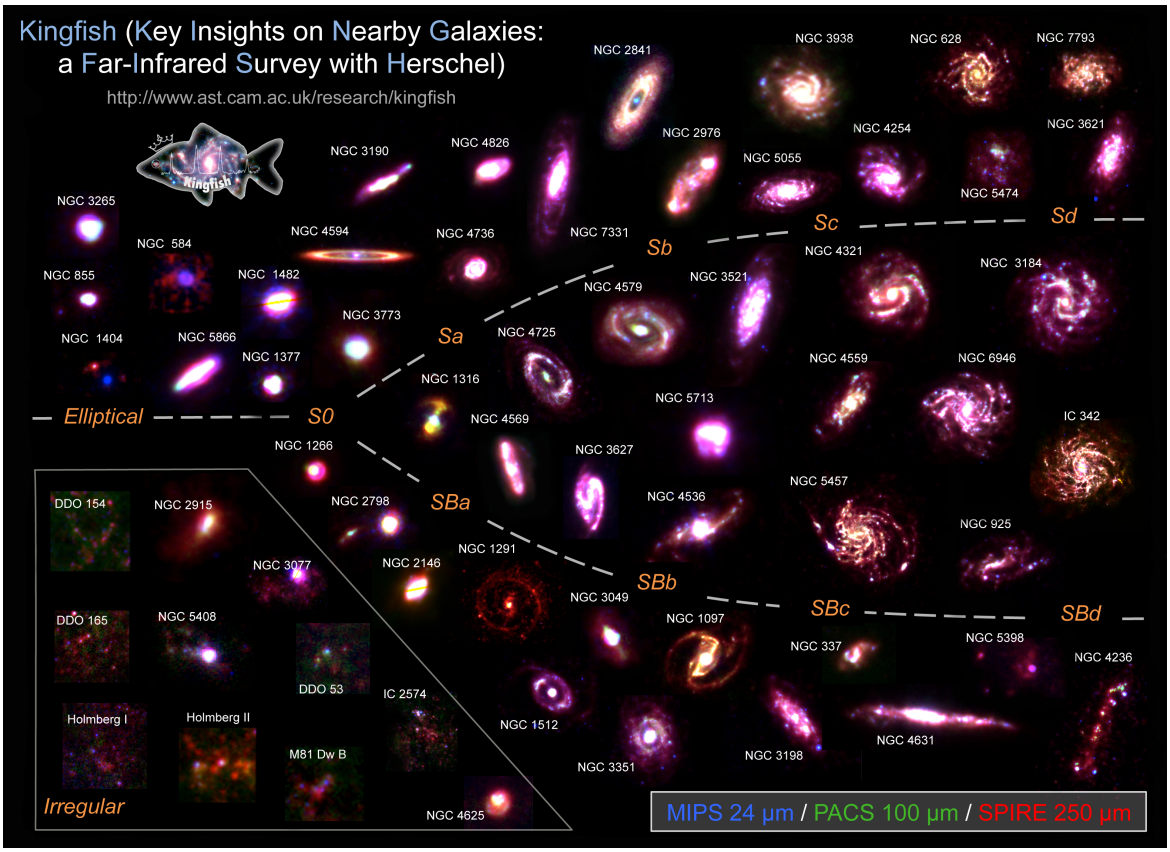

Fig. 1.2 KINGFISH Hubble tuning fork. The image shows more than 60 nearby galaxies classified into the Hubble sequence. Three colours, blue, green and red, trace the dust of different temperature, from warm to cold. The Sd and SBd classes are for spiral galaxies with broken arms and very faint bulges, introduced by de Vaucouleurs. This diagram is taken from http://www.ast.cam.ac.uk/ioa/research/kingfish/Site_3/KINGFISH_Hubble_tuning_fork.html.

from left to right along the Hubble sequence. The formation and evolution of galaxies is more complex due to the interplay of many factors, including star formation, stellar feedback, cosmic gas accretion and mergers. In fact, the morphological mix of galaxies is different at higher redshifts relative to the local Universe. At the massive end, Buitrago et al. (2013) showed that there were more late-type galaxies and peculiar galaxies before $z \sim 1$, while elliptical galaxies became predominant after $z \sim 1$. For all galaxies, it was found that at a higher redshift ($z \sim 3$), peculiar galaxies are predominant, with early- and late-type galaxies taking up only a small fraction (Conselice et al., 2005; Mortlock et al., 2013). As shown in Fig. 1.3, the fraction of disc (shown in the middle panel) and elliptical (shown in the left panel) galaxies grows significantly from $z \sim 3$ to $z \sim 1$.

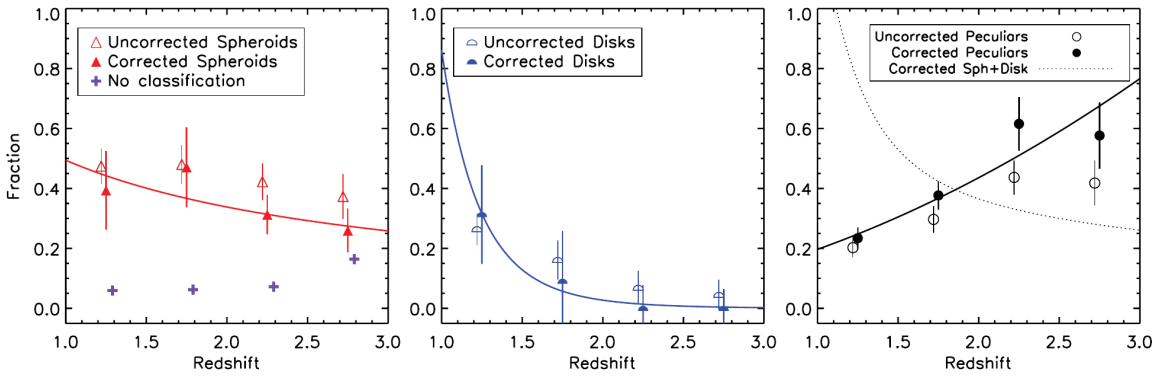

Fig. 1.3 The evolution of fractions of different galaxies from $z \sim 3$ to $z \sim 1$. At $z \sim 3$, peculiar galaxies (in black circles) represent the majority of galaxies, with some elliptical galaxies and few disc galaxies. The fraction of disc and elliptical galaxies increases significantly at lower redshifts and is dominant at $z \sim 1$. The figure is taken from Mortlock et al. (2013).

1.1.2 Statistics of Galaxies

Before discussing the properties of disc galaxies — the subject of study in this Thesis — in detail, we briefly review some general properties of galaxies. One of the most obvious and fundamental properties of galaxies is their luminosity. The luminosity of galaxies varies across about 10 orders of magnitude, e.g. in the B band the absolute magnitudes range from $\mathscr{M}_{\rm B} \approx -1$ to $\mathscr{M}_{\rm B} \approx -25$. The statistic of the luminosity of galaxies per unit volume is described by the luminosity function $\phi(L)$, which usually follows a power-law at the faint end but falls exponentially at the bright end and can be generally fitted by the Schechter function (Schechter, 1976)

$$\phi(L)\mathrm{d}L = \phi^* \left(\frac{L}{L^*}\right)^{\alpha} \exp\left(-\frac{L}{L^*}\right) \frac{\mathrm{d}L}{L^*}, \tag{1.1}$$

where L^* is the scale factor of luminosity, α is the shape parameter, and ϕ^* is the normalisation factor. An example of r-band luminosity function from the Galaxy and Mass Assembly (GAMA) project is shown in Fig. 1.4, where the Schechter function provides a good fit to the observational data.

The physical size of galaxies varies as well. For a given luminosity and redshift bin, the size of galaxies generally follows a log-normal distribution (Shen et al., 2003). The median size of galaxies evolves over redshift: as shown in Fig. 1.5, the effective radius of galaxies increases gradually from $z \sim 3$ to $z \sim 0$ (Trujillo et al., 2007; Buitrago et al., 2008). At $z \sim 3$, the mean effective radius is only 31% of the current value for disc-like galaxies and 14% of the current value for spheroid-like galaxies.

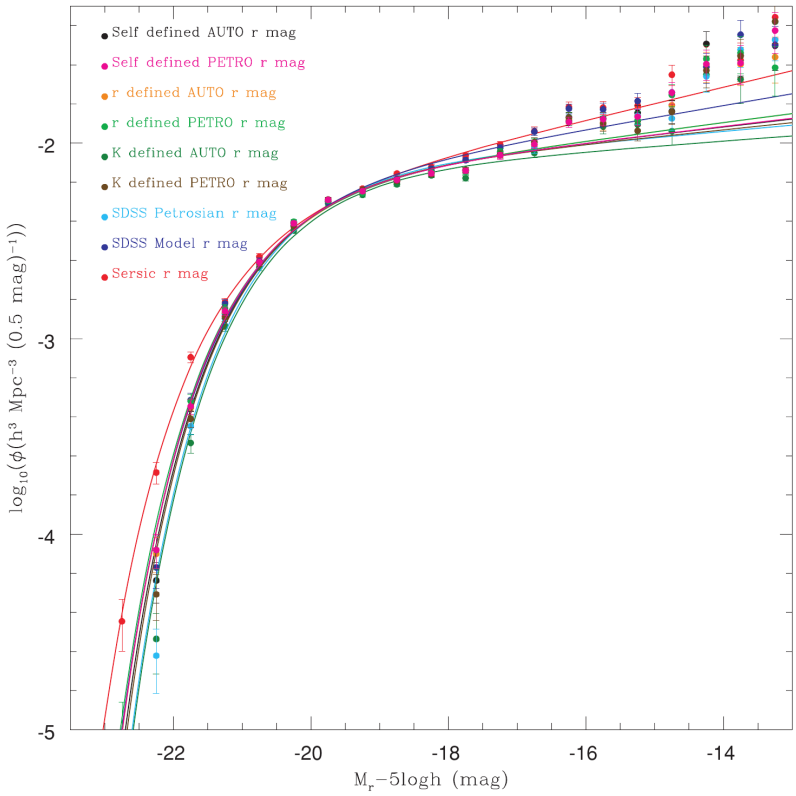

Fig. 1.4 The galaxy luminosity function in the r-band, adapted from Hill et al. (2011). The log of luminosity function ϕ is plotted against the magnitude of the galaxies. The observational data are shown with symbols of different colours representing different aperture definitions for the calculation of luminosity, while their best-fitting Schechter functions are shown with solid curves with corresponding colours. Depending on the choice of aperture, the shape parameter α of the fitting function ranges from -1.203 to -1.063, while the magnitude scale parameter $M^* - 5\log_{10} h$ ranges from -21.142 to -20.596.

The colour of galaxies follows a double-peak distribution, which roughly divides galaxies into two populations. This is loosely related to the classification based on morphology as early-type galaxies are more likely to have old stellar populations and are hence generally red, while late-type galaxies are more likely to be star-forming and hence blue. The metallicity of the galaxies also varies. More massive galaxies are found to have a higher gas-phase metallicity (Tremonti et al., 2004).

As disc and elliptical galaxies have different dynamical structures, their physical properties also follow different scaling relations, namely, the Tully-Fisher relation for disc galaxies and the fundamental plane relation for the elliptical galaxies.

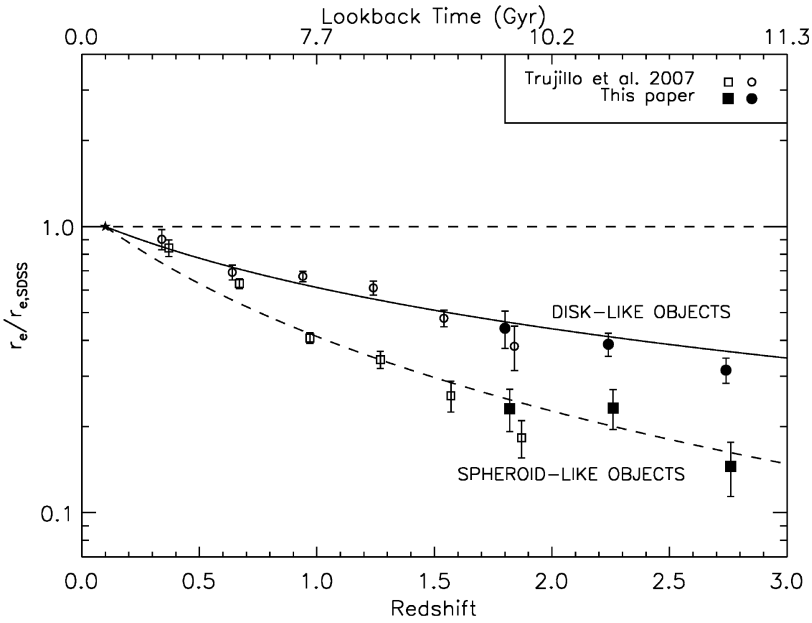

Fig. 1.5 The evolution of the effective radius, r_e, of galaxies from $z \sim 3$ to $z \sim 0$. r_e is in units of the median effective radius of galaxies in the local Universe $r_{e,SDSS}$ (as measured by Shen et al. 2003). Based on their morphology, galaxies are classified as disc-like (plotted as circles) and spheroid-like (plotted as squares). Data from Buitrago et al. (2008) (in solid symbols, noted as "This paper" in the legend) for $1.7 < z < 3$ exhibits a consistent trend as data from Trujillo et al. (2007) (in open symbols) for $z < 2$, showing a gradual growth in size for both disc-like and spheroid-like galaxies from $z \sim 3$ to $z \sim 0$. The figure is taken from Buitrago et al. (2008).

Disc Galaxies

Stars and gas are predominantly rotationally supported in disc galaxies. The rotational velocity is therefore an important property in these systems. The luminosity L and the maximum rotational velocity $V_{\rm max}$ are correlated, according to the Tully-Fisher relation (Tully & Fisher, 1977), i.e.

$$L = AV_{\rm max}^{\alpha}\,, \tag{1.2}$$

where A is a scale parameter and α is the slope of the relation. α typically ranges from 2.5 to 4. It has been further found that the relation between the baryonic mass and the rotational velocity is tighter, known as the baryonic Tully-Fisher relation (BTFR). As shown in Fig. 1.6, the BTFR holds tightly across more than 4 orders of magnitude in mass with a small scatter at the high mass end, and a scatter of ~ 1 dex at the low-mass end, where both rotational velocity and baryonic mass are less well constrained observationally.

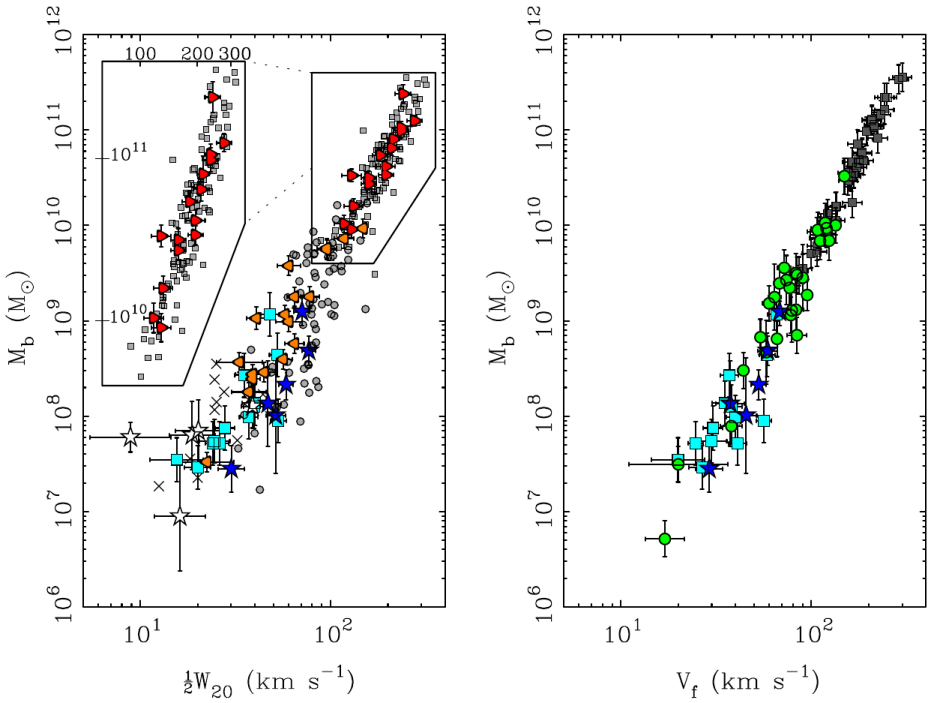

Fig. 1.6 The baryonic Tully-Fisher relation. The baryonic mass M_b of disc galaxies is plotted as a function of line width $\frac{1}{2}W_{20}$ (left) and the flat rotational velocity V_f (right). Both panels illustrate a tight relation over more than 4 orders of magnitude in baryonic mass. The relation between the baryonic mass and the flat rotational velocity is tighter, with a scatter of ~ 1 dex even at the low mass end. The figure is taken from McGaugh (2012).

Elliptical Galaxies

Faber & Jackson (1976) found that the luminosity L of elliptical galaxies is related to their velocity dispersion σ through a power law relation (known as the Faber-Jackson relation)

$$L \propto \sigma^4 \,. \tag{1.3}$$

It was later realised that more generally, the central velocity dispersion σ_e, the effective radius R_e, and the mean surface brightness Σ_e correlate tightly through a relation known as the fundamental plane (Dressler et al., 1987; Djorgovski & Davis, 1987), i.e.,

$$\log R_\mathrm{e} = a + b \log \sigma_\mathrm{e} + c \log \Sigma_\mathrm{e} \,, \tag{1.4}$$

where a, b and c are three fitting parameters. An example of the fundamental plane relation is shown in Fig.1.7. As shown in the figure, Cappellari et al. (2013) found $a = 0.193 \pm 0.0074$,

$b = 1.063 \pm 0.041$ and $c = -0.765 \pm 0.023$ for the ATLAS^{3D} sample of 260 local early-type galaxies, with a scatter of $\Delta = 0.091$ dex.

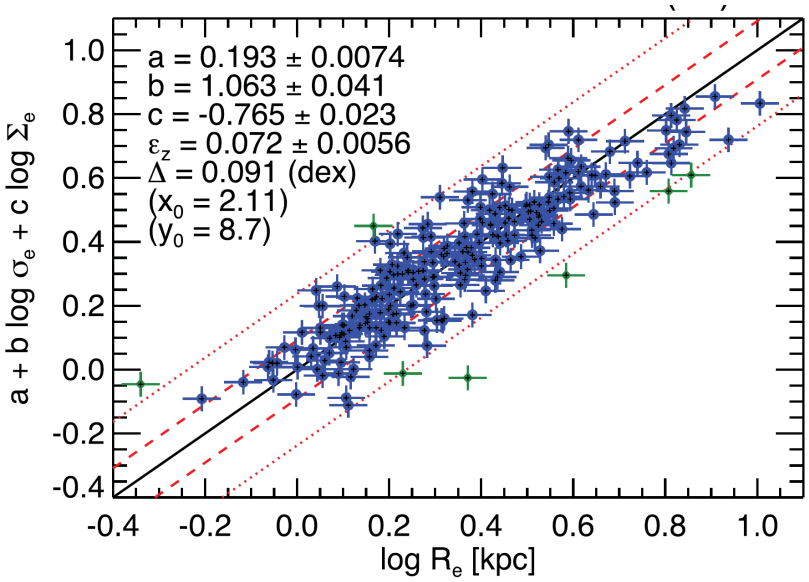

Fig. 1.7 Fundamental plane for elliptical galaxies. A combination of velocity dispersion σ_e and mean surface brightness Σ_e, is plotted against the effective radius R_e. Galaxies in the ATLAS^{3D} sample are plotted in blue symbols with the exception of outliers which are plotted in green. The best fit of the fundamental plane relation is plotted in black line, with 1σ and 2σ region shown with red dashed and dotted lines, respectively. The best fitting parameters are shown in the top left corner of the plot, along with residual error ε_z and the scatter Δ. This figure is taken from Cappellari et al. (2013).

1.1.3 The Milky Way

Our galaxy, the Milky Way, is a typical spiral galaxy, classified as SBc, i.e. a spiral galaxy with a bar and loosely wound spiral structures (Gerhard, 2002). It is hard to accurately measure the spatial scale and total mass of the Milky Way, but it is generally agreed that the Milky Way comprises mainly a thin stellar disc embedded in a dark matter halo. The stellar disc is estimated to have a mass of $\sim 5.5 \times 10^{10} M_\odot$ to $\sim 6.6 \times 10^{10} M_\odot$, a scale length of ~ 2.6 kpc to ~ 3.3 kpc, and a vertical scale height of ~ 0.3 kpc (Bissantz & Gerhard, 2002; McMillan, 2011; Jurić et al., 2008; López-Corredoira et al., 2002). The Sun is estimated to be 9 kpc away from the Galactic centre and orbiting the Galactic centre at a speed of ~ 220 km/s. Although still matter of debate, most studies have suggested that there are four spiral arms in the Milky Way (Vallée, 2005). The pitch angle of the spiral structures

is estimated to be 12-14 degrees. In this Thesis, the stellar discs are modelled with similar scale length as the Milky Way, but with slightly lower mass of typically $\sim 1 \times 10^{10} M_{\odot}$.

The Milky Way has many satellites, the biggest of which are the Large and Small Magellanic Clouds (LMC and SMC) and the Sagittarius Dwarf Spheroidal Galaxy (Sgr dSph). In terms of distance to the centre of the Milky Way, the Sgr dSph is about 20 kpc away, the LMC 50 kpc away and the SMC 60 kpc away. The LMC is the brightest with a luminosity of $2.2 \times 10^9 L_{\odot}$, while the SMC has a luminosity of $5.9 \times 10^8 L_{\odot}$ and the Sgr dSph $8.6 \times 10^7 L_{\odot}$ (Yniguez et al., 2014). Stellar streams are also found in the outskirts of the Milky Way (see e.g. Belokurov et al., 2006). These are long streams of stars formed due to the tidal stripping of the nearby global clusters and dwarf galaxies.

1.2 The Standard Cosmological Model

Before discussing models of galaxy formation, it is necessary to briefly review the standard model of cosmology. The present-day Universe is found to be in an accelerating state of expansion. In the local Universe, the velocity of the astronomical objects with respect to us is found to be roughly proportional to their distance to us, i.e. following Hubble's law

$$v = H_0 D\,, \tag{1.5}$$

where H_0 is the Hubble constant and v and D are the velocity and the distance of astronomical object to us, respectively. The accelerated expansion was first discovered through the study of type Ia supernovae at a higher redshift ($z \sim 1$) by the Supernovae Cosmology Project (Perlmutter et al., 1999) and the High-Z Supernova Search Team (Schmidt et al., 1998).

Currently, the most promising cosmological model is the ΛCDM model, which adopts Einstein's General Relativity and includes baryonic matter, cold dark matter and vacuum energy (cosmological constant) Λ. Formally, the expansion of the Universe can be described by an expansion factor, $a(t)$, which is a function of time t, such that the spatial scale $r(t)$ satisfies

$$\frac{r(t)}{a(t)} = \text{const}\,. \tag{1.6}$$

Therefore the expansion of distance r is related to the expansion factor through

$$\frac{\dot{a}}{a} = \frac{\dot{r}}{r}\,. \tag{1.7}$$

The Universe, assumed to be homogeneous and isotropic everywhere, can be described by the Friedmann-Lemaïtre-Robertson-Walker metric

$$\mathrm{d}s^2 = c^2\mathrm{d}t^2 - a^2(t)\left(\frac{\mathrm{d}r^2}{1-kr^2} + r^2\mathrm{d}\theta^2 + r^2\sin^2\theta\mathrm{d}\phi^2\right), \tag{1.8}$$

where k is the curvature of the space. When $k = 0$, this describes flatspace, while $k > 0$ gives a three-dimensional sphere, and $k < 0$ gives a three-dimensional saddle. The evolution of the scale factor follows the Friedmann equations

$$\left(\frac{\dot{a}}{a}\right)^2 = \frac{8\pi G}{3}\rho - \frac{k}{a^2} + \frac{\Lambda}{3}, \tag{1.9}$$

and

$$\frac{\ddot{a}}{a} = -\frac{4\pi G}{3}(\rho + 3p/c^2) + \frac{\Lambda}{3}, \tag{1.10}$$

where Λ is the cosmological constant, and ρ and p are the density and pressure of the homogeneous matter. As the scale a changes over time but mass is preserved, ρ and p must change with time as well. For a simple case with only non-relativistic matter, i.e. $k = \Lambda = 0$ and the mean matter density $\bar{\rho} \propto a^{-3}$, it follows that

$$a \propto t^{\frac{2}{3}}, \quad \bar{\rho} = \frac{1}{6\pi G t^2}. \tag{1.11}$$

The expansion rate at the present time t_0 is defined by the Hubble constant $H_0 = \frac{\dot{a}}{a}\big|_{t=t_0}$. Its value is often quoted in terms of the Hubble parameter h, so that $H_0 = 100h\,\mathrm{km}/(\mathrm{s}\cdot\mathrm{Mpc})$. A critical density ρ_{crit} is defined as $\rho_{\mathrm{crit}} = \frac{3H_0^2}{8\pi G}$, corresponding to the current density of matter assuming $k = \Lambda = 0$. In realistic cosmology models, the density of various components in the Universe can then be characterized as fractions of the critical density, with non-relativistic density parameter $\Omega_{\mathrm{m},0} = \rho_{\mathrm{m}}(t_0)/\rho_{\mathrm{crit}}$, radiation density parameter $\Omega_{\mathrm{r},0} = \rho_{\mathrm{r}}/\rho_{\mathrm{crit}}$, and dark energy density paramater $\Omega_\Lambda = \frac{\Lambda}{3H_0^2}$. The non-relativistic density parameter can be further divided as $\Omega_{\mathrm{m}} = \Omega_{\mathrm{b}} + \Omega_{\mathrm{c}}$, where Ω_{b} is the density parameter for baryonic matter and Ω_{c} for cold dark matter. With these, $a(t)$ should change with redshift as (using that the energy density of non-relativistic matter evolves as $\rho_{\mathrm{m}}c^2 \sim a^{-3}$ and of photons evolves as $\rho_{\mathrm{r}}c^2 \sim a^{-4}$)

$$\left(\frac{\dot{a}}{a}\right)^2 = \Omega_{\mathrm{m}}(1+z)^3 + \Omega_{\mathrm{r}}(1+z)^4 + \Omega_\Lambda + (1-\Omega_{\mathrm{m}}-\Omega_{\mathrm{r}}-\Omega_\Lambda)(1+z)^2, \tag{1.12}$$

where redshift z is related to the expansion factor a through

$$z = \frac{1}{a} - 1\,. \tag{1.13}$$

The Universe started with the Big Bang and underwent a process of exponential expansion known as inflation. The inflation resulted in a near flat, homogeneous and isotropic Universe dominated by radiation. Also as a result of inflation, quantum fluctuations that were initially present grew larger. The spectrum of fluctuations, $\mathscr{P}_R$, of the spatial curvature, R, as a function of scale, k, can be approximated by a power-law function

$$\mathscr{P}_R = A_\mathrm{s}\left(\frac{k}{k_*}\right)^{n_\mathrm{s}-1}, \tag{1.14}$$

where A_s is the perturbation amplitude, n_s is the spectral index, and k_* the scale factor. At this stage the Universe was very hot and baryonic matter (e.g. electrons and protons) was ionized. Due to the high temperature, electrons and photons were coupled through Thomson scattering. This scattering can be quantified by the optical depth τ. As the Universe expanded and cooled, electrons and protons combined and formed neutral hydrogen, and photons decoupled from the electrons. Photons from this decoupling are observed as the Cosmic Microwave Background (CMB) radiation. The characteristic angular size of fluctuations in the CMB radiation is quantified by the acoustic scale θ_*.

Six key parameters are used to describe the ΛCDM model, namely the baryonic density parameter, Ω_b, the cold dark matter density parameter, Ω_c, the acoustic scale parameter, θ_*, the optical depth of Thomson scattering, τ, the spectral index, n_s, and the fluctuation amplitude, A_s. These parameters can be constrained by observations of the CMB radiation. The observed CMB radiation is a nearly homogeneous with a spectrum very close to a black body of temperature $T = 2.725\,\mathrm{K}$. Considering the temperature map of the CMB, the main anisotropy is a dipole resulting from the movement of the Local Group. With this removed, the small remaining anisotropies contain useful information to constrain the ΛCDM model. In fact, the temperature fluctuation can be expanded on a basis of spherical harmonic functions, Y_{lm},

$$\frac{\Delta T}{T}(\theta,\phi) = \sum_{l,m} a_{lm} Y_{lm}(\theta,\phi)\,, \tag{1.15}$$

where $\Delta T = T(\theta,\phi) - \bar{T}$ is the difference to mean temperature with the dipole component removed, and a_{lm} are the factors in this expansion. The power spectrum $C_l = \sqrt{\frac{1}{m}\sum_m \left|a_{lm}^2\right|}$ describes the fluctuation of the CMB temperature on different scales, which can be related to different properties of the Universe at the time of decoupling. With a high quality

measurement of the CMB radiation, the Plank collaboration (Planck Collaboration et al., 2016) estimated the six cosmological parameters to be

$$\Omega_{\rm b}h^2 = 0.02225 \pm 0.00016, \tag{1.16}$$
$$\Omega_{\rm c}h^2 = 0.1198 \pm 0.0015, \tag{1.17}$$
$$100\theta_* = 1.04077 \pm 0.00032, \tag{1.18}$$
$$\tau = 0.079 \pm 0.017, \tag{1.19}$$
$$\ln(10^{10}A_{\rm s}) = 3.094 \pm 0.034, \tag{1.20}$$
$$n_{\rm s} = 0.9645 \pm 0.0049. \tag{1.21}$$

1.3 Dark Matter Haloes

Aside from the CMB observations introduced in Section 1.2, there is other evidence for the existence of dark matter as well. One is the rotation curves of disc galaxies, which are found to be low in the centre, to increase with radii in the intermediate region of the disc, and to be roughly constant in the outer parts of the disc. The mass of the disc, which falls exponentially with radius, cannot account for the flat part of the rotation curve; hence matter that does not emit light must be present in the outer parts of galaxies. It is commonly believed that most stellar discs are embedded in a dark matter halo. In fact, observational results indicate that, the total mass and spatial extent of the dark matter halo can be much larger than the total mass and the spatial extent of the baryonic component in disc galaxies (Roberts & Rots, 1973). In this section I briefly review our knowledge of dark matter haloes.

1.3.1 Collisionless Dynamics

Dark matter haloes form through gravitational collapse. In the standard cosmological model, the cold dark matter is collisionless. The evolution of the system, i.e. the density and velocity distribution of the system over time, can be generally described by the distribution function $f(\mathbf{x},\mathbf{v},t)$, where $\mathbf{x}$ is the spatial coordinate and $\mathbf{v}$ is the velocity. The density distribution can be obtained by integrating over the velocity space, $\rho(\mathbf{x},t) = m\int f(\mathbf{x},\mathbf{v},t)\,{\rm d}^3\mathbf{v}$, where m is the mass of each particle. The dynamics of the collisionless system is governed by the Collisionless Boltzmann Equation

$$\frac{\partial f}{\partial t} + \sum_i v_i \frac{\partial f}{\partial x_i} - \sum_i \frac{\partial \Phi}{\partial x_i}\frac{\partial f}{\partial v_i} = 0\,, \tag{1.22}$$

where Φ is the gravitational potential, obeying the Poisson equation

$$\nabla^2 \Phi(\mathbf{x}) = 4\pi G \rho(\mathbf{x}) \,. \tag{1.23}$$

By integrating equation (1.22) over velocity space, we get

$$\frac{\partial n}{\partial t} + \sum_i \frac{\partial}{\partial x_i} \left[n \left\langle v_i \right\rangle \right] = 0 \,, \tag{1.24}$$

where n is the number density field and $\langle v_i \rangle$ is the mean velocity field. This describes the conservation of mass of the system. By multiplying equation (1.22) with v_j and integrating over the velocity space, we get

$$\frac{\partial}{\partial t} \left[n \left\langle v_j \right\rangle \right] + \sum_i \frac{\partial}{\partial x_i} \left[n \left\langle v_i v_j \right\rangle \right] + n \frac{\partial \Phi}{\partial x_j} = 0 \,, \tag{1.25}$$

where $\left\langle v_i v_j \right\rangle$ is the mean $v_i v_j$ field. This equation relates the second moment of the velocity field with the streaming velocity and the potential. Equation (1.24) and (1.25) are known as Jeans Equations. As we will see later in Section 2.3.1, they can be used to access the velocity dispersions of a stellar disc, which is also considered as a collisionless system.

Further integrating equation (1.25) over spatial coordinate gives the tensor virial theorem,

$$\frac{1}{2} \frac{\mathrm{d}^2 I_{jk}}{\mathrm{d}t^2} = 2K_{jk} + W_{jk} + \Sigma_{jk} \,, \tag{1.26}$$

which describes the relation between

- the inertia tensor $I_{jk} = \int \rho x_j x_k \, \mathrm{d}^3\mathbf{x}$,
- the kinetic energy tensor $K_{jk} = \frac{1}{2} \int \rho \left\langle v_j v_k \right\rangle \mathrm{d}^3\mathbf{x}$
- the Chandrasekhar potential energy tensor $W_{jk} = -\int \rho x_k \frac{\partial \Phi}{\partial x_j} \mathrm{d}^3\mathbf{x}$ and
- the surface pressure term $\Sigma_{jk} = -\sum_i \int x_k \rho \left\langle v_j v_i \right\rangle \mathrm{d}S_i$, where the integral is over the surface of the object.

Taking the trace of equation (1.26), we get the scalar virial theorem

$$\frac{1}{2} \frac{\mathrm{d}I}{dt^2} = 2K + W + \Sigma \,, \tag{1.27}$$

which establishes the relation between the moment of inertia, $I = \int \rho r^2 \, \mathrm{d}^3\mathbf{x}$, the kinetic energy, $K = \frac{1}{2} \int \rho \left\langle v^2 \right\rangle \mathrm{d}^3 \, \mathbf{x}$, the total gravitational energy, $W = \int \rho \mathbf{x} \cdot \nabla \Phi \, \mathrm{d}^3\mathbf{x} = -\frac{1}{2} \int \rho \Phi \, \mathrm{d}^3\mathbf{x}$ (when

external contributions to the gravitational energy are negligible), and the work done by external pressure, $\Sigma = -\int \rho \left\langle v^2 \right\rangle \mathbf{x} \cdot \mathrm{d}\mathbf{S}$.

For an equilibrium system where the work of external pressure and gravitational energy from external objects can be ignored (e.g. when the system can be considered isolated), equation (1.27) becomes

$$2K + W = 0\,. \tag{1.28}$$

This simple relation between the total kinetic and gravitational energy is useful for estimating large-scale quantities of systems like dark matter haloes.

1.3.2 Spherical Collapsing Model

After inflation, the Universe was highly homogeneous and isotropic, with small, linear density perturbations. They grew subject to gravitational attraction and a fraction of those became non-linear and collapsed into haloes when a given critical density was reached. The cold dark matter started building structures in this way before the baryonic matter as the latter was coupled with photons through Thomson scattering.

In the spherical collapse model (Gunn & Gott, 1972), an axisymmetric system consisting of spherical mass shells is studied. Here I describe a simple case where $\Lambda = 0$ and $\Omega_\mathrm{m} = 1$, but similar results can be obtained for more realistic cases. The acceleration of a thin shell of radius r is described by

$$\frac{\mathrm{d}^2 r}{\mathrm{d}t^2} = -\frac{GM}{r^2}\,, \tag{1.29}$$

where M is the mass enclosed in this shell, and G is the gravitational constant. The first integral of equation (1.29) is then

$$\frac{1}{2}\left(\frac{\mathrm{d}r}{\mathrm{d}t}\right)^2 - \frac{GM}{r} = \mathscr{E}\,, \tag{1.30}$$

where $\mathscr{E}$ can be thought as the effective total energy of the shell, which should be negative for the collapsing shells. The solution is

$$r(\theta) = A(1-\cos\theta)\,, \quad t(\theta) = B(\theta - \sin\theta)\,, \tag{1.31}$$

where θ is an angle parameter with $0 < \theta \leq 2\pi$, and A and B are constants satisfying $A^3 = GMB^2$ and $A^2/(2B^2) = -\mathscr{E}$. The shell starts from a small radius (meaning small t and θ as well), and expands to maximum radius r_max at time t_max. Based on equation (1.31) this happens when $\theta = \pi$, which means $t_\mathrm{max} = \pi B$ and $r_\mathrm{max} = 2A$. The radius falls to 0 when $\theta = 2\pi$. The collapsing time is defined as $t_\mathrm{col} = 2\pi B = 2t_\mathrm{max}$.

The second order expansion of equation (1.31) yields

$$r(\theta) = A\left(\frac{\theta^2}{2} - \frac{\theta^4}{24}\right), \tag{1.32}$$

$$t(\theta) = B\left(\frac{\theta^3}{6} - \frac{\theta^5}{120}\right). \tag{1.33}$$

Substituting θ with t gives (to second order)

$$r(t) = \frac{A}{2}\left[\left(\frac{6t}{B}\right)^{2/3} - \frac{1}{20}\left(\frac{6t}{B}\right)^{4/3}\right]. \tag{1.34}$$

The density within the shell is then

$$\rho = \frac{M}{\frac{4}{3}\pi r^3} = \frac{1}{6\pi G t^2}\left[1 + \frac{3}{20}\left(\frac{6t}{B}\right)^{2/3}\right]. \tag{1.35}$$

Equation (1.11) states that the mean density $\bar{\rho}$ in this matter-dominated Universe evolves as $(6\pi G t^2)^{-1}$. One can find the overdensity of the halo as

$$\delta = \frac{\rho - \bar{\rho}}{\bar{\rho}} = \frac{3}{20}\left(\frac{6t}{B}\right)^{2/3}. \tag{1.36}$$

This indicates that, at early times when t is small, the overdensity is small as well. At the time the shell expands to its maximum radius, $t_{\rm max} = \pi B$, hence $\delta = 1.06$, and at the time of collapse $t_{\rm col} = 2\pi B$, hence $\delta_{\rm c} = 1.69$. As will be mentioned in Section 1.3.3, $\delta_{\rm c}$ is usually used as a criterion to determine if an overdense region will finally collapse.

More realistically, shells do not fall to $r = 0$ at the collapse time. During the collapse each shell experiences many shell crossings which relax the system. It is generally assumed that by the collapse time $t_{\rm col}$, the system undergoes so many shell crossings that it is in equilibrium, i.e. virialized. To calculate the overdensity of the virialized halo, based on the virial theorem, the halo should satisfy $2K_{\rm vir} + W_{\rm vir} = 0$, where $K_{\rm vir}$ is the kinetic energy and $W_{\rm vir}$ is the potential energy for the virialized halo. Roughly, $W = -\frac{GM}{r_{\rm vir}}$, where $r_{\rm vir}$ is the virial radius of the halo. The total energy of the system is

$$E = K_{\rm vir} + W_{\rm vir} = -\frac{GM}{2r_{\rm vir}}. \tag{1.37}$$

At the maximum radius before the collapse, the shell has no kinetic energy, therefore the total energy is

$$E = -\frac{GM}{r_{\rm max}}\,. \tag{1.38}$$

The conservation of energy therefore requires $r_{\rm vir} = r_{\rm max}/2 = A$, which means the mean density of the halo is

$$\rho_{\rm h} = \frac{M}{\frac{4}{3}\pi A^3}\,. \tag{1.39}$$

The overdensity of the halo is therefore

$$\delta = \frac{\rho_{\rm h} - \bar{\rho}}{\bar{\rho}} = \frac{18\pi GMB^2}{A^3} - 1 \approx 177\,. \tag{1.40}$$

Here we have used the relation that $A^3 = GMB^2$. We conclude that, for a virialized halo, the overdensity should be around 177.

In cosmological simulations, an overdensity of 200 is often used to quantify the boundaries of haloes. Typically, the virial radius, r_{200}, of a dark matter halo is defined as the radius of a sphere centred on the centre of the dark matter halo enclosing a region with an overdensity of 200 with respect to the critical density of the Universe. The virial mass, M_{200}, of the halo is defined as the mass enclosed in r_{200}, i.e.

$$M_{200} = \frac{4}{3}\pi r_{200}^3 \cdot 200\rho_{\rm crit}\,. \tag{1.41}$$

The virial velocity v_{200}, a quantity that characterizes the typical velocity amplitude, is related to M_{200} through virial theorem as

$$M_{200} = v_{200}^3/(10GH)\,. \tag{1.42}$$

1.3.3 Mass Function of Dark Matter Haloes

As shown in the previous section, at the time of collapse, $t_{\rm col}$, the critical density for a halo to collapse, $\delta_{\rm c}$, is roughly 1.686. Extrapolating the initial overdensity field $\delta_0(\mathbf{x})$ to time t, regions with overdensity $\delta(\mathbf{x},t) > \delta_{\rm c}$ will form a halo through collapse. This means that in the initial conditions, regions with $\delta_0 > \delta_{\rm c}(t_0)$ will collapse to form a halo at time t, where $\delta_{\rm c}(t_0)$ is the critical overdensity at the initial time, t_0, that will grow to $\delta_{\rm c} = 1.686$ at time t. To count the number of haloes exceeding a certain mass M, Press & Schechter (1974) smoothed the initial overdensity field $\delta_0(\mathbf{x})$ with a kernel function of mass scale M. Similarly to the argument above, regions where the smoothed overdensity field $\delta_{\rm s}(\mathbf{x},M)$ is larger than

$\delta_c(t)$ will collapse to form a halo with mass larger than M. As δ_s is a Gaussian field, its cumulative distribution function is therefore

$$\mathscr{P}(>\delta_c(t_0)) = \frac{1}{\sqrt{2\pi}\sigma(M)}\int_{\delta_c(t_0)}^{\infty}\exp\left[-\frac{\delta_s^2}{2\sigma^2(M)}\right]\mathrm{d}\delta_S\,, \tag{1.43}$$

where $\sigma(M) = \sqrt{\langle\delta_s^2(\mathbf{x},M)\rangle}$ is the standard deviation of δ_s with a kernel function of M. Although intuitively the mass distribution function for the haloes should be $F(>M) = \mathscr{P}(>\delta_c(t_0))$, a "fudge factor" of 2 should be added to the right hand side to account for the fact that half of the mass is originally in underdense regions but will accrete onto haloes nevertheless. Hence,

$$F(>M) = 2\mathscr{P}(>\delta_c)\,. \tag{1.44}$$

The number density of haloes in terms of mass is then

$$n(M,t) = \frac{\bar{\rho}}{M}\frac{\partial F(>M)}{\partial M} = \sqrt{\frac{2}{\pi}}\frac{\bar{\rho}}{M^2}\frac{\delta_c}{\sigma}\exp\left(-\frac{\delta_c^2}{2\sigma^2}\right)\left|\frac{\mathrm{d}\ln\sigma}{\mathrm{d}\ln M}\right|\,, \tag{1.45}$$

where $\bar{\rho}$ is the mean density at time t. If we define a dimensionless variable $\nu = \delta_c(t_0)/\sigma(M)$, the mass function can be then written as

$$n(M,t) = \frac{\bar{\rho}}{M^2}f_{\rm PS}(\nu)\left|\frac{\mathrm{d}\ln\nu}{\mathrm{d}\ln M}\right|\,, \tag{1.46}$$

where $f_{\rm PS}(\nu)$ is an universal shape function[1]

$$f_{\rm PS}(\nu) = \sqrt{\frac{2}{\pi}}\nu\exp(-\nu^2/2)\,. \tag{1.47}$$

Compared to N-body simulations, the Press-Schechter formalism (equation 1.47) is found to overpredict the abundance of low mass haloes and to underpredict high-mass haloes. Based on N-body simulations, several empirical fitting formulas have been suggested, including Sheth & Tormen (1999):

$$f_{\rm Sheth}(\nu) = 2A\left(1+\frac{1}{\nu'^{2q}}\right)\left(\frac{\nu'^2}{2\pi}\right)^{1/2}\exp\left(-\frac{\nu'^2}{2}\right)\,, \tag{1.48}$$

[1]In some works (e.g. Sheth & Tormen, 1999) $\nu f_{\rm PS}(\nu)$ is used instead of $f_{\rm PS}(\nu)$. In this Thesis I adopt $f_{\rm PS}(\nu)$.

where $\nu' = \sqrt{a}\nu$, $a = 0.707$, $q = 0.3$ and $A \approx 0.322$ are fitting parameters; Jenkins et al. (2001):

$$f_{\rm Jenkins}(\sigma) = 0.315 \exp(-\left|\ln \sigma^{-1} + 0.61\right|^{3.8}), \tag{1.49}$$

and Warren et al. (2006):

$$f_{\rm Warren}(\sigma) = A\left(\sigma^{-a} + b\right) e^{-c/\sigma^2}, \tag{1.50}$$

where the best fit is $A = 0.7234$, $a = 1.625$, $b = 0.2538$ and $c = 1.1982$. In fact, using a more detailed model accounting for the ellipsoidal shape of the collapsing halo, Sheth et al. (2001) showed that the calculated shape function f should be in a form of equation (1.48) suggested by Sheth & Tormen (1999). A comparison of the original, spherical collapse model to the ellipsoidal collapse model is shown in Fig. 1.8. As shown in the plot, the latter model provided a better fit to the the mass function obtained from N-body simulations.

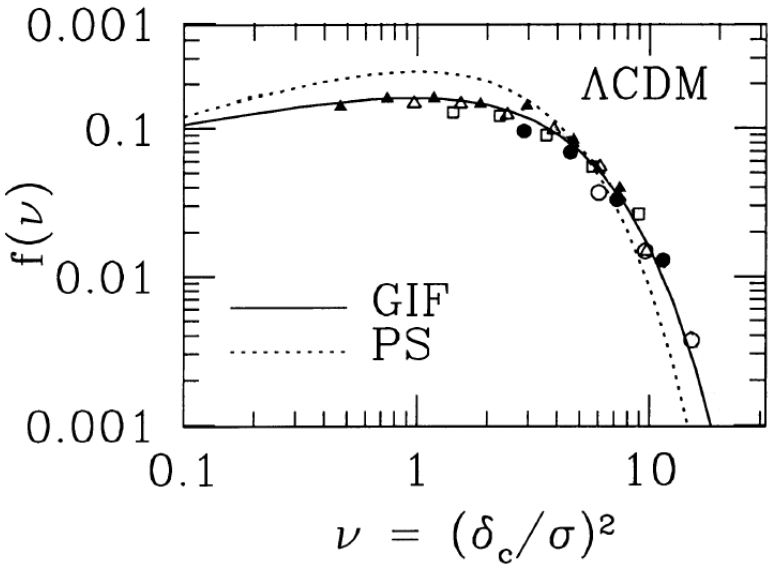

Fig. 1.8 Comparison of Press-Schechter's formula for the halo mass function of the spherical collapse model (dotted line noted as "PS"; following equation 1.47) and ellipsoidal collapse model (solid line noted as "GIF"; following Sheth & Tormen (1999), i.e. equation 1.48). The logarithm of the mass shape function f (as in equation 1.44) is plotted against the logarithm of ν. The simulation results of Sheth & Tormen (1999) are also plotted with symbols, with filled triangles, open triangles, open squares, filled circles and open circles representing $z = 0$, 0.5, 1, 2 and 4, respectively. The ellipsoidal model clearly gives a much better prediction, indicating the ellipsoidal nature of dark matter haloes. The plot is adapted from Sheth & Tormen (1999).

The match with N-body simulations suggests that dark matter haloes may be generally elliptical. Indeed, as will be discussed in Section 2.3.3, cosmological simulations generally find triaxial dark matter haloes rather than spherical ones. Form a theoretical point of view, Bardeen et al. (1986) found that the initial Gaussian perturbation field is already elliptical. It also results that the shape and alignment of the dark matter haloes are affected by the environment. Influenced by the tidal force of larger structures, the major axes of dark mater haloes align preferentially with large-scale filaments (e.g. Bailin & Steinmetz, 2005). The inner halo, however, can be more affected by baryons. Bailin et al. (2005) found that when galactic discs were included in simulations that were dark matter only originally, the inner halo ($r < 0.1r_{\rm vir}$) aligned with the disc, while the outer region ($r > 0.1r_{\rm vir}$) of the dark matter halo was almost unaffected. Also, the inner halo became rounder in simulations with baryons (e.g. Dubinski, 1994; D'Onghia et al., 2010; Zemp et al., 2012; Bryan et al., 2013; Zhu et al., 2016). The triaxiality of the dark matter halo could generate global tidal torques on the stellar disc, which may affect the formation of spiral structures. We study such an effect in Chapter 3.

1.3.4 Hierarchical Formation of Dark Matter Haloes

During the collapse of dark matter haloes, inhomogeneity develops, resulting in more and more mass leaving the low-density region and joining the high density region. This leads to a cosmic web, where most of the dark matter is distributed in "walls" and "filaments". Cosmic filaments further accelerate the clustering of mass and intersect to form knots of high density, where dark matter haloes interact with each other. Baryonic matter, after decoupling from the photon field, joins the clustering process and forms high-density regions inside these haloes. Within the cold dark matter scenario, small galaxies form first and merge into larger objects, which is known as the hierarchical (or bottom-up) galaxy formation model.

Lacey & Cole (1993) showed that the merger history of a halo can be estimated analytically by extending Press & Schechter (1974)'s approach based on two observations: a) $\delta_{\rm c}(t_0)$, the critical overdensity at the initial time that will grow to $\delta_{\rm c} = 1.686$ at time t, decreases over time, because the overdensity field increases as a function of time t, and b) the variation $S = \sigma^2(M)$ of the smoothed overdensity field $\delta(\mathbf{x}, M)$ decreases as M increases. At a certain location, the smoothed overdensity is a function of the smooth kernel mass M and therefore a function of the variation of the field S, as illustrated in Fig. 1.9. At a certain time, haloes form from the matter at this location if a horizontal line of $\delta = \delta_{\rm c}(t_0)$ intersects with the trajectory. The mass of the halo is decided by the maximum mass at the intersections, i.e. the minimum value of S. Over time, the critical overdensity decreases from top to bottom, while its corresponding value of S jumps when there are smaller possible values of S corresponding

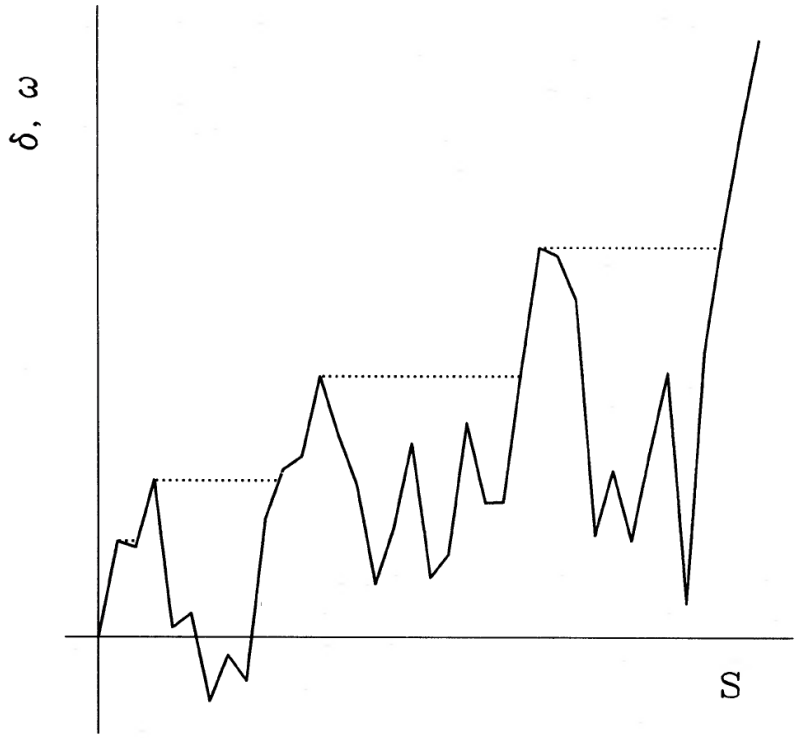

Fig. 1.9 The smoothed overdensity δ (solid curve) and the halo overdensity ω (dashed curve) as a function of the variation S of the smoothed overdensity field. The initial overdensity required to form a halo decreases over time, making jumps in S when there are smaller possible S values, i.e. when the halo becomes part of a larger halo. The merger history can be inferred through walking from top to bottom following the dashed curve. This figure is taken from Lacey & Cole (1993).

to the same overdensity value, as indicated by the dashed curve. Physically, these jumps are events where the halo becomes part of a larger halo, i.e. merger events. By studying the global statistics of these jumps, merger rates of haloes can be estimated.

It is also straightforward to evaluate merger history in cosmological simulations. An illustration of such hierarchical structure formation in the Millennium Run (Springel et al., 2005b) is shown in Fig.1.10. A simulated galaxy with stellar mass $M_* = 3.4 \times 10^{11}\,\mathrm{h}^{-1} M_\odot$ at $z = 0$ is found to be the result of hierarchical mergers of progenitors, which initially formed as early as $z \sim 10$.

1.4 Baryonic Effects

Baryons are important in determining the properties of galaxies. Gas is initially heated by virial shocks when it falls into a dark matter halo. Depending on the mass of the parent

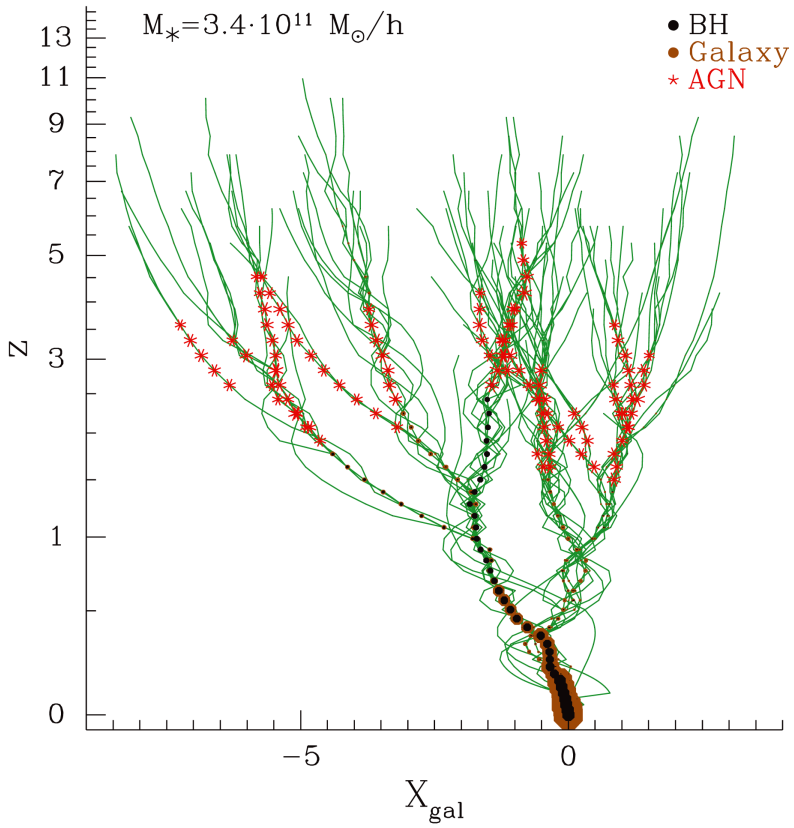

Fig. 1.10 A merger tree of a simulated galaxy in the Millennium Run. Each branch represents a galaxy evolving over redshift (from top of the plot to bottom) that later merges with a larger galaxy. The horizontal axis shows the displacement of the progenitor galaxies with $X_{\rm gal} = \sum_{i=1}^{3}(x^i_{\rm gal} - x^i_{\rm cur})$, where $x^i_{\rm gal}$ and $x^i_{\rm cur}$ are the i-th coordinate of the progenitor galaxies and the merged galaxy at $z = 0$, respectively. The red stars show the evolution of active galactic nuclei (AGN). The brown and black dots represent stars and black holes in the galaxy, with the size of the dots proportional to the the masses of the corresponding component. This plot illustrates the hierarchical formation of galaxies, with smaller galaxies forming first and merging into larger ones. The figure is taken from Marulli et al. (2009).

halo and on the hydrodynamical state of gas, it may then cool through radiative cooling[2]. The pressure of the cool gas is less effective in holding it against gravity, leading to further condensation and ultimately to the formation of stars. The efficiency of star formation is in turn constrained by other heating (and cooling) sources including the UV background and the feedback from stars and active galactic nuclei (AGN). In this section we review the above-mentioned baryonic physics that effects the formation of galaxies.

[2]Note that some gas has such a short cooling time that it is not effectively shock heated as it accretes onto the halo.

1.4.1 Heating and Cooling of the Primordial Gas

As measured from the CMB radiation, when the electrons decoupled from the photons, their temperature was less than $3\,K$, while observations indicate that gas in galaxies can be as hot as $10^6 \sim 10^7\,\mathrm{K}$. Frenk et al. (1990) showed with N-body simulations that the infall of matter into galaxy clusters can create a large amount of kinetic energy, which can then be transferred into thermal energy in the gas through shock heating, leading to hot gas with temperature distribution matching the observations.

At such high temperatures, gas cools through radiative cooling, which involves multiple reactions including collisional excitation, collisional ionization, recombination, dielectric recombination, and free-free emission (see e.g. Black, 1981; Katz et al., 1996). These processes jointly reduce the temperature of the gas and radiate the energy away with photons. As the time for reaching ionization equilibrium is typically shorter than the dynamical time of gas, it is generally assumed that ionization equilibrium is reached when considering the cooling rate of the gas in many cosmological simulations.

1.4.2 Jeans Instability and Star Formation

When the gas cools, it loses pressure support and starts to collapse as a result of Jeans' instability. Considering a cloud of gas, the time for sound wave to cross a cloud of gas is

$$t_\mathrm{s} \sim R/c_\mathrm{s}\,, \tag{1.51}$$

where R is the radius of the cloud and c_s is the sound speed. This time characterises the time for the cloud to respond to a perturbation by changing pressure. The free-fall time for the cloud is

$$t_\mathrm{ff} = \sqrt{\frac{3\pi}{32G\rho}}\,, \tag{1.52}$$

where G is the gravity constant and ρ is the mean density of the cloud. If $t_\mathrm{ff} < t_\mathrm{s}$, then a perturbation will cause the cloud to collapse before the pressure can react and resist it. This yields a typical scale known as the Jeans length

$$\lambda_\mathrm{J} \sim \sqrt{\frac{k_\mathrm{B}T}{G\mu\rho}}\,, \tag{1.53}$$

where $k_{\rm B}$ is the Boltzmann constant, T is the temperature of the gas, and μ is the mean molecular weight. The Jeans mass is the mass enclosed within the Jeans length

$$M_{\rm J} = \frac{4}{3}\pi\lambda_{\rm J}^3\rho\,. \tag{1.54}$$

Clouds with mass larger than the Jeans mass are subject to Jeans' instability. However, clouds do not collapse indefinitely. During collapse, the temperature increases, and eventually may become high enough to trigger nuclear fusion, which leads to the birth of stars. In reality, the formation of stars cannot be simply explained by the Jeans' instability as complex (megneto)hydrodynamical, thermal and chemical evolution, as well as radiation and different feedback mechanisms, come into play. However, even if the details of the stellar formation process still need to be understood, one can establish relations between the mass of the stellar component and the dark matter component of galaxies at least statistically.

1.4.3 Galaxy-Halo Connection

As detailed in previous sections, the luminosity function of galaxies and the mass function of dark matter haloes significantly differ in shape. To connect the dark matter haloes with baryonic components of galaxies, one can utilize cosmological hydrodynamical simulations (see Section 1.4.4), or employ semi-analytic methods (e.g. Kauffmann et al., 1999; Guo et al., 2011), where models of galaxy evolution are calculated on top of dark matter haloes in a pre-existing N-body dark matter-only simulation.

From an observational point of view, an empirical galaxy-halo relation can be established on a one-to-one basis by rank ordering the two (Kravtsov et al., 2014), or through the relation between the stellar mass function (from observations) and the halo mass function (usually from N-body simulations), which are known as the abundance matching. In this approach, a monotonic relation is assumed between stellar and halo mass. The relation can be established by, for instance, requiring the cumulative mass function to match (e.g. Moster et al., 2013)

$$N_*(>M_*(M_{\rm h})) = N_{\rm h}(>M_{\rm h})\,, \tag{1.55}$$

where $M_{\rm h}$ is the mass of the halo, $M_*(M_{\rm h})$ is the corresponding stellar mass, $N_{\rm h}$ is the cumulative stellar mass function, and $M_{\rm h}$ is the cumulative halo mass function. Alternatively, the relation can be established semi-analytically through optimizing stellar mass to halo mass ratio with Markov chain Monte Carlo (MCMC) method. (e.g. Behroozi et al., 2013).

The stellar mass to halo mass ratio of the Illustris simulation and abundance matching methods is shown in Fig. 1.11. Relatively good agreement can be found for these methods.

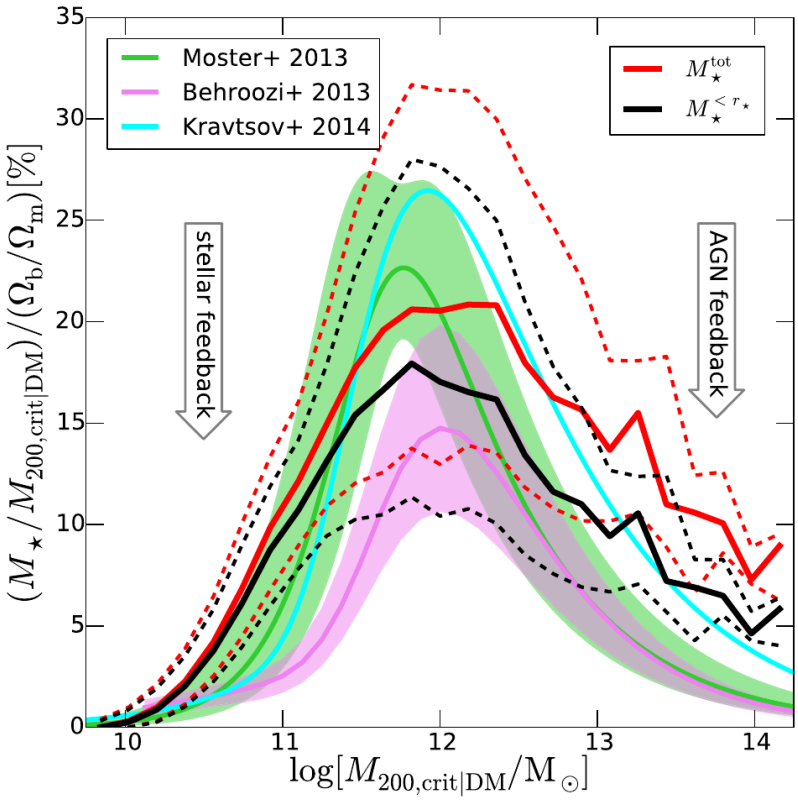

Fig. 1.11 Stellar mass to halo mass ratio in the Illustris simulation compared with the abundance matching results. Solid lines indicates the median value of the Illustris simulation (in black for total mass within a given surface brightness cut in the r-band and in red for mass within two times of half-mass radius) and the abundance matching methods (in green, purple and cyan). Coloured region indicates 1σ region of abundance matching methods, while the dashed curves indicates the 1σ region of the Illustris simulation. Relatively good agreement can be found for various methods. The figure is taken from Vogelsberger et al. (2014).

Generally, the ratio of stellar to halo mass is low for both the low mass and the massive end, with the efficiency of star formation being regulated by various factors, as stated below.

- Photoheating from the UV background. After reionization at $z \sim 6$, the Universe is permeated with photons emitted by galaxies and AGN, which form an UV background, often assumed to be spatially constant, but time dependent. The photoheating from the UV background competes with the radiative cooling of gas, keeping it warm. Combined with the Jeans' instability, this leads to a mass threshold of typically $\sim 10^8$-$10^9 M_\odot$, below which galaxies can not form (e.g. Rees, 1986; Efstathiou, 1992; Hambrick et al., 2011).

- Supernova feedback. Supernova feedback injects energy into the surrounding medium, and may drive galactic-scale winds that remove gas from the galaxy (Dekel & Silk, 1986). Such galactic winds also create turbulence and may trigger star formation, but recent simulation work (e.g. Dale et al., 2013; Rey-Raposo et al., 2017) suggest that overall the star formation is suppressed.

- AGN feedback. AGN are very bright regions in the centre of galaxies that are believed to be powered by the accretion of matter onto black holes. There is both theoretical and observational evidence that AGN feedback can drive strong outflows and hence reduce the star formation rate (see e.g. Silk & Rees, 1998; Fabian, 1999; King, 2003; Sijacki et al., 2007; Costa et al., 2014; Sturm et al., 2011; Rupke & Veilleux, 2013; Cicone et al., 2014). As shown in Fig. 1.11, cosmological simulations like Illustris (see also e.g. EAGLE, Schaye et al. 2015; and Horizon-AGN, Dubois et al. 2016) find that AGN reduce the star formation especially at the massive end.

1.4.4 Cosmological Simulations

Given that the non-linear and complex evolution of galaxies is dependent on various physical and chemical processes regulating baryons, cosmological simulations provide a useful tool to test different implementation of baryonic physics and help us better understand the formation of galaxies.

Cosmological simulations span a wide range of simulated domains with a possibility to zoom into specific regions, ranging from large-scale boxes (e.g. the Millennium simulation, Springel et al. 2005b; the Millennium XXL simulation, Angulo et al. 2012; the Illustris simulation, Vogelsberger et al. 2014; Genel et al. 2014; Sijacki et al. 2015; the EAGLE simulation, Schaye et al. 2015; and the Horizon-AGN simulation, Dubois et al. 2016), to the zoom-in simulations of galaxy clusters (e.g. Gao et al., 2012), Milky Way-like galaxies (e.g. the Aquarius simulation, Springel et al., 2008) and dwarf galaxies (e.g. the FIRE/GIZMO simulation, Wheeler et al., 2015). Some simulations include only dark matter, while others include baryonic matter as well. Due to their collisionless nature, the dark matter and stellar components in these simulations are often treated as particles, with a N-body approach, which will be discussed in detail in Section 2.2. The fluid component of the baryonic matter is treated in various ways.

Smoothed Particle Hydrodynamics (SPH) methods are based on the Lagrangian scheme. SPH codes like GADGET-3 (Springel, 2005) and GASOLINE (Wadsley et al., 2004) model the fluid with tracer particles that can be thought as fluid elements. Each of these particles tracks its thermal energy or entropy in addition, to account for thermodynamics.

In the alternative approach taken by grid-based methods, the whole domain of the fluid is modelled on a grid adopting the Eulerian scheme. For better dynamical range, modern grid-based codes like RAMSES (Teyssier, 2002) usually employ the Adaptive Mesh Refinement (AMR) scheme (Berger & Oliger, 1984; Berger & Colella, 1989). Instead of using an uniform grid, RAMSES refines grid cells to multiple levels when certain criteria, usually relevant to the gradients of the flow variables, are met. This ensures that regions with most complex dynamics are simulated with the finest grids, while significant computing power can be saved by using coarse grids for the smooth regions.

Aside from hydrodynamical solvers, sub-grid physics, including cooling and heating of the gas, star formation and stellar and AGN feedback, are important in cosmological simulations. The Aquila project (Scannapieco et al., 2012) compared different cosmological codes by simulating the same halo. Moderate discrepancies in mass, size, velocity curve and other properties of the galaxy were found among different codes, which were mostly due to differences in star formation and feedback schemes.

Bearing these uncertainties in mind, state-of-the-art large-scale cosmological simulations, with very high resolution and various sub-grid physics included, are an useful tool to study our Universe. Currently, they can resolve up to several tens of thousands galaxies at $z = 0$ and thus compare in a statistical sense theoretical predictions with observations, such as the luminosity and stellar mass function of galaxies, their star formation rates, colours, sizes and morphologies.

It is however to be noted that the formation of spiral structures is still not understood in these cosmological simulations, as it requires detailed and very high resolution studies on the scales of a kpc and below. In the next section, I briefly review established theories of spiral formation.

1.5 Stellar Dynamics of Disc Galaxies and Formation of Spiral Structures

1.5.1 Disc Galaxies

In this Thesis I focus mainly on the spiral structures in disc galaxies. As the name suggests, spiral galaxies, or disc galaxies, have a disc component that consists of stars, gas and dust. There are also bar structures, bulges, pseudo-bulges and black holes in the centres of many spiral galaxies. Observations have shown that the brightness of discs generally falls exponentially with radius, while sometimes a more rapid rise of brightness in the central part, recognised as a bulge, can also be seen (de Vaucouleurs, 1959). Based on the brightness

profile, a stellar disc is usually modelled with an exponentially decreasing density profile. The vertical density structure is usually modelled as an isothermal sheet. As will be explained further in Section 2.3.1, we use this model for our simulations.

Exponential Disc Profile

The exponential brightness profile of the disc indicates an exponential surface density distribution (Freeman, 1970). To explain this, Lin & Pringle (1987) proposed a viscous and star-forming disc model. In their theory, the surface density of the stellar disc is decided by the history of star formation, i.e.

$$\Sigma_*(R) = \int_0^\infty \frac{\Sigma(R,t)}{t_*} dt\,, \tag{1.56}$$

where t_* is the critical time for star formation and $\Sigma(R,t)$ is the gas surface density. The evolution of the surface density of gas depends both on the formation of the stars (as a sink term) and the viscosity ν. The viscous time scale is $t_\nu \sim R^2/\nu$, where ν is the viscosity of the gas. With numerical calculations, Lin & Pringle (1987) showed that if $t_* \approx t_\nu$, the stellar disc will have an exponential surface density distribution and that this outcome is not very dependent on the initial surface density of gas or the rotation curve.

Isothermal Sheet

The vertical density distribution of the disc is usually modelled as an isothermal sheet. Spitzer (1942) originally assumed that at a given radial and azimuthal position of the disc, the vertical distribution of particles should be isothermal, i.e. following a normal distribution in energy,

$$f = \frac{1}{\sqrt{2\pi}\sigma_\mathrm{z}} \exp\left(-\frac{E_\mathrm{z}}{\sigma_\mathrm{z}^2}\right), \tag{1.57}$$

where σ_z is the vertical velocity dispersion and $E_\mathrm{z} = v_\mathrm{z}^2/2 + \Phi(R,z)$ is the energy, consisting of kinetic energy $v_\mathrm{z}^2/2$ and gravitational energy $\Phi(R,z)$. For a disc-like system, it is then assumed that the gravitational potential changes most drastically in the vertical direction, hence the Poisson equation becomes

$$\frac{\partial^2\Phi}{\partial z^2} = 4\pi G\rho(R,z)\,, \tag{1.58}$$

where $\rho(R,z)$ is the density of the stellar component, which can be calculated by integrating the distribution function f over velocity space,

$$\rho(R,z) = \int f \, \mathrm{d}\mathbf{v}^3 = \rho(R,0) \exp\left(-\frac{\Phi(R,z) - \Phi(R,0)}{\sigma_z^2}\right). \tag{1.59}$$

Solving this equation yields

$$\rho(R,z) = \rho(R,0)\mathrm{sech}^2(z/2z_\mathrm{d}), \tag{1.60}$$

where $z_\mathrm{d} = \sigma_\mathrm{z}/\sqrt{8\pi G\rho(R,0)}$, and $\rho(R,0)$ is related to surface density through $\rho(R,0) = \Sigma(R)/4z_\mathrm{d}$. As it will be shown later, in this Thesis the vertical density structure is modelled with this profile.

Velocity Structure

It is common to assume that the velocity structure at a given location of the stellar disc obeys an triaxial Gaussian distribution, specified by the mean velocity $\langle v \rangle$ and the velocity dispersion σ along the direction of three axes. It was found in observations that the three axes of the velocity ellipsoid in the Milky Way may not align with the axes of the disc, but tilt towards the Galactic plane by an angle of $\sim 0.8 \arctan(z/R)$ (Binney et al., 2014). However, for a thin disc studied in this Thesis, it should be safe to assume that the velocity ellipsoid is aligned with the axes of the disc, i.e.

$$\langle v_\mathrm{R} v_\mathrm{z} \rangle = \langle v_\mathrm{R} v_\varphi \rangle = \langle v_\mathrm{z} v_\varphi \rangle = 0. \tag{1.61}$$

For a disc that is in equilibrium with the dark matter halo, we also require no flows in R and z direction, which means

$$\langle v_\mathrm{z} \rangle = \langle v_\mathrm{R} \rangle = 0. \tag{1.62}$$

Combined with the Jeans equation in cylindrical-polar coordinates, one can find that

$$\frac{\partial \rho \langle v_\mathrm{R}^2 \rangle}{\partial R} + \rho\left(\frac{\langle v_\mathrm{R}^2 \rangle - \langle v_\varphi^2 \rangle}{R} + \frac{\partial \Phi}{\partial R}\right) = 0, \tag{1.63}$$

and

$$\frac{\partial \rho \langle v_\mathrm{z}^2 \rangle}{\partial z} + \rho \frac{\partial \Phi}{\partial z} = 0. \tag{1.64}$$

In this Thesis, it is further assumed that the velocity dispersion in R direction is equal to that in z direction. Therefore

$$\langle v_{\rm R}^2 \rangle = \langle v_{\rm z}^2 \rangle = \frac{1}{\rho} \int_0^\infty \rho(z', R) \frac{\partial \Phi}{\partial z'} {\rm d}z' \,, \tag{1.65}$$

and

$$\langle v_\varphi^2 \rangle = \langle v_{\rm R}^2 \rangle + \frac{R}{\rho} \frac{\partial \left(\rho \langle v_{\rm R}^2 \rangle \right)}{\partial R} + V_{\rm c}^2 \,, \tag{1.66}$$

where $V_{\rm c} = \sqrt{R \partial \Phi / \partial R}$ is the velocity of a star on a circular orbit. To find the mean streaming velocity $\langle v_\varphi \rangle$, notice that the velocity dispersion σ_φ and $\sigma_{\rm R}$ are also related through the epicyclic motion of the stars (see equation 1.78)

$$\sigma_\varphi^2 = \frac{\kappa^2}{4\Omega^2} \sigma_{\rm R}^2 = \frac{\kappa^2}{4\Omega^2} \langle v_{\rm R}^2 \rangle \,, \tag{1.67}$$

where κ is the epicyclic frequency of the disc. The mean streaming velocity is then

$$\langle v_\varphi \rangle = \sqrt{\langle v_\varphi \rangle^2 - \sigma_\varphi^2} \,. \tag{1.68}$$

1.5.2 Epicyclic Motion of Stars

In an axisymmetric potential $\Phi(R, z)$, the motion of a star can be considered as 2-dimensional motion in the $R - z$ plane under an effective potential (see e.g. Binney, 1987)

$$\Phi_{\rm eff}(R, z) \, = \, \Phi(R, z) + \frac{L_{\rm z}^2}{2R^2} \,, \tag{1.69}$$

where $L_{\rm z}$ is the constant angular momentum in the z direction. The minimum in $\Phi_{\rm eff}$ satisfies

$$0 = \frac{\partial \Phi_{\rm eff}}{\partial R} = \frac{\partial \Phi}{\partial R} - \frac{L_{\rm z}^2}{R^3} \,, \tag{1.70}$$

$$0 = \frac{\partial \Phi_{\rm eff}}{\partial z} = \frac{\partial \Phi}{\partial z} \,, \tag{1.71}$$

where the second line is satisfied at $z = 0$ when the potential is symmetric for z. In this case, the first line is satisfied when the star is on a circular orbit. The radius of this orbit is defined as the guiding-centre radius $R_{\rm g}$.

When stars are on an orbit close to circular, which is the case for many stars in a disc galaxy, the motion of stars can be treated as perturbations around the guiding centre. One can write the perturbation in R as $x = R - R_{\rm g}$. Expanding the effective potential around $(R_{\rm g}, 0)$

gives (noting that this point is the minimum of $\Phi_{\rm eff}$)

$$\Phi(R,z) = \Phi(R_{\rm g},0) + \frac{1}{2}\left(\frac{\partial^2\Phi_{\rm eff}}{\partial R^2}\right)\Big|_{R_{\rm g},0} x^2 + \frac{1}{2}\left(\frac{\partial^2\Phi_{\rm eff}}{\partial z^2}\right)\Big|_{R_{\rm g},0} z^2, \tag{1.72}$$

which means the motion of the star around the guiding-centre satisfies

$$\ddot{x} = -\left(\frac{\partial^2\Phi_{\rm eff}}{\partial R^2}\right)\Big|_{R_{\rm g},0} x^2, \tag{1.73}$$

$$\ddot{z} = -\left(\frac{\partial^2\Phi_{\rm eff}}{\partial z^2}\right)\Big|_{R_{\rm g},0} z^2, \tag{1.74}$$

which represent the harmonic oscillators. The frequency of the motion is defined with an epicyclic frequency $\kappa = \sqrt{\left(\frac{\partial^2\Phi_{\rm eff}}{\partial R^2}\right)\Big|_{R_{\rm g},0}}$ and a vertical frequency $\nu = \sqrt{\left(\frac{\partial^2\Phi_{\rm eff}}{\partial z^2}\right)\Big|_{R_{\rm g},0}}$. Given the circular velocity $\Omega = \frac{L_z}{R^2}$, it can be shown that

$$\kappa = \sqrt{\left(R\frac{{\rm d}\Omega^2}{{\rm d}R} + 4\Omega^2\right)\Big|_{R_{\rm g},0}}. \tag{1.75}$$

As the circular velocity in a galaxy generally does not grow with radius, and decreases more slowly than the Keplerian case, the epicyclic frequency can be constrained as $\Omega < \kappa < 2\Omega$.

Relation of Velocity Dispersion

To calculate the dispersion of velocity in azimuthal direction σ_φ at a given radius R_0, we consider a star with guiding centre $R_{\rm g}$. Due to the conservation of angular momentum $L_{\rm z} = R^2\dot{\varphi}$, the angular velocity at radius R_0 is

$$\dot{\varphi} - \Omega(R_g) = -\frac{2\Omega}{R_{\rm g}}x, \tag{1.76}$$

where $x = R_0 - R_{\rm g}$. The velocity in tangential direction is

$$v_{\rm y} = R_0\left(\dot{\varphi} - \Omega(R_0)\right) = -x\left(\frac{2\Omega}{R_{\rm g}} + \frac{{\rm d}\Omega}{{\rm d}R}\Big|_{R_{\rm g}}\right) = -\frac{\kappa^2}{2\Omega}x. \tag{1.77}$$

As $\frac{\kappa^2}{2\Omega}$ depends only on the location of the guiding centre, the velocity dispersion relation is therefore

$$\sigma_\varphi^2 = \left\langle v_{\rm y}^2\right\rangle = \frac{\kappa^4}{4\Omega^2}\left\langle x^2\right\rangle = \frac{\kappa^2}{4\Omega^2}\left\langle v_{\rm x}^2\right\rangle = \frac{\kappa^2}{4\Omega^2}\sigma_{\rm R}^2. \tag{1.78}$$

Inner and Outer Lindblad Resonance

For a given pattern that rotates with a pattern speed of $\Omega_{\rm P}$, the stars interact with the pattern most strongly when

$$\Omega_0 = \Omega_{\rm P}\,, \tag{1.79}$$

or when

$$m\,(\Omega_0 - \Omega_{\rm P}) = \pm\kappa\,, \tag{1.80}$$

where Ω_0 is the circular velocity, and m is an integer. Equation (1.79) is called the corotation resonance, which is satisfied at the radius when the circular velocity is equal to the velocity of the pattern. Seen in the rotating frame of the pattern, the star stays at the same location, interacting with the pattern persistently. Equation (1.80) is called the inner and outer Lindblad resonance. In the rotating frame of the pattern, stars at this resonance are in closed orbits (when $m = 2$ the orbits are ellipses), therefore having periodic interaction with the pattern.

1.5.3 Properties of Spiral Structures

Many properties of spiral structures can be directly constrained from observations. The number of arms, m, varies in different galaxies. Using a sample of $\sim 18,000$ SDSS galaxies, Hart et al. (2016) found that about 64% of the sample have two-armed spiral structures, with about 5% one-armed spiral structures, 18% three-armed spiral structures, 6% four-armed spiral structures, and 7% spiral structures with 5 or more arms. They also found that at the massive end, the fraction of two-armed spiral structures falls to 53%, while more spiral structures with 5 or more arms are found.

The spiral structures can also be classified into grand-design spiral structures and flocculent spiral structures based on their morphology. Grand design spiral structures (e.g. M81) are well-defined spiral structures that extend in a large radial range of the disc, with generally two arms (similar structures with more arms are sometimes named as multi-armed spiral structures), while flocculent spiral structures (e.g. NGC 2841) consists of multiple short, transient spiral arms. As will be discussed in Section 1.5.4 and 1.5.5, the grand-design spirals are generally related to tidal interactions, while the flocculent spiral structures could form due to self-gravity of the disc. Kendall et al. (2011) studied 31 nearby spiral galaxies and found that more than half of the sample have two-armed grand-design spiral structures. They also found that the grand-design spiral structures are generally unrelated to bar structures. Instead, most of the galaxies with strong grand-design spiral structures are found to have companions. Kendall et al. (2015) further found that the morphology of spiral structures of this sample is weakly, if at all, related to disc properties such as the mass of stellar and

gaseous disc, disc/bulge ratio and flat velocity, but strongly related to the tidal force from companions.

The pitch angle α of the spiral structures is usually defined as the angle between spiral arms and the tangential direction. Seigar et al. (2006) studied 51 galaxies whose pitch angle ranges from 10° to 50°, and found that their pitch angle correlates with the shear rate $\Gamma = -\frac{1}{2}\frac{R}{\Omega}\frac{\mathrm{d}\Omega}{\mathrm{d}R}$ of the disc through

$$\alpha = (64.25 \pm 2.87) - (73.24 \pm 5.53)\Gamma. \tag{1.81}$$

Grand et al. (2013) found that the relation can be understood with simulations of transient, self-induced spiral structures.

1.5.4 Established Theories on Spiral Structures

It is now generally considered that the formation of spiral structures is a complex process and different factors come into play together, making it hard to understand the formation of spiral structures with a single, simple, unified theory. In the past, different theories have been proposed, explaining different aspects of the formation.

Kinematic Density Wave

During their formation history, galaxies experience a large number of mergers. Also, galaxies generally have many satellites. These facts mean that the galactic disc should often feel strong torques, which might lead to spiral structures. Once formed, the spiral patterns evolve in the disc as kinematic density waves. In fact, Lindblad (1963) found that the observed pattern speed of some spiral structures followed closely the pattern speed of the inner Lindblad resonance, $\Omega_\mathrm{P} = \Omega - \kappa/m$, where Ω is the circular velocity of the guiding centre, κ is the epicyclic frequency and m is the number of arms. For realistic discs the value of $\Omega_\mathrm{P} = \Omega - \kappa/2$ is often roughly constant in the central region. Due to the epicyclic motion of stars, when viewed in a rotating frame with a constant circular velocity Ω_P, the orbits of stars become stationary elliptical orbits. If, for some reason, e.g. an external torque, stationary orbits are arranged in a way such that some regions are denser than the others, as in the right three panels in Fig. 1.12, a spiral structure forms. Such structure is also stationary in the rotating frame, and is therefore rotating with a pattern speed of Ω_P in the stationary frame. If the pattern speed is not constant, but slightly decreases over the radii instead, the spiral structures will still form and persist for a long time, but will slowly wind up due to the fact that the pattern speed in the inner region is faster than that of the outer region.

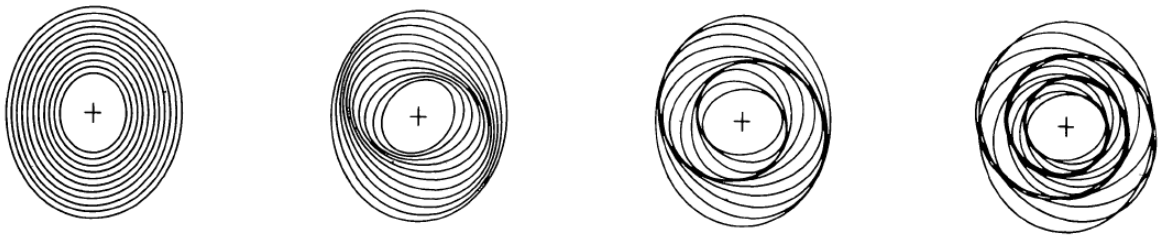

Fig. 1.12 An illustration of different alignments of orbits in the rotating frame of the pattern speed equal to $\Omega - \kappa/2$. The left most panel shows the case when the direction of the orbits is aligned throughout. From left to right, the change of direction over radii becomes faster. Such differing alignment of the orbits gives rise to spiral structures of different intensities and pitch angles. The figure is taken from Kalnajs (1973).

Quasi-Stationary Spiral Structures

Lin & Shu (1964) proposed a hypothesis to explain grand-design spiral structures. In this theory, large density waves, with a scale-length comparable to the whole disc, propagate through the disc and form quasi-stationary spiral structures. The theory is based on the same idea as Lindblad's density wave theory in that they both model spiral structures as waves rather than material arms, but Lin & Shu (1964) treat the surface density of the disc as a field. The behaviour of such waves can be studied by considering small perturbations around the equilibrium state under the balance of gravitational and centrifugal forces. Considering linear perturbations, the solutions are of the form

$$\Sigma'(r,\theta) = \mathrm{Re}\left[\Sigma^{(1)}(r)\exp[i(\omega t - n\theta)]\right], \tag{1.82}$$

where $\Sigma' = \Sigma - \Sigma_0$ is the perturbation of surface density around the equilibrium state with a surface density of Σ_0. $\Sigma^{(1)}(r)$ is the amplitude, and $\omega = \omega_\mathrm{r} + i\omega_\mathrm{i}$ is in general a complex number. When $\omega_\mathrm{i} < 0$, the perturbation is growing. The amplitude term $\Sigma^{(1)}(r)$ can be generally written as

$$\Sigma^{(1)}(r) = S(r)\exp(i\Phi(r)), \tag{1.83}$$

where $S(r)$ and $\Phi(r)$ are real numbers. The surface density perturbation is then

$$\Sigma'(r,\theta) = S(r)\exp(-\omega_\mathrm{i} t)\cos\left[\omega_\mathrm{r} t - n\theta + \Phi(r)\right]. \tag{1.84}$$

If $S(r)$ varies slowly as a function of radius r while $\Phi(r)$ varies quickly, the surface density distribution of the disc is dominated by the cosine component of equation (1.84), which corresponds to a spiral structure whose azimuthal position θ is a function of radius r of the

form

$$\theta = \Phi(r)/n + C\,, \tag{1.85}$$

where C is a constant.

Tight-winding Spiral Waves

The spiral waves are in the regime of tight-winding approximation (also known as the Wentzel–Kramers–Brillouin approximation or WKB approximation) when the wavelength in the radial direction is small. In this approximation the wave can be studied analytically as they are localised. Lin & Shu (1966) and Kalnajs (1965) found that the dispersion relation of the wave in a razor-thin stellar discs satisfies

$$(\omega - m\Omega)^2 = \kappa^2 - 2\pi G\Sigma|k|\mathscr{F}\left(\frac{\omega - m\Omega}{\kappa}, \frac{\sigma_{\rm R}^2 k^2}{\kappa^2}\right), \tag{1.86}$$

where ω, m and k is the angular frequency, number of arms and radial wave-number of the spiral wave, κ, Ω and Σ are the epicyclic frequency, circular velocity and the surface density of the disc, and $\mathscr{F}$ is a dimensionless function

$$\mathscr{F}(s,\chi) = \frac{2}{\chi}(1-s^2)e^{-\chi}\sum_{n=1}^{\infty}\frac{I_n(\chi)}{1-s^2/n^2}\,, \tag{1.87}$$

where I_n is the modified Bessel function.

The disc is stable when ω is always real. The boundary between stable and unstable disc is therefore

$$\kappa^2 = 2\pi G\Sigma|k|\mathscr{F}\left(0, \frac{\sigma_{\rm R}^2 k^2}{\kappa^2}\right). \tag{1.88}$$

Solving this leads to the Toomre's Q parameter (Toomre, 1964),

$$Q = \frac{\sigma_{\rm R}\kappa}{3.36\,G\Sigma}\,. \tag{1.89}$$

When $Q > 1$, the disc is locally stable to axisymmetric instabilities, while for $Q < 1$, the disc becomes locally unstable.

For a wave of a given pattern speed $\Omega_{\rm P} = \omega/m$, equation (1.86) links the radial wave-number, k, with the radius, R, through the circular velocity $\Omega(R)$. When $Q > 1$, equation (1.86) indicates that there is a forbidden region around the corotation radius $R_{\rm CR}$, where the wave cannot propagate. As illustrated in Fig. 1.13, a wave starting as a leading tight-winding wave unwinds and winds up again as a trailing wave while reflecting at the edge of the forbidden region and the inner Lindblad resonance as it propagates radially.

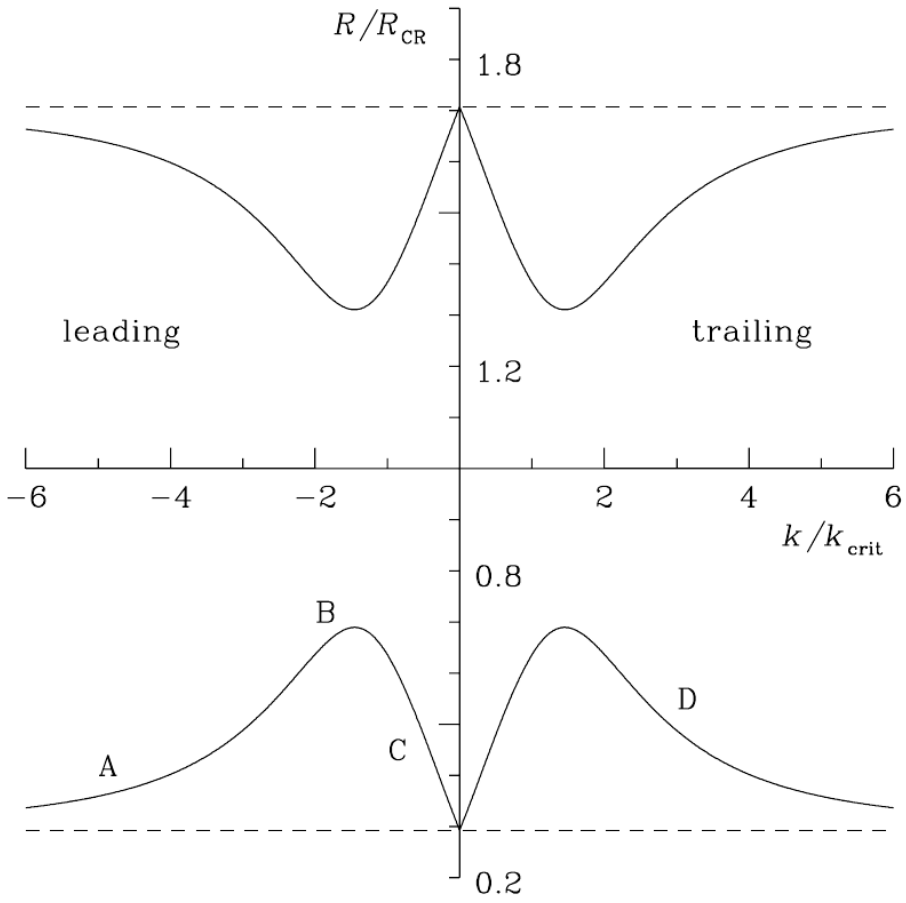

Fig. 1.13 The propergation of a $m = 2$ wave packet in a stellar Mestel disc with $Q = 1.2$ in the plane of R-k, where R is the radius of the disc and k is the radial wave-number. The inner and outer Lindblad resonances are shown in the dashed line. A wave may start from the inner Lindblad resonance with negative (leading), large radial wave number at point A, and propagate outwards to B, where it hits the forbidden region and reflects inwards. The wave generally unwinds and turns into a loose-winding leading wave at C, until it reaches the inner Lindblad resonance and reflects outwards, becoming a trailing long wave. The wave then reflects at the edge of the forbidden region again and ends up propagating inwards as a trailing tight-winding at D. The figure is taken from Binney (1987).

Note that the tight-winding approximation only applies to the case of tight-winding waves, which may not be the case for some spiral structures. To study the properties of these discs, numerical simulations may be required.

Swing Amplification and Feedback Loop

Unlike kinematic density waves, spiral structures can also form due to self-gravity. The typical response to a non-axisymmetric perturbation is called the swing amplification, which is related to the shear rotation and the self-gravity of the disc (Goldreich & Lynden-Bell, 1965; Julian & Toomre, 1966). Consider for a moment a material arm of pitch angle α. Due to the fact that stars at different radii rotate with different angular velocities, the pitch angle changes over time. The cotangent value of α is[3]

$$\cot\alpha = -Rt\frac{\mathrm{d}\Omega}{\mathrm{d}R} = 2At\,, \tag{1.90}$$

where $A = -\frac{1}{2}R\frac{\mathrm{d}\Omega}{\mathrm{d}R}$ quantifies the differential rotation of the disc. The pitch angle α then changes over time as

$$\frac{\mathrm{d}\alpha}{\mathrm{d}t} = -\frac{2A}{1+4A^2t^2}\,. \tag{1.91}$$

This value is small when $|t|$ is large, and reaches a maximum when α is close to 0. At the maximum, $\dot{\alpha} = 2A$ is close to the epicyclic frequency κ, which means that around $\alpha = 0$, the star may feel an attractive force from the material arm persistently, as illustrated in Fig. 1.14. Due to this continuous attractive force, stars generally move towards the arm, thereby enhancing the arm.

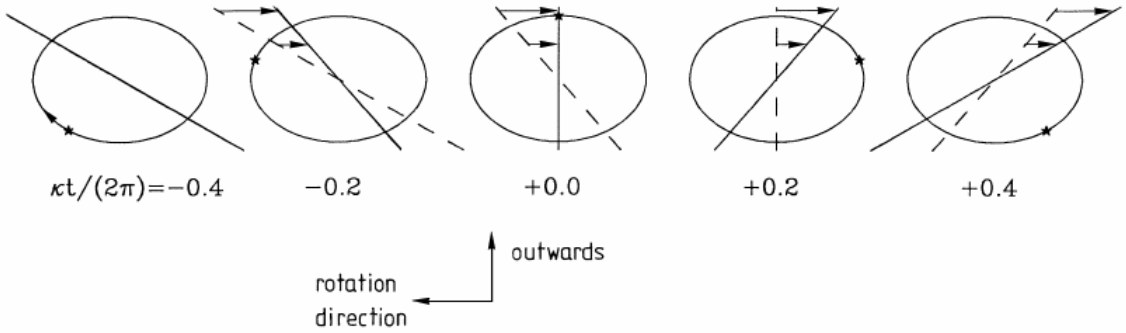

Fig. 1.14 An illustration of swing amplification; the time evolves from left to right. Straight lines in the plot illustrate the material arms, while the ellipse shows the orbit of a star. When $t < 0$, the star is behind the material arm, while when $t > 0$, the star is in front of the arm. The frequency of the star κ is close to the winding rate of the arm. As a result, the star is continuously attracted to the material arm, thereby increasing the overdensity of the arm. This figure is taken from Binney (1987).

[3]Here α is defined so that when the material arm is radial, $\alpha = 0$.

Toomre (1981) studied this process numerically with linear perturbation theory. He found that the amplification amplitude depends both on Toomre's parameter Q and a parameter X with

$$X = \frac{\kappa^2 R}{2\pi G \Sigma m}. \tag{1.92}$$

As shown in Fig. 1.15, the swing amplification is strongest when Q is larger than and close to 1, and when $1 < X < 2$. The amplification can be as high as 100.

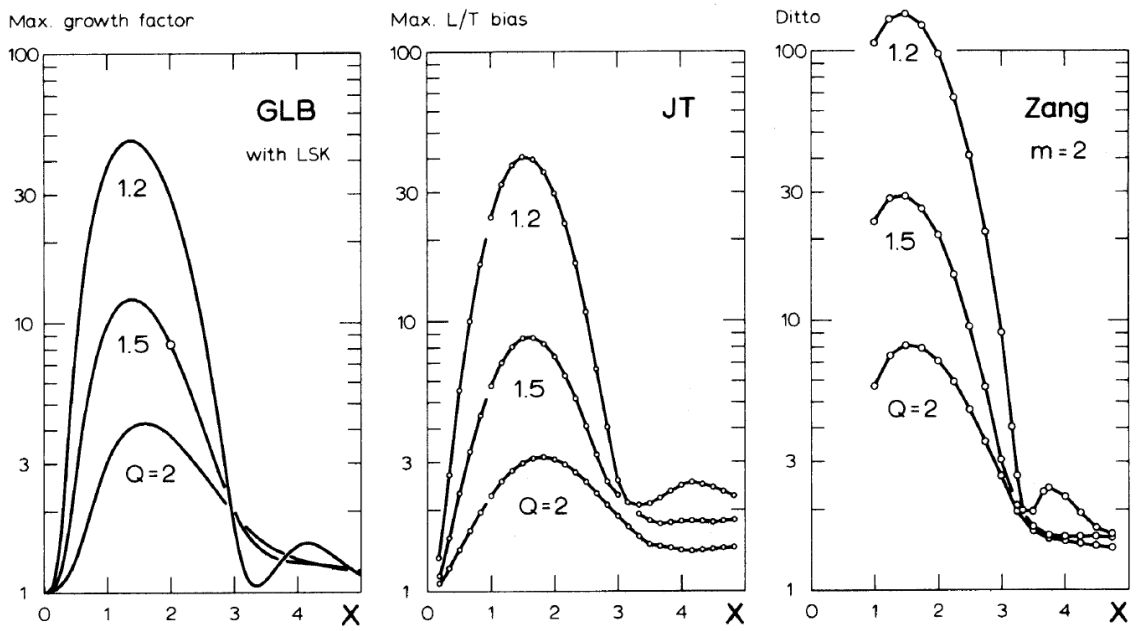

Fig. 1.15 The dependence of swing amplification on factors Q and X. From left to right three different model are shown, including a fluid disc (Goldreich & Lynden-Bell, 1965), a stellar disc (Julian & Toomre, 1966) and a Mestel disc. In all three models the swing amplification is strongest when Q is close to unity and when $1 < X < 2$. The figure is taken from Toomre (1981).

Swing amplification alone cannot lead to spiral structures, as perturbations simply evolve from leading to trailing and get amplified, but soon wind up and disappear. To have persistent spiral structures, a feedback loop is required. A feedback loop is a mechanism that turns trailing patterns back into leading patterns, so that they can be amplified multiple times. Possible feedback mechanisms include reflection at the edge, the centre, or the resonances of the disc and the interaction of trailing patterns.

Scattering in Action Space

Sellwood (2012) demonstrated that in N-body simulations, gravity-induced spiral structures hide more information in the action-space distribution than in the spatial distribution. In that work, razor-thin Mestel discs of finite number of particles were simulated. The Poisson noise in the initial conditions was swing amplified, leading to spiral structures in the disc. The simulation was then restarted at different times before the formation of prominent spiral structures. Before restarting, the azimuthal positions of all stars were shuffled, so that the non-axisymmetric density distribution was smoothed out. If the formation of spiral structures was a result of the spatial re-distribution of the stars, the disc would take a longer time to form spirals. However, the disc required less time to form spirals, such that the total time for spiral formation remained roughly the same with and without shuffling. Therefore the shuffling did not affect the formation of spirals. In fact, as shown in Fig. 1.16, what happened was a scattering in the J_R-J_φ space. Here the two actions are defined as the radial action $J_\mathrm{R} = \frac{1}{\pi}\int_{R_\mathrm{min}}^{R_\mathrm{max}} v_\mathrm{R}\,\mathrm{d}R$, where v_R is the radial velocity, and the angular action $J_\varphi = L_z$. The direction of the scattering is found to be identical to that of the inner Lindblad resonance, while other less significant scattering can also be found along the corotation and outer Lindblad resonances. This diffusion in action space was later understood theoretically by Fouvry et al. (2015) using the inhomogeneous Balescu-Lenard equation.

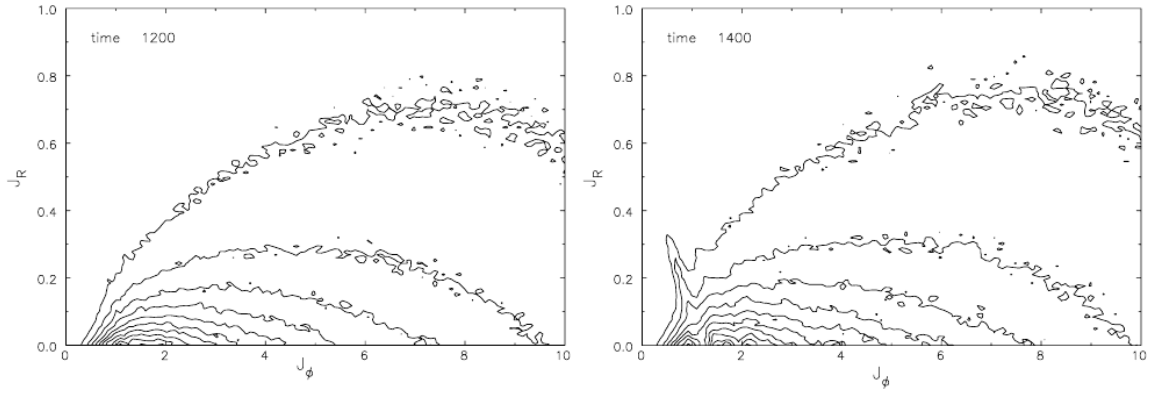

Fig. 1.16 Action space scattering during the formation of spiral structures. The distribution of particles in the J_R-J_φ action space in two different timesteps, $t = 1200$ (top) and $t = 1400$ (bottom) in a simulation carried by Sellwood (2012) is shown. A directed scattering happened between the two snapshots. The figure is taken from Sellwood (2012).

1.5.5 Previous Numerical Works on the Spiral Structures

Previous numerical work has shed much light on the formation and evolution of spiral structures in various aspects including swing amplified spiral structures, externally-driven spiral structures, stellar migration, interstellar medium and disc heating.

Self-induced Spirals

It is easy to form transient spiral structures in N-body simulations due to swing amplification (e.g. Toomre, 1981; Sellwood, 2011; Fujii et al., 2011; Sellwood, 2012; Grand et al., 2012b; D'Onghia et al., 2013). In Toomre (1981), Zang's N-body simulation was introduced. 20,000 particles were used in the simulation to model a thin, infinite disc of constant circular velocity. A sudden quadrupole force was applied to the disc at the beginning of the simulation, triggering $m = 2$ spiral structures immediately. These spiral structures were then amplified greatly through swing amplification both in test particle simulations and in the N-body simulation, which demonstrated the importance of swing amplification. Sellwood (2012) later found that with the same disc model the quadrupole force is not necessary for driving $m = 2$ spiral structures as the shot noise of the initial condition can be amplified to similar spiral structures. The time for spiral structures to develop is longer when the number of particles N is higher, as the level of shot noise is proportional to $N^{-1/2}$. A common feature of discs studied by Toomre (1981) and Sellwood & Carlberg (2014) is that their Toomre's Q parameter is close to unity and the X parameter (see equation (1.92)) favours swing amplification of $m = 2$ modes. With a different disc model, Sellwood & Carlberg (2014) found that modes from two to four arms can be triggered in a similar manner. As shown in Fig. 1.17, the power spectra of these spiral structures are typically horizontal bars, i.e. these modes have constant rotating velocities throughout, indicating that they are material arms rather than density waves.

In reality, stellar discs may not be infinitely smooth due to the other components of galaxies. D'Onghia et al. (2013) modelled the giant molecular clouds with heavy particles. In their simulation, the response to these perturbers is quickly swing amplified to multi-armed spiral structures, which can trigger new generations of spiral structures even when the original perturbers are removed early in the simulation. Although the lifetime of a single spiral structure can be shorter than 1 Gyr, D'Onghia et al. (2013) found that transient spiral structures can trigger the formation of new generations of transient spiral structures, leading to a long-lived spiral pattern. This non-linear effect may provide a mechanism for recurrent spiral structures.

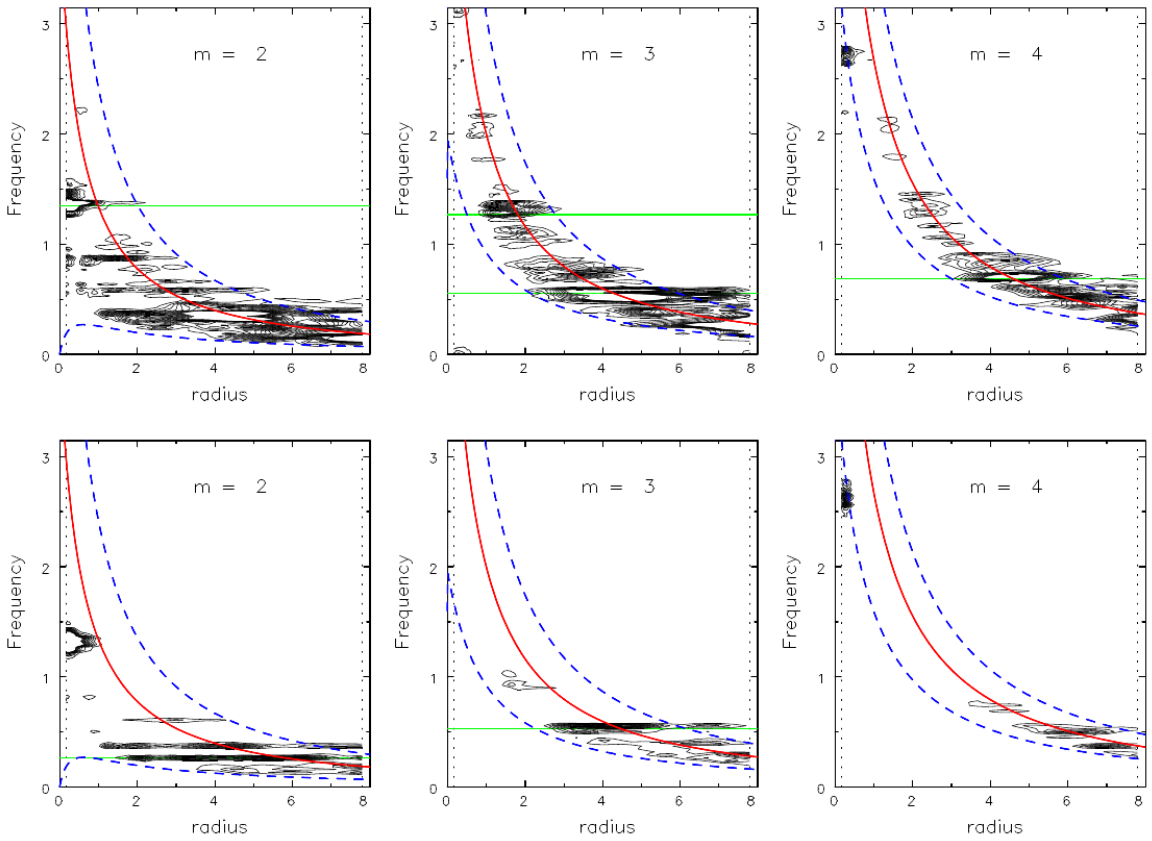

Fig. 1.17 The power spectra of spiral structures studied by Sellwood & Carlberg (2014). Top panels show the power spectra of the early-half of the simulation, while bottom panels show the later-half. Modes of different fold, from $m = 2$ to $m = 4$ are shown from left to right. In each panel, the contours of the power spectra are shown in black. The corotation frequency is shown in red curves, while the inner and outer Lindblad resonances are shown in blue dashed curves. The prominent structure seen for the power spectra is horizontal bars lying between the inner and outer Lindblad resonance, some of which are marked with green lines. Each of these structures corresponds to a rigid-rotating mode in the disc. The figure is taken from Sellwood & Carlberg (2014).

As self-induced spirals are material arms that corotate roughly with the disc, stars close to the arm may interact with the spiral structures persistently and therefore migrate. Grand et al. (2012b) found that stars immediately behind the spiral arms may be accelerated and therefore migrate outward, while stars in front of the arms may be decelerated and migrate inward. They also found that the outward migrators are slightly cooled while the inward migrators are slightly heated. Baba et al. (2013) also found similar cooling effects as migrators underwent aggregation and disaggregation in the ϕ-L_z space. These migrators change the dynamical temperature of the disc and may be the cause for recurrent spiral structures.

Tidally-induced Spiral Structures

The tidal force that either comes from massive objects or the dark matter halo itself naturally leads to spiral structures, that once formed, may persist in the disc as kinematic density waves or quasi-stationary spiral structures. One particularly interesting source of tidal forces is the parent dark matter halo. Dubinski & Chakrabarty (2009) simulated stellar discs in a dark matter halo with quadrupole force terms similar to Toomre (1981). In addition to warps and bars, spiral structures that extend to the edge of the disc were found. Compared to spiral structures formed purely through self-gravity, these spiral structures expand further in radius and are generally more wound up. Khoperskov et al. (2013) found similar spiral structures with triaxial dark matter haloes.

A companion or a subhalo can also generate spiral structures. Dobbs et al. (2010) studied the interaction between M51 (with disc mass $\sim 5.9 \times 10^{10} M_{\odot}$) and its companion NGC 5195 (of mass $\sim 7.07 \times 10^{10} M_{\odot}$). The simulated M51 disc developed prominent two-armed spiral structures and interarm branches that agree well with observations. They also found that the evolution of the spirals is chaotic unlike what is assumed in the Lin-Shu theory. In terms of the mass threshold of the companions, Purcell et al. (2011) found that two-armed spiral structures can form when subhaloes of mass $\sim 10^{10.5}$-$10^{11} M_{\odot}$ pass through the disc 30 kpc away from the disc centre. With a closer impact point of ~ 12 kpc, Pettitt et al. (2016) found that the mass threshold can be as low as $10^{9} M_{\odot}$.

Bar-driven Spiral Structures

The spiral arms in barred spiral galaxies sometimes start at the end of the bar, indicating a possible relation between them in barred galaxies. Sanders & Huntley (1976) studied hydrodynamical simulations of a gaseous disc with a bar potential, and found that two-armed trailing spiral structures form in the gaseous component as a response to the bar. It is, however, also possible that the connection between the bar and the spirals is accidental. In fact, Sellwood & Sparke (1988) argued that in N-body simulations, patterns in the disc can have multiple pattern speed (see also Sellwood & Carlberg, 2014, and Fig. 1.17). In their N-body simulations, there were typically a fast-rotating bar pattern in the inner region and a slow-rotating spiral pattern in the outer region of the disc. Despite the mismatch in pattern speeds, they found that most of the time in their simulation, the two patterns appeared connected, as both spiral structures and the bar have non-negligible width.

Disc Heating

As shown by equation (1.89), the efficiency of swing amplification depends heavily on the dynamical temperature of the disc, σ_R. The stellar disc can be heated in several ways thus suppressing gravity-induced spiral structures. For instance, Sellwood & Carlberg (1984) showed that spiral structures themselves can increase the velocity dispersion of stars and therefore suppress spiral structures. Another way to significantly heat the disc is through companions or subhaloes (Weinberg, 1998; Velazquez & White, 1999; Kazantzidis et al., 2009; Moetazedian & Just, 2016; Gómez et al., 2017). Moetazedian & Just (2016), for example, simulated stellar discs in dark matter haloes taken from the Aquarius project (Springel et al., 2008) and the Via Lactea II simulation (Diemand et al., 2008). The disc underwent a steady thickening and heating as the result of the continual impact of subhaloes.

Gaseous Components

Gaseous discs can influence spiral structures in many ways. Gittins & Clarke (2004) found that gaseous discs develop spiral structures and shocks when placed in a spiral potential, which represents the gravitational force from stellar spiral structures. In their simulation, the gaseous spiral structures did not superpose with stellar spirals, but instead followed their rotation from behind. Shocks in the gaseous component can also trigger star formation, leading to stellar spiral structures consisting of young stars. The formation of giant molecular clouds (GMCs) may also be influenced by the spiral structures. There are two possible mechanisms of GMC formation, one is agglomeration, which is due to the cloud-cloud collision of small gas clumps, and the other is gravitational instability. Dobbs (2008) studied the formation of GMCs and found that when the surface density of the gaseous disc is low, the spatial separation of GMCs indicates that they form mainly through agglomeration, while when the surface density of the gaseous disc is high, both mechanisms may be important.

Gaseous components are also important in dynamically cooling the disc. As shown in Gittins & Clarke (2004) and Dobbs (2008), gas may form giant molecular clouds and hence stars in a spiral potential. Sellwood & Carlberg (1984) found that star formation in the gaseous component can produce “cold” stars in the stellar disc, reducing the heating of the disc due to spiral structures and helping the formation of spiral structures.

In conclusion to this chapter, the formation and evolution of spiral structures is a complex process that involves many physical and dynamical processes. While various theories may be employed to study different spiral structures, the tidal torque of the dark matter haloes and subhaloes may be one of the promising ways. A detailed study connecting the properties

of dark matter haloes simulated in cosmological simulations and the formation of spiral structures is therefore necessary for improving our understanding of spiral formation. In this thesis I attempt to address these issues by studying

- the formation of spiral structures from tidal forces generated by realistic elliptical dark matter haloes and subhaloes,
- the interplay between externally-driven spiral structures and self-induced spiral structures,
- the nature of spiral structures formed through external perturbations, and
- the correlation between the spiral strength and the strength of the torque,

which may hopefully shed light on how the triaxial shape of the dark matter halo and the impact of its subhaloes may influence spiral formation.

Chapter 2

Numerical Approach

2.1 Motivation

While theoretical studies provide indispensable insight into the formation and evolution of spirals, numerical studies are also essential, specifically to test theoretical results, to study non-linear effects or complex interactions of various effects. Early works on the formation of spiral structures already involved N-body simulations. For example, in Toomre (1981), Zang's N-body simulation of a constant-velocity disc represented by 20,000 particles was presented. The disc developed $m = 2$ spiral structures when triggered by a quadrupole potential and continued being swing amplified to higher strength. Swing amplification was studied numerically to reveal how different values of Toomre's Q parameter and disc models influence the amplification factor. It later became clear that the Poisson noise stemming from a finite number of particles is enough to generate spiral structures through swing amplification, as demonstrated by Sellwood (2012). By looking at the action space, Sellwood (2012) also showed that the process of self-induced spiral formation can be understood as scattering in action space. Another interesting property of spiral structures is that they may be recurrent. For example, D'Onghia et al. (2013) studied the influence of massive clouds on the spiral structures with N-body simulations. In their simulation, the first generation of multi-armed spiral structures were triggered by massive clouds in the disc. However, with massive clouds removed after the formation of the first generation of spirals, new generations of spirals were triggered by the already formed spirals directly. Numerical studies as such provide us unique insights into the complex dynamics of spiral structures.

The formation of spirals in reality is even more complicated due to its interplay with various components in the galaxy. When placed in a realistic halo, the stellar disc, in response to the dark matter halo, may form spiral structures (e.g. DeBuhr et al., 2012). Dark matter subhaloes were found to cause warps and flares in the stellar disc as they pass

through the central halo, while dynamically heating and hence stabilising the disc against non-axisymmetric perturbations (D'Onghia et al., 2016; Moetazedian & Just, 2016; Gómez et al., 2017). Gaseous component comes into play as well. Gittins & Clarke (2004) found that a gaseous component develops sharp shock structures when placed in a spiral potential, which influences the star formation rate and may enhance star formation in the disc (Clarke & Gittins, 2006). Newly formed stars reduce the dynamical temperature of the disc, potentially enhancing the self-induced spiral structures.

Spiral structures are known to promote migration of stars. Grand et al. (2012a) found that stars are attracted to spiral structures from both sides when the spiral pattern rotate in the disc. They also found that stars migrate along the spiral arms. Stars behind the spiral structures are dragged forward and migrate outwards, while stars in front of the spiral structures are slowed down and migrate inwards.

As briefly discussed above, the formation and evolution of spiral structures is complicated in nature and related to various factors. As introduced in Chapter 1, dark matter haloes are considered to have a complex structure as well, having generally a triaxial shape and many orbiting subhaloes within. In this work I focus on the interplay of dark matter with the formation and evolution of spiral structures. To resolve the complex evolution of both the dark matter and the stellar disc, numerical simulations are essential to this work.

2.2 N-body Simulation

Systems of stellar discs and dark matter haloes are usually simulated with N-body simulations, represented by stellar and dark matter particles, respectively. Because galaxies are usually gravity-dominated, it is required to compute the gravitational interactions fast and accurately. Various different gravity solvers have been developed for this purpose.

The first gravity solver developed for N-body simulation is the Particle-particle (PP) method, where pairwise gravitational force is calculated directly (e.g. von Hoerner, 1960; Aarseth, 1963). This method generally resolves small-scale interactions such as binaries well, but as its computing time scales with the square of the number of particles $O(N^2)$, it is expensive for simulations with a very large number of particles. To run simulations with a larger number of particles, algorithms with various approximations have been developed, and the time efficiency can be reduced to $O(N \log N)$.

The Tree method (Barnes & Hut, 1986) is one of these methods. In the Tree method, particles are put into an oct-tree[1] based on their spatial distribution. Specifically, the entire domain of particles is enclosed in a cubic root node. The root node is then subdivided into

[1] An oct-tree is a tree where the maximum number of children of every node is 8.

eight child nodes consisting of particles in their corresponding domains. The subdivision continues until each leaf node consists of only one particle. When calculating the gravitational force, the code "walks" from the root node downwards, pausing at each node and deciding whether to walk down further based on the distance and the physical scale of the corresponding spatial domain. If the domain is far enough and small enough, the error by regarding the whole domain as a single mass body is small, the walk stops and approximates the gravitational force induced by all particles in this domain with an imaginary combined particle. The error of such calculation can therefore be controlled by tuning the stopping criteria for the walk.

The Particle-mesh (i.e. PM) method (e.g. Hockney & Eastwood, 1981; Klypin & Shandarin, 1983; Efstathiou et al., 1985) speeds up the calculation of gravitational force field with a different approach. The distribution of particles is first meshed onto a grid. Fourier transformation is applied to the grid to solve the Poisson equation. The force on each particle is then calculated by interpolation. The efficiency of PM method depends on the number of grid cells along one dimension M, as $O(M \log M)$. It is generally faster than the Tree method, but has relatively low dynamical range.

Based on Tree and PM methods, several extensions have been developed to achieve high accuracy without compromising the speed. One extension of the PM method combines the PM algorithm with the idea of Adaptive Mesh Refinement (AMR) scheme. The AMR scheme (Berger & Oliger, 1984; Berger & Colella, 1989) was originally developed to solve partial differential equations (PDEs) with a large dynamic range. The idea is to divide the region into cells of different sizes based on the fineness of structures, determined by properties such as the density gradient, so that PDEs are solved with higher spatial resolution in regions where the gradient of fields is steeper. The combination of the PM method and the AMR scheme, the Adaptive Refinement Tree code (ART; Kravtsov et al., 1997) creates levels of refined meshes in the high-density regions, and applies PM method on each level of the refined meshes to calculate the gravity force accurately. ART improves the accuracy of PM method without losing too much speed, but as the force calculation is still grid-based, the accuracy is not uniform - the force is calculated more accurately in the fine grid regions than in the coarse grid regions.

Another extension to PM method is the Particle-particle-particle-mesh (P^3M) method (see e.g. Hockney & Eastwood, 1981). In this method, the force on a particle is decomposed into two components: force contributed by nearby particles, calculated with a direct method, and by a smooth background component, calculated with a PM algorithm. By combining PP method at a close range and PM method for the field, the P^3M method is more accurate than the PM method, but it can be slower when particles are heavily clustered.

The TreePM method is a combination of the Tree method and the PM method (Xu, 1995). In this scheme, isolated objects of fine structures are selected out from high-density regions to form isolated trees. The remaining particles, categorised as PM particles, do not belong to any particular small-scale structure. Therefore force on them can be calculated very accurately with PM method considering all particles in the system as a whole group. The force on a Tree particle can be decomposed into an internal force $\mathbf{F}_{\rm internal}$ that comes from within the tree and an external force $\mathbf{F}_{\rm external}$ that comes from all other trees and the PM particles, i.e.

$$\mathbf{F} = \mathbf{F}_{\rm internal} + \mathbf{F}_{\rm external}\,. \tag{2.1}$$

The internal force can be calculated by the Tree method, and the external force can be calculated through the PM method with the density field consisting of the remaining particles (including particles in other trees and PM particles). By combining the two methods, TreePM method is fast and still keeps the good dynamic range of the Tree method.

Several comparison of different cosmological simulation codes (e.g. Frenk et al., 1999; Heitmann et al., 2005, 2008; Sembolini et al., 2016) have shown that the results of different gravity solvers agree reasonably well when performed on various test simulations. The maximum difference of density profiles of virialized objects in these simulations is generally lower than 10%, and can be further reduced to 5% if optimal resolution is adopted. The differences can be understood on a case-by-case study. For example, Heitmann et al. (2008) found that AMR has difficulties with small haloes when the grid is not refined enough, i.e. using base grids that are too coarse suppresses the formation of small haloes. Issues have also been found with the TreePM method when the transition from the Tree method to the PM method is not handled very carefully. Fortunately, same issues are not found with the TreePM implementation in GADGET-3 (the code adopted in this Thesis).

The number of particles in a typical N-body simulation has been increasing drastically, as shown in Figure 2.1. From 1970 to 2005, the number of particles included in a N-body simulation increased from less than 1,000 to more than 10^{10}. The increase in the number scale of N-body simulations correlates with years well, similar to the Moore's law, doubling in roughly 18 months. Such drastic improvement over less than 40 years is not only attributed to the fact that the computing power increases as the Moore's law, but also to the fact that gravity solvers improved from the direct method, whose time efficiency is $O(N^2)$, to methods like the TreePM whose time efficiency is $O(N\log N)$. In addition, state-of-the-art simulations are now highly parallel, which further increases feasible number of particles in one simulation.

In this work I focus mainly on the dynamics of the stellar components in galaxies. As spiral, ring and warp structures develop in the disc, the system develops high density regions with complicated morphologies. As the dynamics of stars is dominated by the gravitational

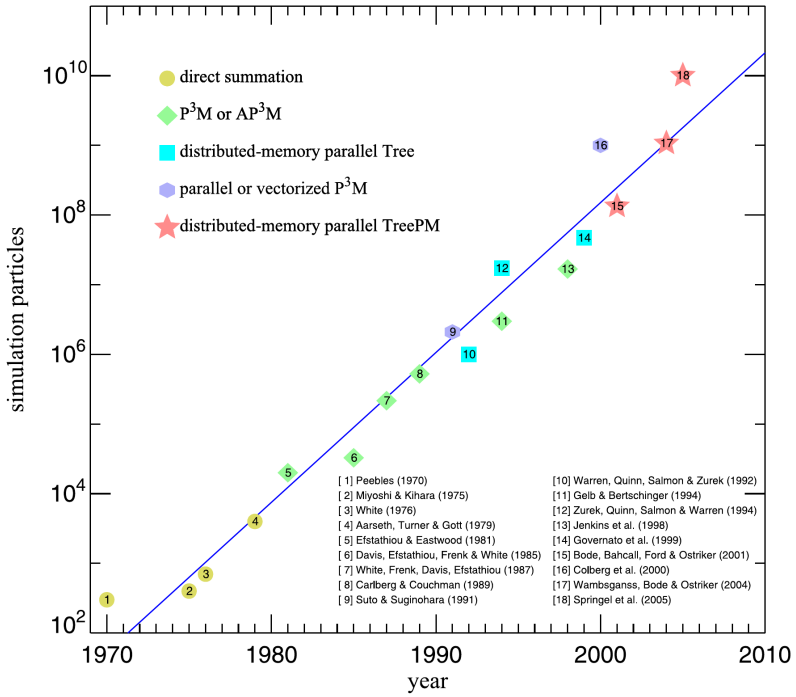

Fig. 2.1 Number of particles in N-body simulations over time. Simulations carried out in different works from 1970 to 2005 are plotted against the Moore's law (shown in the blue line). According to the Moore's law, the computing power of CPUs doubles every 18 months. These works employed different solvers including PP (shown in yellow dots), P^3M and adaptive particle-particle, particle-mesh (AP^3M) method (shown in green diamonds), parallel Tree (shown in cyan squares), P^3M (shown in purple hexagons) and TreePM (shown in red stars) methods. The number scale of N-body simulations, growing from less than 1,000 in 1970 to more than 10^{10} in 2005, falls nicely onto the Moore's law. Note that recent simulations perform slightly better than Moore's law prediction thanks to improvements in the gravity solver. The plot is taken from Dolag et al. (2008) where it was attributed to Volker Springel originally.

force, a gravity solver with good accuracy throughout the disc is required. We therefore choose GADGET-3, a state-of-the-art implementation of the TreePM method to the purpose.

2.2.1 Gadget-3

GADGET-3 is a new version of GADGET-2 (Springel, 2005). It is a N-body/SPH code with a TreePM gravity solver. GADGET-3 is capable of simulating dark matter, stars and gaseous components simultaneously with different categories of particles, accounting for their collisionless or hydrodynamical evolution and gravitational interaction as well as other (sub-grid) physics, such as radiative cooling, heating and star formation.

Gaseous component can be important in the evolution of galactic discs. By interacting with the stars through gravity, gas can enhance the self-gravity of the disc. Moreover, new stars formed from the high density gas clumps can act as a cooling source to the dynamical temperature of the disc by lowering the velocity dispersion. However, modelling gas numerically is very difficult, given that complex cooling and heating processes need to be taken into account. Therefore we do not include gaseous component in this work.

Most of our simulations are instead focused on the dynamics of the stellar and the dark matter components. For galaxies, they can be considered as collisionless components dominated by the gravitational interactions. The dynamics of these systems can be described by the collisionless Boltzmann equation, which is however extremely hard to solve. As a N-body code, GADGET-3 solves the dynamics of the collisionless system by sampling the 6-dimensional phase-space distribution with "particles", whose Hamiltonian is

$$H = \sum_i \frac{\mathbf{p}_i^2}{2m_i a(t)^2} + \frac{1}{2}\sum_{ij} \frac{m_i m_j \varphi(\mathbf{x}_i - \mathbf{x}_j)}{a(t)}, \tag{2.2}$$

where $\mathbf{p}_i$ is the momentum of the i-th particle, $\mathbf{x}_i$ is the spatial coordinate of the i-th particle, m_i is the mass of i-th particle, $a(t)$ is the scale factor from cosmological models and $\varphi(\mathbf{x}_i - \mathbf{x}_j)$ is the gravitational potential of i-th particle from j-th particle. In most of our simulations, we study an isolated galaxy without cosmological context. In these simulations $a(t) = 1$.

Equation (2.2) involves the pairwise potential of particles. A point-mass Newtonian potential only works when the particles are far away, as a stellar or dark matter particle represents a group of stars or dark matter of non-negligible size. It is important in N-body simulations to "soften" the gravitational force when two particles are within the distance of their physical scale. Gravitational softening prevents strong two-body interactions which breaks the collisionless assumption and causes numerical artefacts.

A typical softening has the form of the Plummer model, whose density kernel is

$$\rho_{\mathrm{P}}(r) = \left(\frac{3m_{\mathbf{P}}}{4\pi\epsilon}\right)\left(1 + \frac{r^2}{\epsilon^2}\right)^{-\frac{5}{2}}, \tag{2.3}$$

where the Plummer radius ϵ gives the physical scale of the particle. Such profile leads to a softened gravitational potential of the form

$$\Phi_{\mathrm{P}}(r) = -\frac{GM}{\sqrt{r^2 + \epsilon^2}}, \tag{2.4}$$

which is finite as $r \to 0$, but falls back to Newtonian when r is large.

In GADGET-3, the density field represented by each particle is a spline kernel (Monaghan & Lattanzio, 1985) in the form of

$$W(r,h) = \frac{8}{\pi h^3} \begin{cases} 1 - 6\left(\frac{r}{h}\right)^2 + 6\left(\frac{r}{h}\right)^3, & 0 \le \frac{r}{h} \le \frac{1}{2}, \\ 2\left(1 - \frac{r}{h}\right)^3, & \frac{1}{2} < \frac{r}{h} \le 1, \\ 0, & \frac{r}{h} > 1, \end{cases} \tag{2.5}$$

where h is the scale of the kernel and represents the resolution of the simulation. When compared to the Plummer model, we have $h = 2.8\epsilon$, where ϵ is the Plummer-equivalent softening length of the particle.

2.2.2 Leapfrog Integration

To solve equation (2.2), GADGET-3 calculates the trajectories of tracer particles in the 6-dimensional phase-space with a leapfrog integration. Over a timestep of Δt, two operations are needed to update the phase-space coordinate of a particle: a) a "drift" operation that keeps the velocity but moves the spatial coordinate by $\frac{\mathbf{p}_i}{m_i}\mathrm{d}t$, and b) a "kick" operation that keeps the spatial coordinate but "kicks" the velocity by $\mathbf{f}_i\mathrm{d}t$, where $\mathbf{f}_i = -\sum_j m_i m_j \frac{\partial \varphi(\mathbf{x}_i - \mathbf{x}_j)}{\partial \mathbf{x}_i}$ is the gravitational force felt by the particle. Two variations of leapfrog are the Drift-Kick-Drift (DKD) and the Kick-Drift-Kick (KDK) variance. In the DKD variance, during each timestep Δt, the particle first perform a half-step of the "drift" operation (by drifting the particles for $\frac{1}{2}\Delta t$), followed by a complete "kick" operation and finishes by the second half-step of the "drift" operation. Contrarily, the KDK variance does a half-step of "kick", a full-step "drift" and then a half-step "kick".

A very important feature of a leapfrog integration is that it is symplectic (e.g. Saha & Tremaine, 1992; Quinn et al., 1997), meaning that each step of its integration is a canonical transformation. This feature guarantees the preservation of Poincaré invariants such as the total energy (when the Hamiltonian is time-independent) and total angular momentum (when the Hamiltonian is axisymmetric). This ensures a good stability for the simulation even when the timestep is crude.

For orbits of stars, we are most concerned about the conservation of total energy. Fig. 2.2 demonstrates energy conservation (represented by the preservation of semi-major axis) of the leapfrog algorithm compared to the Runge-Kutta method. The two variances of the leapfrog algorithm, shown in the top panels, perform much better than the second-order Runge-Kutta method, and preserve orbital energy comparable to or better than the fourth-order Runge-

Kutta method, although a precession of axis is seen for the DKD variance. GADGET-3 utilises the leapfrog algorithm due to its symplectic property and its good accuracy.

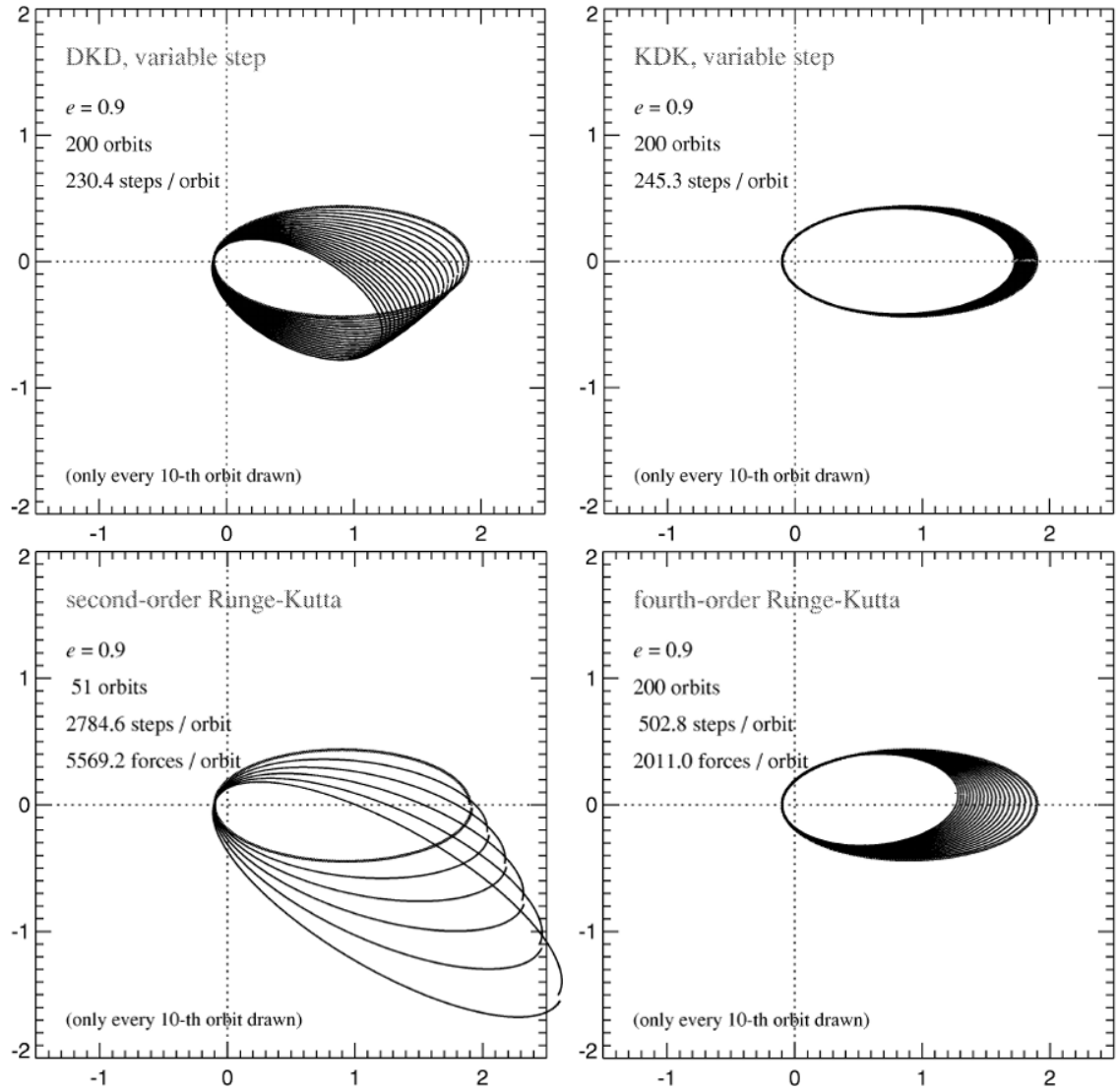

Fig. 2.2 A comparison between the leapfrog Drift-Kick-Drift variance (top left panel), Kick-Drift-Kick variance (top right panel), the second-order Runge-Kutta (bottom left panel), and the fourth-order Runge-Kutta (bottom right panel) integration. Trajectories of stars calculated with these four methods are shown. The error of the energy can be inferred from the error of semi-major axis. The leapfrog algorithm preserves the energy of the orbits much better than the second-order Runge-Kutta method. Even the fourth-order Runge-Kutta integration, whose integration error is two orders of magnitude lower than the leapfrog method, does not perform better than the DKD variance by much and performs worse than the KDK variance. It is also interesting to notice that the KDK variance has smaller errors. This figure is taken from Springel (2005).

2.2.3 TreePM Method and Domain Decomposition

A typical simulation in this Thesis consists of $N = 10^6$ to $N = 10^8$ particles. As mentioned earlier, GADGET-3 implements the TreePM method as the gravity solver. In GADGET-3, particles are placed on an oct-tree based on their spatial distribution. Each node is coupled to a rectangular cuboid region. The rectangular region is subdivided into 8, each with half the side length. Naturally these 8 sub-divided regions are each coupled to one of the 8 children nodes in the oct-tree. Aside from being tightly connected to the geometry of the system, the oct-tree is also generally shallower than a binary tree as each node has more children. This lowers the number of walks required and provides better memory efficiency. An illustration of the tree is shown in top panel of Fig. 2.3. A quad-tree built for a 2D simulation is shown, but in real 3D simulations, oct-trees are built.

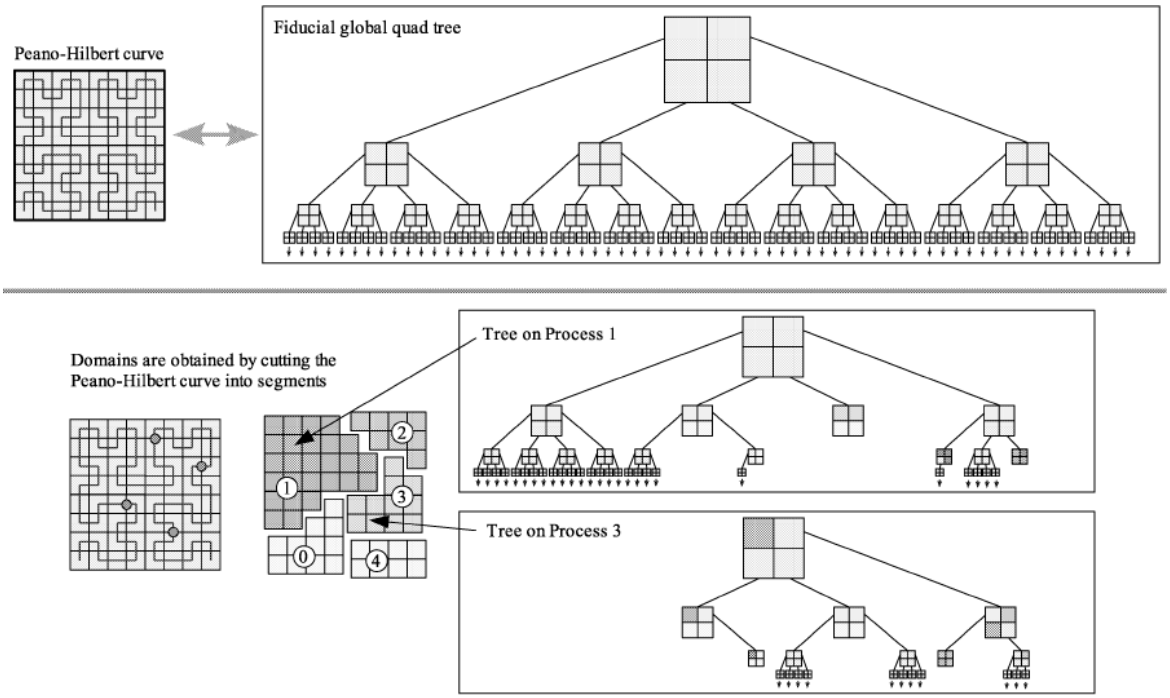

Fig. 2.3 Illustration of the tree structure in GADGET-3 in 2D. The top panel shows the full tree constructed for a non-parallel simulation. The tree built for the system is closely coupled to the domain decomposition of the simulated region. Note that in a 3D simulation, an oct-tree is used instead of a quad-tree shown in the illustration. The bottom panel shows the tree generated for a parallel simulation. The finest blocks are ordered in a Peano-Hilbert order and this series of blocks are cut into sections. Each processor takes one of the sections to build a tree upon it. Pseudo-particles representing domains on other processors are also inserted into the trees to make the tree complete and make it possible to look up the data from other processors when needed. This figure in taken from Springel (2005).

2.2.4 Parallel Computing

GADGET-3 can be ran in parallel on high performance clusters through the use of Message Passing Interface (MPI). Multiple processes are simultaneously spawned on each of the CPUs used for the simulation, each responsible for a fraction of the simulated domain. These processes communicate through MPI during each step to calculate cross-domain forces and to exchange particles.

As described in Section 2.2.3, particles are put in an oct-tree in the Tree method implementation of GADGET-3. For serial simulations, a perfect oct-tree can be built for the whole domain similar to the top panel in Fig. 2.3. When parallel, a part of the tree is built for each node using the Peano-Hilbert curve. As shown in the bottom left panel of Fig. 2.3, for 2D case, a Peano-Hilbert curve can be built by placing a U-shaped curve in the most coarse grid and replacing each node with a U-shape curve recursively as the grid refines. In the 3D case such curve can be built similarly. As shown in the middle bottom panel of Fig. 2.3, the Peano-Hilbert curve preserves the locality of the grid very well, i.e. a section of the curve usually corresponds to a tightly packed domain. Therefore the whole simulation domain can be decomposed by cutting the Peano-Hilbert curve into sections of the same number as the number of tasks. For each section, its corresponding region is then assigned to one of the tasks. As shown in the bottom right panel of Fig. 2.3, for each task, a fragment of the tree is built, and a placeholder is used when a region belongs to another task. Communications between tasks are made when expansion over such placeholders are required.

The PM part of the algorithm is also parallel. This is done by dividing the domain into slabs, applying Fast Fourier Transform (FFT) to two long sides of the slab locally, and then applying FFT globally over the third direction. The requirement to apply FFT globally may cause drawbacks in the efficiency when number of tasks is large, but luckily in most cases, and especially in simulations in this Thesis, this is not an issue, as PM takes a minor portion of the time cost.

As huge snapshot files are created during the simulation (containing all the necessary particle data), GADGET-3 has also the option to write and read files in parallel, which saves a significant amount of time on high performance clusters.

2.3 Numerical Model

Most of the simulations in this Thesis include a live stellar disc. The dark matter halo is simulated with dark matter particles in some of the simulations but included as analytic dark matter potentials in the others. They are either spherical or triaxial. Illustrations of stellar discs and dark matter haloes adopted are shown in Fig. 2.4. Stellar discs (left panel) in this

Thesis have a scale length of $R_S = 3.13\,\mathrm{kpc}$. The scale height R_h is set to be 10% of the scale length, which defines a very thin disc. Patterns in the disc typically extend as far as $\sim 5R_S$ in the disc, which is about 15 kpc. The dark matter haloes (middle and right panels) are generally more than 10 times larger than the disc in physical scale. Different dark matter haloes are used, and their radius ranges from $R_{200} = 159\,\mathrm{kpc}$ to $R_{200} = 245\,\mathrm{kpc}$. An orange square of a side-length of 40 kpc is drawn in the centre of the middle panel for a comparison of scale. For triaxial haloes, the length of the three semi-principal axes are denoted as a, b and c. In this work we also use shape parameters p and q to describe the shape of a triaxial halo; they are defined as $p = b/a$ and $q = c/a$. In the illustration the halo has an axis ratio of $p = 0.95$ and $q = 0.85$.

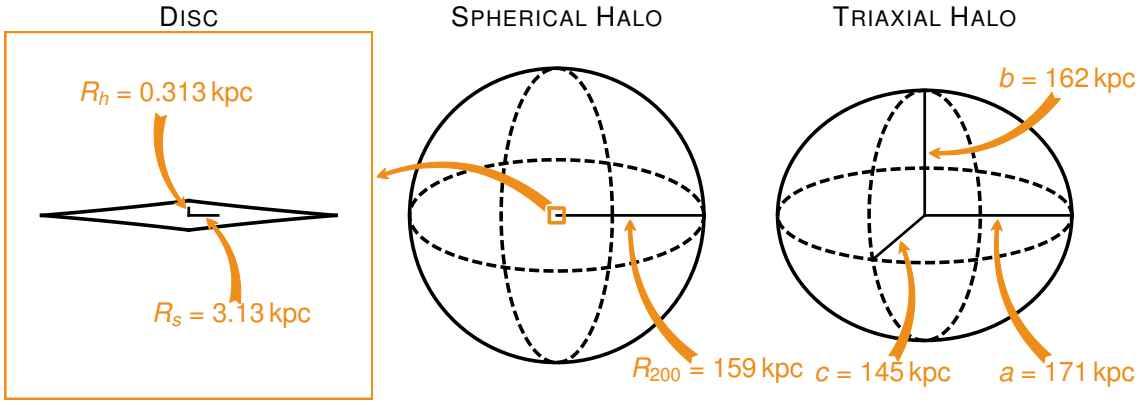

Fig. 2.4 Illustrations of typical components used in this work. Left panel: an illustration of the edge-on view of the stellar disc. Stellar discs have a scale length of $R_S = 3.13\,\mathrm{kpc}$, and a scale height of 0.313 kpc. Structures typically extend from the centre of the disc to $\sim 5R_S$. Middle panel: an illustration of a typical spherical dark matter halo used in this work. Stellar discs are embedded in the central region of the dark matter halo, shown as an orange square with a side length of 40 kpc. Right panel: an illustration of a typical triaxial halo in this work. Three semi-principal axes, a, b and c, are used to describe the shape of these haloes.

The general setup of the system is described in the following sections.

2.3.1 Stellar Discs

We set up our disc model following the description in Springel et al. (2005a). The most important properties of the disc are listed below. The disc has an exponential surface density profile and an isothermal sheet profile vertically, described by

$$\rho_*(R,z) = \frac{M_*}{4\pi z_0 R_S^2}\mathrm{sech}^2\left(\frac{z}{z_0}\right)\exp\left(-\frac{R}{R_S}\right), \tag{2.6}$$

where R_S is the scale length of the disc, M_* is the total mass of the stars and z_0 is the scale height. For most of our simulations, we choose $R_S = 3.13\,\mathrm{kpc}$, $M_* \sim 10^{10} M_\odot$ and $z = 0.1\,R_S$.

Based on the mass distribution of such a disc, the circular velocity is given by

$$V_c^2(R) = \frac{GM_{dm}(<R)}{R} + \frac{2GM_*}{R_S} y^2 \times [I_0(y)K_0(y) - I_1(y)K_1(y)], \tag{2.7}$$

where $M_{dm}(<R)$ is the mass of dark matter enclosed within a radius R, I_n and K_n are real-valued modified Bessel functions of the first and second order and $y = R/(2R_S)$. The velocity structure of the disc is assumed as a triaxial Gaussian distribution with axes aligned to the axes of the disc. As described in Section 1.5.1, the mean streaming velocity in azimuthal position, $\langle v_\varphi \rangle$, and the velocity dispersion in three directions are calculated numerically based on equation (1.65) to equation (1.68).

It is worth mentioning that the scale length R_S is not a free parameter here. In fact, it can be derived from the angular momentum of the disc. For a halo profile given in the next section, the angular momentum of the halo can be written as

$$J_{dm} = \lambda G^{1/2} M_{dm}^{3/2} r_{dm}^{1/2} \left(\frac{2}{f_c}\right)^{1/2}, \tag{2.8}$$

where the factor f_c is determined by the exact shape of the halo, λ is a free parameter called the spin parameter, r_{dm} is the virial radius and M_{dm} is the virial mass. By assuming that the specific angular momentum of the disc is the same to that of the halo, we can work out the angular momentum of the disc as $J_* = m_*(J_* + J_{dm})$, where $m_* = M_*/(M_{dm} + M_*)$ is the mass ratio of the disc. Since the angular momentum of the disc can also be calculated directly by

$$J_* = M_* \int_0^\infty V_c(R) \left(\frac{R}{R_S}\right)^2 \exp\left(-\frac{R}{R_S}\right) \mathrm{d}R, \tag{2.9}$$

the exact value of R_S can be worked out numerically. In this work we tune the spin parameter λ so that the scale length of the disc is always $R_S = 3.13\mathrm{kpc}$.

2.3.2 Analytic Dark Matter Haloes

Dark matter halo generally has much larger mass than a stellar disc. It is difficult to run a live stellar disc embedded in a live dark matter halo because one either needs to run the simulation with much larger number of dark matter particles or use dark matter particles with a much larger particle mass. The first approach is acceptable for some cosmological simulations that focuses more on the evolution of the dark matter halo, but does not work for our simulations

where we focus mostly on the detailed dynamics of stellar discs. The second approach is not ideal either as massive dark matter particles create non-negligible perturbations to the disc. Since we mainly want to study the evolution of stellar discs in response to dark matter haloes, we use analytic dark matter haloes for most of our simulations.

Spherical Profiles

Several different spherical profiles are used to model the dark matter haloes, including the NFW, the Hernquist and the Einasto profile.

The NFW profile (Navarro et al., 1996) has the form of

$$\rho_{\rm NFW}(r) = \frac{\rho_{\rm N0}}{(r/r_{\rm s})(1+r/r_{\rm s})^2}\,, \tag{2.10}$$

where $\rho_{\rm N0}$ is the scale density and $r_{\rm s}$ is the scale radius. Concentration parameter c is used to describe the shape of the profile. It is a dimensionless parameter defined as the ratio of the virial radius r_{200} and the scale radius $r_{\rm s}$, i.e. $c = r_{200}/r_{\rm s}$. Another dimensionless parameter $\delta_{\rm c} = \rho_{\rm N0}/\rho_{\rm crit}$ can be defined for the profile, where $\rho_{\rm crit}$ is the critical density, $\rho_{\rm crit} = 3H^2/8\pi G$, with H being the Hubble constant. $\delta_{\rm c}$ is linked to c as the mean density enclosed in r_{200} is $\rho_{200} = 200\rho_{crit}$. $\delta_{\rm c}$ can be calculated from c with

$$\delta_{\rm c} = \frac{200}{3}\frac{c^3}{\ln(1+c) - c/(1+c)}\,. \tag{2.11}$$

The Hernquist profile (Hernquist, 1990) has the form of

$$\rho_{\rm Hern}(r) = \frac{\rho_{\rm H0}}{(r/a)(1+r/a)^3}\,, \tag{2.12}$$

where a is a parameter that controls the concentration. The mass enclosed within a given radius r has a simple form,

$$M_{\rm in}(r) = 2\pi a^3 \rho_{\rm H0}\frac{(r/a)^2}{(1+r/a)^2}\,, \tag{2.13}$$

which also means that the virial mass is approximately $M_{200} = 2\pi a^3\rho_{\rm H0}$. Same as the NFW profile, the density of dark matter halo in the Hernquist profile is inversely proportional to the radius, i.e. $\rho(r) \sim r^{-1}$ when $r \ll r_{200}$. By matching a Hernquist halo and a NFW halo that have the same inner profile and the same virial mass, one can relate a and $r_{\rm s}$, i.e.,

$$a = r_{\rm s}\sqrt{2[\ln(1+c) - c/(1+c)]}\,, \tag{2.14}$$

where the concentration parameter c is defined for the NFW profile but can also be defined for the Hernquist profile in this way.

The Einasto profile (Einasto, 1965) is described by

$$\rho_{\rm Ein}(r) = \rho_{\rm E0} \exp\left[-\frac{2}{\alpha}\left((r/R)^{\alpha} - 1\right)\right], \tag{2.15}$$

where α is a shape parameter and R is a scale parameter. Unlike the r^{-1} profile of the NFW and the Hernquist profile, the Einasto profile as a constant inner density limit.

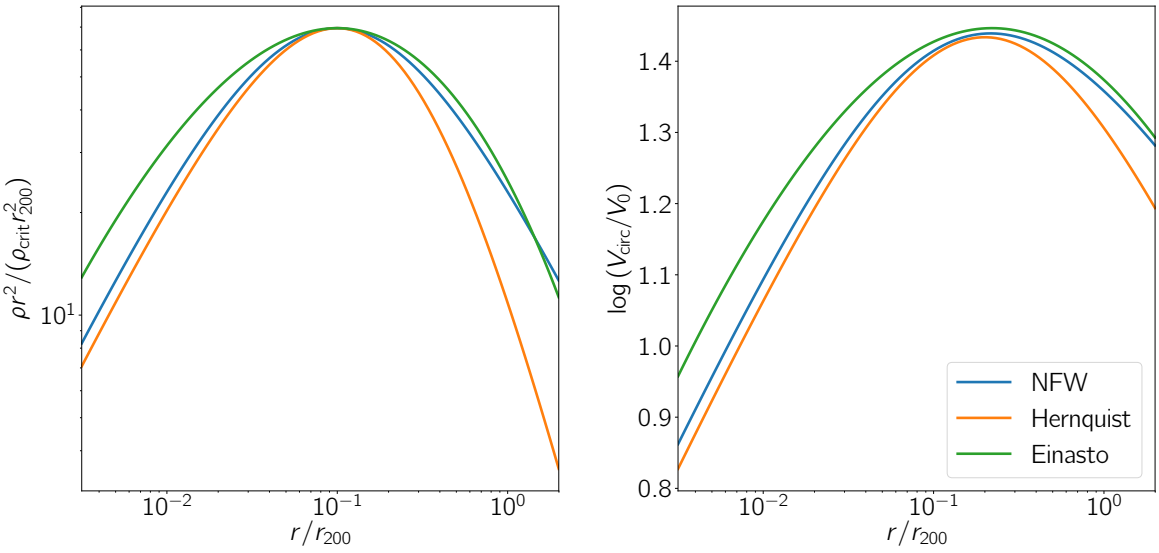

Fig. 2.5 A comparison of NFW, Hernquist and Einasto profiles. Left panel: density multiplied by the square of radius, ρr^2, over radii. For the NFW halo (blue curve) $c = 10$. The Einasto profile (green curve) is shown with $\alpha = 0.170$. The parameters of the three profiles are chosen so that ρr^2 peaks at the same radius with the same density. Therefore parameters of the Hernquist profile (blue curve) are different from equation (2.14) that matches the innermost region of the two profiles. In the outer region, the Einasto profile drops most quickly as it exponentially decreases, followed by the Hernquist profile which declines as $\sim r^{-4}$. The NFW drops of most slowly as $\sim r^{-3}$. Right panel: velocity curve over radii in the unit of $V_0 = \sqrt{G\rho_{\rm crit} r_{200}^2}$. The velocity curve of the three profiles is similar with the Einasto profile having the highest velocity spanning the inner and outer region, followed by the NFW profile and then the Hernquist profile.

A comparison of the three profiles is shown in Fig. 2.5. As illustrated in the left panel, the inner region of the NFW and the Hernquist profile can be matched very well. As $r \to \infty$, the density of the NFW profile scales as $\rho_{\rm NFW} \sim r^{-3}$, while the Hernquist profile scales as $\rho_{\rm Hern} \sim r^{-4}$. To better compare the three profiles, a different Hernquist halo is used, so that the peak ρr^2 value and the peak radius match. The Einasto profile has $\alpha = 0.170$, which

Navarro et al. (2010) found to be the best fit for the Aq-A-1 halo, the highest resolution halo in the Aquarius project. Although not apparent in the plotted region due to a low α, the Einasto profile does not grow as quickly as the NFW and the Hernquist profile as $r \to 0$. In the outer limit, the Einasto profile drops off much more quickly with an exponential decrease.

All three profiles provide good fits to a realistic dark matter halo. In simulations where the exact form of the halo is not important, the Hernquist profile is applied for its two advantages: a) it converges quickly because its density scales with r^{-4} in the outer region, and b) it has a simple mathematical form of the density profile, the enclosed mass, and the potential. We therefore use the Hernquist profile for most of our idealised simulations. In simulations where a good analytic profile representing Aquarius haloes is needed, we employ modified versions of the Einasto profile as it fits the Aquarius halo well (Navarro et al., 2010).

Triaxial Profiles

As mentioned in Section 2.3.3, cosmological simulations produce triaxial dark matter haloes rather than the spherical ones. One generally applied method (see e.g. Binney, 1987; Jing & Suto, 2002) to model the triaxial halo is to represent it with a series of isodensity ellipsoidal shells. The density profile can be obtained by replacing the radius r in equation (2.10) (2.12) and (2.15) with

$$R^2 = x^2 + y^2/p^2 + z^2/q^2\,, \tag{2.16}$$

where $p = b/a$ and $q = c/a$, are the ratio of the semi-principal axes a, b, and c. Very complicated triaxial dark matter haloes can be modelled in this way with p and q changing over radii according to a given halo model.

A drawback of this method is that it is difficult to compute the potential of such dark matter haloes analytically. In this Thesis I apply an alternative method following Bowden et al. (2013), where the triaxial component of the dark matter halo is modelled with two extra spherical harmonic functions. The total density profile of our model is

$$\rho(r,\theta,\phi) = \rho_{\rm S}(r) + \rho_{\rm T1}(r,\theta) + \rho_{\rm T2}(r,\theta,\phi)\,, \tag{2.17}$$

where $\rho_{\rm S}$ is the spherical component and $\rho_{\rm T1}$ and $\rho_{\rm T2}$ are two triaxial components. They are defined as

$$\rho_{\rm T1}(r,\theta) = \rho_{\rm t1}(r) Y_2^0(\theta)\,, \tag{2.18}$$

and

$$\rho_{\rm T2}(r,\theta,\phi) = \rho_{\rm t2}(r) Y_2^1(\theta,\phi)\,, \tag{2.19}$$

where $Y_2^0(\theta) = \frac{3}{2}\cos^2\theta - \frac{1}{2}$, $Y_2^2(\theta,\phi) = 3\sin^2\theta\cos 2\phi$ are spherical harmonic functions of the 2nd order. We then use different forms of $\rho_{\rm T1}$ and $\rho_{\rm T2}$ to model different shapes of dark matter haloes based on different initial spherical dark matter profiles.

For the Hernquist halo profile, we want $\rho_{\rm T1}$, $\rho_{\rm T2}$ and the corresponding gravitational potential to be analytical. We start by noting that the Hernquist profile satisfies $\rho \to r^{-1}$ as $r \to 0$ and $\rho \to r^{-4}$ as $r \to \infty$. To modify the inner and the outer triaxiality, the two extra spherical harmonic terms should have the same asymptotic behaviour. It results that if we define their gravitational potential to be

$$\Phi_{\rm T1}(r,\theta,\phi) = 4\pi G \frac{\rho_1 r_1^4 r}{(r+r_1)^3} Y_2^0(\theta,\phi)\,, \tag{2.20}$$

and

$$\Phi_{\rm T2}(r,\theta,\phi) = -4\pi G \frac{\rho_2 r_2^4 r}{(r+r_2)^3} Y_2^2(\theta,\phi)\,, \tag{2.21}$$

the density of the two triaxial components will be of the following form

$$\rho_{\rm t1} = 4\rho_1 \frac{r_1^4(r_1^2+5r_1 r+r^2)}{(r+r_1)^5 r}\,, \tag{2.22}$$

and

$$\rho_{\rm t1} = 4\rho_2 \frac{r_2^4(r_2^2+5r_2 r+r^2)}{(r+r_2)^5 r}\,, \tag{2.23}$$

where r_1, r_2, ρ_1 and ρ_2 are four model parameters, and the asymptotic behaviour is the same as the Hernquist profile. The four parameters, r_1, r_2, ρ_1 and ρ_2 can be tuned for desired axis ratio in the inner and outer region.

In simulations where an Einasto profile is used to represent a realistic dark matter halo, We calculate $\rho_{\rm T1}$ and $\rho_{\rm T2}$ numerically. To achieve a certain p and q profile, we choose $\rho_{\rm T1}$ and $\rho_{\rm T2}$ so that the total density has isodensity surfaces of the desired shape. Detailed description of this method can be found in Appendix 4.B.

2.3.3 Live Dark Matter Haloes

In simulations where the effects of dark matter subhaloes is studied, live subhaloes are included in the simulation. We take our live subhaloes as well as dark matter main halo profiles from reruns of the Aquarius project (Springel et al., 2008).

The Aquarius project is a series of dark matter only simulations aiming to produce Milky Way-sized dark matter haloes. A cosmological simulation is carried first in a periodic cube of side length 137 Mpc with 900^3 particles representing an average region of the Universe.

Six Milky Way-sized dark matter haloes, named as Aq-A to Aq-F, are selected from the simulation and resimulated at higher resolution from $z = 127$ to $z = 0$. At $z = 0$, these haloes have a virial mass ranging from $M_{200} = 8.2 \times 10^{11} M_{\odot}$ to $M_{200} = 1.84 \times 10^{12} M_{\odot}$, and a virial radius from $r_{200} = 188\,\mathrm{kpc}$ to $r_{200} = 245\,\mathrm{kpc}$. For each halo, the simulation is run at different levels of resolution. In Aq-A-1, the simulation with the highest resolution, there are more than 4 billion particles simulated, and about 1.5 billion of them belongs to the dark matter halo. A single high resolution particle has a mass of $m_{\mathrm{P}} = 1.712 \times 10^{3} M_{\odot}$ and a gravitational softening length of $\epsilon = 20.5\,\mathrm{pc}$.

Resimulating Aq-A-1 with more than 1 billion particles can be time consuming. However, since this study focuses on the dynamics of the stellar disc, we use a lower resolution version, Aq-A-4, for our simulations, which has $\sim 6.4 \times 10^{6}$ particles in the halo. The high resolution particles have a mass $m_{\mathrm{P}} = 3.929 \times 10^{5} M_{\odot}$ and gravity softening length of $\epsilon = 342.5\,\mathrm{pc}$. As stellar discs are simulated with a much higher resolution, dark matter particles in the main halo can perturb the disc and lead to numerical artefacts. To prevent such problems, we only include the live subhaloes, and replace the main halo with a realistic dark matter potential as modelled in Section 2.3.2.

Navarro et al. (2010) found that the spherically averaged density profiles of the Aquarius haloes are consistent across haloes and across resolution levels, as illustrated in the left panel of Fig. 2.6. The radial density profile of the Aquarius haloes can be well fitted with an Einasto profile with the shape parameter α ranging from 0.130 to 0.174. The best fit for the Aq-A-1 halo is the Einasto profile with $\alpha = 0.170$. The shape of the Aquarius haloes is generally triaxial. As illustrated in the right-hand panel of Fig. 2.6, Vera-Ciro et al. (2011) found that the inner region of Aquarius haloes generally has $b/a \sim 0.5$ and $c/a \sim 0.4$, where a, b and c are the lengths of the three semi-principal axes of iso-density surfaces of the halo. The outer region of the halo are generally rounder with ratios typically between 0.6 and 0.9. It is to be noted that the Aquarius simulation is dark matter-only. For example, Zemp et al. (2012) found that when the baryonic matter is included in the simulation, the inner halo is rounder. In some of our simulations where an analytic model of the Aquarius dark matter halo is required, a model with rounder inner halo is used to account for the baryonic effects.

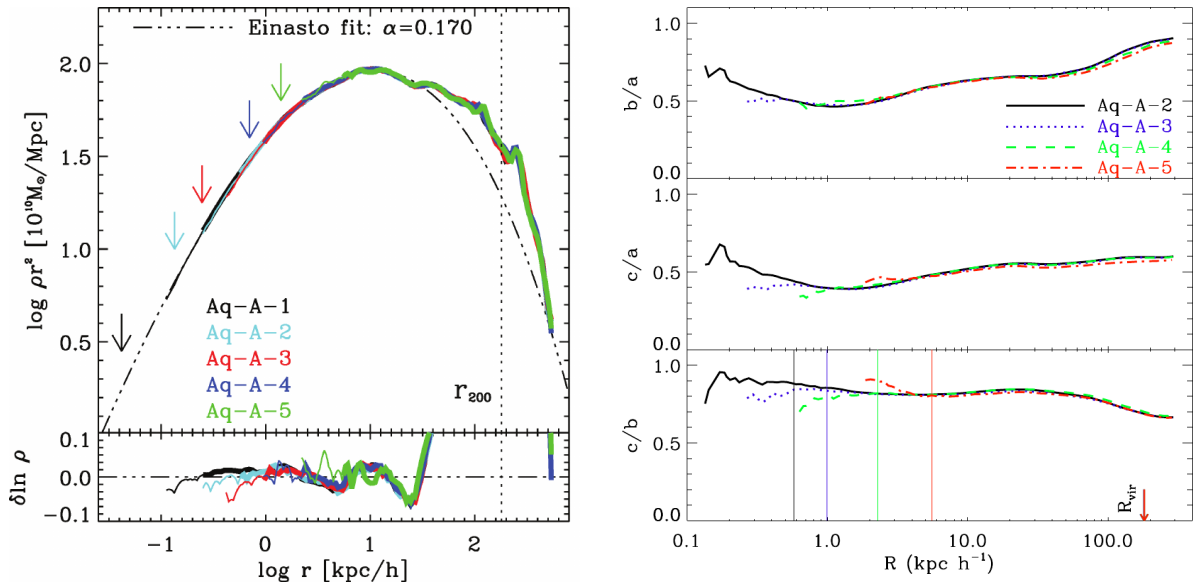

Fig. 2.6 The density and shape profile of the Aquarius haloes, taking Aq-A haloes as an example. Left: The radial density distribution of the Aq-A haloes, taken from Navarro et al. (2010). The density profile of the Aq-A haloes is shown with dashed lines in different colours for different resolutions, with their spatial resolution indicated with arrows. The best fit Einasto profile for Aq-A-1 halo, with $\alpha = 0.170$, is shown with the dotted dashed curve. The virial radius of the haloes is shown with the dotted line. The radial density profile converges very well across different resolutions. The Einasto profile fits the halo well inside $r < 0.1\,r_{200}$. In the outer region, a "bump" in the radial density distribution can be found due to the substructures. Right panel: the shape parameter of Aq-A haloes taken from Vera-Ciro et al. (2011). Here a, b and c are the lengths of the three semi-principal axes of iso-density surfaces of the halo. Again haloes of different resolution converge well. The Aq-A haloes are most triaxial in the central region ($r \sim 1\,\mathrm{kpc}/h$) with $b/a \sim 0.5$ and $c/a \sim 0.4$. They gradually turn less triaxial in the outer region. At the virial radius R_{vir}, $b/a \sim 0.8$ and $c/a \sim 0.6$.

Chapter 3

Stellar Spiral Structures in Triaxial Dark Matter Haloes

In this chapter, we employ very high resolution simulations of isolated Milky Way-like galaxies to study the effect of triaxial dark matter haloes on exponential stellar disks. Non-adiabatic halo shape changes can trigger two-armed grand-design spiral structures which extend all the way to the edge of the disk. Their pattern speed coincides with the inner Lindblad resonance indicating that they are kinematic density waves which can persist up to several Gyrs. In dynamically cold disks grand-design spirals are swing amplified and after a few Gyrs can lead to the formation of (multi-armed) transient recurrent spirals. Stellar disks misaligned to the principal planes of the host triaxial halo develop characteristic integral shaped warps, but otherwise exhibit very similar spiral structures as aligned disks. For the grand-design spirals in our simulations their strength dependence with radius is determined by the torque on the disk, suggesting that by studying grand-design spirals without bars it may be possible to set constraints on the tidal field and host dark matter halo shape.

3.1 Introduction

For many years spiral structures in galaxies have been the subject of extensive observational, theoretical and numerical studies, but their origin still remains unclear. While the morphologies of spiral structures vary considerably, they can be generally classified into two broad categories: 'grand-design' spirals with mostly two arms that extend over a large range of radii and 'flocculent' spirals that consist of many small fragments of arms. Both kinds of spirals are mostly trailing rather than leading.

Theories of formation and evolution of spirals fall into two categories: (a) self-induced spiral formation, in which spiral structures form due to gravitational interaction between finite number of stars, and (b) externally driven spiral formation, in which spiral structures form as a response to external perturbations.

Lindblad proposed a theory of quasi-stationary spiral structures for grand-design spirals (e.g. Lindblad, 1963). In his theory, spiral structures are in fact kinematic density waves with a pattern speed of $\Omega_{\rm P} = \Omega - \kappa/n$, where Ω is the corotation velocity, κ is the epicyclic frequency and n is the number of arms (typically equal to 2). In a frame moving with this pattern speed, the orbits of the epicyclic motion of the stars become ellipses without precession, which guarantees that the density field of the disc remains constant in this rotating frame. When orbits are arranged in a way that the highest density falls into a spiral-like shape (e.g. Kalnajs, 1973), constantly rotating stationary grand-design spiral structures can survive in the disc (Lindblad, 1956). Lin & Shu (1964) developed a theory of density waves of quasi-stationary spiral structures further. They regarded spiral structures as large-scale waves propagating through the disc in a linear regime (see also Bertin & Lin, 1996).

'Flocculent' spiral structures (and some of the 'grand-design' spirals) are considered to be caused by instabilities due to self-gravity. To form spiral structures of this kind, two important processes are needed: swing amplification of small perturbations and a feedback loop. The local stability of a razor-thin disc with respect to axisymmetric tightly wound perturbations is characterized by Toomre's Q parameter (Toomre, 1964). For stellar discs, we have

$$Q = \frac{\sigma_R \kappa}{3.36\, G\Sigma}, \tag{3.1}$$

where σ_R is the velocity dispersion in the radial direction and Σ is the surface density. When $Q > 1$, the disc is locally stable to axisymmetric perturbations, while for $Q < 1$, the disc becomes locally unstable. Considering the case of non-axisymmetric perturbations, Julian & Toomre (1966) studied the stability of differentially rotating discs and showed that due to self-gravity, small perturbations can be greatly amplified. Toomre (1981) explored the theory further and showed that strong swing amplification can occur when Q is slightly higher than 1, i.e. if the disc is locally stable but the self-gravity is still strong and the wavelength ratio X is appropriate (typically between 1 and 3):

$$X = \frac{k_{\rm crit} R}{m} = \frac{\kappa^2 R}{2\pi G \Sigma m}, \tag{3.2}$$

where R is the radius, m is the number of arms and $k_{\rm crit} = \kappa^2/(2\pi G\Sigma)$ is the critical wavelength of the swing amplification. In this process small leading waves are amplified to strong trailing waves and the amplification factor can be as high as 100. Toomre (1981) also

demonstrated that swing amplification can act on global spiral patterns and greatly amplify their strength, though external torques, for example, are sufficient to form those patterns. Similarly, Grand et al. (2012b) showed that two-armed spiral structures in barred galaxies can be dominated by swing amplification.

Recent studies combining numerical and analytic efforts have further shown that stars interact with each other over long periods of time through resonances. Sellwood (2012) found that stars are scattered at the inner Lindblad resonance as the transient spiral structures form, leading to a re-distribution in the action space. When stars are rotated randomly to erase non-axisymmetric features without affecting the distribution in action space, spiral structures restore rapidly, indicating that the scattering at inner Lindblad resonance is more fundamental than the change in the density field. Such a scattering has been recently studied by Fouvry & Pichon (2015) using a dressed Fokker–Planck formalism, which offers a powerful tool to probe the evolution of discs as a function of their properties.

While a number of past numerical studies found that spirals fade out quickly over time (for a recent review see Dobbs & Baba, 2014, and references therein), recent studies showed that in a stellar disc with more than a few million particles spiral arms persist for longer periods of time, indicating that previous results were suffering from discreteness effects (e.g. Fujii et al., 2011; Grand et al., 2012a). D'Onghia et al. (2013) showed that with a sufficiently high number of particles (of the order of 10^8), stellar discs with Q slightly larger than 1 can stay stable over a few galactic years. When, however, density perturbations are introduced in the disc (in the form of heavy particles), a transient spiral pattern forms which itself can act as the source of newly formed spiral arms. Sellwood & Carlberg (2014) studied the power spectra of such transient spirals, and found that they are superposition of several rigid rotating modes lying between the inner and the outer Lindblad resonance. They also found that such waves scatter particles towards new regions of a disc, thus changing the impedance of the disc, reflecting the waves and hence giving rise to new standing waves. In fact, Fouvry et al. (2015) showed that such simulations of spiral structures dominated by self-gravity in discrete discs can be characterized by the Balescu–Lenard equation, whose predictions on the properties of the secular orbital diffusion agree very well with simulations.

Taken together, these recent numerical works indicate that to study stellar spiral structures that may form in response to external perturbations, discs need to be represented with a very high number of resolution elements, to both minimize arteficial spiral heating and the Poisson noise in the initial conditions, ensuring that the growing time of transient spirals is long enough compared to the evolution of grand-design spirals.

For the triggering mechanism of the grand-design spiral structures, additionally to bars (e.g. Salo et al., 2010; Athanassoula, 2012) and close companions (e.g. Purcell et al., 2011),

torques caused by the host dark matter halo have been invoked as well. Even though the properties of dark matter haloes, such as their exact shape and mass distribution (and the back-reaction of baryons), are still not precisely known, already early work (e.g. Binney, 1978; Barnes & Efstathiou, 1987; Frenk et al., 1988) have indicated that the haloes are generally triaxial. Follow-up studies with a variety of configurations, including dispersionless gravitational collapse models (Warren et al., 1992), self-interacting dark matter models (Yoshida et al., 2000), haloes formed in different cosmological models (Jing et al., 1995; Thomas et al., 1998), and more recent higher-resolution studies (e.g. Bryan et al., 2013; Zhu et al., 2016) all find that the dark matter haloes are triaxial. Several generalizations of analytical, spherical halo models that include halo triaxiality were also proposed (Jing & Suto, 2002; Bowden et al., 2013). Analysing high resolution Aquarius simulations (Springel et al., 2008), Vera-Ciro et al. (2011) showed that due to the cosmic growth history of dark matter haloes, their triaxiality can change rapidly over time, implying that the disc will be subject to a time-dependent torque. It is generally believed that the inclusion of baryons leads to a reduction of halo triaxiality (Dubinski, 1994; D'Onghia et al., 2010; Zemp et al., 2012; Bryan et al., 2013; Zhu et al., 2016), with haloes becoming more oblate, especially in the central region. However, the resulting mildly triaxial halo mass distribution may still impart a significant torque on to the disc of the central galaxy.

In fact, DeBuhr et al. (2012) have found that the gravitational potential of a disc can flatten the halo, while in return bars and warps can develop in the disc under the influence of the flattened halo. For grand-design spiral structures, Dubinski & Chakrabarty (2009) studied the impact of external torque on the disc. In their simulations, it is assumed that while the inner part of the dark matter halo is aligned with the disc, the outer region is misaligned and tumbling, causing an external torque. Under such external torque, Dubinski & Chakrabarty (2009) found that grand-design two-armed spiral structures can develop in the disc, along with warps and bars. More recently, Khoperskov et al. (2013) found that grand-design spiral patterns can form in discs within haloes which are gradually turned from spherical into triaxial (see also Khoperskov & Bertin, 2015).

None the less, the relation between the triaxiality of dark matter haloes and the spiral structures in discs is still not fully understood. Therefore, a careful study employing very high resolution discs is needed to understand the influence of halo shapes on the disc structure which is the aim of this paper. Also since there are two different kinds of spiral structures, grand-design and flocculent ones, it is important to understand how they form in triaxial haloes.

The paper is organized as follows. In Section 3.2, we introduce the methodology together with galaxy and halo models we use. Our results are then presented in Section 3.3. In

Section 3.3.1, we examine the numerical effects caused by the finite resolution of simulations which act as perturbations of the density field of stellar discs (see also Appendix 3.A). In Section 3.3.2, we study the effect of how triaxial haloes are introduced into the system with very high resolution simulations, while in Section 3.3.3 we study spiral pattern generated by time-dependent triaxial haloes as predicted by cosmological simulations. We then focus on the impact of triaxial haloes of different shapes on the discs in Section 3.3.4. In Section 3.3.5, we discuss the nature of transient spirals that emerge out of grand-design spiral structures due to non-linear effects. The underlying mechanism of the grand-design spirals is then studied in Section 3.3.6 (for discs misaligned with the major axes of the halo, see Appendix 3.B). Finally, in Section 3.4 we summarize our results.

3.2 Method

3.2.1 The Numerical Approach

We perform simulations of stellar discs embedded in different dark matter halo models with GADGET-3, whose previous version GADGET-2 is described in Springel (2005). GADGET-3 is an *N*-body/smoothed particle hydrodynamics code. In the code, stars are represented by a finite number of stellar particles. Our choice of the number of star particles varies from 10^5 to 10^8, so for a Milky Way-like galaxy a single star particle in the simulation typically represents about 10^6–10^3 stars. Their dynamics is simulated with the *N*-body algorithm.

Gaseous component is very important in the evolution of galactic discs. By interacting with the stars through gravity, gas can enhance the self-gravity of the disc. Also it can develop sharp shocks when placed in a gravitational potential caused by spiral structures (Gittins & Clarke, 2004; Dobbs & Bonnell, 2006, 2007). Moreover, new stars formed out of the high-density gas clumps can act as a cooling source to the dynamical temperature of the disc by lowering the velocity dispersion. However, modelling gas numerically is very difficult, given that complex cooling and heating processes need to be taken into account. Therefore, we do not include gaseous component in this work.

Analytic representation of dark matter haloes is employed in all of the simulations. Given that the total mass of the dark matter halo is much larger than the total mass of the disc, if we represent dark matter halo with particles, we need much more dark matter halo particles than star particles (a number that turns out to be prohibitively large!), so that the Poisson noise in the halo is comparable to that in the disc. In fact, for testing purposes, we ran a simulation of a live disc within a live halo, both of them with 10^8 particles. In this simulation, strong transient spiral structures form almost instantly, making it impossible to study the possible

Table 3.1 Numerical parameters for simulations with different number of star particles. For simulations listed below, the total mass of the stars is either $M_* = 1.9 \times 10^{10} M_\odot$ (low-Q discs) or $M_* = 9.5 \times 10^9 M_\odot$ (high-Q discs). Number of star particles N, mass of a single star particle, m, and gravitational softening length, $\varepsilon_{\rm grav}$, are listed below.

$M_*(M_\odot)$	N	$m(M_\odot)$	$\varepsilon_{\rm grav}$(pc)
1.9×10^{10}	10^5	1.9×10^5	163
1.9×10^{10}	10^6	1.9×10^4	76
1.9×10^{10}	10^7	1.9×10^3	35
1.9×10^{10}	10^8	1.9×10^2	16
9.5×10^9	10^5	9.5×10^4	163
9.5×10^9	10^6	9.5×10^3	76
9.5×10^9	10^7	9.5×10^2	35
9.5×10^9	10^8	95	16

effects of the halo shape on the disc. To avoid this effect, we would need much more dark matter particles. However, we are primarily interested in the behaviour of the disc rather than that of the dark matter halo. To make sure that the halo does not induce numerical artefacts to the system and to direct computational resources on the object we are interested in, we used analytic dark matter halo models rather than the dark matter particles. It is worth mentioning that with our methodology we cannot study the back-reaction of the disc on to the dark matter halo. To somewhat mitigate this issue, we study static dark matter haloes of different shapes.

For computation of the gravity, the GADGET-3 code employs the TreePM method (Springel, 2005). The combination of the two methods, the Tree method and the Particle-Mesh (PM) method, gives us high efficiency in calculating gravitational forces with high accuracy. Constant gravitational softening length $\varepsilon_{\rm grav}$ for star particles is used in all simulations. Typical values of $\varepsilon_{\rm grav}$ used in our simulations are shown in Table 3.1.

3.2.2 Modelling of Stellar Discs

We set up our disc model following the description in Springel et al. (2005a). The disc has an exponential surface density profile and an isothermal sheet profile vertically, described by

$$\rho_*(R,z) = \frac{M_*}{4\pi z_0 R_{\rm S}^2} \mathrm{sech}^2\left(\frac{z}{z_0}\right) \exp\left(-\frac{R}{R_{\rm S}}\right), \tag{3.3}$$

where $R_{\rm S} = 3.13\,$kpc is the scalelength of the disc, M_* is the total mass of the stars and $z_0 = 0.1 R_{\rm S}$ is the scaleheight. The total mass of the system, $M_{\rm T} = M_* + M_{\rm dm}$ is $9.5 \times 10^{11} M_\odot$ in all our simulations. However, two kinds of discs with different disc mass ratios $m_{\rm d} = M_*/M_{\rm T}$ are used: one with $m_{\rm d} = 0.02$ and minimum Toomre's Q parameter $Q_{\rm min} \sim 1$ (hereafter referred

to as the 'low-Q' disc), the other with $m_{\rm d} = 0.01$ and $Q > 1.3$ (hereafter referred to as the 'high-Q' disc). As shown by previous works (e.g. Vandervoort, 1970; Romeo, 1992), discs with finite thickness are more stable than razor-thin ones. Therefore, although for razor-thin discs, $Q \sim 1$ leads to violent axisymmetric perturbations, in our simulations with finitely thin discs such axisymmetric perturbations are weaker. The radial profiles of Q parameter for different discs and as a function of time are shown in Fig. 3.18 in Appendix 3.A. The circular velocity and velocity dispersion of the stars in the disc are worked out analytically based on the density distribution of the system (for further detail, see Springel et al. (2005a)).

3.2.3 Spherical Dark Matter Haloes

Both Hernquist (Hernquist, 1990) and triaxial dark matter haloes derived from it are used as our halo models. The Hernquist profile of a halo is described by

$$\rho_{\rm HQ}(r) = \frac{M_{\rm dm}}{2\pi}\frac{a}{r(r+a)^3}\,, \tag{3.4}$$

where $a = 30\,$kpc is a scale length factor that controls the distribution of the mass. The potential of the Hernquist halo is given by

$$\Phi_{\rm HQ}(r) = -\frac{GM_{\rm dm}}{r+a}\,. \tag{3.5}$$

Here, the mass of the halo is $M_{\rm dm} = M_{\rm T}(1-m_{\rm d})$. The virial radius of the halo, R_{200}, is set to be $160\,$kpc.

3.2.4 Triaxial Dark Matter Haloes

To derive a triaxial halo from a Hernquist halo, we followed Bowden et al. (2013) and added two low-order spherical harmonic terms to the potential, i.e.

$$\Phi(r,\theta,\phi) = \Phi_{\rm HQ}(r) + \Phi_{\rm T}(r,\theta,\phi)\,, \tag{3.6}$$

with the triaxial part $\Phi_{\rm T}(r,\theta,\phi)$ being

$$\Phi_{\rm T}(r,\theta,\phi) = 4\pi G\frac{\rho_1 r_1^4 r}{(r+r_1)^3}Y_2^0(\theta,\phi) - 4\pi G\frac{\rho_2 r_2^4 r}{(r+r_2)^3}Y_2^2(\theta,\phi)\,, \tag{3.7}$$

where $\Phi_{\rm HQ}$ is the potential of the Hernquist profile and $Y_2^0(\theta,\phi) = \frac{3}{2}\cos^2\theta - \frac{1}{2}$, $Y_2^2(\theta,\phi) = 3\sin^2\theta\cos 2\phi$ are spherical harmonic functions.

Table 3.2 Halo models used in this work. a, b and c are major axis lengths of isodensity surface in the x, y and z direction. p and q are the ratios of b to a and c to a. The suffixes of the two parameters, 0 and ∞, indicate whether the parameter is for the inner or the outer limit. In model T_{O2}, the discs do not lie in the x–y plane. The position of the disc plane is defined with the first two Euler angles following the standard notation. In other words, it is decided by (1) setting coordinates x'–y'–z' to initially coincide with x–y–z coordinates, (2) rotating x'–y'–z' coordinates along the z' axis for an angle α, (3) rotating x'–y'–z' coordinates along the x' axis for an angle β and (4) putting the disc in the x'–y' plane.

Model	p_0	q_0	p_∞	q_∞	α	β
S	1	1	1	1	0	0
T_1	0.6	0.4	1	1	0	0
T_2	0.95	0.85	0.6	0.5	0	0
T_3	0.85	0.85	0.85	0.85	0	0
T_{O2}	0.95	0.85	0.6	0.5	0	$\pi/4$

Hence,

$$\rho(r,\theta,\phi) = \rho_{\rm HQ}(r,\theta,\phi) - 4\rho_1 \frac{r_1^4(r_1^2+5r_1r+r^2)}{(r+r_1)^5 r} Y_2^0(\theta,\phi) + 4\rho_2 \frac{r_2^4(r_2^2+5r_2r+r^2)}{(r+r_2)^5 r} Y_2^2(\theta,\phi). \quad (3.8)$$

Here ρ_1, r_1, ρ_2 and r_2 are four free parameters that can be used to control the shape of the halo in the inner and outer regions, i.e. the ratio of major axis lengths of the isodensity surface in the y and x direction at the inner and outer limit, $p_0 = \lim_{r\to 0} b/a$ and $p_\infty = \lim_{r\to\infty} b/a$ and similarly in the z and x direction, $q_0 = \lim_{r\to 0} c/a$ and $q_\infty = \lim_{r\to\infty} c/a$. Once shape parameters p_0, q_0, p_∞ and q_∞ are given, one can calculate the corresponding ρ_1, r_1, ρ_2 and r_2 following Bowden et al. (2013). For most of the simulations the disc lies in the x–y plane, but we also ran several simulations in which the discs have a 45° angle to the x–y plane.

The names and parameters of all halo models are listed in Table 3.2. The S model is the original spherical Hernquist halo. T_1 model is spherical outside and triaxial inside, while T_2 is the opposite. In T_3 model, the inner and outer limits of the major axis length ratios are $p_0 = q_0 = p_\infty = q_\infty = 0.85$. However the major axis length ratios p and q are not constant throughout the halo. As shown in Fig. 3.10, the ratio p is slightly lower than 0.85 for $0 < R < 5R_{\rm S}$. This is due to the fact that we are using an analytical model for the triaxial halo, which only constrains the ratios of major axis lengths for the $r \to 0$ and the $r \to \infty$ limits. The parameters for T_2 are chosen to be comparable to the results of cosmological simulations described in Zemp et al. (2012).

3.3 Results

3.3.1 Finite Resolution Effects

We start by first investigating the finite resolution effects on the disc properties by using an increasing number of star particles to represent the disc. In total, we ran six simulations with the same *S* halo, i.e. spherical Hernquist halo without any triaxial terms, but with different disc mass ratio $m_{\rm d}$ and different numbers of star particles in the disc. For two of these simulations, we used an $m_{\rm d} = 0.01$ disc with 10^6 and 10^8 star particles. As mentioned before, in these disc models, Toomre's Q parameter is greater than 1.3 throughout the disc. For the rest of the simulations, $m_{\rm d}$ is set to 0.02 and we use from 10^5 to 10^8 star particles. For some regions in these discs, $Q \sim 1$, which means that the swing amplification is strong.

In simulations with low-Q discs, transient spiral structures develop. As shown in Fig. 3.17 in Appendix 3.A, these spiral structures are multi-armed, typically from 7-armed to 10-armed. The strength of these spiral structures at radius R can be quantified with

$$S(R) = \sqrt{\sum_{m=1}^{12} \left| \frac{\hat{\Sigma}_m(R)}{\hat{\Sigma}_0(R)} \right|^2}, \tag{3.9}$$

where $\hat{\Sigma}_m(R)$ is the Fourier transformation of the surface density $\Sigma(R,\theta)$ of the disc at fixed radius R along the azimuthal coordinate θ, i.e.

$$\hat{\Sigma}_m(R) = \frac{1}{2\pi} \int_{-\pi}^{\pi} \Sigma(R,\theta) \mathrm{e}^{-\mathrm{i}m\theta} \mathrm{d}\theta \,. \tag{3.10}$$

Here we sum over $m = 1$–12 to include the effect of all spiral structures with $m \leq 12$. Structures with higher m, which represent smaller structures in the disc, are excluded because they are subject to random noise in the disc. The evolution of $S(R)$ over a time span of 10 Gyr at a fixed radius $R = 2R_{\rm S}$ is shown in Fig. 3.1.

Strong spiral structures develop in all four simulations with low-Q discs. The maximum spiral strength for these simulations is roughly the same regardless of the number of star particles. However, simulations with a higher number of particles take longer time to grow spiral structures, in agreement with the findings from Sellwood (2012) and Fujii et al. (2011). This shows that self-gravitating discrete discs in our simulation can be well characterized by Balescu–Lenard equation, whereby the time-scale of structure growth is inversely proportional to the number of particles in the system (Fouvry et al., 2015). In particular, it takes more than 7Gyr for the simulation with 10^8 star particles to fully develop spiral structures. Also note that spiral strength in simulations with 10^5–10^7 particles decreases

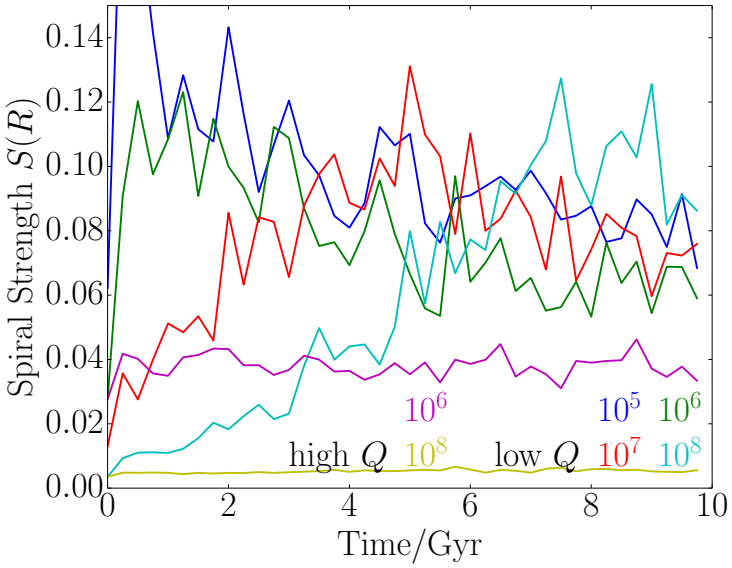

Fig. 3.1 The growth of transient spiral structures with time for discs with 10^5, 10^6, 10^7 and 10^8 particles. Spiral strength $S(R)$ is defined in equations (3.9) and (3.10), where all $m \leq 12$ modes are taken into account. Spiral structures grow in all four low-Q discs, but not in high-Q discs. For the high-Q disc with 10^6 particles, the strength is higher than that of 10^8 particles due to higher Poisson noise, but does not grow over time. The scale time for growing spirals is longer for simulations with more star particles. For simulation with 10^5–10^7 star particles, spiral strength decreases after reaching the peak value due to the spiral heating.

after reaching the maximum, because of spiral heating. For 'dynamically hot' discs with $Q > 1.3$, the spiral strength is always comparable to the initial value, indicating that the swing amplification is weak, as expected.

To further study the resolution effects, we replace the spherical halo with triaxial haloes described in Table 3.2. Fig. 3.2 shows the surface density of a 10^5 particle disc in the T_1 halo at time $t = 0.5\,\mathrm{Gyr}$. T_1 halo is triaxial inside and spherical outside, which means that the non-axisymmetric force introduced by this halo in the central region of the disc is very high. However, the disc in the T_1 halo still develops a multi-armed transient spiral structure, though the distribution of the spiral arms is more asymmetric than the one in the spherical halo. This indicates that when the Poisson noise in the disc is very high, swing amplification of the disc dominates the whole process and external torques cannot significantly influence the strength of the arms. To study carefully the effects of triaxial haloes, swing amplification of Poisson noise caused by finite resolution needs to be suppressed. For the rest of this paper, we thus perform simulations with 10^8 star particles, so that the growth of transient spiral structures caused by swing amplification of the Poisson noise in the initial conditions is sufficiently slow.

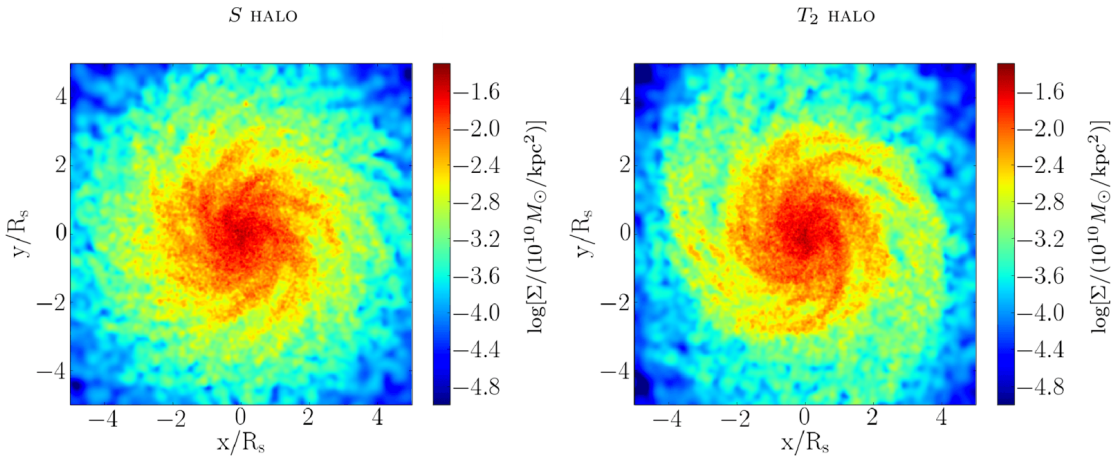

Fig. 3.2 Surface density of a disc in the spherical and the T_1 triaxial halo at time 0.5Gyr. Values on the colour bar are $\log(\Sigma/10^{10}\mathrm{M}_{\odot}\mathrm{kpc}^{-2})$, where Σ is the surface density. In both simulations the disc has 10^5 particles. The surface densities of the two discs are similar. This indicates that when the Poisson noise is significant, swing amplification of Poisson shot noise is the dominating factor over the influence of a triaxial halo.

3.3.2 Time-dependent Triaxial Haloes

The top row of Fig. 3.3 shows the surface density, density variation with respect to the initial conditions and the residual density of the high-Q disc with 10^8 star particles in the T_2 halo at 3Gyr. Here residual density refers to the normalized density difference to the average surface density over azimuthal coordinate,

$$\Sigma_{\mathrm{res}}(R,\phi) = \frac{\Sigma(R,\phi) - \bar{\Sigma}(R)}{\bar{\Sigma}(R)}, \tag{3.11}$$

where $\bar{\Sigma}(R)$ is the average density at radius R, i.e. $\bar{\Sigma}(R) = \frac{1}{2\pi}\int_0^{2\pi}\Sigma(R,\phi)\mathrm{d}\phi$. We use a high-$Q$ disc to avoid the possible interference due to the swing amplification of the disc, which we study later on in Section 3.3.5. As shown in the top row of Fig. 3.3 strong grand-design two-armed spiral structures form. These spiral structures are very sharp, tightly wound up and global. Unlike the spiral structures formed due to swing amplification (see Fig. 3.17), which only exist in the intermediate part of the disc (i.e. for $1 \lesssim R/R_{\mathrm{S}} \lesssim 3.5$), the spiral structures in triaxial halo extend to the edge of the disc. This agrees with Dubinski & Chakrabarty (2009) where an external torque due to the tumbling dark matter halo drives the formation of the spiral structures. However, it is unclear whether these spiral structures are caused by the triaxial halo alone or by the impulsive process of introducing triaxial haloes to the system with a disc that is initially in equilibrium with a spherical halo.

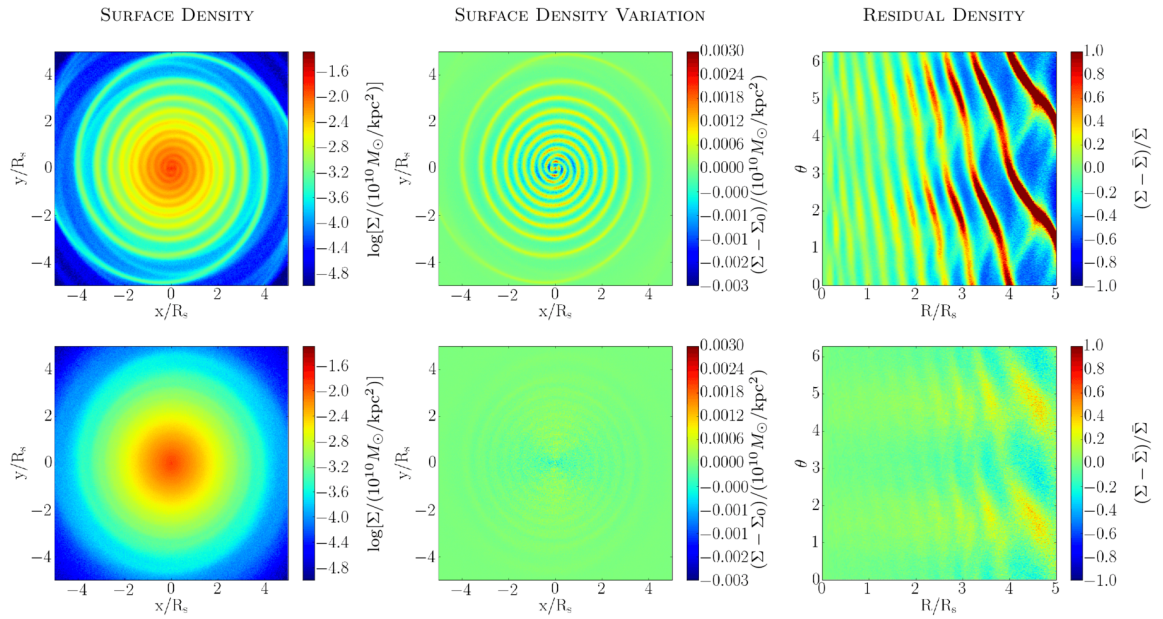

Fig. 3.3 Surface density, i.e. $\log(\Sigma/10^{10}\mathrm{M}_{\odot}\mathrm{kpc}^{-2})$, its variation to the initial conditions and residual density of high-Q discs in a simulation with 10^8 star particles in a T_2 halo at $t = 3$Gyr. Top row: simulation with a static T_2 halo. Bottom row: halo is initially spherical and then gradually turns into a T_2 halo with a scale time of $\tau = 1$Gyr. In the simulation with a static T_2 halo, strong two-armed spiral structures form. The spiral structures keep winding up after their formation. By the time $t = 3$Gyr, spirals are tightly wound up. With triaxiality of the halo introduced gradually, very weak spiral structures form in the disc, indicating that the spiral structures found in the simulation with a static triaxial halo are caused by the sudden change of the halo shape.

To fully understand the formation mechanism of these grand-design spiral structures, we run simulations in which the shape of the halo changes from spherical to triaxial gradually, so that initially the disc is in the equilibrium with the halo and no impulsive change to the system occurs. As shown in equations (3.6) and (3.7), the analytic potential we employed in our simulations consists of two parts: a spherical Hernquist potential and a triaxial part. We hereby extend equation (3.6) so that the triaxial part of the halo can be turned on and off gradually with a function $f(t)$,

$$\Phi(r,\theta,\phi) = \Phi_{\mathrm{HQ}}(r,\theta,\phi) + f(t)\Phi_{\mathrm{T}}(r,\theta,\phi)\,. \tag{3.12}$$

When $f(t) = 0$, the dark matter halo is a purely spherical Hernquist halo, while when $f(t) = 1$, the dark matter halo is a fully developed triaxial halo.

The bottom row of Fig. 3.3 shows the surface density and the residual density of a simulation with a gradually introduced T_2 halo. In this simulation the growth of the triaxial

part of the potential is set to

$$f(t) = 1 - \exp(-t/\tau_{\rm I})\,, \tag{3.13}$$

where the scale time $\tau_{\rm I} = 1$Gyr. The time shown in Fig. 3.3 is 3Gyr, when the triaxial transformation of the halo is almost complete, with $f = 0.95$. With the initially spherical halo growing slowly to triaxial, as shown in the residual density map in the rightmost panel, the spiral structure is very weak inside $3R_{\rm S}$, while relatively weak two-armed structures develop in the outer region.

The fact that only weak spiral structures develop when the triaxiality of the halo is introduced gradually indicates that triaxial halo alone does not necessarily lead to spiral structures. In fact, by comparing the orbital period $\tau_{\rm O}$ of the stars and the time-scale $\tau_{\rm I}$ of introducing the halo, we find that the time-scales of the two processes determine whether a strong spiral structure will develop. The orbital period $\tau_{\rm O}$ is very small in the innermost regions of the disc. The introduction of triaxiality has a much longer time-scale $\tau_{\rm I} = 1$Gyr, which can be seen as an adiabatic perturbation in the centre. $\tau_{\rm O}$ becomes longer at larger radii. At $R = 3R_{\rm S}$, $\tau_{\rm O} = 0.315$Gyr, which is still shorter than the $\tau_{\rm I}$, but the introduction of the halo is starting to make an effect. At about $R = 5R_{\rm S}$, $\tau_{\rm O} \sim 0.5$Gyr. Now introduction of the triaxial halo can no longer be considered as adiabatic, and the change of halo shape starts to have a significant effect on the disc.

The spiral structures formed in this simulation on larger scales are shown in the first row of Fig. 3.4. Here the normalized density difference to the initial density

$$\overline{\Delta\Sigma} = \frac{\Sigma - \Sigma|_{t=0}}{\Sigma|_{t=0}} \tag{3.14}$$

is shown so that the structures in outer regions where density is significantly lower can be clearly seen. As shown in different columns (which are for $t = 1, 2$ and 3 Gyr), structures form at larger radii and grow inwards. However, due to the changing of the halo potential, ring structures also form in the disc[1] and to a certain extent interfere with the spiral structures, making it hard to distinguish genuine spiral structures from rings. We therefore run another simulation with self-gravity in the disc turned off, as shown in the middle row of Fig. 3.4. Two-armed grand-design spiral structures still form in this simulation, but rings do not interfere with spirals through self-gravity anymore. Instead, they superimpose with each other so that the rings are now seen as fine lines in each arm of the spiral structures. We therefore conclude that rings, though forming easily as a response to the change of the halo

[1] These are a numerical byproduct caused by the initial setup of stellar velocities which are not in perfect equilibrium with the changing halo potential, but do not influence any of our results.

potential and modifying the shape of the spiral structures, are not essential for the spiral forming process.

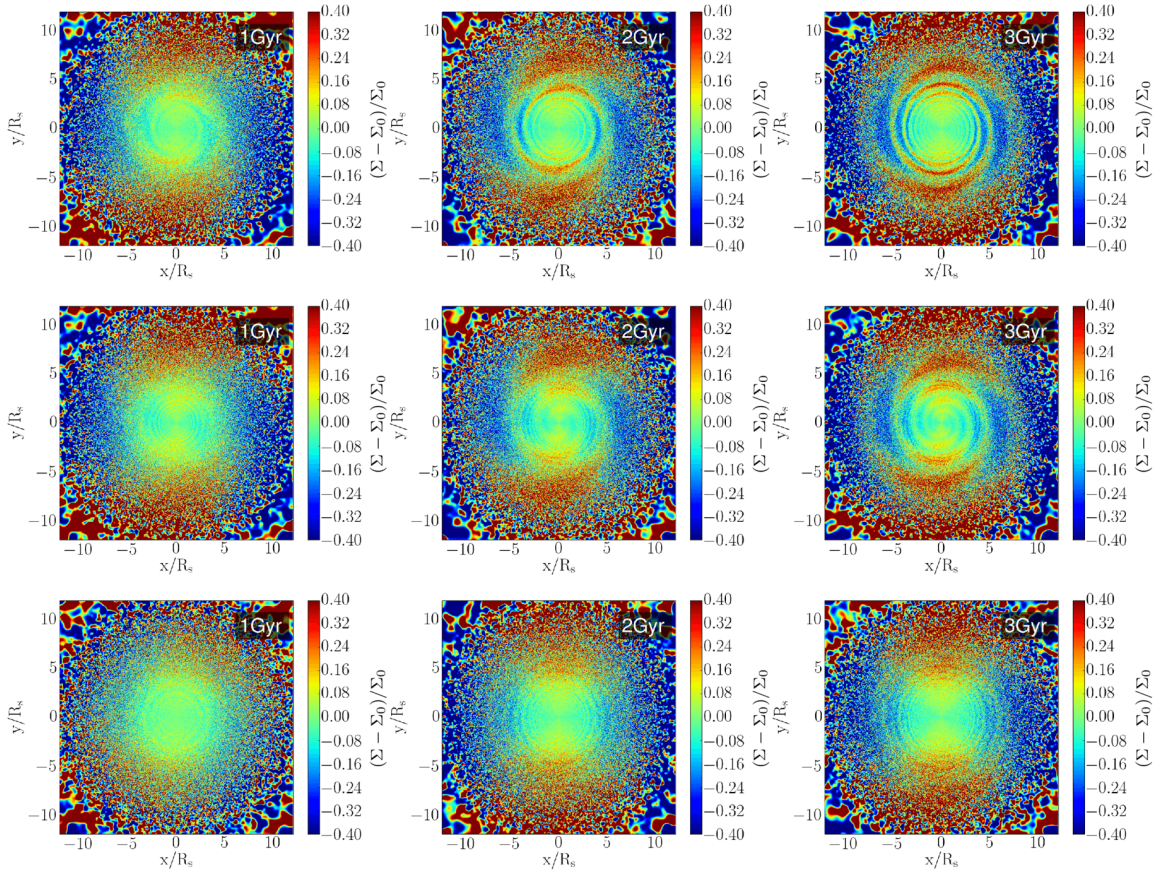

Fig. 3.4 Discs in a T_2 halo with a gradually increasing triaxiality with time. The relative difference of surface density to the initial conditions is shown. Top: with self-gravity. Middle: without self-gravity. Bottom: with self-gravity and a smoother introduction of triaxiality in the halo, i.e. $f_6(t)$ as defined in equation (3.15). With self-gravity in the disc turned off, it can be clearly seen that a two-armed spiral structure forms outside and grows inwards. However, for the simulation with self-gravity, this spiral pattern interferes with rings that form due to the change of halo profile. When the triaxiality of the halo is introduced in a smoother way, no prominent spiral structures can be found. This indicates that discs can survive in triaxial haloes without developing spiral structures if the shape of the halo changes smoothly enough.

We explore this problem further with a smoother $f(t)$ function. We generalized equation (3.13) to

$$f_n(t) = (1 - \frac{1}{n} e^{-t/\tau_1}(1 + (n-1)e^{-t/\tau_1}))^n, \tag{3.15}$$

where n is the smoothing factor and $f_1(t)$ falls to the original form used in equation (3.13). This generalization satisfies $f_n(0) = 0$ and $f_n(t) = f_1(t)$ to the first order in e^{-t/τ_1} as $t \to \infty$.

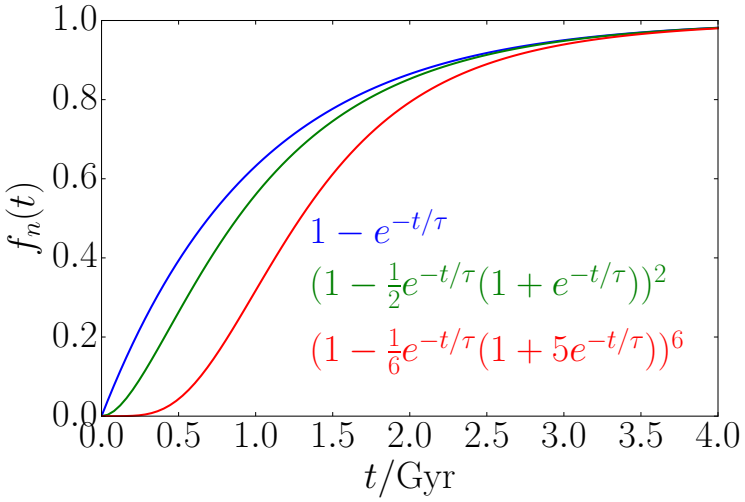

Fig. 3.5 Time dependence of $f_n(t)$ for smoothing factor $n = 1, 2$ and 6. $f_n(t)$ shows the same trend as $f_0(t)$ as $t \to \infty$. However higher n indicates a smoother growth of f_n at the beginning of the simulation.

As shown in Fig. 3.5, for a higher n, the growth of $f(t)$ at the early stage of the simulation is smoother. In practice we ran a simulation with $n = 6$. Self-gravity is included in this simulation as well. The result of this simulation is shown in the bottom row of Fig. 3.4. No prominent spiral structures develop. This demonstrates that the triaxial shape of a halo itself does not necessarily lead to spiral structures. Rather, non-adiabatic change of the halo shape, i.e. halo changing on a time-scale shorter than or comparable to the orbital period of the stars, will cause grand-design spiral structures to form.

Khoperskov et al. (2013) have reported that in their simulations similar grand-design two-armed spiral structures form within a halo growing slowly enough from a spherical one to a triaxial one with a time-scale more than four times longer than the rotation periods of the stars at the outer part of the disc. In contrast, we have shown in Fig. 3.4 that with a carefully chosen growth function $f(t)$ of the triaxiality of the halo, the development of the spiral patterns is not necessary. We therefore conclude that the spiral structures formed in their simulations are also due to the fact that the introduction of the triaxiality is not adiabatic enough.

As also shown in the bottom row of Fig. 3.4, when the change of halo shape is adiabatic enough, the most prominent feature of the disc is its ellipticity. It has been shown that the ellipticity of the potential in the disc plane as well as the ellipticity of the disc itself can be constrained by the scatter of Tully–Fisher relation and by the photometry (Franx & de Zeeuw, 1992; Debattista et al., 2008). The potential ellipticity is defined as $\varepsilon = b_\Phi/a_\Phi$ where a_Φ

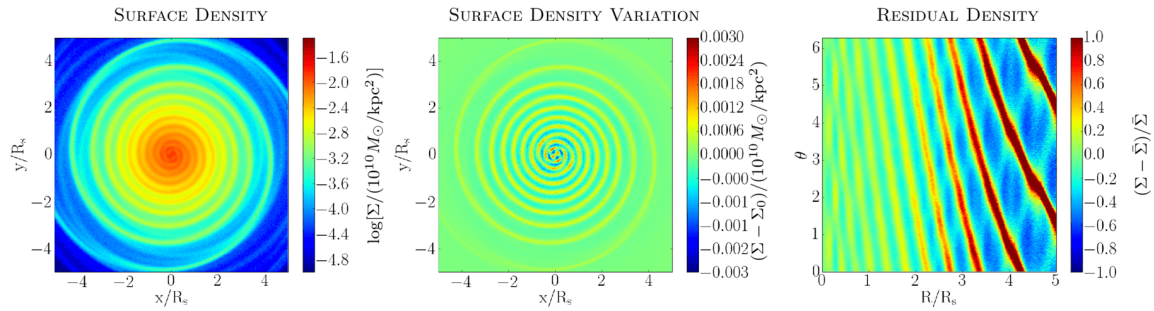

Fig. 3.6 Simulated discs at $t = 3$ Gyr in a halo that has a time-dependent triaxiality. Halo starts as the T_2 halo, but is quickly turned into a spherical halo with a scale time of $\tau = 0.2$Gyr. The grand-design spiral structures still exist for a long time, indicating that once formed, grand-design spiral patterns can survive in a spherical halo.

and b_Φ are the length of major and minor axis of the surface of a constant potential. In our T_2 model, it varies from $\varepsilon = 0.055$ to 0.075 in the disc plane from the inside to the outside. The ellipticity of the disc, defined similarly by contours of disc surface density, is $\varepsilon_{\rm D} = 0.05$. Both of the ellipticities are consistent with $\varepsilon < 0.1$ and $\varepsilon_D = 0.06$ as suggested by Franx & de Zeeuw (1992).

To understand if triaxial haloes are needed for these grand-design spiral structures to survive for longer periods of time, we also run a simulation with the halo shape turning from triaxial to spherical abruptly, with

$$f(t) = \exp(-(t/\tau_{\rm D})^2)\,, \tag{3.16}$$

with a time-scale $\tau_{\rm D} = 0.2$Gyr. In this simulation strong spiral structures form at the beginning of the simulation almost instantly, as expected. We run simulation further in time and find that the spiral structures can persist for much longer time. The surface density, its variation to the initial conditions and the residual density of the disc at $t = 3$Gyr are shown in Fig. 3.6. The halo is extremely close to spherical as early as $t = 0.5$ Gyr, with $f \sim 10^{-3}$. Spiral structures survive in this spherical halo for at least 2Gyr and remain strong. Therefore, triaxial haloes, proven above not necessary for forming spiral structures, are not needed for persisting spiral structures either.

It is interesting to note that Toomre (1981) studied properties of a disc galaxy with an external torque turned on and off rapidly. Though both in Toomre's and in our simulations, two-armed spiral structures form, they are different in at least two ways. First, in Toomre (1981), the Toomre's Q parameter and the wavelength ratio X are both in the range that favours the swing amplification of $m = 2$ modes, while in our simulation, for $m = 2$ the wavelength ratio X is too high for swing amplification to become significant. Actually in

our simulations the modes for the X to fall into the range $1 < X < 3$ that favours the swing amplification require $7 \lesssim m \lesssim 10$, which are the typical number of arms for transient spiral structures seen in Fig. 3.17. Therefore, though the swing amplification plays an important role in the development of the grand-design spiral structures in Toomre (1981), it plays a minor role in our simulations. In fact, as shown later in Section 3.3.5, the swing amplification may destroy the grand-design spiral structures at later times. Secondly, Toomre (1981) found that the grand-design spiral structures in their simulation decay after several rotational periods, while in our simulations the grand-design spiral structures can survive for a longer time. While disc properties and simulation methodology in our work are quite different, this indicates that the formation mechanism of the spiral structures may be different in Toomre (1981) and our simulations. In fact, the spiral structures in our simulations can be well explained by the kinematic density wave theory, as shown in Section 3.3.5.

3.3.3 Time-dependent Triaxial Haloes from Cosmological Simulations

As shown in the previous section, spiral structures only form when the axisymmetric change of halo potential is rapid enough. It is natural to ask whether this process is possible in a realistic halo. In fact, Vera-Ciro et al. (2011) found that haloes in self-consistent cosmological simulations like the Aquarius runs (Springel et al., 2008) can have very rapid change in triaxiality over time even when not experiencing very violent major mergers. To directly explore the impact of such realistic triaxiality changes on stellar discs, we set up two isolated halo models. For both models, the axial ratios $p = b/a$ and $q = c/a$ at the outer side of the halo follow Aquarius halo Aq-B-4 [see fig. 5 in Vera-Ciro et al. (2011) at ~ 5.4 Gyr of their simulated time]. The first model we consider has constant axial ratios with time in the central region. The limit of triaxiality as $r \to 0$ is set to be $p_0 = b/a|_{r\to 0} = 0.95$ and $q_0 = c/a|_{r\to 0} = 0.85$ similar to the T_2 model (following Zemp et al., 2012), to account for the likely impact of baryonic matter.

This model is rather conservative as it does not account for any time variation of triaxiality in the innermost halo regions. Thus, for the second model, we directly calculate the time evolution of the inner triaxiality of the Aq-B-4 halo. Due to the possible influence of a baryonic component, which is not captured by the Aquarius simulation (as it contains dark matter only), we expect that the average inner triaxiality will be smaller, but that the time fluctuations of triaxiality triggered by mergers, for example, will be comparable as predicted by dark matter-only cosmological simulations. We hence impose inner halo triaxiality fluctuations as directly evaluated from the Aq-B-4 halo on top of more realistic $p_0 = b/a|_{r\to 0} = 0.95$ and $q_0 = c/a|_{r\to 0} = 0.85$ values, rather than taking the absolute Aq-B-4 inner triaxiality average values, which are in the range of ~ 0.6. With this "recalibration" our

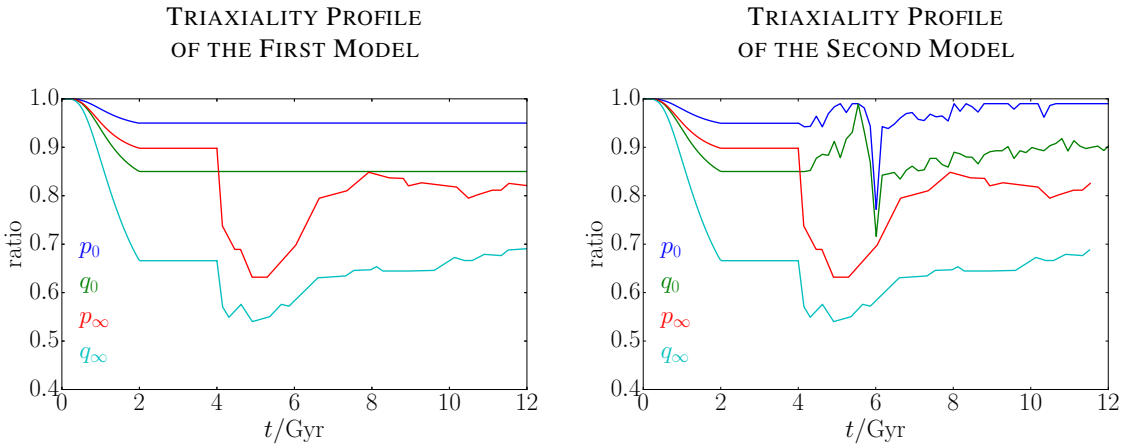

Fig. 3.7 Time dependence of the major axial ratios of the halo isodensity surface. For both models, from 0 to 2 Gyr, the halo grows from spherical to triaxial smoothly. At 2 Gyr, the triaxiality of the outer halo is the same as that of the Aq-B-4 halo at 5.4 Gyr of the original simulation, as shown in fig. 5 of Vera-Ciro et al. (2011). The halo is kept static until 4 Gyr, allowing the disc to fully relax. From 4 Gyr, the outer side of the halo evolves similarly to the Aq-B-4 halo starting from 5.4 Gyr in the Aquarius simulation, while the limits of the major axial ratios as $r \to 0$ remain constant for the first model (left-hand panel), but evolve following a recalibration based on the Aq-B-4 simulation for the second model (right-hand panel).

second model more closely reflects the possible inner triaxiality time evolution as would be obtained by very high resolution Aq-B-4 simulation which would include baryons. Thus the impact of halo triaxiality on the stellar disc should be more realistic than in our first model.

The time dependence of halo triaxiality of our models is shown in Fig. 3.7. We start from a spherical halo and change the triaxiality of the halo adiabatically to the configuration resembling the Aq-B-4 halo at 5.4 Gyr of the original simulation, and let the disc relax for 2 Gyr before the outer halo triaxiality starts to evolve similarly to the Aq-B-4 halo onwards in time. In the left-hand panel of Fig. 3.7 we show our first model where the inner halo triaxiality is kept constant, while in the right-hand panel, corresponding to our second model, realistic cosmological fluctuations of inner halo triaxiality are imposed (as measured from the Aq-B-4 simulation directly) on top of the same constant values as in the first model.

A prominent feature in the right-hand panel of Fig. 3.7 is a sharp dip at around 6 Gyr. A minor merger is found to be the cause for such a sharp change, as illustrated in Fig. 3.8. We trace this merger event backwards in time, and find that the satellite that causes this merger event has initially $\sim 23\%$ of the mass of the Aq-B-4 halo. As it inspirals towards the centre of the Aq-B-4 halo, which lasts for about 3 Gyr, it loses most of its mass gradually due to

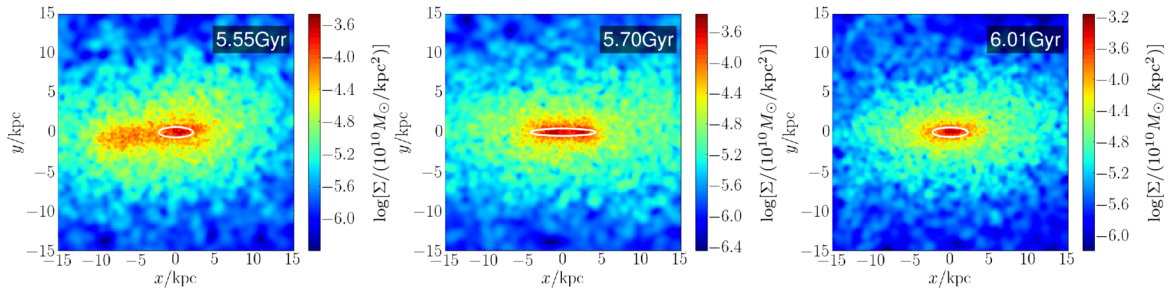

Fig. 3.8 Time sequence of the central Aq-B-4 halo from 5.55 to 6.01 Gyr. The panels show the projected density of the dark matter halo. White ellipse represents the fit to the halo shape at $\sqrt[3]{abc} = 1$ kpc, where a, b and c are the lengths of the three axes. A satellite merges with the Aq-B-4 halo during this period, which leads to a temporary but abrupt halo shape change.

dynamical friction and tidal stripping. None the less, the core of the satellite disrupts the centre of the Aq-B-4 halo significantly as it finally merges with it.

For both models, as intended the disc shows no sign of spiral structures in the growing and relaxing phase over the first 4 Gyr. However, when our halo triaxiality starts to evolve like that of the Aq-B-4 halo, clear spiral structures form in about 2 Gyr, as shown in Fig. 3.9. The spiral structures persist and sharpen over time for at least another 3–4 Gyr. The morphology of the spiral structures is very similar to those shown in Section 3.3.2. Generally, the spiral structures of the second model with changing inner triaxiality are much stronger than that of the first model. Also, for the second model the spiral strength is high all through the disc[2], while for the first model, the spiral structures are stronger in the outer part of the disc, which is expected since the inner limit of triaxiality is fixed. None the less, the spiral strength of the first model is still considerable as the relative surface density fluctuations reach 40%. We therefore conclude that in a realistic, cosmologically motivated case, changes in the halo triaxiality are abrupt enough to cause spiral structures, even when we assume a conservative evolution for the innermost halo. In reality, due to minor mergers, the inner shape of the halo may change in a way similar to our second model, therefore leading to strong spiral structures similar to the right-hand panels of Fig. 3.9. More detailed investigation of this issue, which depends on the complex interplay of baryons and inner halo triaxiality fluctuations with time is beyond the scope of this work and is left for a future study.

It is also possible that in reality the disc is misaligned with respect to the halo's major plane. We explore this in Appendix 3.B and find that the misaligned disc no longer stays in a plane as it evolves. Integral shaped warps form in the disc. Two-armed spiral structures still form and are similar to those formed in discs that lie in the x–y plane of the triaxial haloes.

[2]The evolution of the spiral strength of the second model will be discussed later in Section 3.3.6.

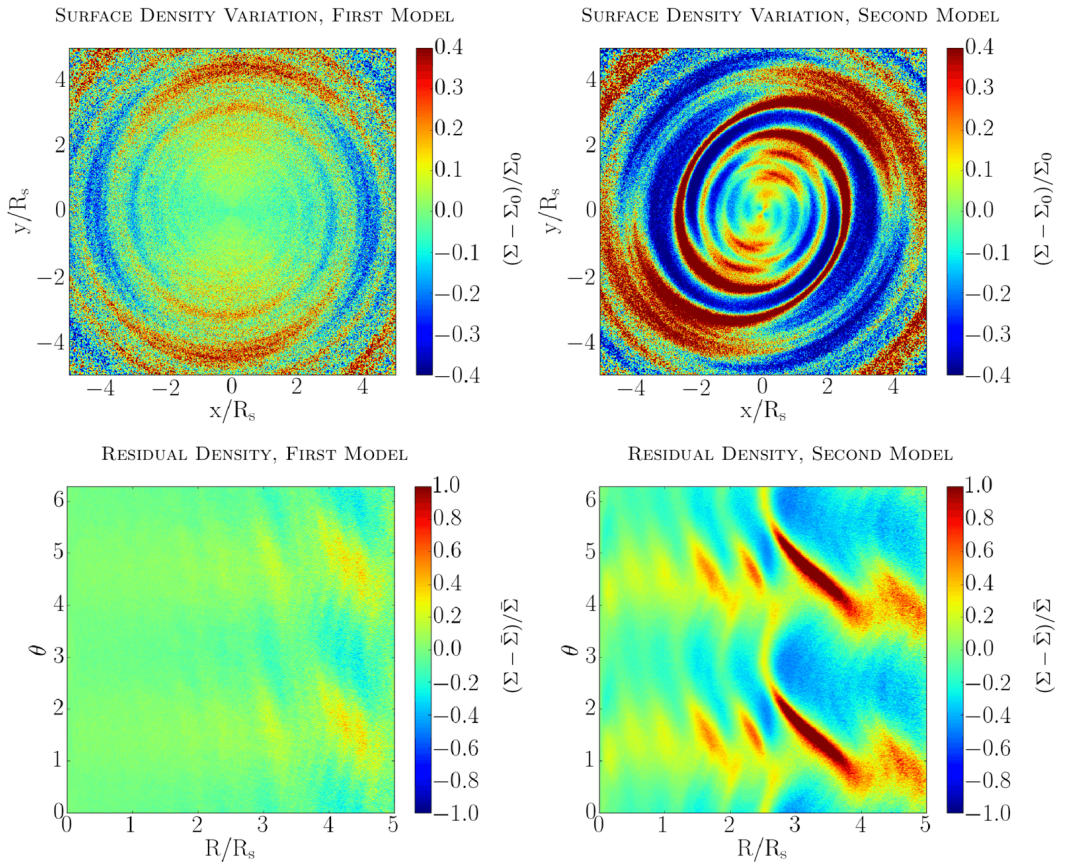

Fig. 3.9 Surface density difference to the initial conditions (top) and residual densities (bottom) at $t = 6\,\mathrm{Gyr}$ of discs evolved in simulations shown in Fig. 3.7. The halo starts to behave like Aq-B-4 halo after $t = 4\,\mathrm{Gyr}$ in this simulation. At $t = 6\,\mathrm{Gyr}$, clear spiral structures already develop for both simulations, while for the second model with varying inner triaxiality, the spiral strength is larger, and spirals form further in.

However, the outer parts of the spiral structure are distorted, due to the fact that they are no longer in the disc plane.

3.3.4 Dependence of Spiral Strength on the Halo Shape

We performed three additional simulations to further study the influence of different halo shapes on the spiral structure strength. In these simulations, we employ low-Q discs and various static triaxial dark matter haloes. The disc is originally in equilibrium with a spherical halo. An abrupt introduction of the triaxiality in the halo is the cause of spiral structures, as shown in Section 3.3.2.

Three halo models, T_1, T_2 and T_3, introduced in Table 3.2, are used in these simulations. The ratio of major axes, $p = b/a$, of these haloes at different radii is shown in the left-hand

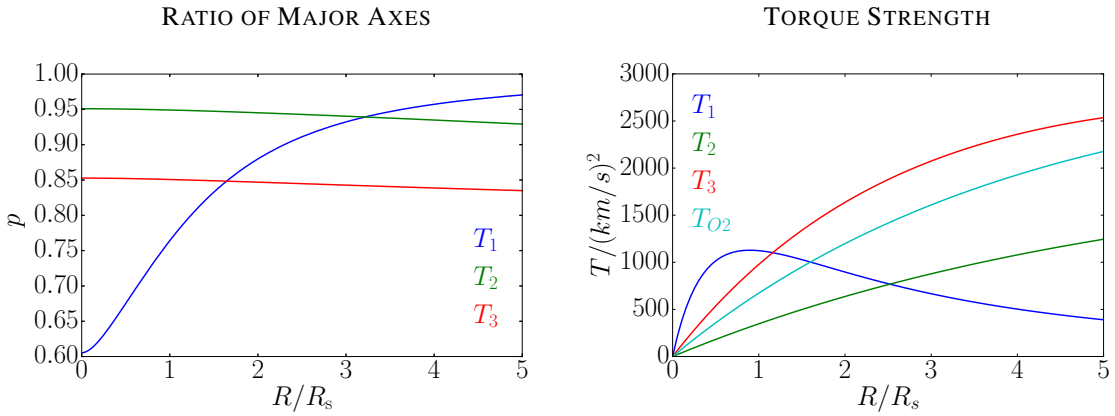

Fig. 3.10 Shape and torque strength of the dark matter halo models as a function of R/R_S. Left: ratio of major axes, $p = b/a$, as a function of R/R_S for halo models T_1, T_2 and T_3 listed in Table 3.2. Right: absolute value of the torque perpendicular to the disc plane that a star with azimuthal coordinate $\theta = \pi/4$ and radius R feels for simulations with halo models T_1, T_2, T_3 and T_{O2}. The simulation with halo model T_{O2} is discussed later in Appendix 3.B.

panel of Fig. 3.10. T_1 model is more triaxial inside, T_2 model is more triaxial outside, and the ratio of the major axis of the halo in the T_3 model is equal at the innermost and the outermost limits, and slightly lower in between. In all three simulations, spiral structures develop instantly in response to the abrupt change of the halo shape from the spherical one. Surface density Σ, residual density $\Sigma_{\rm res}$ and the relative spiral strength of different m modes, S_m, of the discs in these simulations are shown in Fig. 3.11. Here the relative spiral strength S_m is defined as

$$S_m(R) = \left|\hat{\Sigma}_m(R)/\hat{\Sigma}_0(R)\right|, \tag{3.17}$$

where $\hat{\Sigma}_m(R)$ is the Fourier transformation of the surface density of the disc at radius R along the azimuthal coordinate, as defined in equation (3.10). In practice, the spiral strength fluctuates over time at a given radius. To show the mean trend of the strength with respect to the radius, we therefore plot the averaged spiral strength over a time interval from 0.35 to 0.85 Gyr.

As shown in the top three rows of Fig. 3.11, two-armed spiral structures form in all three simulations. The spiral strength for $m = 2, 4, 6$ and 8 has a similar radial profile within each simulation, indicating that the spiral strength measured for higher m modes is largely due to the two-armed spiral structures. However, for different simulations, the relative spiral strength, S_m, varies differently with radius R. Generally, spiral strength depends on the halo triaxiality. This can be understood by comparing the torque generated by the triaxial halo, as shown in the right-hand panel of Fig. 3.10. The torque and the strength of the spiral

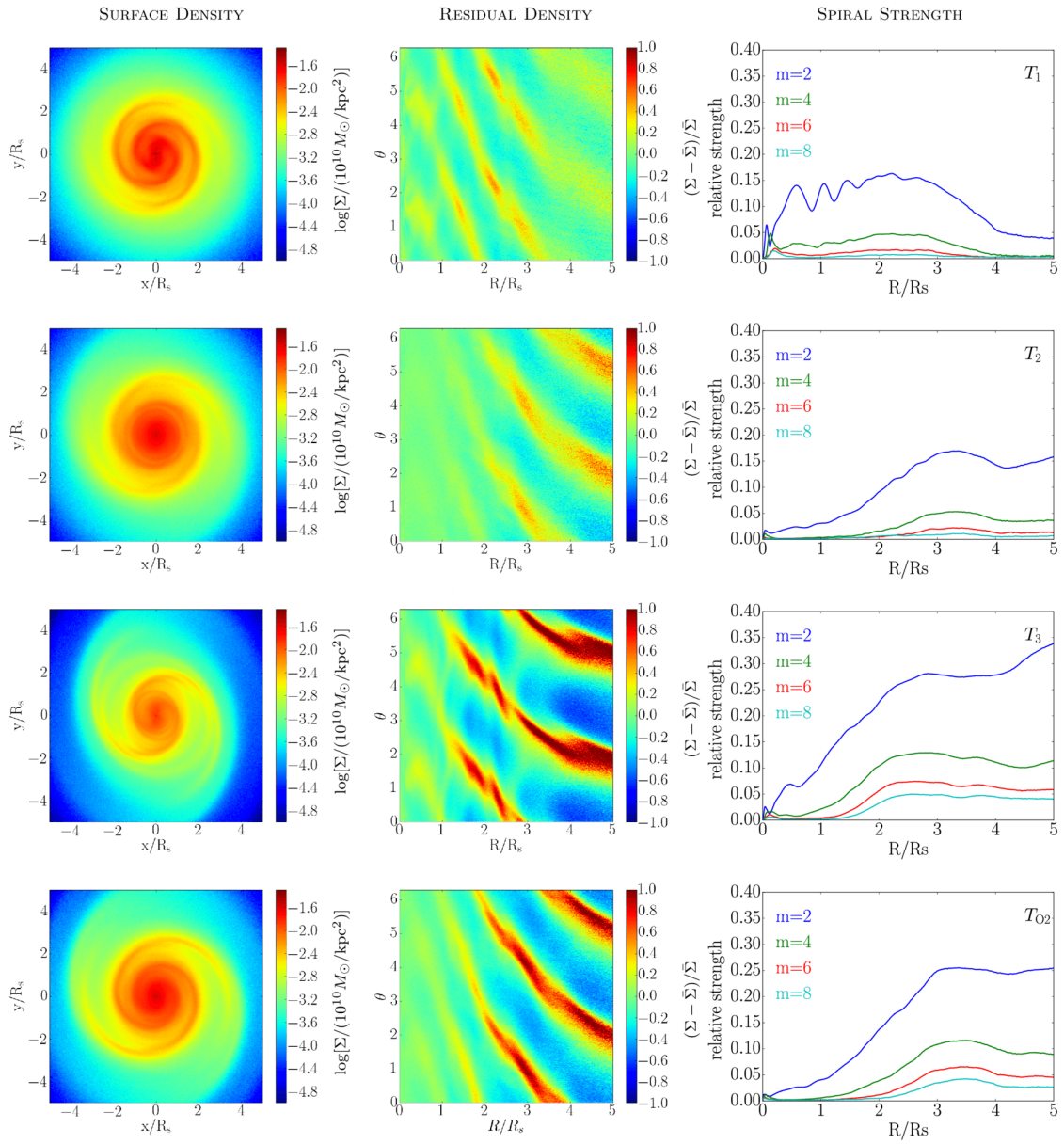

Fig. 3.11 Surface density, residual density and spiral structure strength of discs in simulations with T_1, T_2, T_3 and T_{O2} haloes (from top to bottom). Left column: surface density in Cartesian coordinates at time $t = 0.5\,\mathrm{Gyr}$. Central column: residual density in polar coordinates at time $t = 0.5\,\mathrm{Gyr}$. Right column: spiral strength for different modes averaged over a time interval from 0.35 to 0.85 Gyr. This time interval in chosen so that the spiral structures are fully developed in the disc. Note that spiral strengths with the odd m modes are not shown because they are much weaker. For the halo that is more triaxial inside (T_1), the spiral structure is stronger inside, while for the halo that is more triaxial outside (T_2), the spiral structure is also stronger outside. For T_3 halo which has $b/a \sim c/a \sim 0.85$, the spiral structure strength is generally higher than the other two simulations, expect for the central region where the spiral structure strength is lower than that of the T_1 halo. For the T_{O2} halo, the disc plane is determined by the direction of the total angular momentum, as discussed later in Appendix 3.B.

structures show almost identical trends as a function of radius for all three simulations, i.e. by comparing different simulations, one can find that the strength of the spiral structures at a given radius is higher for the simulation where the torque at that radius is stronger, and vice versa.

3.3.5 Swing Amplification of Spiral Fragments

As shown in Fig. 3.1, for a low-Q disc with 10^8 star particles located in a spherical halo, transient spiral structures develop in several Gyr due to swing amplification. To explore if this process will also take place in simulations with a triaxial halo, we run the simulation with a T_2 halo for a longer time.

As shown previously in Fig. 3.11, at first only two-armed spiral structures develop in the disc. However after some time transient multi-armed spiral structures gradually form in the central region of the disc. Various properties of the disc in this simulation at $t = 3\,\mathrm{Gyr}$ are shown in Fig. 3.12. It can be seen from the surface density of the disc that two kinds of spiral structures co-exist in the disc, with transient spiral arm structures dominating the inner region of the disc, and two-armed grand-design spiral structures taking up the outer region.

Generally, the swing amplification is strong when the Q parameter is close to unity. Fig. 3.12 shows that regions with low $\tilde{Q}(R,\theta) = \frac{\sigma_R \kappa}{3.36 G\Sigma}$ value (note that Toomre's Q parameter is the angular average of $\tilde{Q}$) lie perfectly within the spiral structures. This indicates that the spiral arms, with their higher density, can attract more stars into the spiral arms, hence magnifying the strength of the spiral structures. Also, in the part of the disc with $R_\mathrm{S} < R < 3.5R_\mathrm{S}$, the $\tilde{Q}$ parameter is generally slightly higher than 1 outside of the spiral structures. This explains why transient spiral structures form in this region due to swing amplification, while for $R > 3.5R_\mathrm{S}$ azimuthally averaged $\tilde{Q}$ value is significantly higher than 1.

To further explore the interaction between grand-design spiral structures and swing amplification, we compare the discs formed in three different simulations: one with a low-Q disc in a T_2 halo, one with a low-Q disc in a spherical halo, and one with a high-Q disc in a T_2 halo. The surface density and residual density of the discs in these simulations at $t = 3\,\mathrm{Gyr}$ are shown in Fig. 3.13. By comparing the simulations with low-Q and high-Q disc in T_2 haloes, one can see that the transient arms do not form in the simulation with the high-Q disc, where the swing amplification is very weak. This proves that the swing amplification is the reason for the formation of the transient spiral structures seen in the central regions of the low-Q disc.

We additionally performed a simulation with self-gravity of the disc turned off with a low-Q disc in a T_2 halo, whose result is shown in Fig. 3.14. No transient spiral structures form in this simulation, although two-armed grand-design spiral structures still form. Without

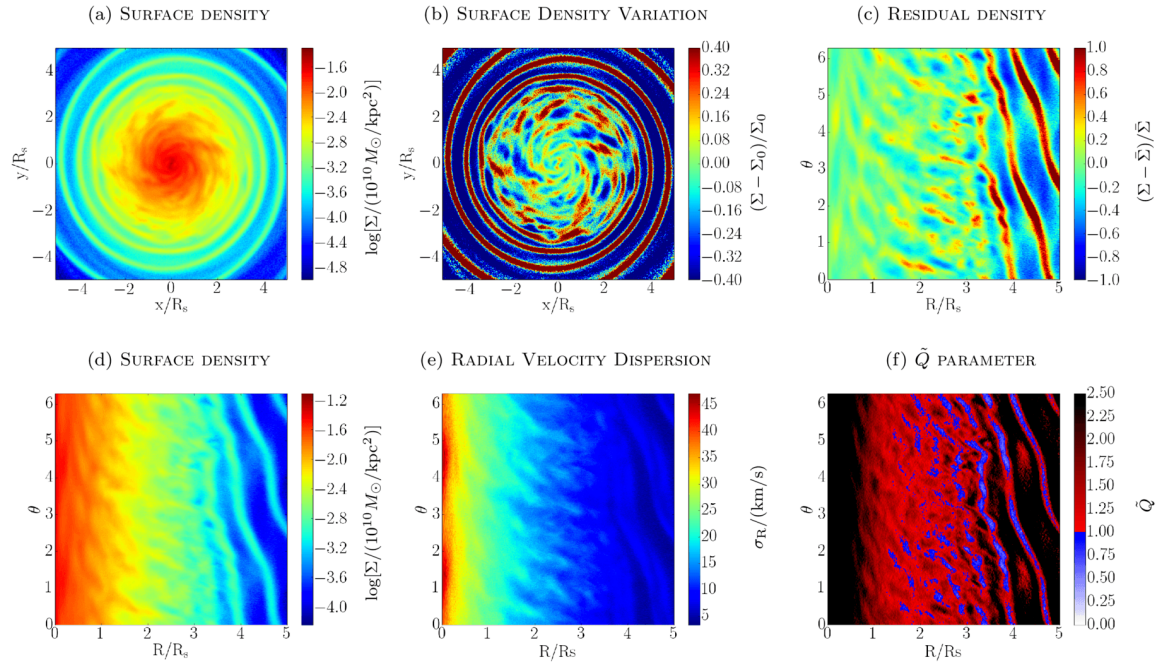

Fig. 3.12 Maps of various quantities of a low-Q stellar disc in the T_2 halo at time 3 Gyr. Panel (a) shows the surface density in Cartesian coordinates. To show the structures throughout the disc more clearly, we subtracted the initial surface density Σ_0 from the surface density Σ at 3Gyr and then divided it by Σ_0. The result is shown in panel (b). Panel (c) shows the residual density map in polar coordinates. In panel (d), (e) and (f), surface density, dispersion of the velocity in the radial direction, σ_R, and $\tilde{Q}$ parameter are shown in polar coordinates. Here $\tilde{Q}(R,\theta) = \frac{\sigma_R \kappa}{3.36 G\Sigma}$. Toomre's Q parameter is the angular average of $\tilde{Q}$. $\tilde{Q}$ quantifies the local stability of the disc. Two different types of spiral structures co-exist in the disc. Outside $3.5R_S$ is the grand-design two-armed spiral structure caused by the triaxial halo, while inside $3.5R_S$ there are more arms and they are all transient.

self-gravity, there is no swing amplification process in the disc. This further demonstrates that transient arms are caused by the swing amplification, while two-armed grand-design spiral structures are not formed due to the swing amplification.

We also compare the simulations with low-Q discs in S and T_2 haloes as shown in Fig. 3.13. Transient spiral structures form in both cases. However, the transient spiral structures formed in the T_2 halo are significantly stronger than that formed in the S halo. For the simulation with the T_2 halo, two-armed spiral structures formed in the central region of the disc at early times are gradually swing amplified and form the first generation of transient spiral structures later, while for the simulation with the S halo, transient spiral structures form due to the swing amplification of the Poisson noise in the initial conditions. With 10^8 particles in the disc, the Poisson noise is much weaker perturbation to the density field of the

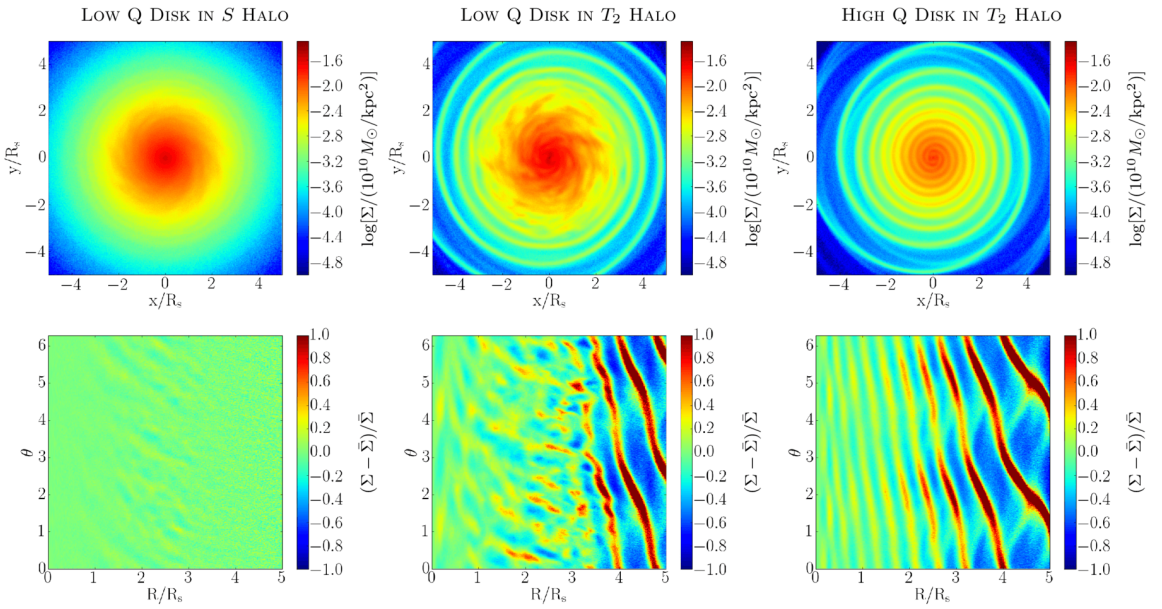

Fig. 3.13 Surface density (top row) and residual density (bottom row) for discs in three different simulations at time $t = 3\,\mathrm{Gyr}$. By comparing the left and the middle column we find that the strength of the transient spiral structures is stronger for the disc in a triaxial halo, although they are both formed due to swing amplification. As shown in the right column, transient multi-armed spiral structures do not form with a high-Q disc.

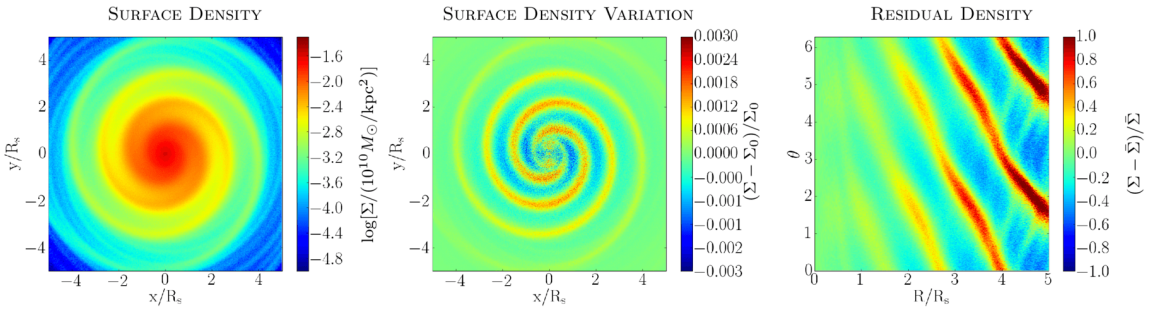

Fig. 3.14 Simulation of low-Q disc in T_2 halo without self-gravity at time $t = 3\mathrm{Gyr}$. Without self-gravity, transient spiral structures no longer form, while the grand-design spiral structures still persist.

disc than grand-design spiral structures. Therefore, transient spiral structures formed in a T_2 halo are much stronger than that in an S halo.

3.3.6 Formation Mechanism of Two-Armed Spiral Structures

To understand the formation mechanism of two-armed spiral structures, we study the modes of spiral structures following Sellwood & Carlberg (2014), by measuring the power spectra

of the discs in T_2 haloes. The surface density Σ of the disc at time t, radius R and azimuthal angle θ can be expressed by the summation of a series of waves

$$\Sigma(R,\theta,t) = \sum_{\Omega_f}\sum_{m} A(R,m,\Omega_f)\mathrm{e}^{\mathrm{i}(\Omega_f t + m\theta)}, \tag{3.18}$$

where m is the number of arms and $\Omega_f = m\Omega_\mathrm{P}$ is m times the pattern speed Ω_P. In other words, Σ is the Fourier transform of the power A. Values of $A(R,m,\Omega_f)$ are complex numbers, as they are a combination of cos and sin waves. We are more interested in the absolute value $|A(R,m,\Omega_f)|$, which is the total strength of the mode of m and Ω_f at R. The power spectra are a good tool to study the waves in the disc, as they show the dominant rotational modes across the disc. In our simulations, since the surface density in the central region is much higher than that in the outer region, small fluctuations in the centre can have a higher power than the spiral structures located further out. In order to show the power spectra of the spirals clearly, we calculate power spectra of the residual surface density instead of the surface density.

Power spectra of low-Q and high-Q discs in T_2 haloes for a time interval from 2 to 7.5 Gyr are shown in Fig. 3.15. For the power spectra of $m = 2$ modes, the highest power lies at the inner Lindblad resonance where the pattern speed is $\Omega_\mathrm{P} = \Omega - \kappa/2$, with Ω being the rotation speed of the stars and κ being the epicyclic frequency. Since the high power values occur within a narrow region across the disc, there is only one dominating rotating mode in the disc, with rotating speed of $\Omega - \kappa/2$. The high-power region in the power spectra of the $m = 2$ modes of the high-Q disc spans throughout the disc, but the high-power region for the low-Q disc is located only at the outer region of the disc. This is because the inner region of the low-Q disc is disrupted by the swing amplification, as previously shown in Fig. 3.13. We have also checked the $m = 2$ power spectra of the simulation with self-gravity turned off. The high-power region lies at the inner Lindblad resonance similarly to the simulation of high-Q disc with self-gravity, indicating that self-gravity plays a minor role here. For the power spectra of $m = 9$ modes, the power strength of the low-Q disc is more than five times higher than that of the high-Q disc, because the latter does not form prominent transient multi-armed spiral structures. Horizontal structures present in the power spectra for the $m = 9$ modes of the low-Q disc are shown to be the characteristic features of the transient spiral structures due to the swing amplification by Sellwood & Carlberg (2014).

The fact that the regions of the highest power of $m = 2$ modes lie at the inner Lindblad resonance with and without self-gravity indicates that the two-armed grand-design spiral structures are indeed kinematic density waves, as proposed by Lindblad (1956). For a large region in the disc, the value of $\Omega - \kappa/2$ in our simulations can be regarded as roughly

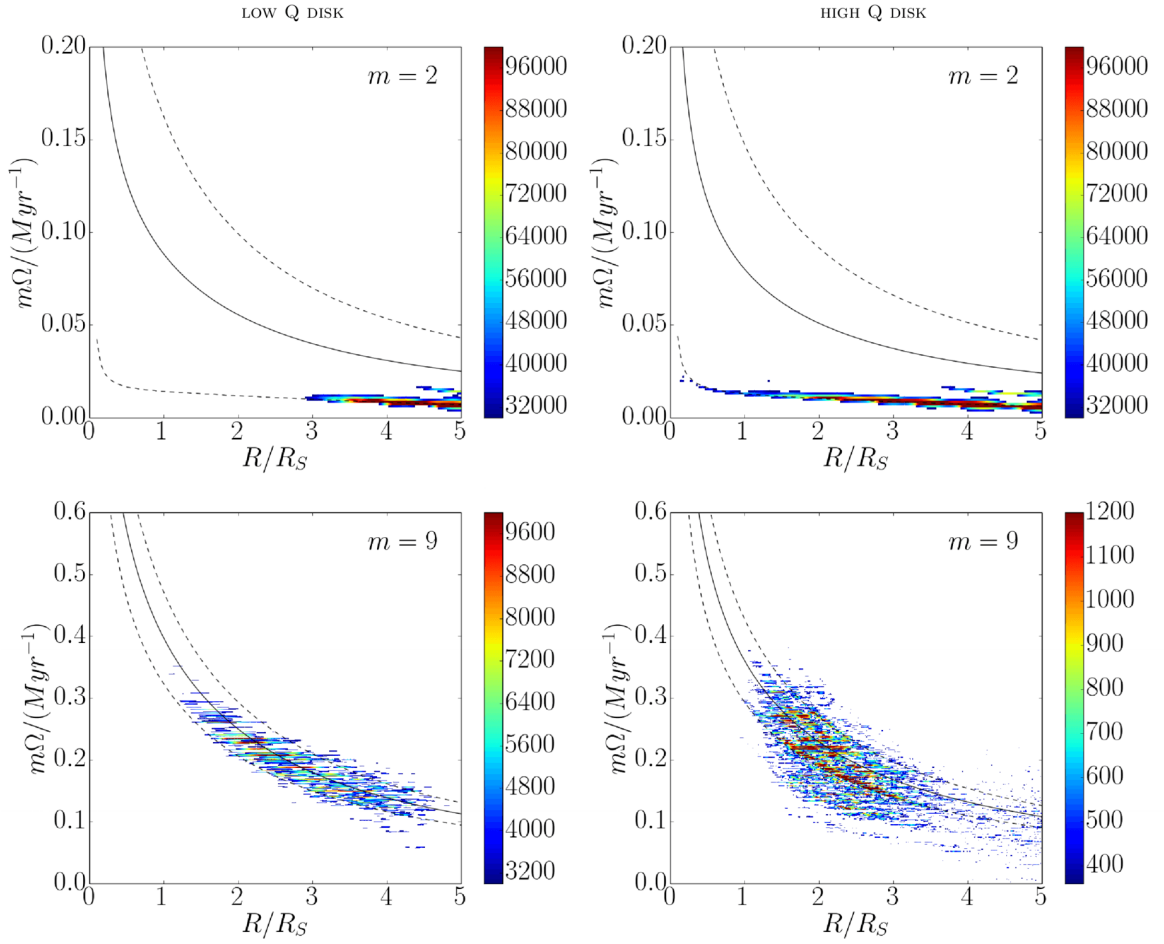

Fig. 3.15 Power spectra of the low-Q disc (left) and the high-Q disc (right) for a time interval 2–7.5 Gyr in T_2 haloes for $m = 2$ modes (top) and $m = 9$ modes (bottom). In each panel, black solid curve indicates corotation line with pattern speed $\Omega_P = \Omega$, where Ω is the angular velocity of the stars, while black dashed curves are inner and outer Lindblad resonances with $\Omega_P = \Omega \pm \kappa/2$, with κ being the epicyclic frequency. For $m = 2$, the dominating feature corresponds to the grand-design spiral structures. For the low-Q disc this structure only exists in the outer region, because the grand-design spiral structures are distorted by swing amplification. For the high-Q disc where swing-amplification is weak, the grand-design spiral modes extend down to the innermost regions. The grand-design spiral structures lie at the inner Lindblad resonance. The dominating features of $m = 9$ modes are the horizontal structures crossing the corotation line, which are the typical structures of swing amplified modes. The strength of these modes in high-Q disc is roughly an order of magnitude lower than in the low-Q disc, as can be seen from the colour bar. Other high-m modes are not shown, as they are all qualitatively similar to the $m = 9$ power spectra.

constant. Due to the epicyclic motion of the stars, in a frame rotating with this angular speed, stars have stationary elliptical orbits. Therefore, in such a frame if the orbits of the stars are arranged to be more crowded in some regions than the others initially, the crowded regions will remain crowded. Seen from a rest frame, this corresponds to a pattern moving with the pattern speed $\Omega_P = \Omega - \kappa/2$. In our simulations, such arrangement of the orbits is caused by sudden introduction of triaxial haloes. Once formed, such patterns can survive in the disc for several Gyr (see also Fig. 3.6 and discussion in Section 3.3.2). It is also worth noticing that the curve of $\Omega - \kappa/2$ is not perfectly flat, as it slightly decreases with radius. Because of this, the pattern speed of the spiral structures is slightly decreasing with radius as well, which explains the winding of the spirals at later times, as shown in e.g. Fig. 3.3.

The lifetimes of grand-design spirals are shown in Fig. 3.16. Here we plot the strength of the $m = 2$ modes as a function of time for radii $R = 1R_S, 3R_S$ and $5R_S$. For simulations with high-Q discs, in general, spiral strengths peak at $1 \sim 4$ Gyr and then gradually decline. Spiral strengths larger than 0.1 can persist for up to $5 - 10$ Gyr, depending on the radius probed. The peak values correlate strongly with the torque strength shown in Fig. 3.10, i.e. the peak value of the spiral strength is stronger when the torque strength is stronger. For the simulation with a low-Q disc and a T_2 halo, at the beginning, the growth of the spiral strength is similar to the simulation with the same halo but with a high-Q disc, but the strength of the spirals in the low-Q disc starts to decrease earlier, in 1–2 Gyr. This is the time when the low-Q

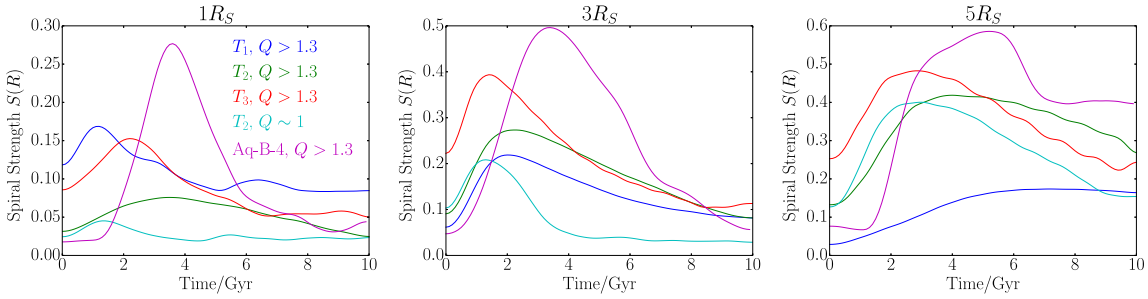

Fig. 3.16 The strength of the $m = 2$ spiral structures as a function of time for radii $R = 1R_S, 3R_S$ and $5R_S$ in various simulations. For simulations with T_1, T_2, and T_3, the halo is static and triaxial, while for the simulation with the Aq-B-4 halo (second model), the halo shape changes over time as in the right-hand panel of Fig. 3.7. For better comparison the time of the Aq-B-4 simulation has been shifted so that $t = 0$ corresponds to $t = 4$ Gyr in Fig. 3.7. Curves have been smoothed with a Hann function over a ~ 2 Gyr time span to show the general trends more clearly. For simulations with high-Q discs, spiral strengths peak at 1–4 Gyr and then gradually decrease over several Gyr. In the T_2 halo with low-Q disc the strength of grand-design spirals is affected by transient spirals after $1 - 2$ Gyr. Simulation with the Aq-B-4 halo shows stronger spiral strength due to its higher triaxiality and fluctuating evolution.

disc starts to develop transient spiral structures due to swing amplification, which favours spiral structures with higher m modes. Simulation with the halo which traces the Aq-B-4 triaxiality with time (second model) generally shows a similar trend as the simulations with static haloes, though it has a higher peak strength. This is caused by two effects: (a) the ratio of the axes of the Aq-B-4 halo is generally lower and (b) the ratio is fluctuating.

3.4 Conclusions

In this paper, we used very high resolution N-body simulations to investigate the influence of triaxial haloes on to stellar discs, especially on the formation of spiral structures. In our simulations, the haloes are implemented as analytic potentials rather than dark matter particles to minimize possible numerical artefacts caused by Poisson noise and to allow us to perform many very high resolution simulations of the stellar discs, which are represented with up to 10^8 particles. While high-Q discs are stable against spiral structures in spherical haloes, we found that two-armed grand-design spiral structures form in such discs if they are abruptly embedded within triaxial haloes. These spiral structures extend all the way to the edge of the disc. Their strength dependence with radius is determined by the torque from the triaxial halo experienced by the disc. We further showed that these spiral structures have the following features.

- They do not form when the halo turns from spherical to triaxial adiabatically. This indicates that the impulsive introduction of triaxial haloes leads to the grand-design two-armed spiral structures.
- Realistic fluctuations in halo triaxiality with time, as predicted by cosmological simulations, also lead to very prominent grand-design two-armed spirals, as we have explicitly demonstrated using the Aquarius simulations (Springel et al., 2008; Vera-Ciro et al., 2011).
- They form in discs that have $Q > 1.3$, i.e. when the swing amplification process is weak in the disc. This demonstrates that swing amplification is not necessary for the formation for these spiral structures.
- They form even if the self-gravity of the disc is turned off, which again excludes swing amplification as the essential formation mechanism.
- Once formed, they can survive in spherical haloes. Triaxial haloes are therefore not necessary for maintaining the spiral structure.

- Their power spectra peak at the inner Lindblad resonance that satisfies $\Omega_{\rm P} = \Omega - \kappa/2$, which is almost flat for a large region of the disc in our model, in agreement with the kinematic density wave theory proposed by Lindblad (1956). This offers a way to test the occurrence of this grand-design arm formation mechanism by comparing to the observed pattern speeds.

Furthermore, we showed that the swing amplification process and the time variation of the halo triaxiality can in fact interfere with each other. When the time-scale of the growth of transient spiral structures due to the swing amplification is very short, which in our case occurs when the number of the star particles used in the simulation is low, only transient arms form, while their distribution becomes more asymmetric in a triaxial halo. When the process of swing amplification is slow enough, two-armed grand-design spiral structures form in the first place. However, these spiral structures break up and get swing amplified into transient arms at later times. Moreover, at a given resolution spiral structures formed in this way grow faster than those formed in a spherical halo where the Poisson noise in the initial conditions is the only source for the swing amplification.

The sudden introduction of triaxiality into an initially spherical halo in equilibrium with the stellar disc is clearly a very idealized setup and is not directly applicable to observed systems. However, we have shown that similar spiral structures develop as long as the time-scale of the gravitational potential perturbation is shorter than the orbital period of stars. Self-consistent cosmological simulations indicate that both inner and outer halo triaxiality can change rapidly and significantly on short time-scales as massive satellite flybys, mergers, large-scale inflows and tumbling triaxial haloes are known to alter gravitational potentials rapidly and to introduce torques. The formation of spiral structures in these cases shares a similar underlying mechanism with our simplified simulations, as we have verified explicitly, where the strength of arms formed depends on the gravitational torques, and where grand-design arms form. Furthermore, if stellar discs are subject to swing amplification, additional rapid perturbations in gravitational potentials and torques might be conducive to the development of transient arms.

*This work was performed on: DiRAC Darwin Supercomputer hosted by the University of Cambridge High Performance Computing Service (http://www.hpc.cam.ac.uk/), provided by Dell Inc. using Strategic Research Infrastructure Funding from the Higher Education Funding Council for England and funding from the Science and Technology Facilities Council; DiRAC Complexity system, operated by the University of Leicester IT Services, which forms part of the STFC DiRAC HPC Facility (www.dirac.ac.uk). This equipment is funded by BIS National E-Infrastructure capital grant ST/K000373/1 and STFC DiRAC Operations grant ST/K0003259/1; COSMA Data Centric system at Durham University, operated by the Institute for Computational Cosmology on behalf of the STFC DiRAC HPC Facility. This equipment was funded by a BIS National E-infrastructure capital grant ST/K00042X/1, STFC capital grant ST/K00087X/1, DiRAC Operations grant ST/K003267/1 and Durham University. DiRAC is part of the National E-Infrastructure.

Appendix

Appendix 3.A Disc Stability in Spherical Halo

Fujii et al. (2011), Sellwood (2012), D'Onghia et al. (2013) and several other works have found that the Poisson noise in the disc due to a low number of star particles can be greatly swing amplified causing transient spiral structures to form. As stated in Section 3.3.1, we performed several simulations to study this effect. Two competing factors, the initial Poisson noise level set by the number of particles N and the gravitational stability of the disc quantified by Toomre's Q parameter, are considered. Our simulations include two runs with a high-Q disc containing 10^6 and 10^8 star particles and four runs with low-Q discs containing 10^5, 10^6, 10^7 and 10^8 star particles. Surface densities of discs at 2.5 Gyr are shown in Fig. 3.17. For high-Q discs, no spiral structures form. For discs with low-Q, strong spiral structures form in simulation with 10^6 and 10^7 star particles, while very weak spiral structures are present in simulation with 10^8 star particles. For the simulation with low-Q with 10^5 star particles, the spiral structures can barely be seen due to two reasons: (a) as shown in Fig. 3.1, the strength of spiral structures in this simulation decreases after several hundred million years, (b) number of particles is too low to show weak spiral structures.

For simulations with low-Q discs with 10^6–10^8 star particles, the spiral structures are most prominent in the region $R_S < r < 3R_S$. We checked the evolution of such spiral arms and found that each single arm is not long-lived. The arms break up quickly and new arms emerge from the fragments of the old arms. The stars in the disc are rotating anticlockwise; therefore, the spiral structures are trailing, which is in the agreement with the prediction of the swing amplification mechanism.

The average Q value as a function of radius is shown in Fig. 3.18. Blue lines denote the Q value in the initial conditions. Q parameter for simulations with low-Q discs is shown with solid curves. For low-Q discs, in the region of $R_S < r < 3R_S$, the Q parameter is either less than 1 or slightly over 1. Due to the fact that discs are not razor-thin, they are stable to axisymmetric perturbations even when Q is slightly lower than 1, but the swing amplification is still strong. This explains why transient spiral structures are strongest in this region. For

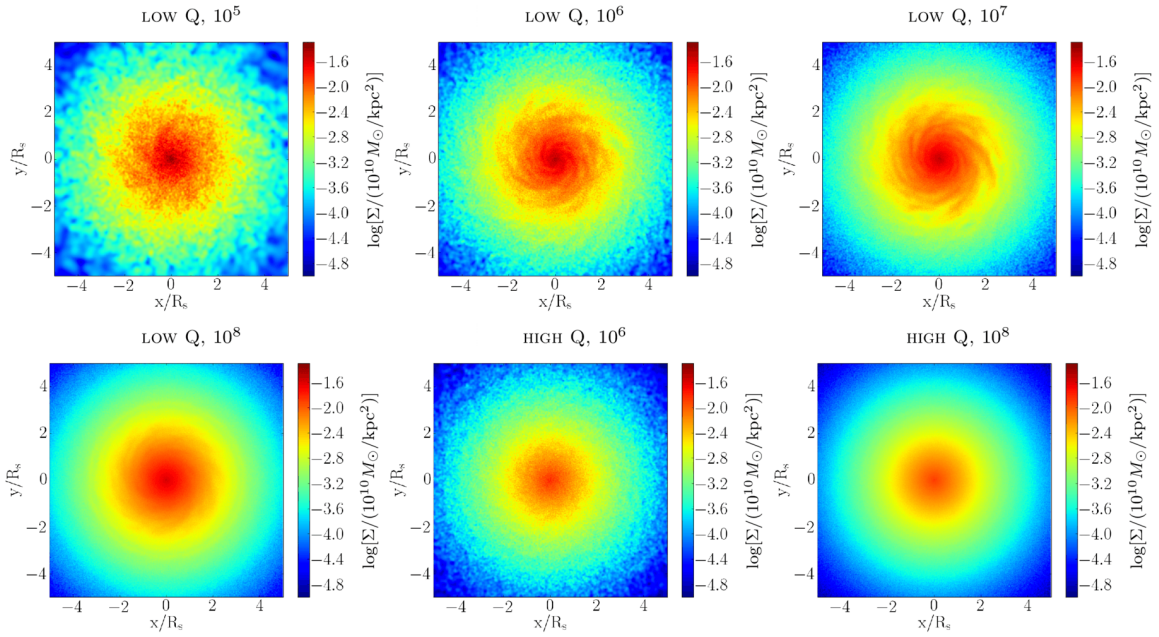

Fig. 3.17 Surface density of the low-Q and high-Q stellar disc at time $t = 2.5$Gyr. For low-Q discs, four simulations with increasing number of particles, ranging from 10^5 to 10^8, are shown. Strong spiral structures develop when the particle number is lower than 10^8, while for the disc with 10^8 particles, very weak spiral structures can also be seen. For 10^5 particles, the spiral structures initially present fade away before $t = 2.5$Gyr. For high-Q discs, simulations with 10^6 and 10^8 star particles are shown. No prominent spiral structures can be found in such simulations.

simulation with a lower number of particles, Q value grows faster over time. At later times, Q is so high that swing amplification is no longer strong, which leads to the decreasing of spiral strength. In simulations with discs with $Q > 1.3$, Q parameter is higher than 1.3 all through the disc, as shown in the right-hand panels of Fig. 3.18 with dashed curves. Due to a high Q, spiral structures do not grow prominently in the disc.

In conclusion, the growth of self-induced spirals depends on two factors: the initial Poisson noise level and the gravitational stability of the disc. The initial Poisson noise level sets the initial strength of perturbations that are amplified later. The higher number of particles, the longer time it takes to grow perturbations to a prominent level. The stability of the disc decides the actual growth rate of the perturbation. For a highly stable disc, it may take very long time to grow perturbations in a self-induced manner.

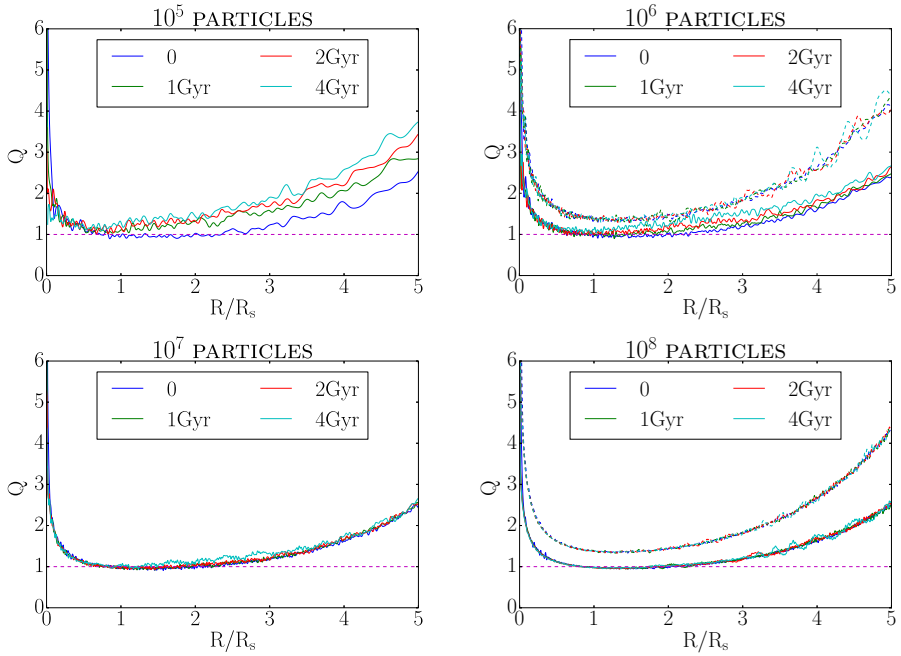

Fig. 3.18 Toomre's Q parameter as a function of radius. Plots for four identical low-Q discs simulated with different number of particles (from 10^5 to 10^8) are shown with solid lines, while high-Q discs with 10^6 and 10^8 particles are shown with dashed lines in the right-hand panels. Lines of different colour stand for different times, as annotated in legends. In particular, blue lines in each plot denote the Q–r relation at the initial time. The swing amplification is strong if Q is close to 1. As spiral structures develop, the 'temperature' of the disc raises for low particle numbers, i.e. 10^5 and 10^6, resulting in an increase of Q at later times. This increase of Q coincides with the decrease of spiral strength of corresponding models shown in Fig. 3.1. For high-Q discs, no prominent spiral structures develop, leading to hardly any changes in Q profile.

Appendix 3.B Discs in Misaligned Triaxial Haloes

We now focus on to the influence of triaxial haloes if the disc does not lie in the x–y plane of the halo. Even though for isolated systems it has been shown that the inner part of the halo realigns on a dynamical time with the disc (Binney et al., 1998), in cosmological simulations large misalignments are found (e.g. Hahn et al., 2010; Debattista et al., 2013; van de Voort et al., 2015), indicating that discs in misaligned haloes need to be studied. The top row of Fig. 3.19 shows the projection of the disc on to its initial plane in the simulation with a T_{O2} halo, i.e. a halo that is more triaxial outside with the disc plane that initially has a 45° angle with respect to the x–y plane of the halo, at three different times, $t = 0.7, 1.3$ and $2\,\mathrm{Gyr}$. At $0.7\,\mathrm{Gyr}$, the overall shape of the projection starts to be compressed. This compression becomes stronger over time. At around $t = 2\,\mathrm{Gyr}$, the projection of the disc is strongly

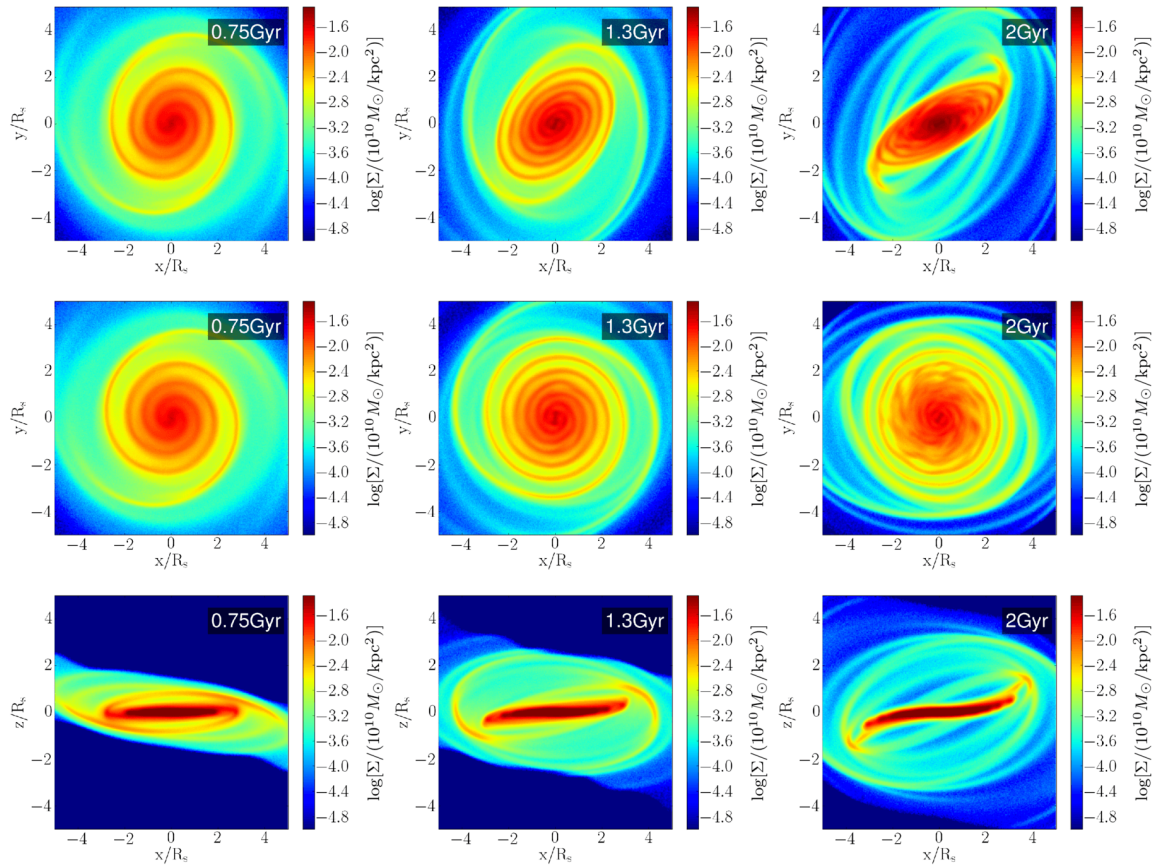

Fig. 3.19 Evolution of a disc in a misaligned triaxial halo. Top: projection of density on the initial plane. Middle: projection of density on the disc plane, whose normal direction is defined by the total angular momentum. Bottom: edge-on column density of the disc. Grand-design two-armed spiral structures still form in this case, while the orientation of the disc is changing as well. It can be also seen from the edge-on plot that warps develop in the disc at later times.

compressed in one direction. This compression of the projection on to a fixed plane indicates that the inclination of the disc is changing. In a triaxial halo, the gravity force does not always point directly to the centre. It does not even lie in the disc plane if the disc plane does not coincide with the x–y, x–z or y–z plane of the halo. The perpendicular component of the gravity force results in a non-zero torque that is not in the direction of angular momentum, which leads to the change of the disc's inclination.

We can infer the normal direction of the disc with the direction of the angular momentum vector, as long as the stars stay roughly in a plane. To achieve, this we calculate the total angular momentum

$$\boldsymbol{L} = \sum_i m \boldsymbol{r}_i \times \boldsymbol{v}_i \tag{3.19}$$

at each timestep, where m is the mass of a single particle, $\boldsymbol{r}_i$ and $\boldsymbol{v}_i$ are the position and velocity vector of the i-th star particle.

The middle row of Fig. 3.19 shows the projection of the disc onto the plane that is perpendicular to the total angular momentum vector. We can see that the morphology of the spiral structures is similar to the disc that is not misaligned with respect to the x–y plane of the halo, for example similar to the disc shown in Fig. 3.12. However, in the outer parts of the disc the shape of the spiral arms is distorted.

We can understand the distortion of the disc by looking at it edge-on. As shown in the bottom row of Fig. 3.19, the disc develops an integral shape warp at later times, indicating that the disc no longer stays in a plane. Also more and more mass spreads along the z direction. It is also worth noticing that though the warping of the disc shows a trend for the disc to become aligned with the major axis of the halo, which is 45° from the initial normal direction of the disc, in fact most of the mass of the disc stays in roughly the same initial plane at time $t = 2\,\mathrm{Gyr}$.

The warp of the disc before 0.75 Gyr is very weak. Therefore we can compare the strength of the spiral structures at early times, e.g. 0.5 Gyr, in this simulation with the simulations where the discs lie in the x–y plane of the triaxial halo, as shown in the bottom row of Fig. 3.11 and the right-hand panel of Fig. 3.10. The strength of the spiral structures in this simulation also matches with the gravitational torque caused by the triaxial halo. In fact, the strength of the torque in this simulation lies between the simulations with T_2 and T_3 haloes, as well as the corresponding strength of the spiral structures.

At later times, the outer part of the disc no longer stays in the disc plane. As shown in the middle row of Fig. 3.19, the outer part of the spiral structures is distorted. We plot the density projection of the disc in polar coordinates, as illustrated in the left-hand panel of Fig. 3.20. For $R/R_\mathrm{S} > 3.5$, radius of the spiral structures no longer increases strictly as the angle goes anticlockwise. To investigate if this is due to the warp of the disc, we rotate every pixel in this plot on to the disc plane again while keeping the azimuthal coordinate θ unchanged, so that the spiral structure all through the disc can be compared on the same plane. This is done by changing the radius R of each pixel to $\sqrt{R^2+\bar{z}^2}$, where

$$\bar{z} = \frac{1}{\Sigma(R,\theta)} \int_{-\infty}^{\infty} \rho(R,\theta,z) z \mathrm{d}z, \tag{3.20}$$

is the mean height of the mass at (R,θ). The result in shown in the right-hand panel of Fig. 3.20. The radius of the spiral structures increases strictly anticlockwise, as is the case for the spiral structures in all other simulations with discs in the x–y plane of the halo. This

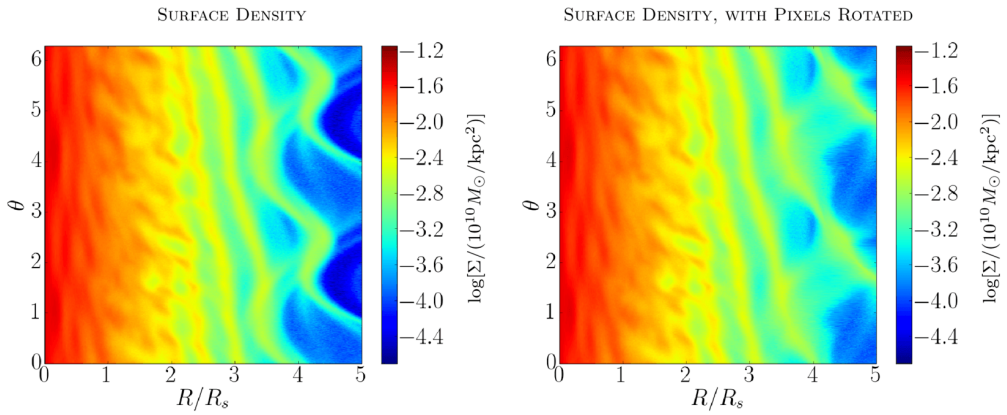

Fig. 3.20 Surface density of a disc in a misaligned triaxial halo at 2 Gyr in polar coordinates. The outer part of the disc is not in the plane defined by the angular momentum of the disc. The spiral arms are distorted if the density is directly projected on to the disc plane (left). However, if we rotate every pixel on to the disc plane (right), the morphology of the spiral structure becomes similar to the simulations with discs within the x–y plane of the haloes.

indicates that the distortion of the outer part of the spiral structures is simply due to the projection.

In conclusion, when the disc is misaligned with the halo, the spiral structures still grow in response to the torque. Their strength corresponds to the strength of the torque, similar to the simulations with discs lying in the halo plane. Even though warps develop at later times, they interfere very little with the spiral structures. The morphology of the spiral structures is unaffected as long as the radii of the spiral structures are calculated with the height from the disc taken into account.

Chapter 4

Impact of Cosmological Satellites on Stellar Discs: Dissecting One Satellite at a Time

Within the standard hierarchical structure formation scenario, Milky Way-mass dark matter haloes have hundreds of dark matter subhaloes with mass $\gtrsim 10^8\,\mathrm{M}_\odot$. Over the lifetime of a galactic disc a fraction of these may pass close to the central region and interact with the disc. We extract the properties of subhaloes, such as their mass and trajectories, from a realistic cosmological simulation to study their potential effect on stellar discs. We find that massive subhalo impacts can generate disc heating, rings, bars, warps, lopsidedness as wells as spiral structures in the disc. Specifically, strong counter-rotating single-armed spiral structures form each time a massive subhalo passes through the disc. Such single-armed spirals wind up relatively quickly (over $1-2$ Gyrs) and are generally followed by co-rotating two-armed spiral structures that both develop and wind up more slowly. In our simulations self-gravity in the disc is not very strong and these spiral structures are found to be kinematic density waves, directly related to the inner Lindblad resonance of the disc. We demonstrate that there is a clear link between each spiral mode in the disc and a given subhalo that caused it, and by changing the mass of the subhalo we can modulate the strength of the spirals. Furthermore, we find that the majority of subhaloes interact with the disc impulsively, with resonances playing a minor role. As a result the strength of spirals generated by subhaloes is proportional to the time-integrated strength of the torque they exert. We conclude that only a handful of encounters with massive subhaloes is sufficient for re-generating and sustaining spiral structures in discs over their entire lifetime.

4.1 Introduction

The Cold Dark Matter scenario predicts a hierarchical growth of structures in our Universe, whereby low mass objects form first and more massive structures are assembled later on in course of merging and accretion. Hence, dark matter haloes are expected to contain a large number of smaller mass haloes, often dubbed subhaloes, which are gravitationally bound within. With the aid of high resolution cosmological simulations, properties of these subhaloes can be directly studied. For example, the Aquarius simulation (Springel et al., 2008) reports an average mass fraction of 11.2% for subhaloes within r_{50}, where $\sim 300,000$ subhaloes in the highest resolution simulation are resolved. The abundance function of subhaloes generally agrees well among different simulations (Bullock, 2010), where the abundance of subhaloes above a given mass threshold is roughly inversely related to their mass through a power law function, i.e. there are more small mass subhaloes than large mass subhaloes (Springel et al., 2008; Gao et al., 2004; Diemand & Moore, 2011).

In the hierarchical growth scenario, dark matter haloes accrete infalling subhaloes continuously. As subhaloes orbit in their host dark matter halo, their orbits usually decay and they lose mass due to dynamical friction and tidal stripping. In a semi-analytical study Taylor & Babul (2004) found that the mass loss in a single orbit varies from 25% to 45%, depending on the orbit eccentricity and the concentration of the subhalo (see also numerical works by e.g. Boylan-Kolchin et al., 2008; Jiang et al., 2008). As a combined result of both effects, most subhaloes that survive reside in the outer region of the dark matter halo and are prevalently newly accreted. In fact, Gao et al. (2004) found that only 8% of the subhalo mass survived from $z = 1$ to $z = 0$.

In our local group observed satellite galaxies are considered to be embedded in dark matter subhaloes (e.g. Mateo, 1998; Collins et al., 2010). The observed velocity curves of local group dwarf irregular (dIrr) and dwarf spheroidal (dSph) galaxies can be well fit by two components, one following the visible-light distribution while the other being considered as a dark matter component. When compared with visible satellites, cosmological simulations often over-predicts dark matter subhaloes. This is known as the missing satellites problem (Klypin et al., 1999; Moore et al., 1999). Taking into account the lower luminosity limit of observations, at least part of the problem can be solved (Tollerud et al., 2008; McConnachie et al., 2009; Koposov et al., 2015). It is however also believed that other factors may be at play. Apart from an alternative dark matter model, e.g. the Warm Dark Matter model that produces much less small scale structures (for recent work see e.g. Lovell et al., 2014; Bose et al., 2017), one may solve the missing satellites problem by studying various baryonic effects. For instance, baryons may alter the central region of the subhaloes to a core (Navarro et al., 1996), which enhances the tidal stripping effect on subhaloes (Peñarrubia et al., 2010);

photoionization background and supernova feedback can suppress star formation in low mass satellites (Efstathiou, 1992; Larson, 1974; Dekel & Silk, 1986; Sawala et al., 2016); baryonic discs may destroy the subhaloes through strong tidal effects (D'Onghia et al., 2010). Such baryonic effects reduce the number of dark matter subhaloes and weaken or prevent formation of visible galaxies in some of the dark matter subhaloes, making them "invisible". One way to probe such "invisible" dark matter subhaloes is through their dynamical interactions with baryonic components, e.g. streams (Erkal & Belokurov, 2015).

Another possible way to detect invisible dark matter subhaloes is through their interactions with the stellar disc. Stellar discs are found to be very sensitive to perturbations, including massive molecular clouds (D'Onghia et al., 2013) and large-scale torques (Dubinski & Chakrabarty, 2009; DeBuhr et al., 2012). In particular, Hu & Sijacki (2016) found that a realistic triaxial dark matter halo can lead to two-armed grand-design spiral structures. Given that subhaloes exist widely in dark matter haloes, it is necessary to understand their interactions with the spiral structures.

Gravity-induced spiral structures may develop in strong self-gravitating discs (see e.g. Sellwood & Carlberg, 2014; Hu & Sijacki, 2016). Flocculent, re-current, multi-armed spiral structures form in this scenario. However, discs embedded in a realistic dark matter halo may experience disc thickening and heating in response to subhaloes, therefore weakening the self-gravitating effect. The vertical scale of the disc in expected to extend by at least 50% to 100%, with warps also developing in the disc (Velazquez & White, 1999; Kazantzidis et al., 2009; Weinberg, 1998). Moreover, the velocity dispersion of stars in the vertical direction is found to increase when satellites interact with the disc (Moetazedian & Just, 2016; Gómez et al., 2017), which leads to an increase in Toomre's Q parameter and can stabilise the disc against self-gravitating modes.

Previous studies with single test subhaloes have shown that massive subhaloes impacting with discs can generate grand-design spiral structures (but see also Dubinski et al., 2008). Purcell et al. (2011) found that subhaloes of mass $\sim 10^{10.5}\,\mathrm{M}_\odot$ to $10^{11}\,\mathrm{M}_\odot$ passing as close as 30 kpc from the disc centre are able to generate realistic two-armed grand-design spiral structures. Pettitt et al. (2016) found that the mass limit can be pushed as low as $10^9\,\mathrm{M}_\odot$ with a closer impact point of 12 kpc, where very weak two-armed spiral structures can be seen from the Fourier analysis. They also demonstrated that the spiral response in gaseous and stellar components are very similar.

In this work we aim to study the influence of subhaloes on stellar discs with a more realistic setup to address the following problems: *a)* how subhaloes with realistic properties and trajectories extracted from cosmological simulations interact with the stellar disc, *b)* how

multiple subhaloes impacting the disc in succession influence each other, and *c)* how the strength of the spiral structures depends on the properties of the subhaloes.

In Section 4.2, we introduce our simulation setup. We present the dark matter properties of our main simulation in Section 4.3.1, where realistic subhaloes impacting the central disc are identified. Disc heating due to subhaloes is discussed in Section 4.3.2. Non-axisymmetric modes including the spiral structures that develop are studied in Section 4.3.3. The kinematic properties of these modes are then studied in Section 4.3.4. We then demonstrate the link between the subhalo properties and spiral modes in Sections 4.3.5, 4.3.6 and 4.3.7. Finally, in Section 4.4 we present our conclusions.

4.2 Method

4.2.1 The Numerical Approach

All simulations in this paper are performed with GADGET-3, an updated version of GADGET-2 (Springel, 2005). GADGET-3 is an N-body/SPH code, where different simulated components, such as dark matter and stars, are represented with particles. The gravitational interaction of the particles are calculated with the TreePM method.

We model our static dark matter halo based on the Aq-A-4 dark matter halo from the Aquarius simulation (Springel et al., 2008). The Aquarius simulations is a dark matter-only cosmological simulation aimed to reproduce Milky Way-sized haloes. At $z = 0$ the Aq-A-4 halo has the virial mass of $M_{200} = 1.84 \times 10^{12} \mathrm{M}_{\odot}$ within the virial radius $r_{200} = 246\,\mathrm{kpc}$, consisting of 1.85×10^7 dark matter particles, each with a mass of $m_{\mathrm{DM}} = 3.93 \times 10^5\,\mathrm{M}_{\odot}$ and a softening length of $\varepsilon = 342\,\mathrm{pc}$. Detailed description of how we model the dark matter halo from the Aquarius simulation is included in Section 4.2.2.

The stellar disc is initially modeled with an exponential surface density profile and a vertical isothermal sheet profile following Springel et al. (2005a), i.e.

$$\rho_*(R,z) = \frac{M_*}{4\pi z_0 R_{\mathrm{S}}^2} \mathrm{sech}^2\left(\frac{z}{z_0}\right) \exp\left(-\frac{R}{R_{\mathrm{S}}}\right), \tag{4.1}$$

where $M_* = 9.5 \times 10^9\,\mathrm{M}_{\odot}$ is the total mass of the disc, $R_{\mathrm{S}} = 3.13\,\mathrm{kpc}$ is the scale length of the disc and $z_0 = 0.1\,R_{\mathrm{S}}$ is the scale height of the disc. We choose these parameters so that they match with the high-Q disc in Hu & Sijacki (2016). As shown in Hu & Sijacki (2016), high-Q disc responds to external torques, but does not form any noticeable self-gravity-induced spiral structures due to its low surface density, thus enabling us to focus on the kinematic properties. Also, as found in Hu & Sijacki (2016), stellar discs, setup to be in equilibrium within a

spherical halo, develop two-armed grand-design spirals when placed in a triaxial halo directly. To avoid this and study the effect of subhaloes, we grow the disc in an adiabatically changing dark matter halo, explained in detail in Section 4.2.3.

To account for baryonic effects (i.e. the influence of baryons on halo shape) but exclude any unwanted perturbations due to the discreteness noise, we setup our initial conditions in three steps as follows:

- **Phase-1:** We restart the cosmological simulation of the Aq-A-4 halo from $z = 1.3$ with adiabatically grown static, stellar disc potential to obtain the dark matter halo profile for the final simulation (Phase-3).
- **Phase-2:** We then simulate a live stellar disc, with properties described above, in an adiabatically changing dark matter halo potential, starting from a spherical halo and finishing with the halo shape obtained at the end of Phase-1. This step is needed to prepare the initial conditions of the stellar disc for the final simulation.
- **Phase-3:** In the final step we perform a simulation with a static dark matter halo potential (obtained from Phase-1), live dark matter subhaloes (directly taken from the Aq-A-4 run) and the live stellar disc obtained at the end of Phase-2. With this setup we can isolate the impact of subhaloes on the stellar disc.

Further details of the three steps are explained in the following sections.

4.2.2 Phase-1: Simulating the Response of the Live Dark Matter Halo to the Static Stellar Disc Potential

The Aquarius simulation is a dark matter-only simulation hence the effect of baryons on the dark matter distribution is not taken into account. This is a reasonable approximation in the outer region of the halo, where the baryonic matter is not dominant, but may result in a very different inner halo profile and shape.

To include the effect of baryons, we restart the Aquarius Aq-A-4 simulation from $z = 1.3$, adding a stellar disc potential which is numerically calculated from the density profile shown in Equation (4.1). In the simulation, we first grow the disc potential adiabatically from $z = 1.3$ to $z = 1$. In the original Aq-A-4 simulation, both the centre and the orientation of the main halo change over time. We modify the central position and the orientation of the disc position accordingly, so that the disc is always at the centre of the halo and aligned with the minor axis of the halo. We then keep the disc static from $z = 1$ to $z = 0$, and study the properties of dark matter distribution.

Specifically, the column density distribution of dark matter in the Phase-1 simulation is shown in the top panels of Figure 4.1 at three different redshifts. The total mass of the halo and its subhaloes increases from $1.35 \times 10^{12}\,\mathrm{M}_\odot$ at $z = 1$ to $2.29 \times 10^{12}\,\mathrm{M}_\odot$ at $z = 0$, which is mirrored by the increase in the physical size of the halo as evidenced in the panels.

We then separate the dark matter component into two groups. We find all self-bound structures in the simulation, as identified by the SUBFIND algorithm (Springel et al., 2001; Dolag et al., 2009), at any snapshot between $z = 1$ and $z = 0$. Of these, all structures that at any time belong to subhaloes, are marked as subhaloes and are simulated as a "live" component in the final simulation (Phase-3), using their coordinates and velocities at $z = 1$. The bottom panels of Figure 4.1 show column density distribution of subhaloes only. All other dark matter particles in the simulation are considered to be part of a "smooth" component (i.e. the difference between the top and bottom panels) and are represented with an analytic potential in the Phase-3 simulation (for further details see Appendix 4.A and Figure 4.12).

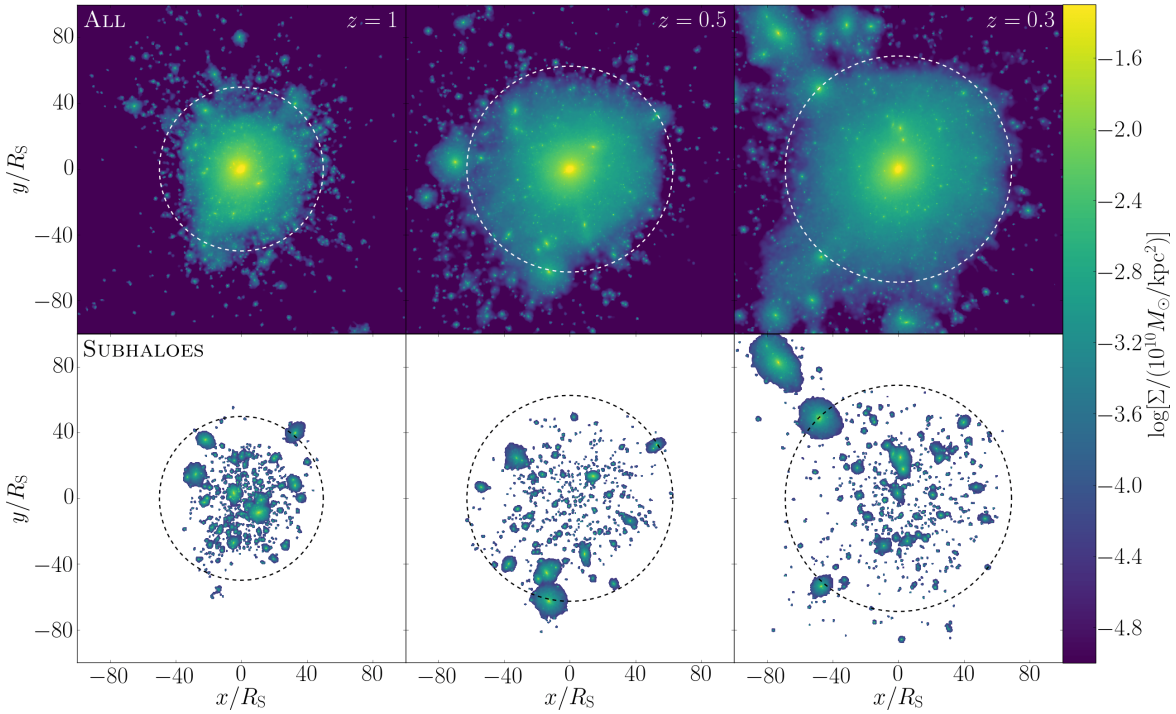

Fig. 4.1 Column density of the dark matter in the Phase-1 simulation in the $x-y$ plane at $z = 1$, $z = 0.5$ and $z = 0.3$, from left to right, respectively. Top row: the column density of all dark matter particles. Bottom row: the column density of subhaloes only. Total mass of the main halo and its subhaloes increases from $1.35 \times 10^{11}\,\mathrm{M}_\odot$ to $2.29 \times 10^{12}\,\mathrm{M}_\odot$ from $z = 1$ to $z = 0$, while the number of subhaloes changes from 893 to 1083. Dashed circles indicate the virial radius at these three epochs. The spatial coordinate is in the unit of the scale length of the disc $R_\mathrm{S} = 3.13\,\mathrm{kpc}$.

The smooth component can be represented by the sum of a spherical and a triaxial part. Density profile of the spherical part, $\rho_{\rm S}(r)$, is constructed by spherically averaging the smooth component. We fit it with three Einasto profiles joined together (see left panel of Figure 4.12 and Appendix 4.A). Compared to the dark matter halo profile in the original Aquarius simulation, our profile is more contracted in the centre due to the disc potential. Our disc model has a relatively low mass ($\sim 1\%$) compared to the main halo. This is to ensure that the effects due to self-gravity is suppressed, so that we can focus on the impact of external perturbations. The influence of the disc would be higher with a higher mass model. Following Bowden et al. (2013) and Hu & Sijacki (2016) the triaxial part is represented by two spherical harmonic functions, aiming to reproduce our desired axis ratio profile. The axis ratio profile of the smooth component in our simulation is calculated following a similar method to Vera-Ciro et al. (2011), where we iteratively compute the eigenvalues and eigenvectors of the "reduced" inertia matrix of an ellipsoid of a certain radius. We find that the axis ratio of the smooth component significantly fluctuates as a function distance from the centre and is rather triaxial in the centre (see solid curves in the right panel of Figure 4.12). This occurs as we only introduce a stellar disc to modify the dark matter halo shape and do not consider larger scale contribution from stars or gas. This would make the disc very elliptical and unstable. To avoid this issue, we impose a much smoother halo shape variation with radius (see dashed curves in the right panel of Figure 4.12), where the outer axis ratios are comparable to those obtained from our Phase-1 simulation.

Having computed $\rho_{\rm S}(r)$ and the axis ratios in $x-y$ plane, $p(r)$, and in $x-z$ plane, $q(r)$, we can calculate the density profile of the triaxial part as follows

$$\rho_{\rm T1}(r) = \left(1 - \frac{3q(r)^{\alpha}}{1+p(r)^{\alpha}+q(r)^{\alpha}}\right)\rho_{\rm S}(r) \tag{4.2}$$

and

$$\rho_{\rm T2}(r) = \frac{1}{2}\frac{1-p(r)^{\alpha}}{1+p(r)^{\alpha}+q^{\alpha}}\rho_{\rm S}(r), \tag{4.3}$$

where $\alpha = -{\rm d}\log\rho_{\rm S}(r)/{\rm d}\log r$ is the slope of the spherically averaged density profile. We enclose a brief explanation of these formula in Appendix 4.B. Hence, the total density profile of the halo is

$$\rho(r,\theta,\varphi) = \rho_{\rm S}(r) - \rho_{\rm T1}(r)Y_2^0(\theta) + \rho_{\rm T2}(r)Y_2^2(\theta,\varphi), \tag{4.4}$$

whose potential can be then integrated numerically using the Green's function, as shown in Appendix 4.C.

4.2.3 Phase-2: Introducing a Live Disc in a Static, Triaxial Dark Matter Halo Potential

The stellar disc is setup initially following Equation (4.1) and has 10^6 stellar particles. The total mass of the halo inside $5R_{\rm S}$ is $\sim 1.6\times10^{11}M_{\odot}$, while the mass of the disc inside $5R_{\rm S}$ is $\sim 9\times10^{9}M_{\odot}$. The dynamics of the central disc is therefore dominated by the dark matter halo as expected. Due to the high-Q profile of the stellar disc, the swing amplification is weak. We therefore do not need higher number of particles to prevent transient gravity-induced spiral structures from forming (for further details see Hu & Sijacki, 2016). The stellar disc is initially in equilibrium with a spherical halo, and as shown in Hu & Sijacki (2016) it will develop strong two-armed spirals if we put it directly into our smooth triaxial dark matter halo model. To avoid such structures and focus on the effect of subhaloes alone we have to evolve the disc inside a dark matter halo that changes adiabatically from spherical to triaxial. We change the halo in a way similar to Section 3.3 in Hu & Sijacki (2016). Namely, we start the simulation with the spherical part of the halo only, while the triaxial part of the halo grows adiabatically with time, where the total potential of the halo is

$$\Phi(r,\theta,\phi) = \Phi_{\rm S}(r) + f(t)\Phi_{\rm T}(r,\theta,\phi)\,. \tag{4.5}$$

Here $\Phi_{\rm S}$ is the static spherical part, $\Phi_{\rm T}$ is the triaxial part and the growth factor $f(t)$ changes from 0 to 1 following

$$f(t) = (1-\frac{1}{6}{\rm e}^{-t/\tau_{\rm I}}(1+5{\rm e}^{-t/\tau_{\rm I}}))^6\,, \tag{4.6}$$

where we have set timescale $\tau_{\rm I} = 1\,$Gyr as in our previous work. We evolve the system for 5 Gyr and find no prominent structures in the disc. The surface density of the final stellar disc is shown in the top left panel of Figure 4.4.

4.2.4 Phase-3: Simulating Live Stellar Disc in Static Triaxial Dark Matter Halo with Live Subhaloes

With the halo and the disc setup in Phase-1 and Phase-2, we are now able to perform our final simulation starting from $z = 1$ that studies the influence of subhaloes on the stellar discs. In this simulation, three components are included:

- A static, triaxial dark matter potential. We include it rather than live dark matter particles because it will save some computational resources and more importantly it will not induce numerical perturbations in the disc due to the Poisson noise (note that due to very different spatial scales of the disc and the halo, dark matter particle mass

would need to be considerably larger than the disc particle mass), thus making it much more robust to study the influence of subhaloes only.

- Live subhaloes. The live subhalo particles are taken directly from the Phase-1 simulation at $z = 1$. As mentioned earlier, they consist of particles that are gravitationally bound to any subhalo of our main halo at $z = 1$ or at any later time, based on the SUBFIND algorithm. In this way we ensure that there is a realistic number of subhaloes during the whole period of the Phase-3 simulation. We have in total 2,035,019 live dark matter particles included, each having a mass of $m_{\rm DM} = 3.93 \times 10^5\,{\rm M}_\odot$.
- A live disc. The live disc is taken from the Phase-2 simulation at 5 Gyr. As explained above, it is in equilibrium with the triaxial dark matter potential, and no prominent spiral structures exist in the disc.

4.3 Results

4.3.1 Properties of Subhaloes that Interact with the Disc

The column density of dark matter at $z = 1$ is shown in the top row of Figure 4.2. Outside of the main halo there is a large number of subhaloes that may fall in at a lower redshift. A zoom-in view of the column density of all subhaloes in the Phase-3 simulation at $z = 1$ is shown in the middle row of Figure 4.2. From all these subhaloes we select the ones that interact with the disc based on the following criteria: *a)* their impact radius r is less that $5\,R_{\rm S}$, *b)* their mass exceeds $10^9\,{\rm M}_\odot$. There are more subhaloes that either hit the disc plane further out or have a lower mass, but we filter them out as they play a minor role in the development of spiral structures in the disc as we have explicitly checked (see e.g. Appendix 4.D). The properties of impacting subhaloes based on our criteria above are listed in Table 4.1. They hit the disc at various redshifts from $z = 1$ to $z \sim 0.4$ and have different angle of incidence and rotation direction. Generally, as expected, subhaloes that are further away from the centre of the halo hit the disc at a lower redshift. We indicate their initial locations at $z = 1$ in the first two rows of Figure 4.2 with different letters, and we plot their trajectories once close to the disc in the bottom row of Figure 4.2, along with the column density of the disc.

The impact radius $R_{\rm i}$ is typically between $0.7R_{\rm S}$ and $2.9R_{\rm S}$. The half-mass radius of the subhaloes at the time of maximum mass before the impact is lower than the impact radius for all subhaloes except for subhalo C and G, for which $R_{\rm hm}$ and $R_{\rm i}$ are comparable. However, note that at the time of impact, the half-mass radius decreases to 10-40% of its maximum value before the impact as a result of tidal stripping, which means that at the

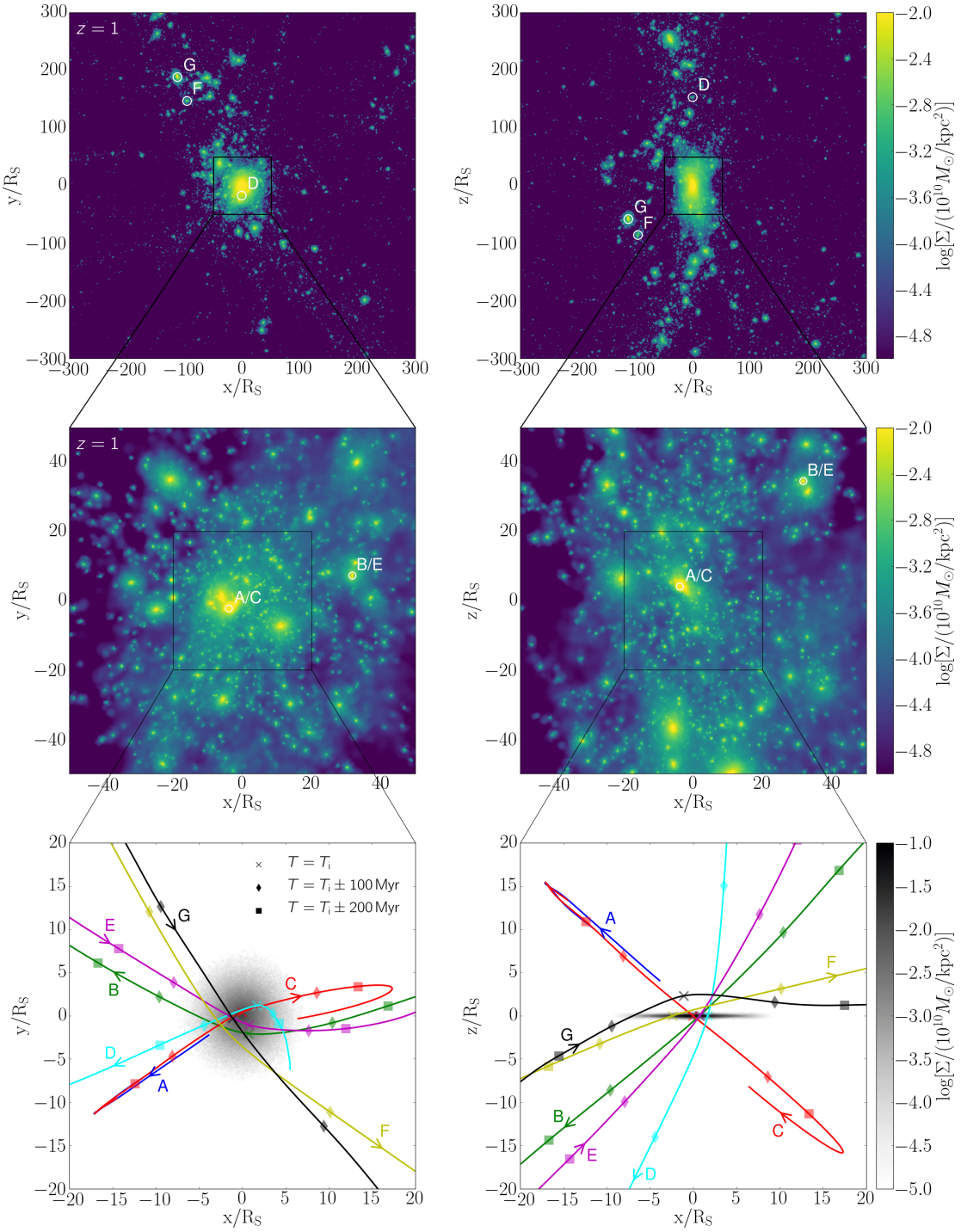

Fig. 4.2 Distribution of dark matter in x-y plane (left) and x-z plane (right). Plots in the top row show the column densities of all dark matter particles at $z = 1$. Plots in the middle row show the column densities of all subhalo particles in the inner halo region at $z = 1$. Different letters indicate the initial position of different subhaloes which interact with the disc at a later time. Plots in the bottom row show the trajectories of the subhaloes that interact with the disc (see Table 4.1). In particular, subhaloes A and C are the same subhalo hitting the disc at two different redshifts, so are subhaloes B and E. The location of subhaloes at the time of impact is marked with crosses, while location at 100 Myr before and after the impact is marked with diamonds and at 200 Myr with squares. The column density of the stellar disc is also shown in the bottom row for comparison.

Table 4.1 Subhaloes that interact with the disc in the Phase-3 simulation. Redshift of maximum mass before the impact, $z_{\max}$, maximum mass before the impact, $M_{\rm sub}$, half-mass radius at the time of maximum mass before the impact, $R_{\rm hm}$, redshift of impact, $z_{\rm i}$, radius of impact, $R_{\rm i}$, the angle of incidence, $\theta_{\rm in}$ and the rotation direction is listed. The half-mass radius and the impact radius is shown in units of the scale length of the disc, $R_{\rm S} = 3.13\,{\rm kpc}$. The angle of incidence is defined as the angle between the trajectory and the normal direction of the disc. When $\theta_{\rm in} > 90$, the subhalo hits the disc from below. For rotation direction, "R" stands for retrograde, while "P" stands for prograde.

id	$z_{\max}$	$M_{\rm sub}$ $[10^{10}{\rm M}_\odot]$	$R_{\rm hm}$ $/R_{\rm S}$	$z_{\rm i}$	$R_{\rm i}$ $/R_{\rm S}$	$\theta_{\rm in}$	rotation direction
A*	1.22	1.63	1.28	1.02	1.81	57	R
B	0.99	0.37	1.85	0.87	2.19	132	R
C	0.95	0.53	1.28	0.80	0.70	129	R
D	0.76	0.14	1.93	0.46	2.12	165	P
E	0.80	0.12	1.57	0.42	1.63	44	P
F	0.46	0.13	1.20	0.37	2.85	78	P
G†	0.47	4.8	6.39	0.39	-	-	P

*At the start of the simulation, subhalo A is very close to the disc and moving away from it. Based on its velocity we estimate that it hits the disc at $z = 1.02$.

†As shown in Figure 4.2, subhalo G moves through the disc plane about $10R_{\rm S}$ away from the disc centre, therefore it is not considered as a close impact. However, thereafter subhalo G flies over the disc, largely parallel to it, at a distance of less than $3R_{\rm S}$, which has a substantial influence on the disc. We therefore include subhalo G in this table but omit its impact radius and the angle of incidence. The impact redshift $z_{\rm i}$ is defined as the redshift when subhalo G is closest to the centre of the main halo.

time of impact, the subhaloes should be considered as objects of relatively small size. It is therefore a reasonable estimate to consider an impacting subhalo in our simulation as a point mass.

A closer look at each subhalo reveals that there are in fact only 5 subhaloes in the 7 subhalo events, as subhalo A and C are the same subhalo hitting the disc twice, so are subhaloes B and E. It is also worth noting that subhalo A does not hit the disc during the Phase-3 simulation. It goes through the disc at $z = 1.02$, before the beginning of the Phase-3 simulation, and at the start of Phase-3, it is located very close to the disc, moving away from it. Subhalo G does not hit the disc within $5R_{\rm S}$, but crosses the disc plane further away from the disc centre. However, it is very close to the disc at $z \sim 0.4$ passing over the disc at a distance of no more than $3R_{\rm S}$, as shown by the black curve in the bottom row of Figure 4.2.

As mentioned in Section 4.2.4, an analytic dark halo potential is employed in the Phase-3 simulation instead of a live dark matter main halo. To study its influence on the subhaloes and understand if it is biasing our results in any way, we compared the mass loss and trajectory of each subhalo listed in Table 4.1 in the Phase-3 simulation with its counterpart in the Phase-1

simulation, where a live main halo is present (but not a live stellar disc). We find that the mass loss of each subhalo at the moment of impact is similar between the two simulations, ranging from 50% to 80% (for further details see Appendix 4.E). The mass loss is mainly induced by tidal disruption in both simulations. We also note that due to dynamical friction, the subhaloes in the Phase-1 simulation move slower than those in the Phase-3 simulation, which delays the time of the impact by up to 1 Gyr, but subhaloes have comparable velocities at impact and spend similar amounts of time in the vicinity of the disc. Therefore, with respect to the properties of subhaloes, using an analytic main halo potential instead of a live dark matter main halo should not affect our results below.

4.3.2 Disc Heating in Response to Subhaloes

As the subhaloes interact with the disc its properties change, as shown in Figure 4.3, especially at later times when the massive, fly-by subhalo G interacts with the disc. The spherically averaged surface density of the disc (top left panel) fluctuates in the outer region due to strong spiral and ring structures caused by subhaloes. In the innermost region, the density of the disc grows mildly at later times as a bar gradually forms. Top middle panel shows the radial profile of Toomre's Q parameter which is defined as

$$Q = \frac{\sigma_{\rm R}\,\kappa}{3.36\,G\Sigma}\,, \tag{4.7}$$

where $\sigma_{\rm R}$ is the velocity dispersion in the radial direction, $\kappa = \frac{2\Omega}{R}\frac{\rm d}{{\rm d}R}(R^2\Omega)$ is the epicyclic frequency (with Ω being the rotation angular velocity of stars), G is the gravitational constant and Σ is the surface density. Toomre's Q parameter quantifies how strong the swing amplification is in the disc. We found in Hu & Sijacki (2016) that the disc is stable to swing amplification of the Poisson noise when $Q > 1.3$ throughout the disc, thus we ensure this is the case for our initial setup (see blue curve at $z = 1$).

In our Phase-3 simulation Toomre's Q parameter increases in the outer region of the disc after $z \sim 0.5$, which can be explained by the significant increase of the velocity dispersion in the radial direction, $\sigma_{\rm R}$, shown in the bottom left panel of Figure 4.3. The velocity dispersion in the other two directions, σ_φ and $\sigma_{\rm z}$, also increases similarly (see bottom middle and right panels). This is caused by the interaction of the disc with subhalo G, as we will discuss in detail in Section 4.3.6.

We quantify the thickness of the disc, $z_{\rm h}$, by computing the standard deviation of the z coordinate of stellar particles, i.e. $z_{\rm h} = \sqrt{\langle z^2\rangle - \langle z\rangle^2}$. The fly-by subhalo G leads to strong warp structures in the disc, which causes the disc thickness, $z_{\rm h}$, to increase significantly at later times, as shown in the top right panel of Figure 4.3. Further smaller mass subhaloes

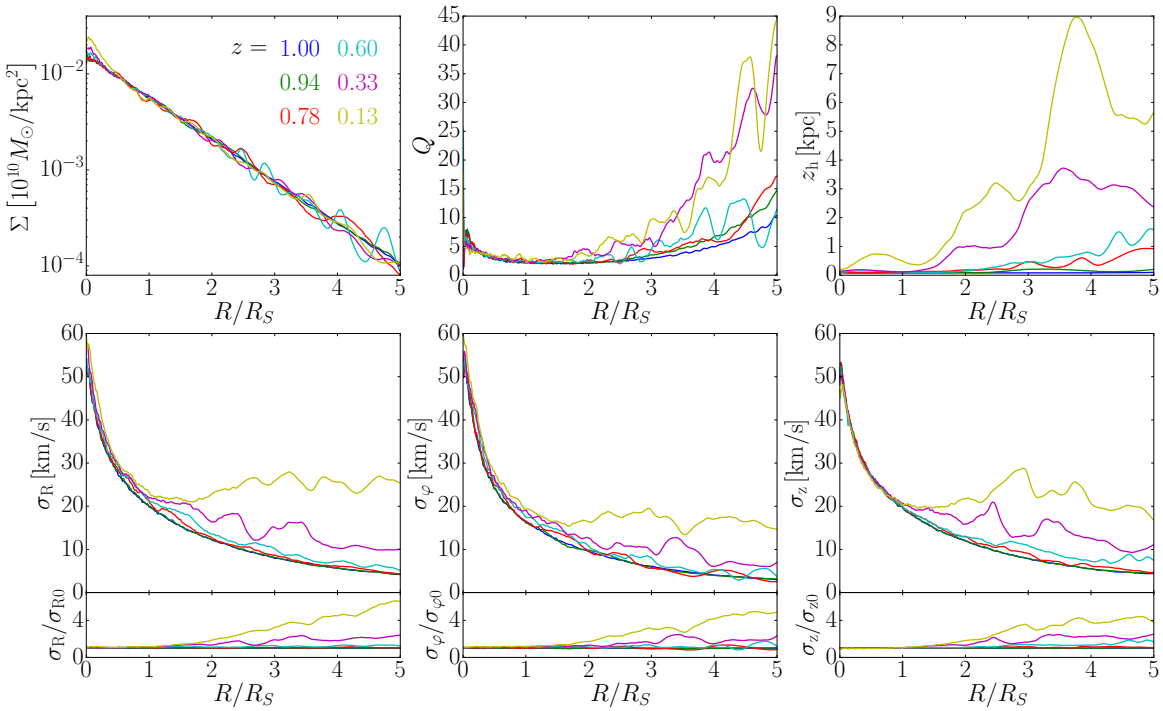

Fig. 4.3 The time evolution of disc's surface density, Σ, Toomre's Q parameter, disc thickness, $z_\mathrm{h} = \sqrt{\langle z^2 \rangle - \langle z \rangle^2}$, and velocity dispersion in the radial, azimuthal and vertical direction, σ_R, σ_φ and σ_z, respectively. The surface density of the disc fluctuates in the outer region and increases somewhat in the innermost region at later times. The Toomre's Q parameter increases significantly in the outer region, i.e. for $R \gtrsim 2R_\mathrm{S}$, which can be explained by the increase of σ_R. Warp structures develop in the disc after $z = 0.5$, leading to a large increase of the disc thickness in the outer region.

interact with the disc in the wake of subhalo G which increases the disc thickness further from $z = 0.33$ to $z = 0.13$. Note that all of the examined disc properties are affected by the subhaloes primarily in the outer regions, while in the innermost disc region, i.e. for $R < 2R_\mathrm{S}$, these global disc properties change much less. This is not the case for the modes triggered in the disc which we discuss in the section below.

4.3.3 Modes in the Disc Triggered by Subhaloes

The interaction of subhaloes with the stellar disc leads to the development of spirals, rings, warps and bars. Figure 4.4 shows the time evolution of the surface density (top panels) and the residual surface density (bottom panels) from $z = 1$ to $z = 0.13$. By construction, the disc is free of spiral structures at $z = 1$ and it is slightly elliptical due to the triaxial dark matter halo. Thereafter, at least three distinct episodes of single-armed spiral structures appear

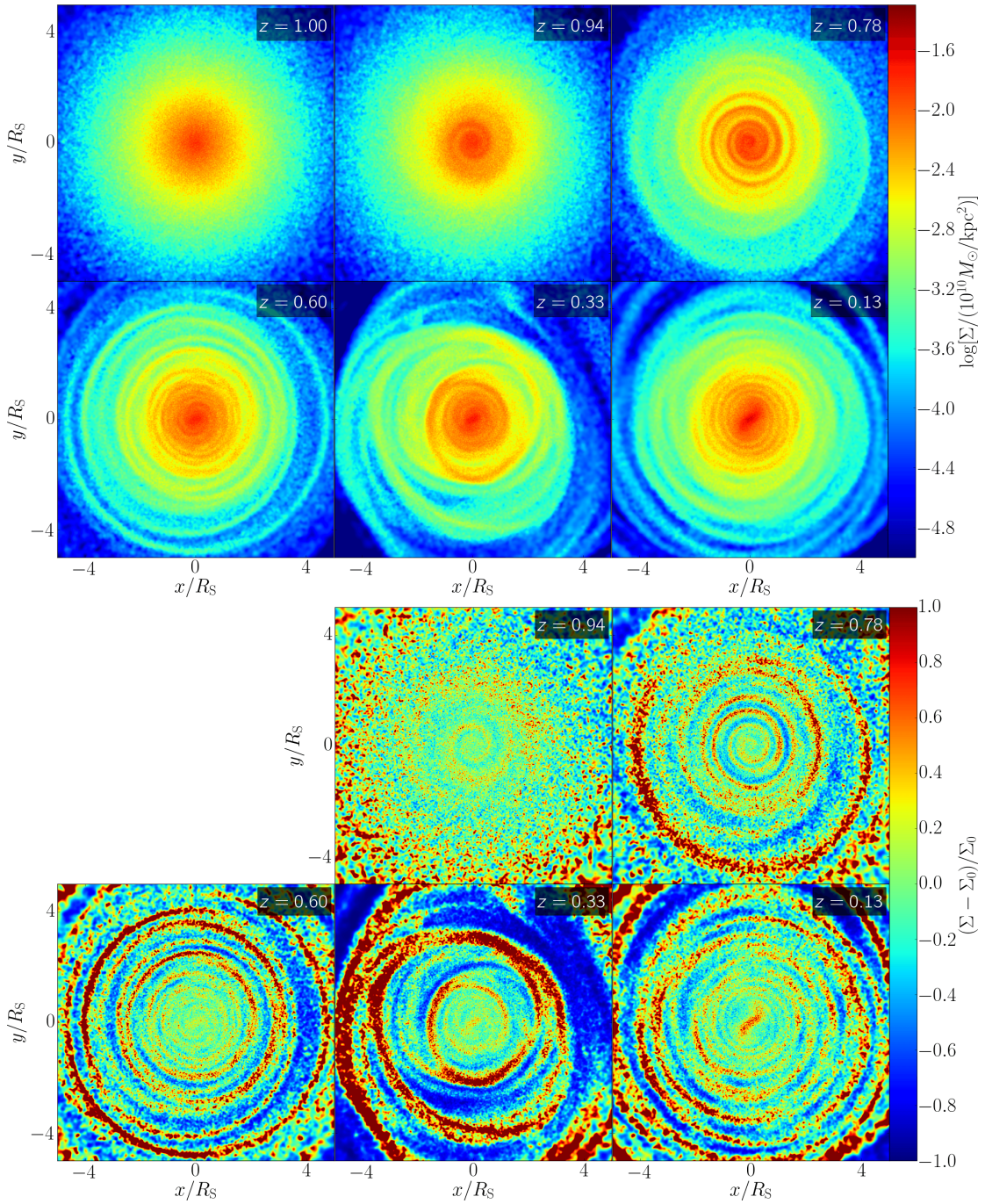

Fig. 4.4 The evolution of the surface density Σ (top panels) and the normalized residual surface density $(\Sigma-\Sigma_0)/\Sigma_0$ (bottom panels) at different redshifts, where Σ_0 is the surface density at $z=1$. Single-armed spiral structures develop very quickly in the disc centre and they are counter-rotating and trailing. These initial spiral structures wind up over time as the second episode of spirals forms in the disc at $z=0.78$. Newly formed single-armed spiral structures wind up as well and become weaker at $z=0.60$, when the two-armed spiral structures start to become apparent in the disc centre. The disc stays quiet for a while until $z=0.33$, when a strong perturbation by subhalo G disturbs the disc in the outer region. This significantly warps the disc and generates the central bar. For $z<0.2$ spirals wind up and weaken. The disc recovers to a quasi-stable state overtime and at $z=0.13$, two-armed spiral structures are visible again in the central region of the disc.

in the disc: one shortly after the beginning of the simulation, one at $z \sim 0.78$, and one at $z \sim 0.33$. These single-armed spiral structures are counter-rotating and trailing, which we study in detail in Section 4.3.4. Two-armed spiral structures also develop in the disc and are clearly visible when the single-armed spirals wind up, namely at $z \sim 0.60$ and at $z \sim 0.13$. Both single-armed and two-armed spiral structures extend from the centre of the disc to the edge of the disc when fully developed. While disc remains largely axisymmetric during most of the simulated time, at $z \sim 0.33$ the interaction with the very massive subhalo G causes warps, rings, and lopsidedness in the disc, and the formation of the central bar. At lower redshifts, spirals wind up and weaken and the disc then evolves towards a more axisymmetric and quasi-stable state. Note that the strength of different modes in the disc can be quite high, especially in the outer regions, as can be seen from the bottom panels, and we turn to quantify this next.

The time evolution of the strength of $m = 1$ (left panel) and $m = 2$ (right panel) modes is shown in Figure 4.5. Here the strength of the modes is the relative strength of the Fourier

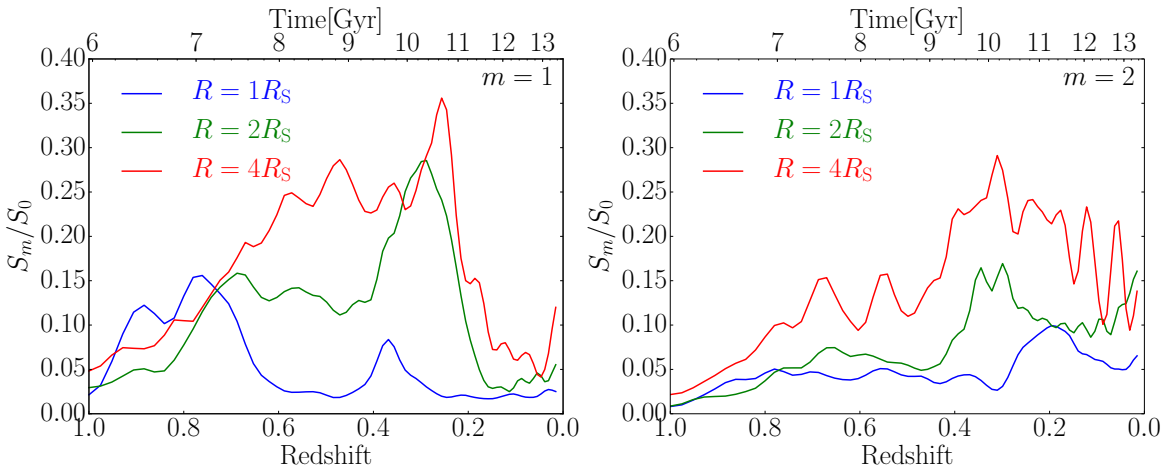

Fig. 4.5 Strength of the modes in the disc as a function of time evaluated at 1, 2 and $4R_S$ for $m = 1$ modes (left panel) and $m = 2$ modes (right panel). Here the relative strength S_m/S_0 is shown, where S_m is defined in equation (4.8). S_0, the strength of $m = 0$ modes, is the spherically averaged surface density at radius R by definition. For the $m = 1$ case, multiple generations of modes are triggered over time, first one at $z \sim 1$, second one at $z \sim 0.78$, and third one at $z \sim 0.33$. Distinct generations of modes can be better identified in the inner than the outer region, as the winding time for the inner region is much shorter such that the different generations of modes do not interact significantly. The third generation of modes is also prominent in the $m = 2$ case.

transform of the surface density $\Sigma(R,\theta)$ of the disc over the azimuthal coordinate θ, i.e.,

$$S_{\rm m}(R) = \left| \frac{1}{2\pi} \int_{-\pi}^{\pi} \Sigma(R,\theta) e^{-im\theta} d\theta \right| , \tag{4.8}$$

where m is the number of folds of the structure. For $m = 0$, S_m is simply the average surface density of a ring in the stellar disc at radius R. As expected, the evolution of $m = 1$ modes at $R_{\rm S}$ correlates with Figure 4.4 very well, showing three distinct episodes of modes from $z = 1$ to $z = 0$. The estimated life time for each of the three episodes of spirals, measured by the full width at half maximum, is $\sim 1\,$Gyr. Therefore, to have persistent single-armed spirals in the stellar disc, there should be every few Gyr massive enough subhaloes hitting the stellar disc. For the outer region of the disc at $2R_{\rm S}$ and $4R_{\rm S}$, similar generations can also be found, but less distinctively. This is because: *a)* more (smaller) subhaloes hit the outer region of the disc, leading to a noisier evolution history of the mode strength, and *b)* the life time of each episode of modes is longer due to the much lower winding rate, as shown later in Section 4.3.4. $m = 2$ modes generally have lower strength and are less distinctive, due to their even slower winding rate. Nevertheless, strong $m = 2$ modes are generated at $z \sim 0.35$, corresponding to the third episodes of $m = 1$ modes. We will explore the connection between different modes generated in the disc and individual subhaloes in Section 4.3.5.

4.3.4 Nature of the Spiral Structures

We now turn to study the nature of the spiral structures by looking at their power spectra. As explained in detail in Hu & Sijacki (2016), the power spectra of the stellar disc are the Fourier transforms of the disc's surface density over time and the azimuthal coordinate. The power spectra of the density field are typically plotted in the pattern speed-radius plane for each mode. If the power contour follows the Lindblad resonance, the spiral structures are kinematic density waves (Lindblad, 1963), while if the power spectra show patterns of horizontal bars between the inner and outer Lindblad resonance, the spiral structures are related to self-gravity (Sellwood & Carlberg, 2014).

The power spectra of our stellar disc in the Phase-3 simulation are shown in Figure 4.6. Here we plot the power spectra for $m = 1$ (left panels) and $m = 2$ (right panels) modes for the redshift ranges of $0.5 < z < 1$ and $0 < z < 0.5$. The first redshift range corresponds to the first two episodes of spirals, while the second redshift range corresponds to the third episode of spirals.

We plot the power for $m = 1$ modes in negative pattern speed because the single-armed spirals are found to be counter-rotating (i.e. to have negative pattern speed). In fact, the inner Lindblad resonance $\Omega_{\rm r} - \kappa/m$ is also negative for $m = 1$ modes. As shown in the left panels

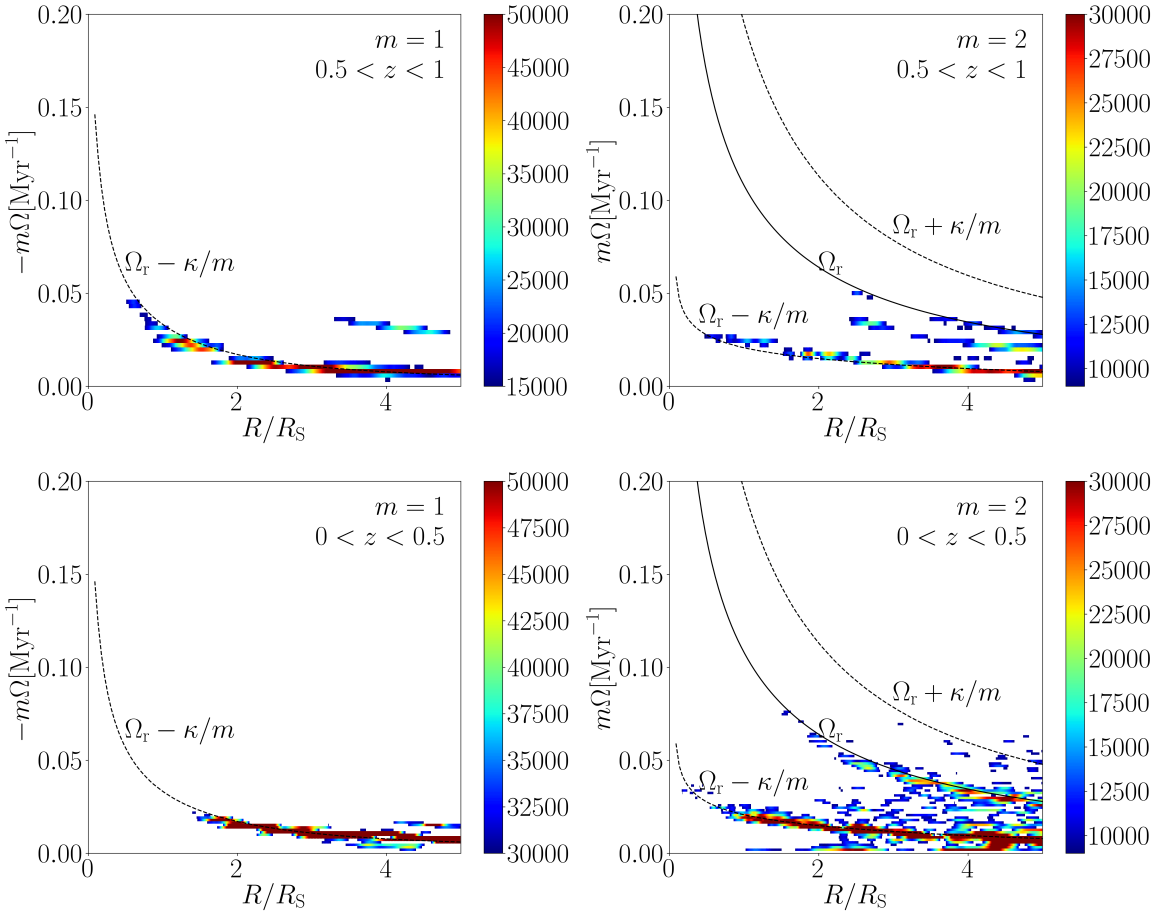

Fig. 4.6 Power spectra of the $m = 1$ (left panel) and $m = 2$ (right panel) modes for the time intervals from $z = 1$ to $z = 0.5$ (top panels) and from $z = 0.5$ to $z = 0$ (bottom panels). For $m = 1$ modes, the power of rotating patterns is shown in the $-m\Omega$-R plane, where $-m\Omega$ is negative pattern speed multiplied by the number of modes m and R is the radius from disc centre. For $m = 2$ modes, the power is shown in the $m\Omega$-R plane. The co-rotation curve Ω_r is plotted with a solid curve, while the Lindblad resonances $\Omega = \Omega_r \pm \kappa/m$ are plotted with dashed curves, where Ω_r is the rotating speed of stars and κ is the epicyclic frequency. It can be seen that power spectra follow closely the inner Lindblad resonance both for $m = 1$ and $m = 2$ modes, indicating the kinematic density wave nature of the modes. The power of patterns between $z = 0.5$ and $z = 0$ is stronger than that between $z = 1$ and $z = 0.5$, which agrees with Figure 4.4 and 4.5.

in Figure 4.6, at all radii the highest power follows closely the inner Lindblad resonance, indicating that the modes in the disc are indeed kinematic density waves. We should always expect grand-design single-armed spiral structures of this kind to be counter-rotating as long as $\kappa > \Omega_r$.

For $m = 2$ modes, the power spectra are weaker than in the case of $m = 1$ modes, in agreement with Figure 4.5. The highest power of $m = 2$ modes also follows the inner Lindblad resonance closely. There are other weaker powers away from the inner Lindblad resonance, which should be relevant to other weaker resonances. The winding rate of spiral structures depends on the slope of the Lindblad resonance curve, which is much steeper for $m = 1$ modes than the generally flat inner Lindblad curve for $m = 2$. This explains why the life time of the single-armed spiral structures, typically less than 2 Gyr, is lower than the life time of two-armed spiral structures studied in Hu & Sijacki (2016).

In combination with Figure 4.4 which demonstrates that two-armed spiral structures become prominent almost always after the winding of single-armed spirals, we conclude that subhaloes trigger both $m = 1$ and $m = 2$ modes in the disc simultaneously, but with $m = 1$ modes initially stronger than $m = 2$ modes. In the inner disc, the winding rate of the $m = 1$ modes is much faster than that of the $m = 2$ modes, leading to a much quicker decrease of the strength of the $m = 1$ modes. $m = 2$ modes, winding up much slower, become prominent after $m = 1$ modes wind up.

We also search for the self-gravitating spiral modes for higher m values. The typical strength of these modes is more than one magnitude lower than that of the kinematic modes. This is expected as the disc has high Toomre's Q parameter.

4.3.5 The Impact of Each Halo

We now aim to establish a direct link between different modes generated in the disc and the individual subhaloes that interact with the disc. We start by studying the first generation of modes (i.e. $0.85 < z < 1$). These modes develop immediately after the simulation starts, which is the time when subhalo A is very close to the disc centre. As mentioned in Section 4.3.1, subhalo A is moving away from the disc at the start of the simulation. To study the relation between subhalo A and the first generation of modes, we restart the Phase-3 simulation with the subhalo A removed[1]. As highlighted by the light blue region in Figure 4.7, when the subhalo A is removed, $m = 1$ modes before $z = 0.85$ at $1\,R_S$ seen in the original simulation essentially no longer develop. For $R = 2\,R_S$ and $R = 4\,R_S$ we see similar decrease in mode strength, but compared to $R = 1\,R_S$, the influence of removing subhalo A persists longer because the winding rate of $m = 1$ modes at $1\,R_S$ is much higher than that of the outer region.

[1]To modify the mass of subhalo A (and other subhaloes), we do the following. We first find the redshift where the subhalo has the maximum mass before the impact. We find all particles belonging to the subhalo at this redshift, and change their mass in the initial conditions. We then restart the simulation to see the impact of changed mass.

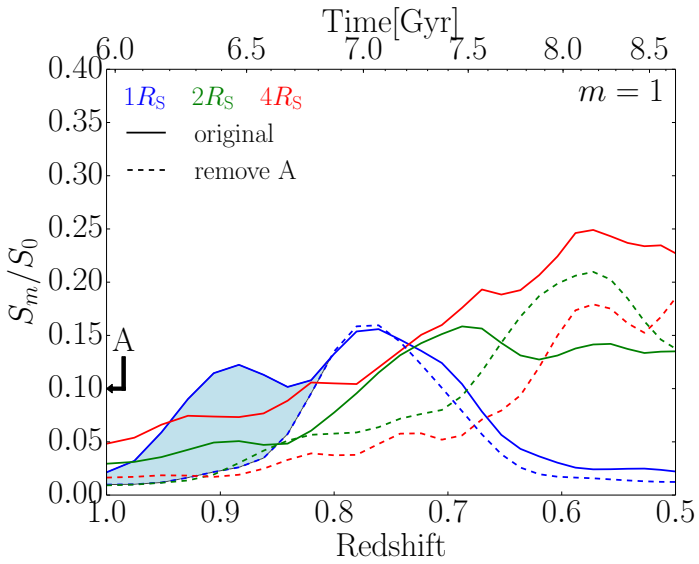

Fig. 4.7 Comparison of the strength of the modes in the original simulation (continuous curves) and a simulation where subhalo A is removed (dashed curves). As highlighted with a light blue shade, when the subhalo A is removed, no prominent modes form between $z = 1$ and $z = 0.85$ at $1\,R_S$. This is also true at 2 and $4\,R_S$, indicating that the first generation of modes is caused by the impact of subhalo A.

The second generation of modes at $1\,R_S$ develops between $z \sim 0.87$ and $z \sim 0.6$, which coincides with the time of impact of subhaloes B and C. Recall that subhalo C is the same subhalo as A, whose influence on the second generation of modes can be studied with Figure 4.7. By removing subhalo A/C, the strength of the second generation of modes at $1\,R_S$ reduces only slightly for $0.6 < z < 0.75$. To study the influence of subhalo B, we first restart the original simulation with subhalo B removed. The result is shown with the dashed curves in Figure 4.8. As highlighted by the light blue region in the left panel, the strength of the second generation of $m = 1$ modes at $1\,R_S$ decreases greatly when subhalo B is removed, while a mild decrease can be found at $2\,R_S$. For $m = 2$ modes, even though the original spiral strength is low, we can still find a mild decrease in the spiral strength once subhalo B is removed. Thus, the subhalo B is the main cause of the second generation of modes with the subhalo A/C contributing at a lower level.

Subhalo B starts from more than $40\,R_S$ away from the disc centre and is mainly responsible for the second generation of modes, offering us a good test for studying the influence of subhalo properties, especially the subhalo mass, on the modes triggered in the disc. We hence find all dark matter particles that belong to subhalo B in the initial conditions, modify their mass, and restart the simulation. We run several simulations with different mass of

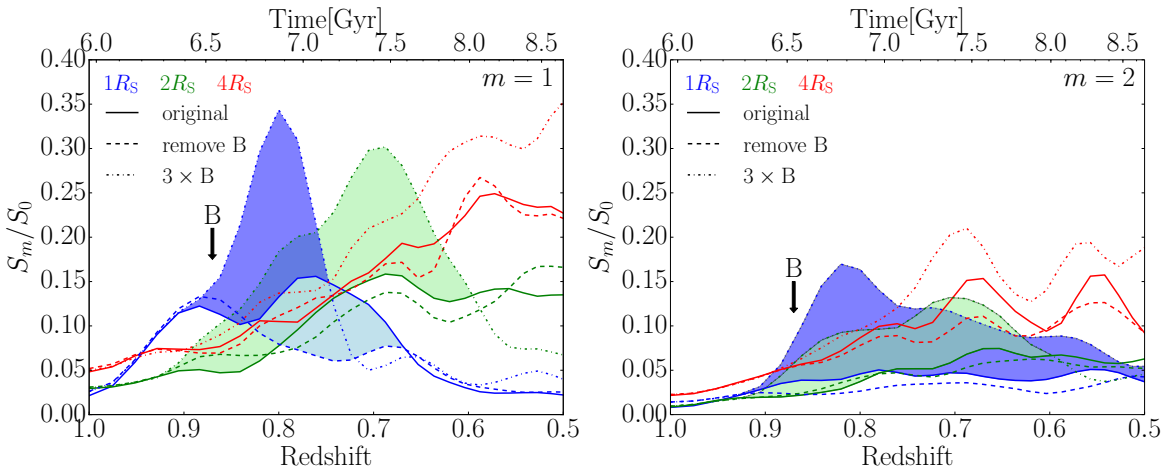

Fig. 4.8 Comparison of the strength of the modes in the original simulation and simulations where either subhalo B (which hits the disc at $z = 0.87$) is removed or its mass is tripled. When subhalo B is removed, the second generation of $m = 1$ modes does not form at $1R_S$, as highlighted by the light blue region, indicating that subhalo B is the main cause of these modes. When the mass of subhalo B is tripled, the strength of both $m = 1$ and $m = 2$ modes is increased, as highlighted by the dark blue region for $1R_S$ and by the green region for $2R_S$. Note that in the simulation with the tripled mass $m = 2$ modes become dominant in central region for $z < 0.75$ (see also Figure 4.9).

subhalo B, including 1.5, 2 and 3 times the original subhalo B mass. [2] The strength of modes when the mass of subhalo B is tripled is shown as dot-dashed curves in Figure 4.8 (other simulations with a lower subhalo B mass give consistent results which lie in between the original subhalo B mass and the tripled mass). We see a clear increase in mode strength for both $m = 1$ and $m = 2$ modes at $1R_S$ (highlighted with the dark blue shade) and $2R_S$ (highlighted with the green shade). We note that for $m = 2$ modes, unlike in the original simulation, strong two-armed spiral structures now develop. This confirms that although the two-armed spiral structures are very weak in the original simulation, they are indeed triggered by the impact of the subhalo B. At $4R_S$ the strength of modes also increases with the higher mass of subhalo B, and the influence remains for several Gyrs.

It is also worth noting that although both $m = 1$ and $m = 2$ modes at different radii start to develop at almost the same time, mode strength at $1R_S$ always reaches its peak before that at $2R_S$. This is caused by their different winding rate. When the mass of subhalo B is tripled,

[2] To increase the mass of subhaloes we increase the mass of each particle in the simulation, which increases the gravitational force within the subhalo, resulting in a immediate shrinkage in the size of the subhalo. We argue that the shrinkage is acceptable because *a)* the maximum shrinkage in spatial scale is about 30%. At the time of impact, the half-mass radius is already small (typically less than $\sim 0.3R_S$). The impact of the size change is therefore negligible, and *b)* we are more interested in the response of the disc to subhaloes of different masses, where the spatial scale of the subhalo plays a minor role.

the second generation of $m = 1$ modes reaches its peak strength $\sim 0.2\,\mathrm{Gyr}$ earlier than in the original simulation at $1\,R_\mathrm{S}$. We verify that when the mass is tripled, the trajectory of subhalo B does not change significantly. Instead, subhalo B interact with the disc earlier because its gravitational force field is stronger and can exert a torque on the disc earlier.

The increase in the strength of both $m = 1$ and $m = 2$ modes is also illustrated in Figure 4.9, where a comparison of the surface density of the original simulation and of the simulation with 3 times subhalo B mass is shown. Similar to the original simulation, single-armed spiral structures are visible first in the simulation with the tripled mass, while two-armed spiral structures can be seen after the single-armed spiral structures wind up. At $z = 0.84$, the single-armed spiral structures with tripled subhalo B mass are much more prominent than that in the original simulation, extending from the centre of the disc to $\sim 2R_\mathrm{S}$. The single-armed spiral structures propagate outwards from $z = 0.84$ to $z = 0.78$. In the outer region, lopsided rings also form. This effect is similar to ring galaxies. As shown by Lynds

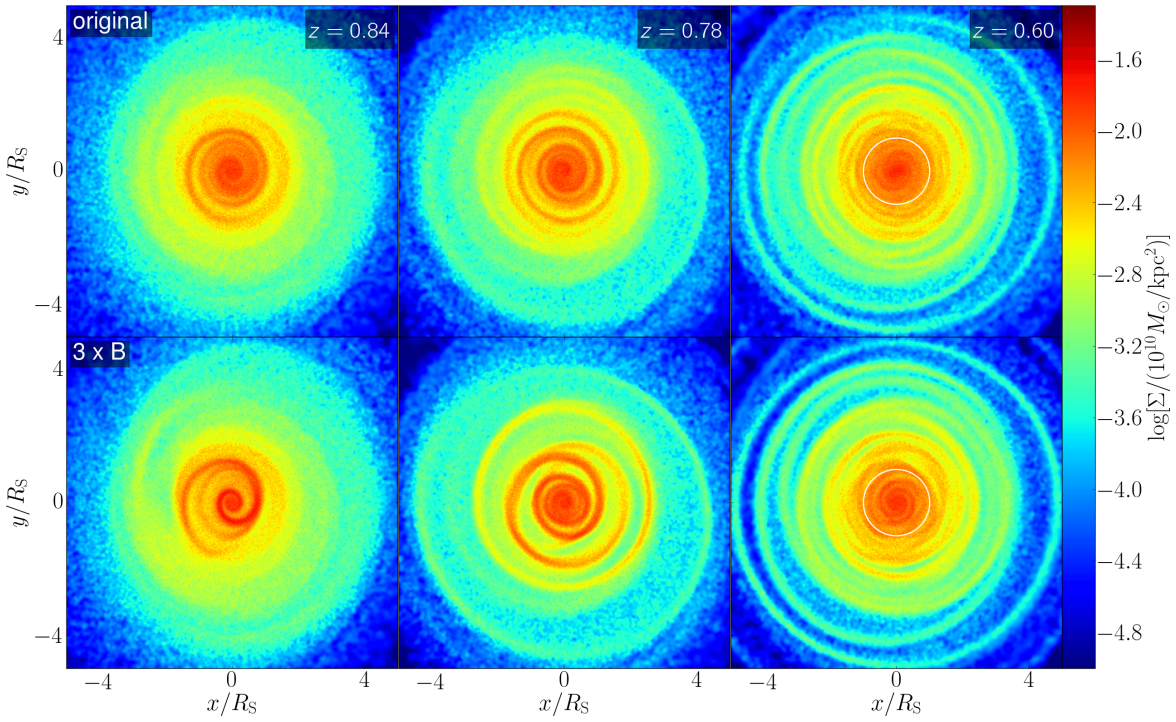

Fig. 4.9 Surface density of the stellar disc in the original simulation (top panels) and the simulation where the mass of subhalo B is tripled (bottom panels). More massive subhalo B leads to very strong modes immediately after it hits the disc. Additionally to the spirals, strong ring structures also develop at $z = 0.78$ in both simulations. When the single-armed spirals wind up at $z = 0.60$, two-armed spiral structures become prominent in the disc centre, as highlighted by the white circles in the right panels. The two-armed spiral structures are more prominent when the mass of subhalo B is increased, in line with Figure 4.8.

& Toomre (1976), vertical impact of a massive point mass perturber can lead to such features. $m = 1$ modes soon wind up, and at $z = 0.60$, very prominent two-armed spiral structures are in the centre of the disc.

We also check that subhaloes A/C and B are indeed the main cause of all modes studied so far by removing both subhalo A and B. As shown in Figure 4.13, almost all modes are removed up to $z = 0.7$. Though there are less massive subhaloes that hit the disc during this period, the evolution of the disc is dominated by these massive subhaloes only. We have similarly removed subhalo D, E and F, but no prominent change in spirals is found. We conclude the mass of these subhaloes is too small to have an appreciable effect. This is confirmed by an additional simulation (see Section 4.3.6), where we increase the mass of subhalo D by a factor of 10 and find that it causes spiral structures in the disc.

4.3.6 Influence of the Fly-by Subhalo

As shown in Table 4.1 and in the bottom panels of Figure 4.2, subhalo G passes very close over the disc plane at $z \sim 0.39$ and as we have anticipated in previous sections it perturbs the disc significantly. We restart the original simulation with subhalo G removed to isolate its impact on the disc more clearly. As shown with dashed curves in Figure 4.10, the strength of the third generation of $m = 1$ modes at $2R_S$ decreases by more than 50%. However, unlike direct impacting subhaloes we studied so far, no prominent difference can be seen for $m = 1$ modes at $1R_S$ at $4R_S$. For $m = 2$ modes, strength at all radii decreases after removing subhalo G. When subhalo G is closest to the disc centre, its projection on the $x-y$ plane of the disc is $\sim 1.16R_S$ away from the disc centre. As will be discussed later, the low strength of spirals in the inner region is related to the resonance effect. For $4R_S$, the $m = 1$ mode is not very effected because there are many more smaller subhaloes that interact with the outer region of the disc.

We notice that some $m = 1$ and $m = 2$ modes are still present in the disc when subhalo G is removed. We find that apart from the influence of the subhalo G, the third generation of modes also consist of: *a)* the remains of previously generated modes, *b)* structures generated by some smaller subhaloes hitting the disc, and *c)* modes triggered by "neighbours" of subhalo G that also fly over the disc at a similar time. To understand the interplay of these different effects, we remove all smaller subhaloes that hit the disc between $z = 0.3$ and $z = 0.5$. This removes the $m = 1$ modes at $1R_S$. As a second experiment, we remove subhalo G and its "neighbours", i.e. subhaloes whose initial positions and trajectories are very similar to subhalo G's. The strength of the modes at $2R_S$ for $m = 1$ and 2 and $4R_S$ for $m = 2$ decreases further, as shown in the light green and red shaded regions in Figure 4.10. We therefore

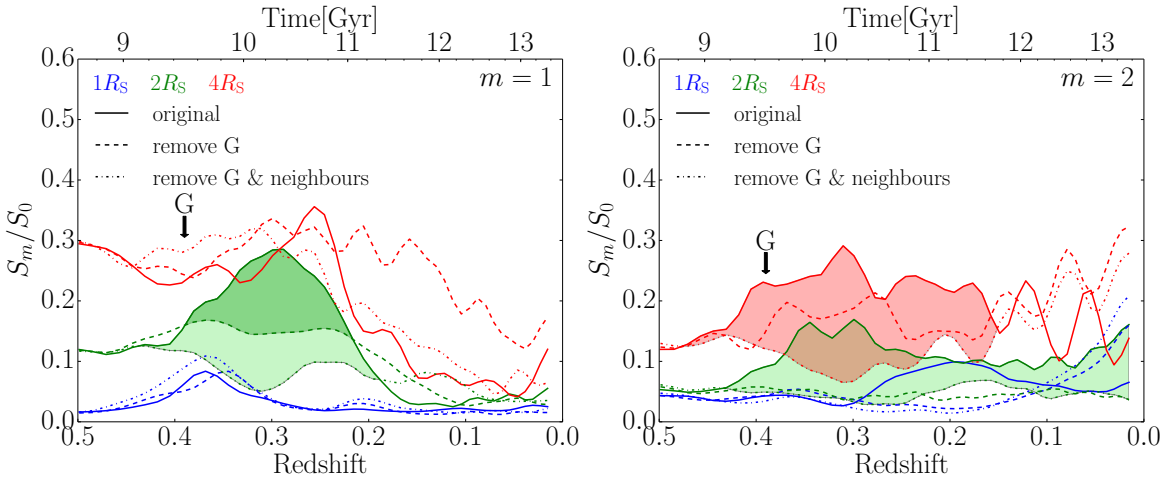

Fig. 4.10 The strength of modes in the simulation where the fly-by subhalo G is removed. We either just remove subhalo G (dashed lines) or the surrounding subhaloes as well (dash dotted lines) which have similar starting positions and subsequent trajectories. The modes at $2R_S$ are greatly reduced, as highlighted by the dark green region. When we remove the neighbouring subhaloes as well, the strength of the modes at $2R_S$ and $4R_S$ is reduced to a greater extend, as highlighted by the light green ($m = 1$ and $m = 2$) and the red ($m = 2$) shaded regions. The strength of modes at $1R_S$ is not effected significantly by the removal of subhalo G, but is caused by smaller mass subhaloes that interact with the disc.

conclude that although subhalo G makes a crucial contribution to the third generation of modes, several other subhaloes also play a role.

4.3.7 Tidally-driven Spiral Structures

For all events, including direct subhalo impacts and the fly-by subhalo interaction, single-armed spiral structures form and dissolve before two-armed spiral structures are apparent. As explained in Section 4.3.4, the longevity of two-armed spirals depends on their flat inner Lindblad resonance curve. Further to this, we find that the interaction of each subhalo with the disc is more of an impulsive nature rather than determined by resonances.

Previous simulation works with a single perturber, e.g. Toomre & Toomre (1972); Howard et al. (1993) have found that prograde perturbers lead to $m = 2$ spiral structures as the $m = 2$ inner Lindblad resonance has a prograde speed (also see Sellwood (2012) and Fouvry & Pichon (2015) for the effect of resonance scattering during secular evolution of discs.) If subhaloes interact with the disc for a long time, resonances with the same pattern speed as the subhalo's rotation angular velocity will have the strongest response. At a first glance this could be the case if we only consider subhaloes A and B. As shown in Table 4.1, subhaloes A and B are both retrograde. If they interact with the disc through resonances, modes with

negative pattern speed, i.e. $m = 1$ modes, will be strongest, which agrees with our findings above. However, we find that the typical rotational velocity of the subhaloes in our simulation is much higher than the typical pattern speed of $m = 1$ and $m = 2$ modes in the stellar disc. As a result, the interaction between subhaloes and the disc is rather impulsive, as we show next with a simulation with a massive prograde subhalo. In this simulation, we restart the Phase-3 simulation with the mass of subhalo D increased by a factor of 10, where subhalo D is prograde. If the subhalo would interact with the disc through resonances, $m = 2$ modes should be the strongest (because they have a positive pattern speed). However, we find that single-armed spiral structures still develop first and have a higher amplitude than the $m = 2$ modes. This indicates that the explanation of resonances does not hold in our simulations.

Instead of resonances, we find that the strength of the spiral structures is more related to the strength of the torque exerted by the subhalo. The torque strength on the stellar disc at radius R exerted by a subhalo is calculated in the following way. For each point on the trajectory of the subhalo, we calculate the gravitational force field $\mathbf{F}(\mathbf{r},t)$ of the subhalo, where $\mathbf{r}$ is the coordinate on the disc and t is time. For simplicity we model the subhalo as a point mass. As mentioned in Section 4.3.1, the half-mass radius of subhaloes at impact is smaller than the impact radius, so the point mass model should be sufficient for the estimation of torque strength. We then calculate the torque field in normal direction of the disc $T_{\rm z}(\mathbf{r},t)$ as

$$T_{\rm z}(\mathbf{r},t) = \left[\mathbf{r} \times \mathbf{F}(\mathbf{r},t)\right]_{\rm z} . \tag{4.9}$$

To quantify the total torque exerted by a given subhalo over its whole trajectory, we integrate the z component of the torque, $T_{\rm z}(\mathbf{r},t)$, of the subhalo over time to get

$$L(\mathbf{r}) = \int_{t_0}^{t_{\rm f}} T_{\rm z}(\mathbf{r},t)\,{\rm d}t\,, \tag{4.10}$$

where t_0 and $t_{\rm f}$ is the starting and the ending time of the impact. As the torque quickly decreases towards 0 when the subhalo is far away, the integral of the torque is not very sensitive to the choice of t_0 and $t_{\rm f}$ as long as the subhalo is sufficiently far away from the disc at both times. At a given radius R, the integrated torque strength L is a function of the azimuthal angle. We then calculate the $m = 1$ and the $m = 2$ component of the torque, L_1 and L_2, with a Fourier transformation of L over the azimuthal coordinate. The spiral strength caused by each subhalo is calculated by subtracting the corresponding peak spiral strength from the spiral strength in the matching simulation where the subhalo is removed.

We show the spiral strength as a function of the time-integrated, normalized torque strength for several subhaloes, including the original subhalo B, subhalo B with double and triple mass, subhalo D with 10 times its original mass and the fly-by subhalo G, in

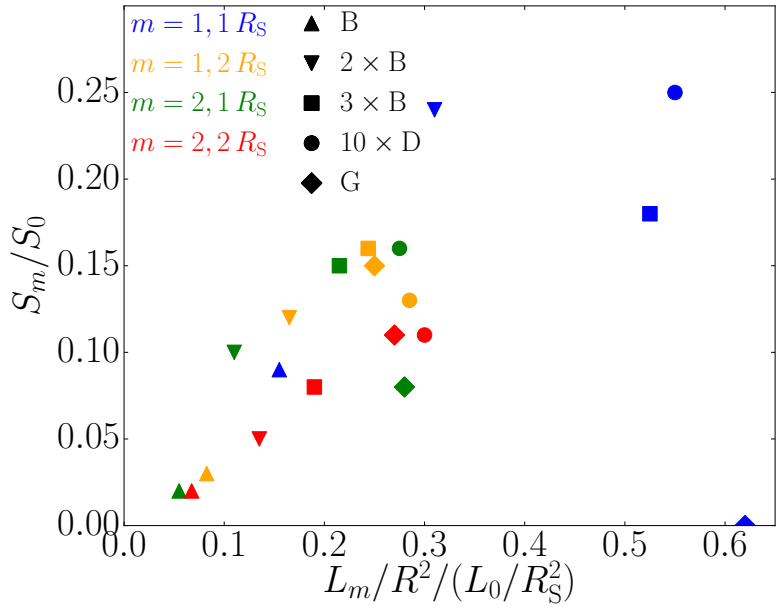

Fig. 4.11 The relation between the relative spiral strength S_m and the corresponding integrated torque strength L_m for $m = 1$ and $m = 2$ modes, where $L_0 = G(10^{10}\mathrm{M}_\odot)(\mathrm{Gyr})(\mathrm{kpc})^{-1}$ is a unit constant. Here we normalize the integrated torque strength L_m by the square of radius, R^2, to account for the fact that the angular acceleration of particles at different radii is proportional to R^{-2}. Different m modes and different radii ($1\,R_S$ and $2\,R_S$) are shown with different colours, while different symbols stand for different subhaloes, as listed in the legend. There is a good proportional relation between the spiral strength and the time-integrated torque strength across different radii and different m modes, with only a few outliers (see main text for more details).

Figure 4.11[3]. For both $m = 1$ and $m = 2$ modes at $1\,R_S$ and $2\,R_S$, the spiral strength is generally proportional to the torque strength. The only exceptions are: *a)* subhalo B with tripled mass (square symbol) at $1\,R_S$ for $m = 1$ modes, whose spiral strength is below the expected value due to a saturation effect, that is, when the strength of the torque is too high, the strength of the spiral no longer grows with the torque strength linearly due to the constraints from the disc, and *b)* the fly-by subhalo G (diamond symbol) at $1\,R_S$ for $m = 1$ and $m = 2$ modes, where the spiral strength is lower than the value expected for its torque strength. This can be understood by considering the resonance explanation, as we detail below.

The underlying reason for the strong relation between the spiral strength and the torque strength is that the time window when the subhalo exerts a strong torque on the disc is very

[3]Note that we have not included subhalo A in this analysis as it has hit the disc before the start of the simulation, thus making it more difficult to calculate the total torque.

short. Specifically, the time span for a subhalo to generate torque on the disc of more than 2% of the peak value is less than 200 Myr, except for the fly-by subhalo G, whose time span is about 400 Myr. The typical orbiting period of patterns in the stellar disc ranges from 200 Myr (for $m = 1$ modes at $1\,R_S$) to 1200 Myr (for $m = 2$ modes at $4\,R_S$). This means that for most of the cases patterns evolve for no more than one orbit during the subhalo impact.

Therefore, modes are generated and evolve in the following way: subhaloes impact the disc impulsively, triggering different m modes. Of these, $m = 1$ and $m = 2$ modes are the strongest because the torque has a strong $m = 1$ and $m = 2$ component. Between these two kinds of modes, $m = 1$ modes are dominant in the disc first partly because they have the shortest winding time, while $m = 2$ modes follow and persist longer because of their flat pattern speed curve. Another cause for stronger $m = 1$ modes lies in the fact that $m = 1$ torques are generally stronger. In fact, we have calculated the strength of $m = 1$ and $m = 2$ components of the torque on a ring in the stellar disc at a fixed radius when the subhalo is placed at different positions with respect to the ring. For most regions the $m = 1$ component is higher in strength. The $m = 2$ strength is higher only in a very small region close to the ring.

For the fly-by subhalo, the impacting time is about two times longer than that of the other subhaloes, comparable to or longer than the period of patterns at $1\,R_S$. In this particular case, resonance effects become important, leading to a spiral strength that is lower than the expected value.

4.4 Conclusion

In this paper, we studied the impact of subhaloes on the stellar disc with a series of N-body simulations based on the Aquarius simulations (Springel et al., 2008). To clearly pin down the stellar disc response to subhaloes with realistic properties extracted from the cosmological simulations, we first performed cosmological dark matter-only simulation where we have adiabatically introduced analytic stellar disc potential. We have then parameterized the main dark matter halo (both in terms of its density profile and shape and subject to the presence of the stellar disc) with an analytic potential, fixed as a function of time, while we have represented the stellar disc and all subhaloes found in the original Aquarius simulation with "live" particles. We found four massive subhaloes (subhalo A to F) that pass through the disc, two of which (subhalo A and subhalo B) hit the disc twice (labeled as subhaloes C and E). We also found a massive subhalo that does not impact the disc in the innermost regions but flies over it with a very small impact parameter (subhalo G).

In general these subhaloes cause disc heating, warping, rings, disc lopsidedness, a central bar, as well as strong single- and two-armed spiral structures. There is a significant disc heating and warping during the simulation but only at lower redshifts when the massive fly-by subhalo G passes close to the disc. This agrees well with other previous studies (e.g. Velazquez & White, 1999; Kazantzidis et al., 2009; Moetazedian & Just, 2016). Increase of the velocity dispersion leads to an increase in Toomre's Q parameter, which helps stabilize the disc from self-gravity-induced spiral structures.

Further to disc heating and warping, strong single-armed and two-armed spiral structures develop in the disc. Generally, single-armed spiral structures are apparent first but wind up quickly, and two-armed spiral structures become prominent after single-armed spiral structures wind up. The winding rate of the spiral structures can be well understood by studying the slope of inner Lindblad resonances, as both single-armed and two-armed spirals turn out to be kinematic density waves whose pattern speed follows inner Lindblad resonances. The curve of $\Omega - \kappa/m$ is steeper for $m = 1$ then for $m = 2$ at all radii, which leads to a faster winding rate of $m = 1$ modes. Nevertheless, the winding rate for the outer region of the disc is significantly lower (both for $m = 1$ and $m = 2$ modes), such that spiral structures can persist for several Gyrs.

In the inner region of the stellar disc, three distinctive generations can be found for the fast-winding single-armed spiral structures, which we attribute to subhalo A, B and G, respectively. We demonstrated such correlation by showing that spiral structures are not present when we remove the corresponding subhaloes, and that the peak strength of spiral structures in most cases correlates very well with the torque exerted by the subhalo. This shows that the majority of interactions between the subhaloes and the disc in our simulations are impulsive with resonances playing a minor role. The fact that strong single-armed spiral structures form in response to each massive subhalo, i.e. with a mass comparable to that of the disc, may provide a way to probe the properties of subhaloes interacting with the central galaxy.

It is worth reiterating that we have not simulated the main dark matter halo with live particles to avoid generations of spurious modes in the disc due to the coarse graininess of the halo (i.e. due to the Poisson noise) which is inevitable in present state-of-the-art simulations. In reality, however, subhaloes will suffer from a stronger dynamical friction caused by the main dark matter halo, which may influence the evolution of the subhaloes. We have verified that this does not effect our results in any significant way, as the mass loss of subhaloes is similar regardless of the presence of the live halo as is the time spent in the vicinity of the disc during which subhaloes exert most torque and resonances.

A live dark matter halo may also have impact on the torque strength and on the waves in the stellar disc. As subhaloes approach the innermost regions, the centre of the dark matter halo and the stellar disc moves slightly in accord with the movement of subhaloes. This may result in a smaller $m = 1$ torque. Additionally, in a live dark matter main halo, subhaloes may lead to distortions in the inner halo, which in turn act upon subhaloes and the disc, and damp bending waves in the disc (Sellwood et al., 1998; Nelson & Tremaine, 1995). As far as the warp structures are concerned, distortions of the inner dark matter main halo due to a passing subhalo can amplify the torques exerted on the disc (Weinberg, 1998; Vesperini & Weinberg, 2000; Gómez et al., 2016). We expect such effects also exist for spiral structures, which may even lead to stronger responses when a live dark matter main halo is present. In this work, we focus only on the impact of torques generated by the subhaloes. A study including the response of the dark matter main halo will require very high resolution simulations (similar to the resolution of level-1 Aquarius simulation), which is beyond the scope of this paper.

Our results demonstrate a clear link between the modes in the disc and the individual passages of massive satellites with realistic masses and orbits extracted from cosmological simulations. Over 7 Gyrs of cosmic time only $2-3$ encounters are needed to continuously re-generate and sustain grand-design spiral arms in the disc. Our stellar disc has been intentionally setup to have a high Toomre's Q profile throughout, making it possible to isolate the effects of subhaloes only. With a disc more dominated by self-gravity we expect that grand-design spiral arms triggered by satellites will themselves be a source of flocculent arms thanks to swing amplification. Hence, stellar disc interaction with satellites, within the standard hierarchical structure formation scenario, appears as a very promising and natural way of generating a variety of spiral structures in the discs as well as bars, warps, tilted rings and lopsidedness.

*This work was performed on: DiRAC Darwin Supercomputer hosted by the University of Cambridge High Performance Computing Service (http://www.hpc.cam.ac.uk/), provided by Dell Inc. using Strategic Research Infrastructure Funding from the Higher Education Funding Council for England and funding from the Science and Technology Facilities Council; DiRAC Complexity system, operated by the University of Leicester IT Services, which forms part of the STFC DiRAC HPC Facility (www.dirac.ac.uk). This equipment is funded by BIS National E-Infrastructure capital grant ST/K000373/1 and STFC DiRAC Operations grant ST/K0003259/1; COSMA Data Centric system at Durham University, operated by the Institute for Computational Cosmology on behalf of the STFC DiRAC HPC Facility. This equipment was funded by a BIS National E-infrastructure capital grant ST/K00042X/1, STFC capital grant ST/K00087X/1, DiRAC Operations grant ST/K003267/1 and Durham University. DiRAC is part of the National E-Infrastructure.

Appendix

Appendix 4.A Fitting Function for the Halo

In this appendix we describe our fitting function to the density distribution of the smooth part of dark matter halo in the Phase-3 simulation. For the radial density distribution, we split the profile into two regions: the main halo profile $\rho_{\rm I}(r)$ and the outer region profile $\rho_{\rm O}(r)$. We fit the main halo region with two Einasto profiles, namely

$$\rho_{\rm I}(r) = \begin{cases} \rho_1 \exp\left[-\frac{2}{\alpha_1}\left((r/R_1)^{\alpha_1}-1\right)\right] & \text{if } r < R_1, \\ \rho_1 \exp\left[-\frac{2}{\alpha_2}\left((r/R_1)^{\alpha_2}-1\right)\right] & \text{otherwise} \end{cases} \tag{4.11}$$

where $R_1 = 10\,{\rm kpc}$ is the scale radius, $\rho_1 = 9\times10^6\,{\rm M}_\odot/{\rm kpc}^3$ is the scale density, $\alpha_1 = 0.2$ and $\alpha_2 = 0.07$ are two shape parameters.

The outer region is fitted with a single Einasto profile,

$$\rho_{\rm O} = \rho_2 \exp\left[-\frac{2}{\alpha_3}\left((r/R_2)^{\alpha_3}-1\right)\right], \tag{4.12}$$

where $R_2 = 1.3\,{\rm Mpc}$ is the scale radius, $\rho_2 = 1.598\times10^2\,{\rm M}_\odot/{\rm kpc}^3$ is the scale density and $\alpha_3 = 3$ is the shape parameter. The spherical density distribution of the whole halo is then

$$\rho_{\rm S}(r) = \rho_{\rm I}(r) + \rho_{\rm O}(r). \tag{4.13}$$

The resulting spherically averaged halo profile, compared with the simulated dark matter halo profile is shown in the left panel of Figure 4.12.

We do not set up the axis ratio profiles of our triaxial dark matter halo model by fitting the triaxial profile of the simulated dark matter halo directly, since we expect a much rounder inner halo profile due to missing baryonic effects. Instead, we model the axis ratios $p = b/a$

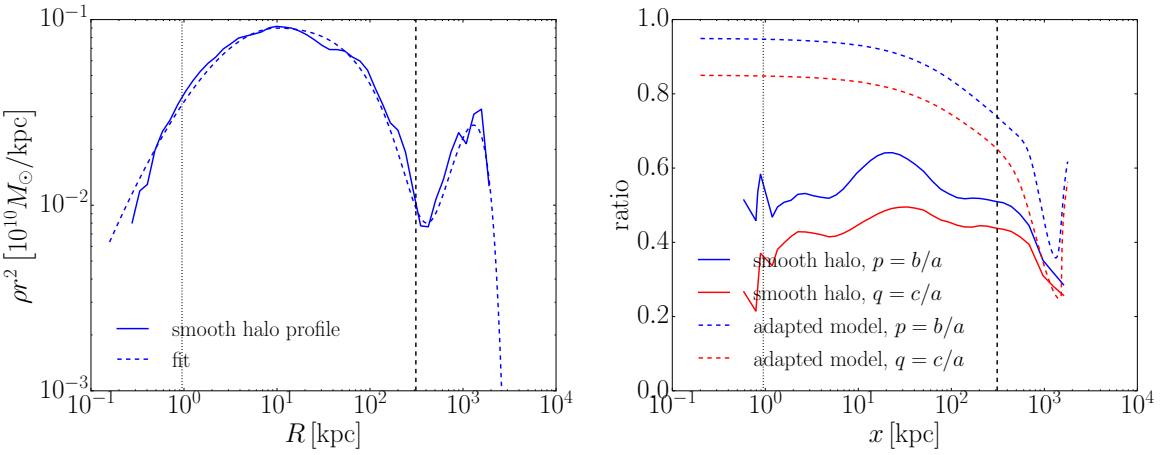

Fig. 4.12 Fit to the smooth part of the halo in a simulation with the Aq-A halo and a static disc potential. The smooth part includes all particles except for those that become part of subhaloes from $z = 1$ to $z = 0$. In both plots, the solid curves represents the data while the dashed curves represent our analytic model. Left: the ρr^2 profile, where ρ is the spherically averaged density. The valley in the density profile at $R = 400\,\mathrm{kpc}$ marks the outer boundary of the main halo. Right: the halo shape, i.e. the ratios of the three axes: $p = b/a$ and $q = c/a$, where a, b and c are the length of three axes with $a > b > c$. We model the dark matter halo with triaxial models whose central region is more spherical than the data to account for the missing baryonic effect. The vertical dotted lines in both plots indicate $2.8\,\varepsilon = 0.96\,\mathrm{kpc}$, where ε is the softening length of dark matter particle. The vertical dashed lines represent the virial radius of the halo.

and $q = c/a$ with the following equation

$$p(r) = 0.35 + \frac{0.6}{1 + \exp\left[\log(r/r_\mathrm{c})/\log(r_\mathrm{s})\right]}, \tag{4.14}$$

and

$$q(r) = 0.25 + \frac{0.6}{1 + \exp\left[\log(r/r_\mathrm{c})/\log(r_\mathrm{s})\right]}, \tag{4.15}$$

where $r_\mathrm{c} = 5.01 \times 10^2\,\mathrm{kpc}$ and $r_\mathrm{s} = 3.16\,\mathrm{kpc}$ are the two shape parameters. The triaxial profile is implemented in the simulation as two spherical harmonic density components as described in Appendix 4.B.

Appendix 4.B Estimating Triaxial Density Profile

We need to relate the triaxial profile of the halo with the density profiles representing two triaxial parts $\rho_{\mathrm{T}1}(r)$ and $\rho_{\mathrm{T}2}(r)$ before we can use it in the simulation. The density distribution

on the three axes is related to $\rho_{\rm T1}$ and $\rho_{\rm T2}$ through

$$\rho_{\rm x}(r) = \rho_{\rm S}(r) + \frac{1}{2}\rho_{\rm T1}(r) + 3\rho_{\rm T2}(r), \tag{4.16}$$

$$\rho_{\rm y}(r) = \rho_{\rm S}(r) + \frac{1}{2}\rho_{\rm T1}(r) - 3\rho_{\rm T2}(r), \tag{4.17}$$

$$\rho_{\rm z}(r) = \rho_{\rm S}(r) - \rho_{\rm T1}(r). \tag{4.18}$$

We have to find $\rho_{\rm T1}(r)$ and $\rho_{\rm T2}(r)$ so that the triaxial profile is satisfied, i.e.

$$\rho_{\rm x}(r) = \rho_{\rm y}(rp(r)) = \rho_{\rm z}(rq(r)). \tag{4.19}$$

This equation is hard to solve analytically. We therefore approximate it by assuming that locally the density profile follows a power law of index $\frac{{\rm d}\log(\rho)}{{\rm d}\log({\rm r})}$. We can rewrite Equation (4.19) as

$$\rho_{\rm x}(r) = \frac{\rho_{\rm y}(r)}{p(r)^{\alpha}} = \frac{\rho_{\rm z}(r)}{q(r)^{\alpha}}, \tag{4.20}$$

where $\alpha = -\frac{{\rm d}\log(\rho)}{{\rm d}\log({\rm r})}$ is the negative power law index. Solving this equation yields Equation (4.2) and (4.3). We implement this approximation and calculated the resulting triaxial profile, as shown in the right panel of Figure 4.12. The profile is rounder in the inner region and gradually decreases to the simulated profile at the outer region, as expected.

Appendix 4.C Calculating Halo Potential from Its Density Profile

The density distribution of our smooth halo follows Equation (4.4). It is trivial to calculate the potential for the spherical component $\rho_{\rm S}(r)$. To calculate potential of the triaxial part, we start from the Poisson's equation

$$\nabla^2\Phi_{\rm T}(r,\theta,\phi) = 4\pi G\rho_{\rm T}(r,\theta,\phi)\,. \tag{4.21}$$

Assuming

$$\Phi_{\rm T}(r,\theta,\phi) = \sum_m\sum_l \Phi^l_{{\rm T},m}(r)Y^l_m(\theta,\phi)\,, \tag{4.22}$$

and taking the density form as

$$\rho_{\rm T}(r,\theta,\phi) = \rho_{\rm T}(r)Y^{l_0}_2(\theta,\phi)\,, \tag{4.23}$$

where l_0 can be 0 and 2 for the two spherical harmonic functions used in our model. We can easily find that $\Phi^l_{\mathrm{T},m}(r)$ is non-zero if and only if $m = 2$ and $l = l_0$. For simplicity we let $\Phi_{\mathrm{T}}(r) = \Phi^{l_0}_{\mathrm{T},2}(r)$. We find

$$\frac{1}{r^2}\frac{\partial}{\partial r}\left(r^2\frac{\partial}{\partial r}\Phi_{\mathrm{T}}(r)\right) - \frac{6}{r^2}\Phi_{\mathrm{T}}(r) = 4\pi G\rho_{\mathrm{T}}(r)\,. \tag{4.24}$$

The second term on LHS is contributed by $\nabla^2 Y^l_2(\theta,\phi)$. Green's function for a delta density function at r_0, i.e. $\rho_{\mathrm{T}}(r) = \delta(r - r_0)$, is

$$\mathscr{G}(r, r_0) = -\frac{1}{5}\frac{r^2_<}{r^3_>}\,, \tag{4.25}$$

where $r_<$ and $r_>$ is the smaller and larger value in r and r_0, respectively. The solution to the equation is hence

$$\Phi_{\mathrm{T}}(r) = 4\pi G\int_0^\infty \mathscr{G}(r, r_0)\rho_{\mathrm{T}}(r_0)r_0^2\,\mathrm{d}r_0\,. \tag{4.26}$$

where we convolve the density profile $\rho_{\mathrm{T}}(r_0)$ over the radius r_0 from 0 to ∞ with Green's fuction $\mathscr{G}(r, r_0)$. The potential and the force of the halo can then be calculated accurately with a 1-dimensional integration in the simulation.

Appendix 4.D Removing subhalo A and B

Further to Section 4.3.5 where we study the impact of each halo, we also run a simulation with subhalo A and B removed at a same time. Note that since subhaloes A and C are the same subhalo hitting the disc twice, in this simulation subhalo C is also removed. As shown in Figure 4.13, when subhaloes A and B are both removed, only very weak modes develop for $z > 0.7$, demonstrating that the first two generation of modes are mainly caused by subhaloes A and B.

Appendix 4.E Subhalo inspirals in live and static haloes

To study the influence of substituting the live main dark matter halo with an analytic halo potential, we compare the inspiral of subhaloes listed in Table 4.1 in the Phase-1 and Phase-3 simulation. The evolution of each subhalo's mass and distance from the centre of the main halo is illustrated in Figure 4.14. As shown in left panels, subhaloes lose significant amount of mass every time they go through the central region of the main halo. The mass loss

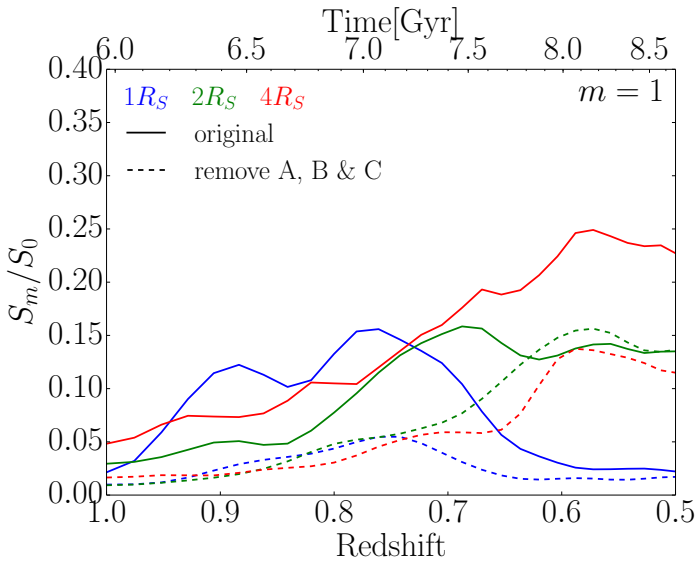

Fig. 4.13 Simulation with subhaloes A and B removed. The first and the second generation of modes are absent, demonstrating clearly that these modes are mostly caused by subhaloes A and B.

with a live halo (in blue) and with an analytic halo (in green) is generally comparable up to the pericentric passage, ranging from 50% to 80%. However, after the passage trough the stellar disc the mass loss of subhaloes is typically larger in the Phase-3 than in the Phase-1 simulation (which does not contain a live stellar disc).

As can be seen from the panels on the right, for subhaloes A, B and C the time of the pericentric passage in the two simulations is very similar (as majority of their trajectory has been computed prior to the start of the Phase-3 with the live dark matter halo present), while other subhaloes reach pericentre somewhat earlier in the Phase-3 than in the Phase-1 simulation. This is due to the fact that in the Phase-3 simulation, the lack of the main dark matter halo leads to a much lower dynamical friction on the subhaloes. Nonetheless, this should not affect our results regarding the response of the stellar disc to the subhaloes. In fact, we have verified that the velocity of the impact is comparable (within a factor of 1.2) and that the time subhaloes spend within half of the apocentre is comparable as well (within factors of 0.85 to 1.17).

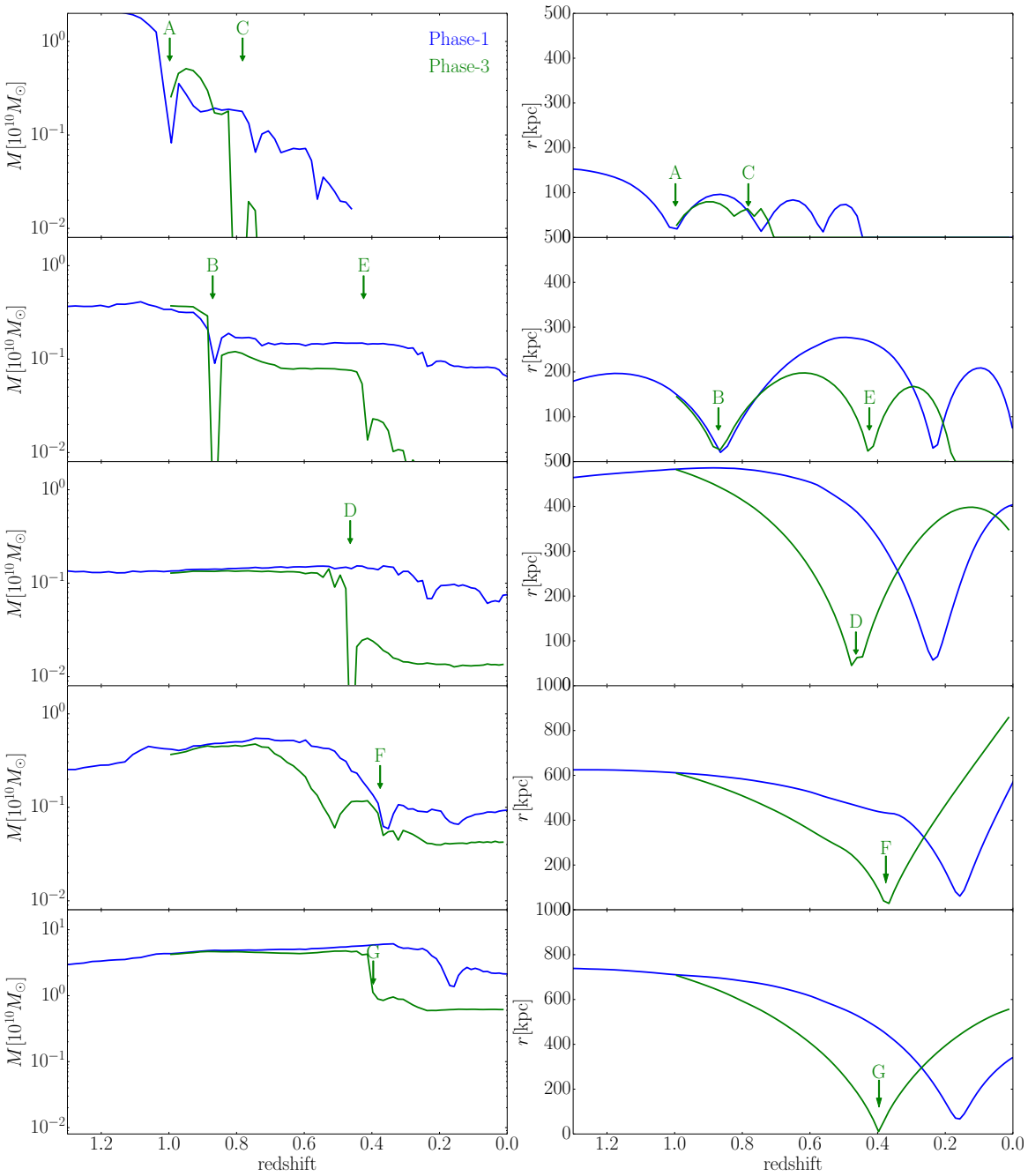

Fig. 4.14 Mass evolution (left) and distance from the centre (right) of subhaloes as they pass through the central region of the halo and the disc. The impact times in the Phase-3 simulation of the subhaloes are marked with vertical arrows. Up to the passage through the pericentre mass loss is comparable in the two simulations. For earlier impacts (subhaloes A, B and C), the impacting time corresponds very well between the two simulations, while impacts happen earlier in the Phase-3 simulation for subhaloes D to G. Note that subhaloes A/C and B/E are largely disrupted at the later times of the simulation, where we truncate the curves.

Chapter 5

Conclusion

The formation of spiral structures is complex and cannot be explained with a single, simple theory. Established works indicate that depending on the property of the disc and the perturbation, different factors including self-gravity, the dynamical temperature of the disc, external tidal torques, and the presence of gas may effect spiral structure formation. In the scenario of tidally-induced spiral structures, the tidal force from the triaxial parent dark matter halo and its subhaloes may exert strong tidal torque on the stellar disc, which may lead to spiral structures. In this Thesis, I carefully performed high-resolution N-body simulations to study this process, with realistic dark matter profiles and discs with different levels of self-gravity.

In Chapter 3 (published as Hu & Sijacki 2016), I performed simulations with stellar discs in analytic, triaxial dark matter potentials. I found that the tidal torque exerted by a triaxial parent dark matter halo leads to two-armed grand-design spiral structures if and only if the triaxiality varies with time non-adiabatically. Further numerical experiments indicated that realistic fluctuations of triaxiality of dark matter haloes, due to the hierarchical structure formation and merging, are sufficient to trigger spiral structures through this mechanism. Spiral structures formed due to tidal torques are well-defined two-armed structures, extending to the edge of the disc. The self-gravity of the disc is not important in the formation of spiral structures of this kind, as similar spiral structures form in simulations with high, low and no self-gravity.

The nature of these spiral structures is kinematic density waves. This is demonstrated by the power spectra of the disc, as the contours of the highest power superpose with the inner Lindblad resonance. The pattern speed of the inner Lindblad resonance slightly decreases as a function of radius. As a result, the spiral structures are slowly winding, with a typical lifetime of several Gyrs.

When misaligned with the dark matter halo, stellar discs develop warps as a response to non-zero torques in the disc plane. After projecting the disc onto its disc plane, I found that the evolution of the spiral structures is similar to the simulation where the disc and the halo are aligned. For all simulations at all radii, there is a good correlation between the spiral strength and the torque strength. This possibly provides a way to infer the triaxiality of the dark matter halo through the strength of spiral structures.

When the surface density of the disc is high, so that the Toomre's Q parameter is close to unity in the inner part of the disc, grand-design spiral structures still form at the beginning of the simulation, if the resolution of the simulation is high enough. However, grand-design spiral structures in the inner disc soon break up to form transient spiral structures similar to those in Sellwood & Carlberg (2014), demonstrating that the gravity-induced spirals dominate the long-term evolution of the disc. Compared to the simulation without a triaxial halo, the strength of transient spiral structures with a triaxial halo is higher, indicating that the grand-design spiral structures forming at the beginning of the simulation serve as a source of swing amplification.

In Chapter 4 (Hu & Sijacki, MNRAS, submitted), I studied the influence of dark matter subhaloes. I first reran the Aquarius simulation (Springel et al., 2008) with an adiabatically-introduced rigid disc potential to account for the influence of disc on the halo profile, and then performed simulations with an analytic, triaxial dark matter halo potential, live subhaloes and a live stellar disc.

In the course of the simulation, from $z = 1$ to $z = 0$, four massive subhaloes interact with the inner $5R_{\rm s}$ of the disc, where $R_{\rm s} = 3.13\,{\rm kpc}$ is the scale length of the disc. In addition, a very massive subhalo flies over the disc plane with the impact radius of less than $3R_{\rm s}$. These events leads to significant disc heating in the outskirts as well as three distinct generations of spiral structures, which can be distinguished most clearly in the inner region of the disc. By changing the mass of each subhalo, we find that the three generations of spiral structures are caused mainly by three different impact events. For each generation, counter-rotating single-armed spiral structures form first. They wind up in about $\sim 1\,{\rm Gyr}$ in the inner disc, before co-rotating two-armed spiral structures become prominent.

The nature of both single-armed and two-armed spiral structures are found to be kinematic density waves, as indicated by their power spectra. When $m = 1$, the pattern speed of the structures is $\Omega_{\rm P} = \Omega - \kappa < 0$, causing the single-armed spiral patterns to be counter rotating. The slope of the pattern speed is larger for $m = 1$ than for $m = 2$, which explains why $m = 1$ spiral structures wind up more quickly than the $m = 2$ spiral structures.

We conclude that the subhaloes interact with the stellar disc impulsively based on the following observations: *a)* the impact time is significantly shorter than the typical period

of a star, *b)* the rotating velocity of subhaloes is generally larger than the pattern speed of resonances in the disc and *c)* the strength of spiral structures correlates well with the normalised torque strength. Similar to Chapter 3, the last finding indicates that it may be possible to infer properties of subhaloes based on the spiral structures they cause.

This Thesis not only sheds new light on the interaction between dark matter halos and stellar discs but it opens new avenues of research to be pursued in future.

Correlation between spiral strength and torque strength. In this Thesis I found a strong correlation between spiral strength and torque strength for both the parent dark matter halo and for the subhaloes. Spiral structures of some observed galaxies are attributed to their companions (e.g. Kendall et al., 2011). It would be interesting to test our simulation results with these observations. When an obvious companion is not present, one may also apply the results of our simulation to infer the properties of the main halo or subhaloes that presumably caused the observed spiral structures.

The effect of live dark matter main halo. In this Thesis I used analytic dark matter main haloes for most of the simulations. As a result, only the influence of dark matter haloes on the stellar disc and the spiral structures are studied. Stellar disc may, however, change the profile, shape and the alignment of the dark matter halo, especially in the inner regions. A simulation with a live dark matter main halo may therefore improve our understanding of the interplay between the disc and the halo. Furthermore employing live dark matter haloes enables one to better account for the distortion of the main halo during a subhalo impact, which is found to have an influence on the total tidal torque.

To include a live dark matter main halo in the simulation that studies spiral structures, one need to either *a)* use dark matter particles with a similar particle mass to the star particles, or *b)* use a similar number of dark matter particles as star particles. We have tested and found that solution *b* does not work, because in this case the mass of each dark matter particle is two orders of magnitude larger than that of the star particles, leading to large numerical perturbations to the stellar disc, similar in nature to the GMCs studied in D'Onghia et al. (2013). Solution *a*, however, is not feasible with the current state-of-the-art simulations. The mass of each star particle in a disc with 10^6 particles is comparable to the mass of high resolution dark matter particles of the level 2 Aquarius simulation, which means more than 5×10^8 dark matter particles are needed. To study the effect of disc self-gravity, one needs a disc with 10^8 star particles, which then requires $\sim 5 \times 10^{10}$ dark matter particles, which is not feasible with the current codes. With the development of computing power, especially with GPU computing and Intel Xeon Phi, one may begin to tackle this problem.

The influence of environment. In this Thesis I simulated isolated galaxy models, without cosmological gas inflows or mergers. Inflows of dynamically cold gas may help the

formation of gravity-induced spiral structures. Minor mergers should behave similarly to the impact of subhaloes, but major mergers may disrupt the disc more drastically. Athanassoula et al. (2016) found that a merger of two galaxies with hot gas haloes could disrupt the halo and form a stellar disc with a bulge, a bar, and spiral structures. One may study the influence of major mergers to see *a)* how much will mergers disrupt spiral structures, and *b)* if the disc is disrupted completely and formed anew, how self-gravity and external torque interplay when spiral structures form in the new disc. As multiple mergers happen in the history of a galaxy, one can study the effect of multiple mergers (minor or major) to see if the frequency of mergers may be high enough to trigger spiral structures persistently.

State-of-the-art cosmological simulations (e.g. Illustris simulation, Vogelsberger et al. 2014; Genel et al. 2014; Sijacki et al. 2015; EAGLE, Schaye et al. 2015; and Horizon-AGN, Dubois et al. 2016) have successfully generated galaxies with realistic disc properties and spiral structures. However, the resolution of these simulations is still too coarse for the study of dynamics of spiral structures. To study the effect of environment, one can extract merger and inflow history of a galaxy from a cosmological simulation and reproduce them in a simulation of an isolated disc with much higher spatial resolution (adopting similar methods used in Chapter 4). Alternatively, one may consider zoom-in cosmological simulations of spiral galaxies formed in large-scale cosmological simulations. These simulations would however be very challenging as they require zoom-ins across several orders of magnitude and would be affected by the same issues disscused for the live haloes.

The effect of the interstellar medium. In this Thesis no gaseous components were included. Further simulations including a gaseous component would be extremely interesting as gas may *a)* form spiral structures in response to tidal torques and stellar spirals or due to swing amplification, *b)* develop shocks that leads to giant molecular clouds and hence star formation. The evolution of the gaseous component is also subject to cooling and heating processes, background and local radiation, AGN and stellar feedback, and chemical evolution, which may influence the efficiency of star formation and therefore the injection of cold component to the stellar disc. Previous simulations have studied these processes (e.g. Sellwood & Carlberg, 1984; Gittins & Clarke, 2004; Dobbs, 2008, see also Section 1.4.3), but a high resolution simulation with both gaseous and stellar disc and state-of-the-art sub-grid physics may help us understand how these process are coupled together. For example, the injection of a cold component may be biased towards certain locations in the disc with regard to the spiral structures, leading to complex changes to the disc structure. Such change may lead to different kinds of spiral structures. Similarly, stellar feedback from the stellar disc may be more concentrated in spiral structures. One can study how such feedback would

influence the gaseous disc and suppress or enchance star formation close to the stellar spiral structures.

References

Aarseth S. J., 1963, MNRAS, 126, 223

Abraham R. G., 1998, ArXiv Astrophysics e-prints,

Alam S., et al., 2015, ApJS, 219, 12

Angulo R. E., Springel V., White S. D. M., Jenkins A., Baugh C. M., Frenk C. S., 2012, MNRAS, 426, 2046

Athanassoula E., 2012, MNRAS, 426, L46

Athanassoula E., Rodionov S. A., Peschken N., Lambert J. C., 2016, ApJ, 821, 90

Baba J., Saitoh T. R., Wada K., 2013, ApJ, 763, 46

Bailin J., Steinmetz M., 2005, ApJ, 627, 647

Bailin J., et al., 2005, ApJ, 627, L17

Bardeen J. M., Bond J. R., Kaiser N., Szalay A. S., 1986, ApJ, 304, 15

Barnes J., Efstathiou G., 1987, ApJ, 319, 575

Barnes J., Hut P., 1986, Nature, 324, 446

Behroozi P. S., Wechsler R. H., Conroy C., 2013, ApJ, 770, 57

Belokurov V., et al., 2006, ApJ, 642, L137

Berger M. J., Colella P., 1989, Journal of computational Physics, 82, 64

Berger M., Oliger J., 1984, Journal of Computational Physics, 53, 484

Bertin G., Lin C. C., 1996, Spiral structure in galaxies a density wave theory. Cambridge, MA MIT Press

Binney J., 1978, MNRAS, 183, 779

Binney J., 1987, Galactic dynamics. Princeton University Press

Binney J., Jiang I.-G., Dutta S., 1998, MNRAS, 297, 1237

Binney J., et al., 2014, MNRAS, 439, 1231

Bissantz N., Gerhard O., 2002, MNRAS, 330, 591

Black J. H., 1981, MNRAS, 197, 553

Bose S., et al., 2017, MNRAS, 464, 4520

Bowden A., Evans N., Belokurov V., 2013, MNRAS, 435, 928

Boylan-Kolchin M., Ma C.-P., Quataert E., 2008, MNRAS, 383, 93

Bryan S. E., Kay S. T., Duffy A. R., Schaye J., Dalla Vecchia C., Booth C. M., 2013, MNRAS, 429, 3316

Buitrago F., Trujillo I., Conselice C. J., Bouwens R. J., Dickinson M., Yan H., 2008, ApJ, 687, L61

Buitrago F., Trujillo I., Conselice C. J., Häußler B., 2013, MNRAS, 428, 1460

Bullock J. S., 2010, preprint, (arXiv:1009.4505)

Cappellari M., et al., 2013, MNRAS, 432, 1709

Cicone C., et al., 2014, A&A, 562, A21

Clarke C., Gittins D., 2006, MNRAS, 371, 530

Collins M. L. M., et al., 2010, MNRAS, 407, 2411

Conselice C. J., Blackburne J. A., Papovich C., 2005, ApJ, 620, 564

Costa T., Sijacki D., Haehnelt M. G., 2014, MNRAS, 444, 2355

D'Onghia E., Springel V., Hernquist L., Keres D., 2010, ApJ, 709, 1138

D'Onghia E., Vogelsberger M., Hernquist L., 2013, ApJ, 766, 34

D'Onghia E., Madau P., Vera-Ciro C., Quillen A., Hernquist L., 2016, ApJ, 823, 4

Dale J. E., Ercolano B., Bonnell I. A., 2013, MNRAS, 431, 1062

Dark Energy Survey Collaboration et al., 2016, MNRAS, 460, 1270

Dawson K. S., et al., 2013, AJ, 145, 10

Dawson K. S., et al., 2016, AJ, 151, 44

DeBuhr J., Ma C.-P., White S. D., 2012, MNRAS, 426, 983

Debattista V. P., Moore B., Quinn T., Kazantzidis S., Maas R., Mayer L., Read J., Stadel J., 2008, ApJ, 681, 1076

Debattista V. P., Roškar R., Valluri M., Quinn T., Moore B., Wadsley J., 2013, MNRAS, 434, 2971

Dekel A., Silk J., 1986, ApJ, 303, 39

Diemand J., Moore B., 2011, Advanced Science Letters, 4, 297

Diemand J., Kuhlen M., Madau P., Zemp M., Moore B., Potter D., Stadel J., 2008, Nature, 454, 735

Djorgovski S., Davis M., 1987, ApJ, 313, 59

Dobbs C. L., 2008, MNRAS, 391, 844

Dobbs C., Baba J., 2014, PASA, 31, 35

Dobbs C. L., Bonnell I. A., 2006, MNRAS, 367, 873

Dobbs C. L., Bonnell I. A., 2007, MNRAS, 376, 1747

Dobbs C. L., Theis C., Pringle J. E., Bate M. R., 2010, MNRAS, 403, 625

Dolag K., Borgani S., Schindler S., Diaferio A., Bykov A. M., 2008, Space Sci. Rev., 134, 229

Dolag K., Borgani S., Murante G., Springel V., 2009, MNRAS, 399, 497

Dressler A., Lynden-Bell D., Burstein D., Davies R. L., Faber S. M., Terlevich R., Wegner G., 1987, ApJ, 313, 42

Dubinski J., 1994, ApJ, 431, 617

Dubinski J., Chakrabarty D., 2009, ApJ, 703, 2068

Dubinski J., Gauthier J.-R., Widrow L., Nickerson S., 2008, in Funes J. G., Corsini E. M., eds, Astronomical Society of the Pacific Conference Series Vol. 396, Formation and Evolution of Galaxy Disks. p. 321 (arXiv:0802.3997)

Dubois Y., Peirani S., Pichon C., Devriendt J., Gavazzi R., Welker C., Volonteri M., 2016, MNRAS, 463, 3948

Efstathiou G., 1992, MNRAS, 256, 43P

Efstathiou G., Davis M., White S. D. M., Frenk C. S., 1985, ApJS, 57, 241

Einasto J., 1965, Trudy Astrofizicheskogo Instituta Alma-Ata, 5, 87

Erkal D., Belokurov V., 2015, MNRAS, 454, 3542

Faber S. M., Jackson R. E., 1976, ApJ, 204, 668

Fabian A. C., 1999, MNRAS, 308, L39

Fouvry J.-B., Pichon C., 2015, MNRAS, 449, 1982

Fouvry J. B., Pichon C., Magorrian J., Chavanis P. H., 2015, A&A, 584, A129

Franx M., de Zeeuw T., 1992, ApJ, 392, L47

Freeman K., 1970, ApJ, 160, 811

Frenk C. S., White S. D., Davis M., Efstathiou G., 1988, ApJ, 327, 507

Frenk C. S., White S. D. M., Efstathiou G., Davis M., 1990, ApJ, 351, 10

Frenk C. S., et al., 1999, ApJ, 525, 554

Fujii M. S., Baba J., Saitoh T. R., Makino J., Kokubo E., Wada K., 2011, ApJ, 730, 109

Gao L., White S. D. M., Jenkins A., Stoehr F., Springel V., 2004, MNRAS, 355, 819

Gao L., Navarro J. F., Frenk C. S., Jenkins A., Springel V., White S. D. M., 2012, MNRAS, 425, 2169

Genel S., et al., 2014, MNRAS, 445, 175

Gerhard O., 2002, in , Matter in the Universe. Springer, pp 129–138

Gittins D. M., Clarke C., 2004, MNRAS, 349, 909

Goldreich P., Lynden-Bell D., 1965, MNRAS, 130, 125

Gómez F. A., White S. D. M., Marinacci F., Slater C. T., Grand R. J. J., Springel V., Pakmor R., 2016, MNRAS, 456, 2779

Gómez F. A., White S. D. M., Grand R. J. J., Marinacci F., Springel V., Pakmor R., 2017, MNRAS, 465, 3446

Grand R. J. J., Kawata D., Cropper M., 2012a, MNRAS, 421, 1529

Grand R. J. J., Kawata D., Cropper M., 2012b, MNRAS, 426, 167

Grand R. J. J., Kawata D., Cropper M., 2013, A&A, 553, A77

Gunn J. E., Gott III J. R., 1972, ApJ, 176, 1

Guo Q., et al., 2011, MNRAS, 413, 101

Hahn O., Teyssier R., Carollo C. M., 2010, MNRAS, 405, 274

Hambrick D. C., Ostriker J. P., Johansson P. H., Naab T., 2011, MNRAS, 413, 2421

Hart R. E., et al., 2016, MNRAS, 461, 3663

Heitmann K., Ricker P. M., Warren M. S., Habib S., 2005, ApJS, 160, 28

Heitmann K., et al., 2008, Computational Science and Discovery, 1, 015003

Hernquist L., 1990, ApJ, 356, 359

Hill D. T., et al., 2011, MNRAS, 412, 765

Hockney R. W., Eastwood J. W., 1981, Computer Simulation Using Particles. McGraw-Hill

Howard S., Keel W. C., Byrd G., Burkey J., 1993, ApJ, 417, 502

Hu S., Sijacki D., 2016, MNRAS, 461, 2789

Hubble E. P., 1926, ApJ, 64

Ivezic Z., et al., 2008, Serbian Astronomical Journal, 176, 1

Jenkins A., Frenk C. S., White S. D. M., Colberg J. M., Cole S., Evrard A. E., Couchman H. M. P., Yoshida N., 2001, MNRAS, 321, 372

Jiang C. Y., Jing Y. P., Faltenbacher A., Lin W. P., Li C., 2008, ApJ, 675, 1095

Jing Y., Suto Y., 2002, ApJ, 574, 538

Jing Y., Mo H., Börner G., Fang L., 1995, MNRAS, 276, 417

Julian W. H., Toomre A., 1966, ApJ, 146, 810

Jurić M., et al., 2008, ApJ, 673, 864

Kalnajs A. J., 1965, PhD thesis, HARVARD UNIVERSITY.

Kalnajs A., 1973, in Proceedings of the Astronomical Society of Australia. p. 174

Katz N., Weinberg D. H., Hernquist L., 1996, ApJS, 105, 19

Kauffmann G., Colberg J. M., Diaferio A., White S. D. M., 1999, MNRAS, 303, 188

Kazantzidis S., Zentner A. R., Kravtsov A. V., Bullock J. S., Debattista V. P., 2009, ApJ, 700, 1896

Kendall S., Kennicutt R. C., Clarke C., 2011, MNRAS, 414, 538

Kendall S., Clarke C., Kennicutt R. C., 2015, MNRAS, 446, 4155

Kennicutt R., et al., 2011, Publications of the Astronomical Society of the Pacific

Khoperskov S. A., Bertin G., 2015, MNRAS, 451, 2889

Khoperskov A. V., Khoperskov S. A., Zasov A. V., Bizyaev D. V., Khrapov S. S., 2013, MNRAS, 431, 1230

King A., 2003, ApJ, 596, L27

Klypin A. A., Shandarin S. F., 1983, MNRAS, 204, 891

Klypin A., Kravtsov A. V., Valenzuela O., Prada F., 1999, ApJ, 522, 82

Koposov S. E., Belokurov V., Torrealba G., Evans N. W., 2015, ApJ, 805, 130

Kravtsov A. V., Klypin A. A., Khokhlov A. M., 1997, ApJS, 111, 73

Kravtsov A., Vikhlinin A., Meshscheryakov A., 2014, preprint, (arXiv:1401.7329)

Lacey C., Cole S., 1993, MNRAS, 262, 627

Larson R. B., 1974, MNRAS, 169, 229

Lin D., Pringle J., 1987, ApJ, 320, L87

Lin C., Shu F. H., 1964, ApJ, 140, 646

Lin C. C., Shu F. H., 1966, Proceedings of the National Academy of Science, 55, 229

Lindblad B., 1956, Stockholms Observatoriums Annaler, 19, 7

Lindblad B., 1963, Stockholms Observatoriums Annaler, 22, 5

López-Corredoira M., Cabrera-Lavers A., Garzón F., Hammersley P. L., 2002, A&A, 394, 883

Lovell M. R., Frenk C. S., Eke V. R., Jenkins A., Gao L., Theuns T., 2014, MNRAS, 439, 300

Lynds R., Toomre A., 1976, ApJ, 209, 382

Marulli F., Bonoli S., Branchini E., Gilli R., Moscardini L., Springel V., 2009, MNRAS, 396, 1404

Mateo M. L., 1998, ARA&A, 36, 435

McConnachie A. W., Irwin M. J., Ibata R. A., Dubinski J., Widrow L. M., e.a. 2009, Nature, 461, 66

McGaugh S. S., 2012, AJ, 143, 40

McLeod D. J., McLure R. J., Dunlop J. S., 2016, MNRAS, 459, 3812

McLure R. J., et al., 2013, MNRAS, 432, 2696

McMillan P. J., 2011, MNRAS, 414, 2446

Moetazedian R., Just A., 2016, MNRAS, 459, 2905

Monaghan J. J., Lattanzio J. C., 1985, A&A, 149, 135

Moore B., Ghigna S., Governato F., Lake G., Quinn T., Stadel J., Tozzi P., 1999, ApJ, 524, L19

Mortlock A., et al., 2013, MNRAS, 433, 1185

Moster B. P., Naab T., White S. D. M., 2013, MNRAS, 428, 3121

Navarro J. F., Frenk C. S., White S. D. M., 1996, ApJ, 462, 563

Navarro J. F., et al., 2010, MNRAS, 402, 21

Nelson R. W., Tremaine S., 1995, MNRAS, 275, 897

Peñarrubia J., Benson A. J., Walker M. G., Gilmore G., McConnachie A. W., Mayer L., 2010, MNRAS, 406, 1290

Perlmutter S., et al., 1999, ApJ, 517, 565

Pettitt A. R., Tasker E. J., Wadsley J. W., 2016, MNRAS, 458, 3990

Planck Collaboration et al., 2016, A&A, 594, A13

Press W. H., Schechter P., 1974, ApJ, 187, 425

Purcell C. W., Bullock J. S., Tollerud E. J., Rocha M., Chakrabarti S., 2011, Nature, 477, 301

Quinn T., Katz N., Stadel J., Lake G., 1997, ArXiv Astrophysics e-prints,

Rees M. J., 1986, MNRAS, 218, 25P

Rey-Raposo R., Dobbs C., Agertz O., Alig C., 2017, MNRAS, 464, 3536

Roberts M., Rots A., 1973, A&A, 26, 483

Romeo A. B., 1992, MNRAS, 256, 307

Rupke D. S. N., Veilleux S., 2013, ApJ, 775, L15

Saha P., Tremaine S., 1992, AJ, 104, 1633

Salo H., Laurikainen E., Buta R., Knapen J. H., 2010, ApJ, 715, L56

Sanders R. H., Huntley J. M., 1976, ApJ, 209, 53

Sawala T., et al., 2016, MNRAS, 457, 1931

Scannapieco C., et al., 2012, MNRAS, 423, 1726

Schaye J., et al., 2015, MNRAS, 446, 521

Schechter P., 1976, ApJ, 203, 297

Schmidt B. P., et al., 1998, ApJ, 507, 46

Seigar M. S., Bullock J. S., Barth A. J., Ho L. C., 2006, ApJ, 645, 1012

Sellwood J. A., 2011, MNRAS, 410, 1637

Sellwood J. A., 2012, ApJ, 751, 44

Sellwood J. A., Carlberg R. G., 1984, ApJ, 282, 61

Sellwood J. A., Carlberg R. G., 2014, ApJ, 785, 137

Sellwood J. A., Sparke L. S., 1988, MNRAS, 231, 25P

Sellwood J. A., Nelson R. W., Tremaine S., 1998, ApJ, 506, 590

Sembolini F., et al., 2016, MNRAS, 457, 4063

Shen S., Mo H. J., White S. D. M., Blanton M. R., Kauffmann G., Voges W., Brinkmann J., Csabai I., 2003, MNRAS, 343, 978

Sheth R. K., Tormen G., 1999, MNRAS, 308, 119

Sheth R. K., Mo H. J., Tormen G., 2001, MNRAS, 323, 1

Sijacki D., Springel V., Di Matteo T., Hernquist L., 2007, MNRAS, 380, 877

Sijacki D., Vogelsberger M., Genel S., Springel V., Torrey P., Snyder G. F., Nelson D., Hernquist L., 2015, MNRAS, 452, 575

Silk J., Rees M. J., 1998, A&A, 331, L1

Spitzer Jr. L., 1942, ApJ, 95, 329

Springel V., 2005, MNRAS, 364, 1105

Springel V., White S. D. M., Tormen G., Kauffmann G., 2001, MNRAS, 328, 726

Springel V., Di Matteo T., Hernquist L., 2005a, MNRAS, 361, 776

Springel V., et al., 2005b, Nature, 435, 629

Springel V., et al., 2008, MNRAS, 391, 1685

Sturm E., et al., 2011, ApJ, 733, L16

Taylor J. E., Babul A., 2004, MNRAS, 348, 811

Teyssier R., 2002, A&A, 385, 337

Thomas P. A., et al., 1998, MNRAS, 296, 1061

Tollerud E. J., Bullock J. S., Strigari L. E., Willman B., 2008, ApJ, 688, 277

Toomre 1964, ApJ, 139, 1217

Toomre 1981, in Structure and evolution of normal Galaxies. pp 111–136

Toomre A., Toomre J., 1972, ApJ, 178, 623

Tremonti C. A., et al., 2004, ApJ, 613, 898

Trujillo I., Conselice C. J., Bundy K., Cooper M. C., Eisenhardt P., Ellis R. S., 2007, MNRAS, 382, 109

Tully R. B., Fisher J. R., 1977, A&A, 54, 661

Vallée J. P., 2005, AJ, 130, 569

Vandervoort P. O., 1970, ApJ, 161, 87

Velazquez H., White S. D. M., 1999, MNRAS, 304, 254

Vera-Ciro C. A., Sales L. V., Helmi A., Frenk C. S., Navarro J. F., Springel V., Vogelsberger M., White S. D. M., 2011, MNRAS, 416, 1377

Vesperini E., Weinberg M. D., 2000, ApJ, 534, 598

Vogelsberger M., et al., 2014, MNRAS, 444, 1518

Wadsley J. W., Stadel J., Quinn T., 2004, New Astronomy, 9, 137

Warren M. S., Quinn P. J., Salmon J. K., Zurek W. H., 1992, ApJ, 399, 405

Warren M. S., Abazajian K., Holz D. E., Teodoro L., 2006, ApJ, 646, 881

Weinberg M. D., 1998, MNRAS, 299, 499

Wheeler C., Oñorbe J., Bullock J. S., Boylan-Kolchin M., Elbert O. D., Garrison-Kimmel S., Hopkins P. F., Kereš D., 2015, MNRAS, 453, 1305

Xu G., 1995, ApJS, 98, 355

Yniguez B., Garrison-Kimmel S., Boylan-Kolchin M., Bullock J. S., 2014, MNRAS, 439, 73

Yoshida N., Springel V., White S. D., Tormen G., 2000, ApJ, 544, L87

Zemp M., Gnedin O. Y., Gnedin N. Y., Kravtsov A. V., 2012, ApJ, 748, 54

Zhu Q., Marinacci F., Maji M., Li Y., Springel V., Hernquist L., 2016, MNRAS, 458, 1559

de Vaucouleurs G., 1959, in , Astrophysik IV: Sternsysteme/Astrophysics IV: Stellar Systems. Springer, pp 311–372

de Vaucouleurs G., 1974, in , The Formation and Dynamics of Galaxies. Springer, pp 1–53

van de Voort F., Davis T. A., Kereš D., Quataert E., Faucher-Giguère C.-A., Hopkins P. F., 2015, MNRAS, 451, 3269

von Hoerner S., 1960, ZAp, 50